Silicon carbide and nano-carbons containing cobalt catalysts for the Fisher-Tropsch synthesis

Yuefeng Liu

UNIVERSITÉ DE STRASBOURG

ÉCOLE DOCTORALE DES SCIENCES CHIMIQUES

ICPEES, UMR 7515 CNRS

THÈSE

présentée par

Yuefeng LIU

soutenue le : **16 Septembre 2013**

pour obtenir le grade de

Docteur de l'université de Strasbourg

Discipline / Spécialité : Chimie /Chimie Physique

Silicon carbide and nano-carbons containing cobalt catalysts for the Fischer-Tropsch synthesis

Catalyseurs à base de cobalt supportés sur carbure de silicium et nano-carbones pour la synthèse de Fischer-Tropsch

Membres du jury

Dirtecteur de Thèse:	**Dr. Cuong PHAM-HUU**	Directeur de recherche, UDS, Strasbourg
Rapporteur externe:	**Prof. Magnus RONNING**	Professeur, NTNU, Trondheim (NO)
Rapporteur externe:	**Dr. Andrei KHODAKOV**	Directeur de recherche, USTL, Lille
Examinateur:	**Prof. Sylive BEGIN-COLIN**	Professeur, UDS, Strasbourg
Examinateur:	**Dr. Francis LUCK**	Directeur scientifique, TOTAL, Paris

Acknowledgements

Doing my PhD in France has been a fruitful experience both at a professional and personal level. It has afforded me the opportunity to interact with interesting people around the world. I wish to express my sincerely gratitude to all the people who have contributed to this work as well as to those who have helped me during this pleasant and enjoyable period of time.

This thesis has been performed in the Institut de Chimie et Procédés pour l'Energie, l'Environnement et la Santé (ICPEES, CNRS UMR 7515) in the University of Strasbourg. I will be always appreciative to the faculty, students and staff in the University of Strasbourg, especially in ICPEES where I established a fruitful experience in my research career. I would like also to express my great thanks to the China Scholarship Council (CSC) for the finical support during the PhD degree.

I will be always grateful to my supervisor, Dr. Cuong Pham-Huu, for his guidance, kindness and understanding during my PhD study and research, who always ready to help me and provides me a clearly instruction on the direction of my research. More importantly, affected me deeply with his scientific attitude. During these three years, my research career is gradually opened followed by his scientific sensitivity and insistence in research.

I want to thank Dr. Christian MEMY from IPCMS with his wide knowledge and deep insight in ^{59}Co NMR experiment, with whom I spent meaningful and fruitful three months in physics, Dr. Charlotte Pham and Dr. Patrick Nguyen from SiCat for supporting the SiC-based materials and useful discussions during my research work, and Dr. Ovidiu Ersen from IPCMS with his extremely kindness and for his help during the TEM (EFTEM and 3D-TEM) experiments.

I am indebted to Dr. Magnus Ronning (NTNU), Dr. Andrei Khodakov (USTL), Prof. Sylive Begin-Colin (UdS), Dr. Francis Luck (TOTAL), Dr. Charlotte Pham (SICAT, Membre invité) and Dr. Christian MEMY (UdS, Membre invité) who gave

me the honor and pleasure to form the jury of my thesis, judging constructively my work.

Many thanks would be gave to Benoit de Tymowski for his help at my stating in my thesis to let me going my research work without too much brambles; Fabrice Vigneron, a typical gentle french man, who always help me in time in my heavy experiment work. Houssernou Ba, a full of energy boy, with whom we work out a lot of exciting research results; Jean-Maro Nhut for the help to my french abstract to make peolpe understood by his professional french langegure (of course); Chau Cam Hoang TRAN, a sunshine girl, with whom we produced many (a kilogram....) and verious kinds of carbon materials beads.

My thanks are also equally addressed to the crew in Carbon Nanostructures and Catalysis group for a memorable experience: Dominique Bégin, Dinh Lam Nguyen, Izabela Janowska, Xiaojie Liu, Walid Baaziz, Cuong Duong-Viet, Lai Truong-Phuoc, Seetharamulu Podila, Yu Liu, Shabnam Hajiesmaili, Ouanassa Guellati... I also would like to thank Véronique Verkruysse, Thierry Romero, Pierre Bernhardt, Thierry Dintzer, Secou Sall, Michel Wolf and Alain Rach for their kindly helps over and over again.

Thanks to my great Chinese friends in Strasbourg (Yunjie, Ying, Fuchao, Zhenghua, Quan, Wen, Li…) for their support in good and bad times, and in China (Donghua, Long, Shanhua, Hongliang, Kui, Xinlong, Hongsheng, Dan…), who, despite the distance, were always just beside me.

Out of all these people above all, I would like to thank my family: my parents, typically peasant in China, who spent their whole lives to make me strong and knowledge; Jingjie Luo, my wife, who give me all her love.

Yuefeng LIU

15th, July, 2013, at Strasbourg, France

Table Contents

Résumé - Abstract

1. Introduction

Un des principaux défis de notre siècle est la production et la consommation d'énergie durable. C'est pourquoi, les développements des nouvelles technologies en faveur des faibles émissions de CO_2 devront tenir compte des différentes matières premières existantes et non pleinement exploitées à ce jour, telles que le gaz naturel, le charbon et la biomasse.[1-2] Le gaz de synthèse ($CO + nH_2$) est obtenu soit par reformage du gaz naturel soit par gazéification du charbon et de la biomasse, avant d'être transformé dans des unités de Fischer-Tropsch. Ces unités dérivent du concept originel inventé au début des années 1920 par Franz Fischer et Hans Tropsch,[3-4] et ont suscité un intérêt croissant de la part de la communauté scientifique et industrielle durant ces dernières décennie.[5-8] La synthèse de Fischer-Tropsch (FTS) est aussi utilisée dans d'autres processus de transformation du gaz de synthèse ($2H_2 + CO$) en hydrocarbures liquides comme les procédés Gas-To-Liquids (GTL), Biomass-To-Liquids (BTL) ou Coal-To-Liquids (CTL) permettant de convertir par hydrocraquage les distillats lourds en coupes légères à plus forte valeur ajoutée (naphta, kérosène, gazole et lubrifiants).[9-10]

Depuis ces dernières décennies, de nombreuses unités de production F-T se sont développées afin de valoriser les ressources de charbon ou de gaz naturel à travers le monde, en accord avec les législations environnementales de plus en plus strictes (Figure 1), et permettent de produire environ 400,000 barils par jour.[11] La production reste relativement faible comparée à la production totale d'environ 85 millions de barils par jour de pétrole brut. Toutefois, étant donnée la demande en carburant propre dans le domaine des transports on devrait s'attendre à un fort développement d'unités de production F-T dans un avenir proche. De plus, ces hydrocarbures liquides resteront un moyen important pour le stockage et l'utilisation d'énergie sous forme compacte pour les nombreuses années à venir. L'intérêt de

la technologie FT est également lié à l'exploitation intensive des gaz de schiste durant ces dix dernières années, ce qui modifie sensiblement les ressources du gaz naturel et, par conséquent, son prix.

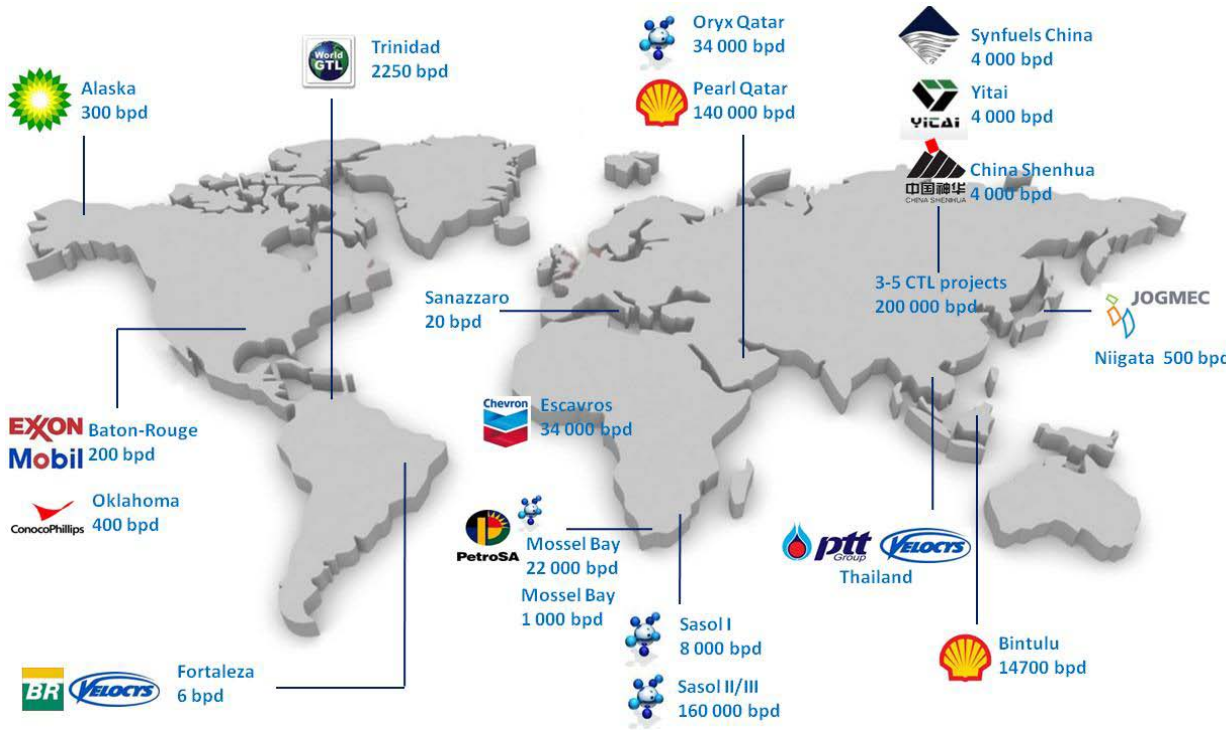

Figure 1. Implantation des unités de production Fischer-Tropsch opérationnelles ou en cours de construction à travers le monde. Source TOTAL.

Les grandes ressources prouvées de gaz naturel et de charbon ont suscité le développement croissant de la réaction de FT pour les prochaines décennies, dans le domaine des transports et des produits chimiques. La réaction F-T doit fonctionner à conversion et sélectivité très élevées afin de réduire les étapes ultérieures de retraitement. Cependant, étant donnée la forte exothermicité de la réaction de F-T (-165 kJ/mol), une conversion trop élevée conduit souvent à la formation d'un gradient de température au sein du lit catalytique, ce qui préjudiciable à la sélectivité globale du procédé en favorisant les l'hydrogénation d'intermédiaires et la réaction de craquage au dépend de la formation d'hydrocarbures à longue chaîne. Les réacteurs multi-tubulaires à lit fixe (Multi-Tubular Fixed Bed MTFB) sont les plus utilisés dans les unités FT car ils présentent de meilleures

facilité dans leur mise en oeuvre.[12-13] Les catalyseurs se présentent sous forme d'extrudés de taille millimétrique afin de réduire les pertes de charge à travers le lit catalytique. Le diamètre des réacteurs MTFB est limité à quelques centimètres et la conversion du CO est maintenue en dessous de 70 % afin d'éviter tous problèmes liés à la formation de points chauds ou à l'emballement de la température du réacteur, néfastes à la sélectivité de la réaction mais également pour la sécurité de l'installation. En général, une partie des produits liquides de réaction sont recyclés dans le réacteur afin d'évacuer la chaleur de réaction.[14] L'ensemble des inconvénients cités ci-dessus a conduit à des études sur le développement de nouvelles technologies de réacteurs de FT, mais également à la recherche de nouveaux supports de catalyseurs ayant une forte conductibilité thermique et une distribution de taille des pores adéquate. Le développement de nouveaux matériaux supports ayant de meilleures propriétés physiques et chimiques permettront d'améliorer la réaction de FT en réduisant autant que possible la perte de sélectivité rencontrée pour des conversions élevées en CO.

Les catalyseurs supportés à base de cobalt sont largement utilisés pour leur activité et leur sélectivité élevées dans le procédé de FT. L'utilisation dans la réaction de FT en lit fixe du carbure de silicium (SiC), comme support de catalyseur, pur ou dopé par différents éléments, a été longuement étudiée au sein de notre groupe, et d'intéressants résultats ont été obtenus.[15-16] Les mousses de SiC dopées à l'alumine permettent d'obtenir dans les mêmes conditions de réaction une meilleure conversion du CO par rapport à son homologue SiC non dopé. De plus, la sélectivité en composés C_{5+} obtenue sur le catalyseur à base de SiC est augmentée de façon significative comparée à celle obtenue sur catalyseurs traditionnels. Cependant, le développement de nouveaux catalyseurs performants en terme d'activité FT et en terme de sélectivité en C_{5+} est encore nécessaire. D'autre part, les matériaux carbonés, et en particulier les matériaux nanocarbonés, tels que les nanotubes et nanofibres de carbone, ont été largement étudiés comme support de catalyseur dans la réaction FT, et les nanotubes de carbone (NTC) ont même été considérés comme nouveau support pour cette réaction. Dans cette thèse, nous allons étudier différents types de catalyseurs à base de cobalt supportés sur α-alumine à large pore, recouverts de nanotubes de carbone, mais aussi sur

carbure de silicium, dopé ou recouvert de TiO_2, pour la réaction de F-T. Les résultats obtenus seront comparés à ceux reportés dans la littérature.

2. Supports hiérarchiquement structurés à base de nanotubes de carbone

2.1. Nanoparticules de cobalt déposées sur nanotubes de carbone/α-Al_2O_3

Les précédentes études menées au laboratoire ont montré l'influence de la nature du support catalytique sur l'activité et la sélectivité de la réaction de F-T, mais aussi sa surface spécifique, son volume poreux et sa distribution de taille de pores.[17-18] Le support va ainsi contribuer aux propriétés finales du catalyseur de F-T et sa nature influer indirectement sur son activité. En outre, dans des conditions favorables de croissance des chaînes carbonées, l'activité des catalyseurs supportés au cobalt ne dépend que faiblement de la dispersion de ce dernier et de la nature du support.[19-24] L'α-Al_2O_3 s'avère être le support le plus performant en terme de sélectivité en C_{5+} grâce notamment à sa structure à larges pores, ce qui permet de réduire considérablement les limitations de transferts de masses. Par contre elle a une activité inférieure à celles obtenues sur les supports traditionnels comme la γ-alumine ou la silice.[25-29] En outre, il s'avère que les nanotubes de carbone (NTC) utilisés comme support, présentent d'excellentes performances catalytiques dans la réaction de F-T, grâce notamment à leurs propriétés exceptionnelles, i.e. forte conductivité thermique et électrique, grande surface effective accessible en raison de sa structure unique ouverte.[30-41] De nombreux travaux antérieurs ont portés sur le rôle des particules métalliques, déposées à l'intérieur ou à l'extérieur des NTC,[38, 42] la taille des particules de cobalt,[32, 43] ou le diamètre et la taille des pores des nanotubes[30, 40] sur les performances catalytiques. Par contre aucune étude à notre connaissance n'a porté sur l'utilisation d'un support hiérarchiquement structuré à base de nanotubes de carbone déposés sur une matrice macroscopique de forme et de taille contrôlées.

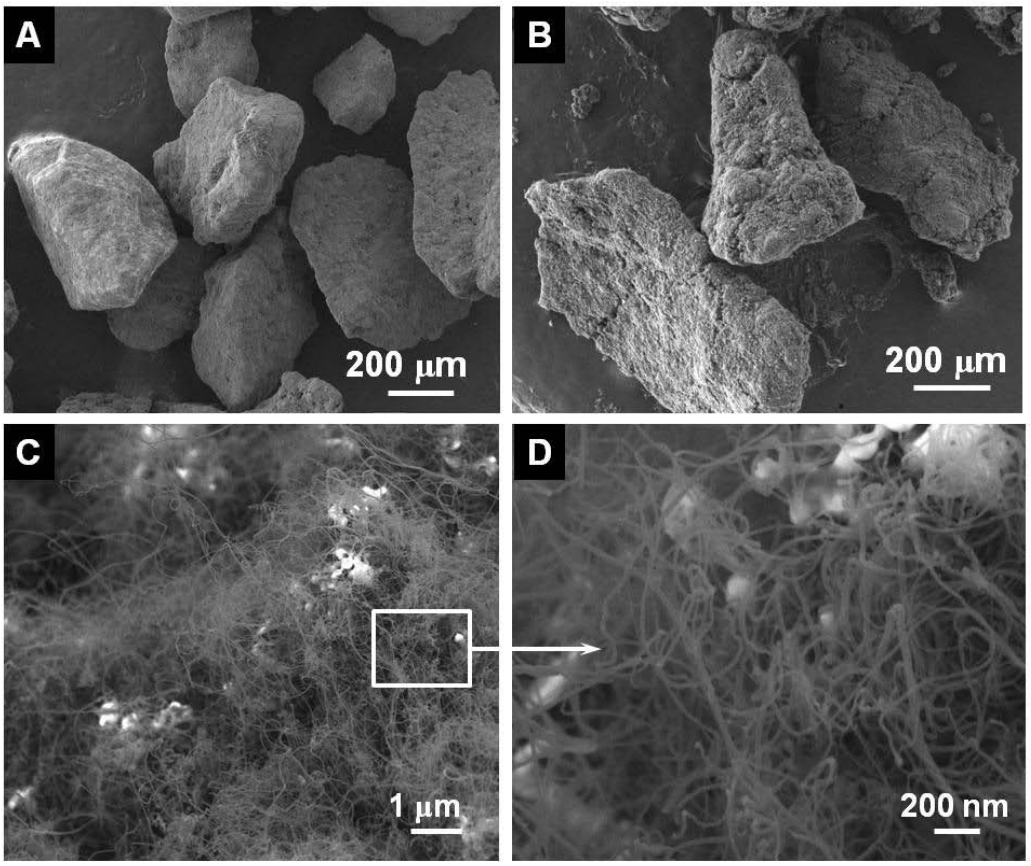

Figure 2. Images MEB basse résolution de **(A)** l'α-Al_2O_3 et **(B,C)** NTC-α-Al_2O_3 **(D)** Image MEB haute résolution de NTC-α-Al_2O_3

Etant donné son caractère fortement exothermique et sa multitude de réactions secondaires, le procédé F-T est l'un des plus complexes en terme de réaction triphasée. La sélectivité en hydrocarbures à longue chaîne (C_{5+}) dépend fortement du profil de température du réacteur, et par conséquent le choix du catalyseur ou du support doit répondre à différents critères: bonne conductivité thermique du support,[44] faible perte de charge à travers le lit catalytique dans le cas des réacteurs à lit fixe,[16, 45] utilisation de tous les sites actifs des nanoparticules d'un point de vue macroscopique, structure du support favorisant à la fois l'accessibilité des réactifs et l'évacuation des produits de réaction.[45] Il est donc intéressant de développer de nouveaux catalyseurs composites structurés et thermiquement conducteurs à base de carbone pour la réaction de F-T. Chin et al.[46] ont étudié la réaction de F-T en utilisant des structures hiérarchisées à base de mousse de FeCrAlY, recouverte d'une fine

couche d'Al_2O_3 dense obtenue par la méthode de "metal organic chemical vapor deposition" (MOCVD). Un réseau de nanotubes de carbone alignés, jouant le rôle de microcanaux achève la structure du support, avant le dépôt de la phase active Co-Re. Un tel catalyseur structuré hiérarchiquement grâce aux nanotubes de carbone, présente une plus grande surface d'ancrage des sites actifs, une forte conductivité thermique et un meilleur transfert de masse. Plusieurs études ont aussi montré que la croissance des nanotubes/nanofibres de carbone sur des matériaux macroporeux offrent un meilleur contact entre les sites actifs et les réactifs, une forte conductivité thermique et un meilleur transfert de masse.[47-50]

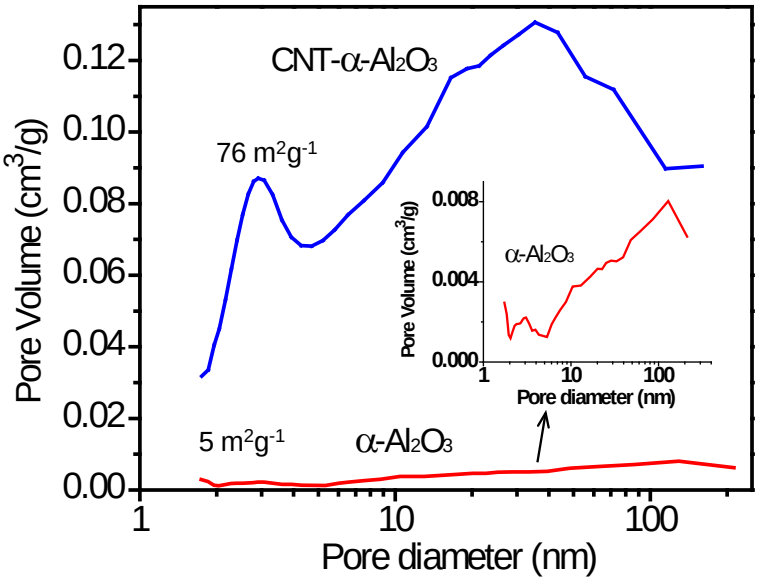

Figure 3. Distributions poreuses des supports à base d'α-Al_2O_3 et de NTC-α-Al_2O_3 par adsorption de N_2 obtenues selon la méthode BJH.

Dans ce chapitre, l'α-Al_2O_3, avec ses larges pores a été recouverte d'une couche de NTC multi-feuillets. Le dépôt en fine couche homogène de NTC enchevêtrés forme un réseau ouvert et structuré, de meilleure conductivité thermique et de plus grande surface effective pour la réaction de F-T (Figure 2). Le composite ainsi obtenu présente une surface spécifique plus élevée et plus accessible, de l'ordre de 76 $m^2 \cdot g^{-1}$ comparé à la surface du support de départ, i.e. 5 $m^2 \cdot g^{-1}$ (Figure 3). De plus, de part leurs géométrie extane, les NTC permettent

de façon significative de réduire la diffusion des réactifs vers les sites actifs mais également d'améliorer l'évacuation des produits de réaction du catalyseur vers la phase gazeuse.

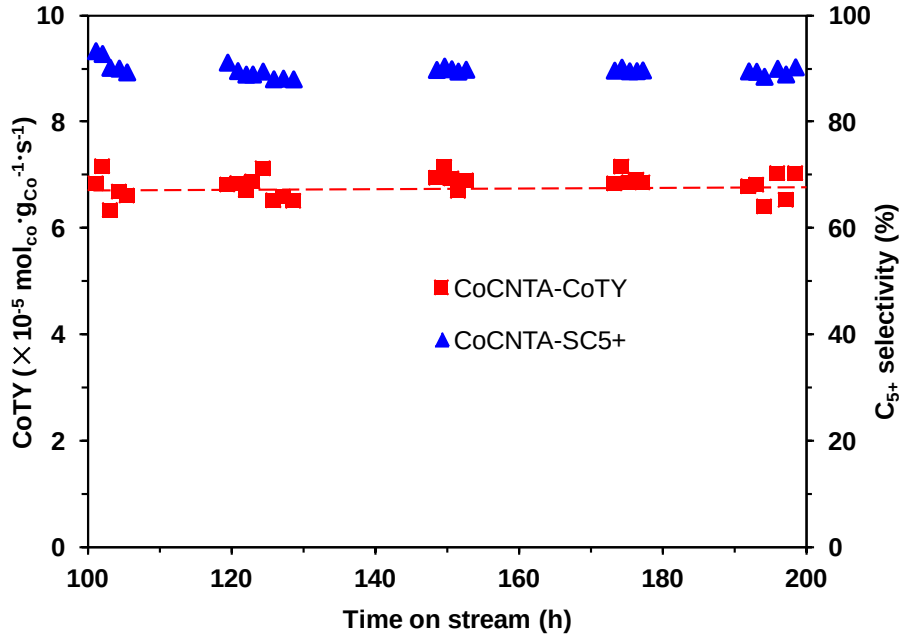

Figure 4. Performances et stabilité du catalyseur CoCNTA en fonction du temps sous flux à 230°C. Conditions de réaction: ratio molaire H_2/CO = 2, gaz de synthèse pur, pression totale = 40 bar, VVH (STP) = 3600 $ml \cdot g_{cat}^{-1} \cdot h^{-1}$.

Ces composites ainsi préparés seront ensuite utilisés en tant que support de catalyseurs avec une phase active à base de cobalt. Les défauts présents à la surface des NTC permettent une meilleure dispersion et stabilisation des nanoparticules cobalt. La conductivité thermique intrinsèque des NTC améliore considérablement la dissipation de la chaleur à travers le lit catalytique, permettant ainsi d'éviter la formation de points chauds locaux pour des conversions de CO élevées. Le catalyseur Co/NTC-α-Al_2O_3 (CoCNTA) a montré de bonnes performances et une très grande stabilité au cours de la réaction, plus de 200 h sous flux réactionnel et dans des conditions relativement sévères par rapport à d'autres catalyseurs reportés dans la littérature (Figure 4). De plus la forme macroscopique de ces composites rend leur utilisation et manipulation plus facile comme support pour les réacteurs lit-fixe, ce

qui permet d'éviter les problèmes de transport et de perte de charge des nanotubes de carbone utilisées sous forme de poudre pulvérulente.

2.2 Catalyseur cobalt supporté sur TiO_2-NTC-α-Al_2O_3 hiérarchiquement structuré

Ce chapitre est consacré à l'étude des performances F-T sur un nouveau type de support hiérarchisé à base de NTC-α-Al_2O_3 recouverte d'une fine couche de TiO_2 avant le dépôt de la phase active de cobalt. L'objectif de cette étude de tirer partie des interactions entre la phase active et le dopant TiO_2 afin d'améliorer la dispersion des clusters d'une part,[51-53] et d'autre part, de réduire la mobilité des particules et par conséquent leur frittage au cours de la réaction F-T et donc leur désactivation.[54-55] L'addition de TiO_2 modifie légèrement la surface spécifique et le diamètre des pores, i.e. 72 $m^2 \cdot g^{-1}$ et 15 nm pour TiO_2-NTC-α-Al_2O_3 au lieu de 76 $m^2 \cdot g^{-1}$ et 11 nm pour NTC-α-Al_2O_3. Les analyses MEB montrent que le réseau de NTC est bien recouvert de TiO_2 et qu'aucun bouchage des pores n'est observé (Figure 5A). Les analyses obtenues par MET du composite TiO_2-NTC-α-Al_2O_3 confirme la formation de nanoparticules homogènes de TiO_2 sur la surface des phases NTC et α-Al_2O_3 (Figure 5B-D).

L'introduction de TiO_2 dans le support hiérarchisé permet une amélioration des performances en F-T. Le catalyseur montre aussi une meilleure activité parmi tous les catalyseurs à base de TiO_2 reportés à l'heure actuelle dans la littérature. Le catalyseur hiérarchiquement structuré à base de TiO_2 (CoTiCNTA) présente une meilleure conversion en monoxyde de carbone (44.3%), comparée à celle obtenue sur les catalyseurs hiérarchisés conventionnels (28.2%, CoCNTA) ou les catalyseurs classiques dopés au TiO_2 (33.4%, CoTiA).

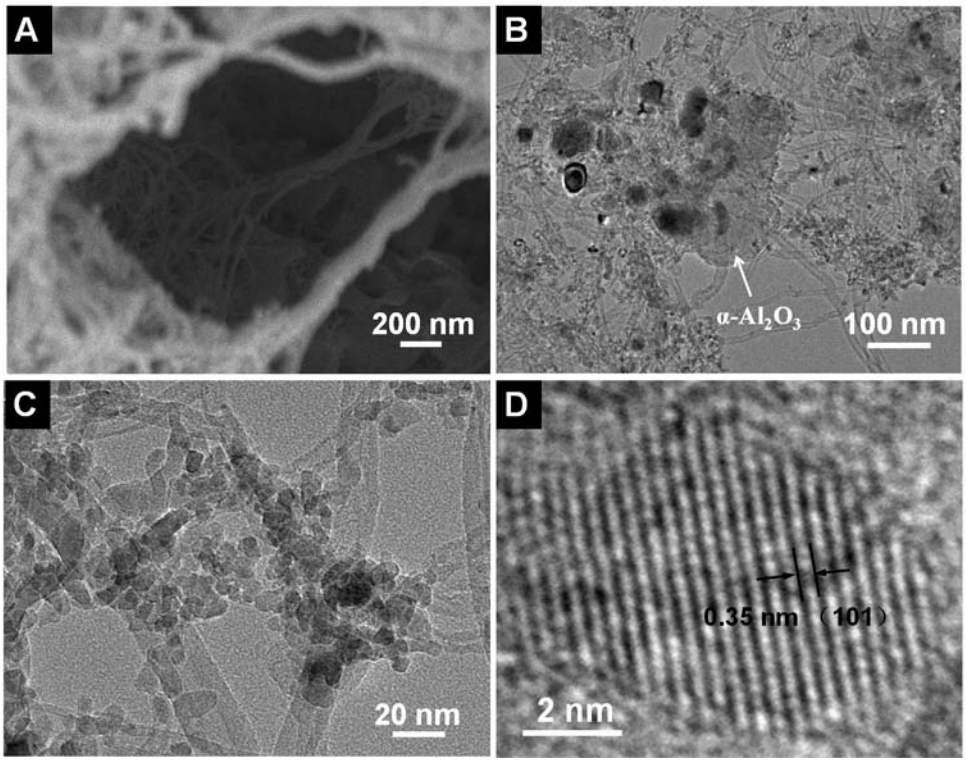

Figure 5. Images MEB (A) et MET (B-C) des composites hiérarchiquement structurés de TiO_2-NTC-α-Al_2O_3. (D) MET haute résolution montrant les nanoparticules de TiO_2 déposées sur composite TiO_2-NTC-α-Al_2O_3 hiérarchiquement structuré.

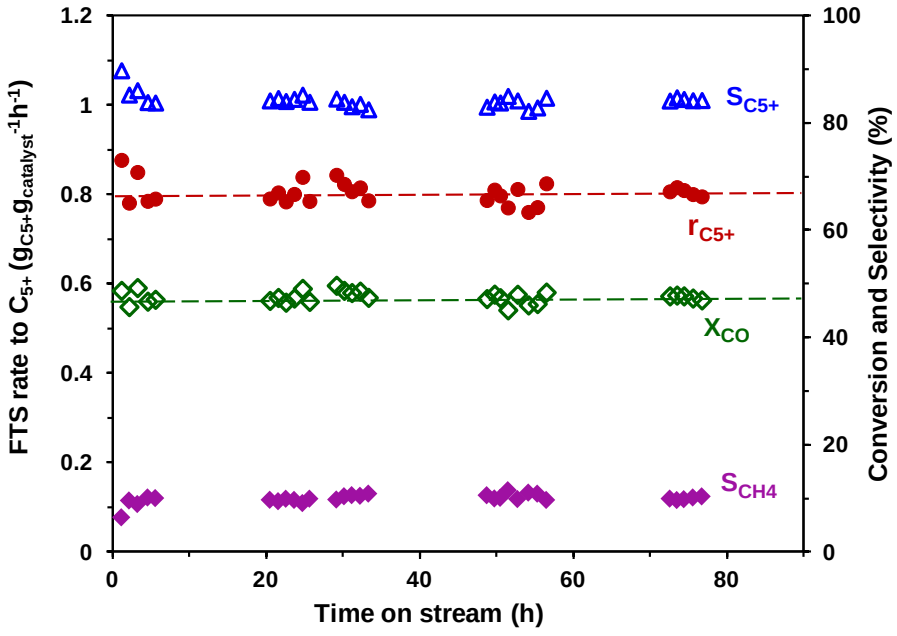

Figure 6. Performances catalytiques du catalyseur CoTiCNTA sous conditions sévères de réaction en fonction du temps sous flux : ratio molaire H_2/CO = 2, gaz de synthèse pur, pression totale = 40 bar, T = 230 °C, VVH (STP) = 7200 $ml \cdot g_{cat}^{-1} \cdot h^{-1}$.

On peut observer sur la Figure 6, que le catalyseur hiérarchiquement structuré et dopé au TiO_2 présente une sélectivité en C_{5+} de l'ordre de 84,5% et une conversion en CO de 47.4% dans des conditions de réaction F-T sévères, i.e. température et pression de réaction relativement élevée (T= 245 °C et 40 bars) et des vitesses de gaz élevées (VVH (STP) =9600 $ml \cdot g_{cat}^{-1} \cdot h^{-1}$). Le taux de F-T exprimé en masse d'hydrocarbures à longue chaînes formés par gramme de catalyseur et par heure ($g_{C5+} \cdot g_{cat}^{-1} \cdot h^{-1}$) est de l'ordre de 0.80 $g_{C5+} \cdot g_{cat}^{-1} \cdot h^{-1}$, ce qui représente le meilleur résultat parmi tous les catalyseurs à base de cobalt, exempts de métaux nobles déjà reportés à notre connaissance, y compris les catalyseurs à base de cobalt supportés sur CNFs.

3. Catalyseur à base de cobalt supporté sur carbure de silicium dopé au titane

Malgré les performances élevées observées, le principal inconvénient de l'utilisation des NTC dans la réaction de F-T reste leur grande sensibilité à l'oxydation, ce qui rend plus difficile l'élimination des résidus carbonés déposés durant la réaction pour la régénération du catalyseur. L'objectif principal dans ce chapitre est axé sur le développement d'un nouveau support hybride constitué de carbure de silicium (SiC) dopé au titane, ayant une grande résistance à l'oxydation, une grande surface spécifique avec des larges pores et de meilleures interactions métal-support. Il convient de noter que les matériaux hybrides à base de SiC synthétisés selon la réaction gaz-solide présentent généralement un réseau de larges pores comme le montre les analyses obtenues par MET et présentées sur la Figure 7. De tels pores permettent d'accélérer le transfert de masse des hydrocarbures liquides de l'intérieur vers la surface externe du catalyseur pendant la réaction F-T, ce qui permet d'éviter un gradient de concentration des réactifs dans les pores, et conduit à une meilleure sélectivité en faveur des produits légers.

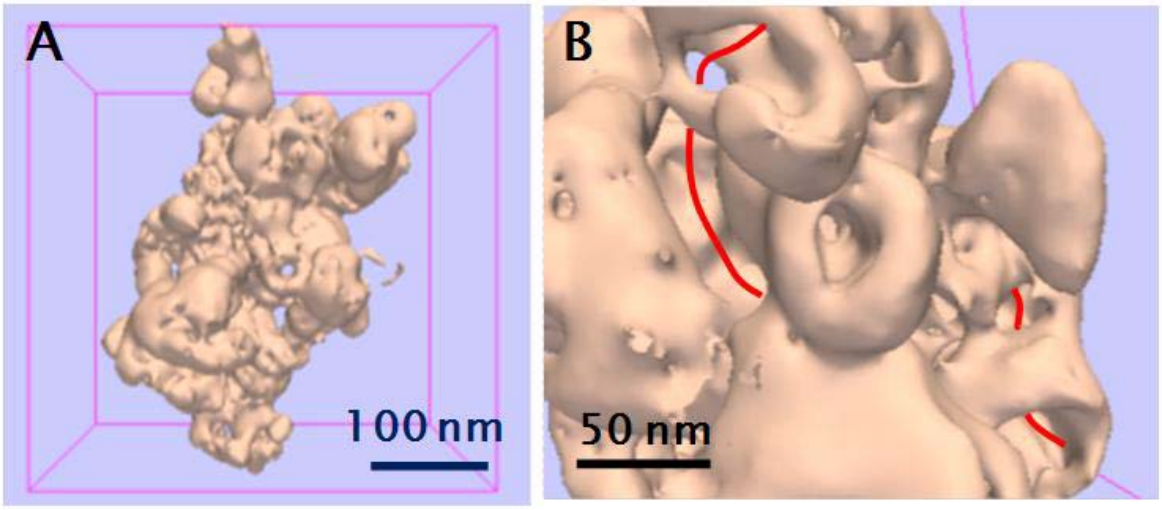

Figure 7. Modèle 3D d'un grain typique de bêta-SiC obtenu par analyses MET, illustrant la morphologie globale et la coexistence de deux types de pores (gauche), ainsi que la présence de larges pores interconnectés (droite), indiqués en ligne rouge.

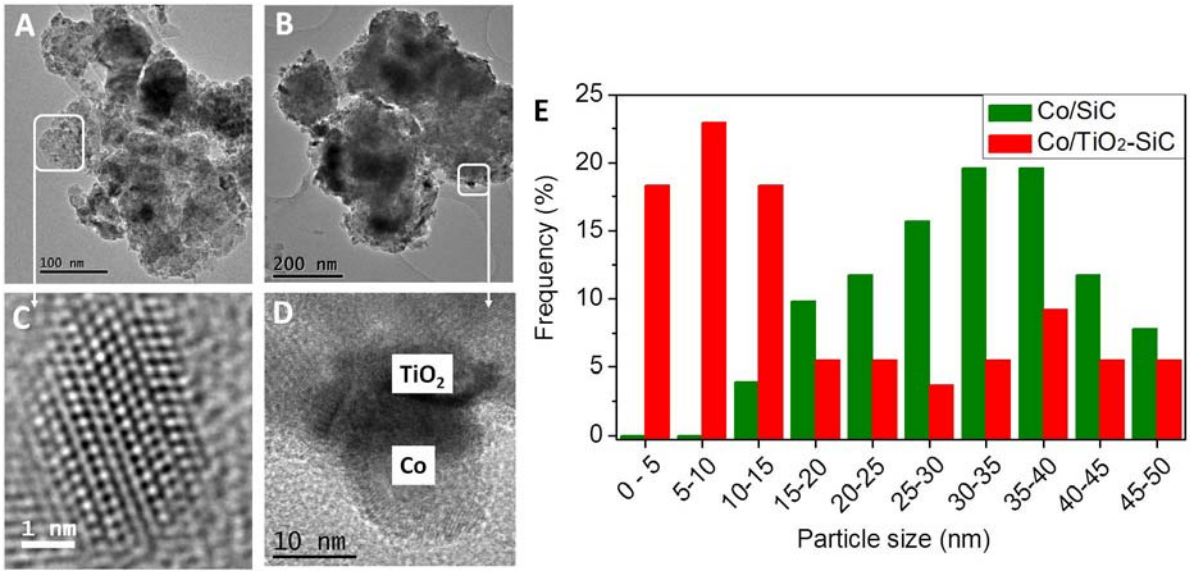

Figure 8. Images MET (A, B) représentant typiquement des grains du catalyseur Co/TiO_2-SiC et HR-TEM (C, D) de nanoparticules de cobalt. (E) Distribution de tailles des particules de cobalt supportées sur SiC et TiO_2-SiC déterminée par analyses statistiques en MET.

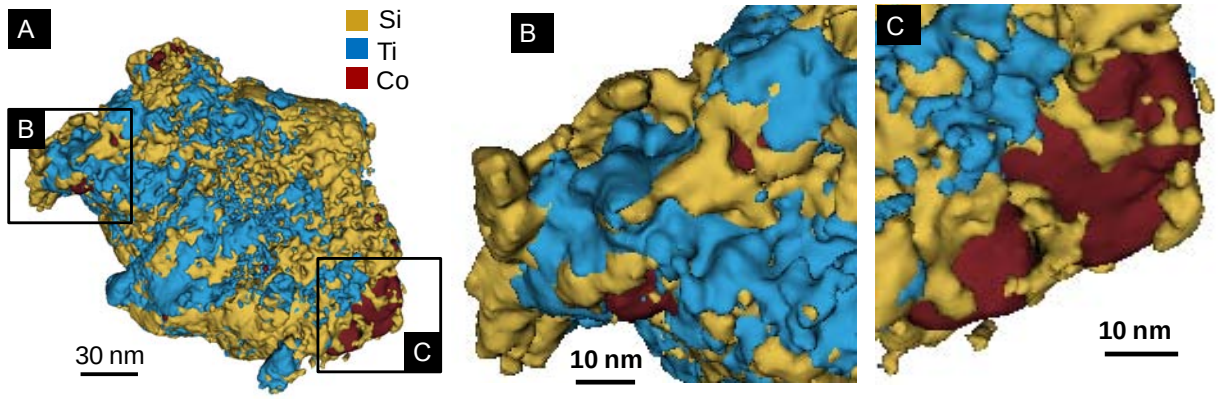

Figure 9. Vue 3D typique obtenue par modèle analytique d'un grain de l'échantillon 10% Co/TiO_2-SiC en utilisant l'analyse tomographique EFTEM des éléments Si, Ti et Co. Cette technique permet d'obtenir des informations directes sur la localisation des particules de cobalt par rapport aux différents constituants du support. Ti est représenté en bleu, Si en jaune et Co en rouge. Le catalyseur a été calciné à 350 °C pendant 2 h avant d'être réduit sous H_2 à 300 °C pendant 6 h.

L'oxyde de titane utilisé comme dopant présente de grandes interactions métal-support avec le précurseur de la phase active à base de cobalt, ce qui conduit à une meilleure dispersion des particules de cobalt par rapport à celles déposées sur la surface de SiC non dopée. Les images HR-TEM obtenues montrent la présence des particules de cobalt à proximité d'une phase de TiO_2, ce qui indique clairement la formation de nanoparticules métalliques de tailles inférieures à 10 nm avec une structure très facettée avec des défauts (Figure 8C). Les particules semblent bien séparées les unes des autres (Figures 8A et B), dues probablement aux fortes interactions métal-support entre les nanoparticules de Co avec la phase TiO_2 phase, empêchant ainsi un frittage excessif au cours du traitement thermique.

Les résultats 3D d'une particule catalytique, obtenues par analyses TEM-EELS avec une résolution de quelques nanomètres (Figure 9), montrent la forte influence du TiO_2 sur la dispersion des particules de cobalt par rapport à celles déposées sur SiC seul. La taille moyenne des particules de cobalt au contact avec la phase TiO_2 est centrée sur 5-15 nm alors que les particules déposées sur SiC seul sont autour de 40 nm (voir la distribution de taille sur la Figure 8E). Une analyse plus détaillée du modèle analytique 3D du grain de catalyseur

révèle que les petites particules de cobalt observées par MET (< 5 nm) sont insérées dans les macro- ou mésopores du support TiO_2-SiC. C'est pourquoi les images MET obtenues en 2D ne présentent que de petites parties des nanoparticules de cobalt, ce qui illustre encore une fois l'intérêt des analyses 3D dans l'obtention d'informations plus précises sur la microstructure du catalyseur. Les résultats obtenus pourraient être attribués aux plus fortes interactions métal-support entre le cobalt et la phase TiO_2, ce qui éviterait l'agglomération des particules de cobalt et /ou leur frittage pendant les étapes d'imprégnation et de traitement thermique. Les petites particules de cobalt ainsi obtenues (10-20 nm) offrent une plus grande surface active, permettant d'améliorer de manière significative les performances en synthèse FT du catalyseur sans sacrifier pour autant la grande sélectivité en hydrocarbures liquides déjà observé sur ce support céramique (voir Figure 8D).

4. Nanoparticules de cobalt supportées sur carbure de silicium dopé au titane

A ce jour, aucune étude ne mentionne l'utilisation dans la réaction de F-T du TiO_2 comme dopant dans un support de conductivité thermique et de porosité élevées comme le SiC. Notre étude a porté sur le développement d'un catalyseur de FT très actif à base d'oxyde de titane recouvrant du β-SiC à porosité élevée. L'influence de la charge en TiO_2 sur les performances de F-T performance a été également étudiée (Figure 10). La surface spécifique de TiO_2 sur SiC est de l'ordre de 39 - 41 $m^2 \cdot g^{-1}$, valeur proche de celle du SiC seul (40 $m^2 \cdot g^{-1}$), ce qui indique que le TiO_2 introduit n'influence pas ou peu la texture du composite final, en raison principalement des larges pores présents dans le SiC. Les courbes de distributions poreuses, obtenues par la méthodes BJH à partir des isothermes d'adsorption sont présentées sur la Figure 11 pour des tailles de pores allant de 2 à 150 nm. On peut observer que tous les supports TiO_2/SiC et SiC présentent une distribution poreuse large et irrégulière. De plus, la taille des mésopores du composite comprises entre 10-20 nm augmente avec la charge en TiO_2.

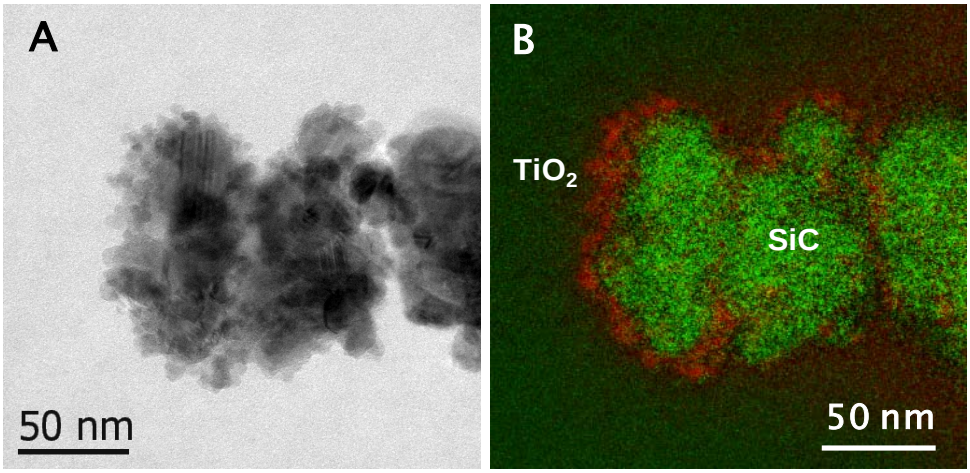

Figure 10. Images (A) MET de TiO_2-SiC et (B) EFTEM correspondant montrent clairement la bonne dispersion de TiO_2 sur la surface du SiC. TiO_2 (rouge), SiC (vert).

Les performances catalytiques de F-T en terme d'activité (activité par masse de cobalt, "cobalt time yield, CoTY" en $\times 10^{-5}$ $mol_{co}g_{Co}^{-1}s^{-1}$) et de sélectivité C_{5+} obtenues sur cobalt supporté sur SiC dopé avec différentes charges de TiO_2, i.e. 5%, 10% et 15%, sont présentées sur la Figure 12A. Les performances de catalyseurs similaires sans dopage au TiO_2, notés Co/SiC, sont également représentées sur la figure pour comparaison. D'après les résultats obtenus, on peut remarquer que l'introduction de TiO_2 dans le support à base de SiC permet considérablement d'améliorer l'activité catalytique de la réaction F-T. L'activité du cobalt (CoTY) augmente de 4 to 4,9 $\times 10^{-5}$ $mol_{co}g_{Co}^{-1}s^{-1}$ sur catalyseur Co/5TiO_2-SiC dopé à 5 % en masse de TiO_2 par rapport à un catalyseur sans TiO_2. Un CoTY de 8,2 $\times 10^{-5}$ $mol_{co}g_{Co}^{-1}s^{-1}$ est obtenu sur catalyseur Co/10TiO_2-SiC contenant 10% TiO_2 à 215 ^{o}C, montrant ainsi des performances catalytiques supérieures. Lorsque la charge de TiO_2 augmente à 15%, l'activité diminue à 5,2 $\times 10^{-5}$ $mol_{co}g_{Co}^{-1}s^{-1}$. Cette perte d'activité F-T pour une charge élevée de TiO_2 est liée à une forte influence du TiO_2 sur l'augmentation de la taille des particules de Co^0 métallique. L'augmentation de l'activité catalytique de F-T est accompagnées d'une légère baisse de sélectivité envers les hydrocarbures liquides, i.e. de 95% sur catalyseur non promu à 92% sur catalyseur dopé à 10% en masse de TiO_2.

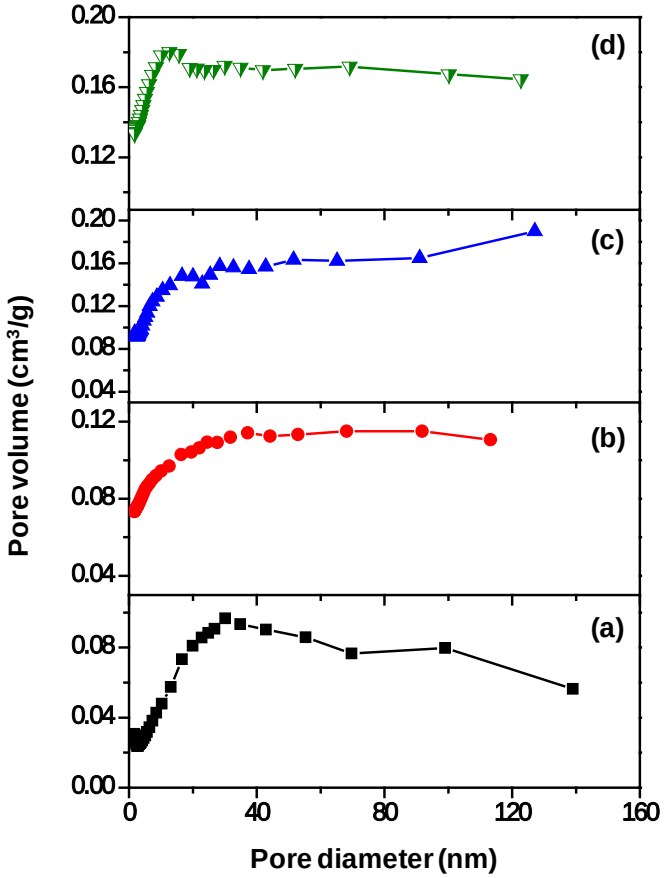

Figure 11. Distribution poreuse obtenue par la méthode BJH pour différentes charges de TiO_2 sur SiC : (a) SiC; (b) 5TiO_2-SiC; (c) 10TiO_2-SiC, (d) 15TiO_2-SiC

La Figure 12B présente les résultats d'un test longue durée sur plus de 80 h sous flux réactionnel, obtenus sur catalyseur Co/10TiO_2-SiC à 215 °C. L'activité par masse de cobalt CoTY et la sélectivté en C_{5+} restent constantes aux alentours de 8,2 $\times 10^{-5}$ $mol_{co}g_{Co}^{-1}s^{-1}$ et 92%, respectivement. Ces résultats indiquent clairement la grande stabilité du catalyseur, et par conséquent que la désactivation due à l'oxydation de surface ou au frittage du cobalt est peu susceptible de se produire dans ces conditions de réaction. On peut toutefois ajouter que le catalyseur testé avait été évalué auparavant à 215 °C sous un GHSV de 2400 $ml \cdot g_{cat}^{-1} \cdot h^{-1}$ pendant plus de 100 h sous flux.

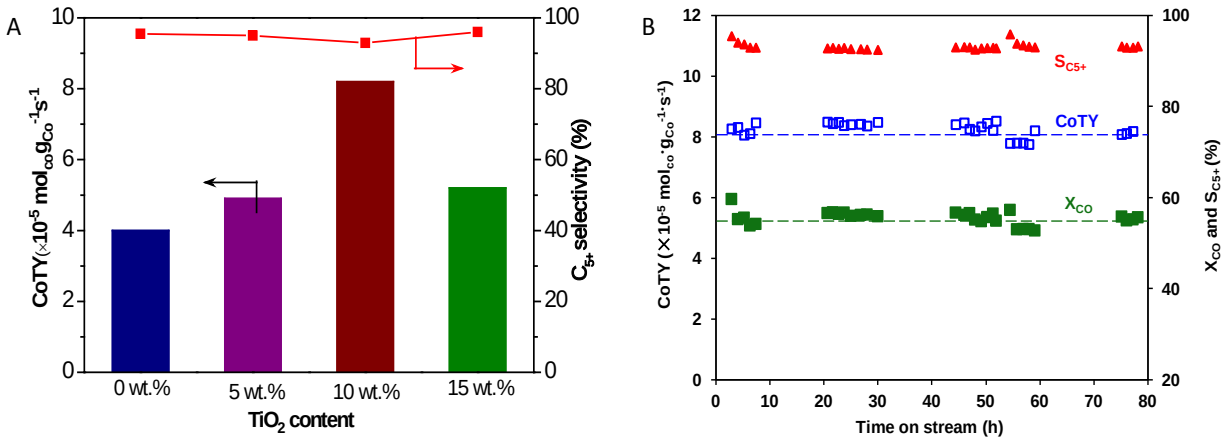

Figure 12. (A) Performances catalytiques en synthèse FT obtenues sur catalyseurs avec différentes charges de TiO_2. (B) Activité et sélectivité C_{5+} en synthèse FT en fonction du temps sous flux sur catalyseur $10Co/10TiO_2$-SiC. Conditions de réaction: ratio molaire $H_2/CO = 2$, température de réaction = 215 °C, pression totale = 40 bar, VVH= 3600 $ml \cdot g_{cat}^{-1} \cdot h^{-1}$.

5. Conclusions et perspectives

D'après la littérature, l'efficacité de la phase active à base de cobalt dans la réaction de Fischer-Tropsch dépend fortement du matériau support. Ce dernier doit entre autre posséder une conductivité thermique élevé (permettant une rapide homogénéisation de la température à travers le lit catalytique), et une structure ouverte (composée de macro- et mésopores ou hiérarchiquement structurée). Dans cette thèse, des matériaux comme le carbure de silicium (β-SiC) ou l'alumine (α-Al_2O_3), ont été choisis comme matière première et utilisés en tant que nouveaux supports dans la réaction de F-T.

Un nouveau support hiérarchisé, à base de α-Al_2O_3 homogènement recouvert d'une couche de nanotubes de carbone NTC, a également été préparé. Ce support possède une surface élevée (76 $m^2 \cdot g^{-1}$) entièrement accessible grâce notamment à leurs tailles nanoscopiques et une absence totale de micropores, contrairement aux supports traditionnels. Les catalyseurs à base de cobalt supporté sur ce type de matériau hiérarchiquement structuré ont montré une grande efficacité pour la réaction de F-T par rapport à l'α-Al_2O_3 ou les catalyseurs classiques à base de cobalt supporté sur NTC. Les performances F-T obtenues

sur ce support peuvent être améliorées en déposant une fine couche de TiO_2 sur la surface des NTC, ce qui améliore considérablement la dispersion du cobalt, et par conséquent l'activité F-T. Le catalyseur présente également une extrême stabilité en fonction du temps sous flux réactionnel.

Pour la première fois le TiO_2, utilisé comme agent dopant a été introduit dans une matrice de SiC au cours du processus de synthèse. Sa grande interaction avec le cobalt conduit à une meilleure dispersion de sa phase active, primordiale pour l'obtention d'une meilleure activité et stabilité dans la réaction de F-T. Les catalyseurs obtenus présentent d'excellentes performances catalytiques avec une grande sélectivité en C_{5+} (> 85%).

Un nouveau catalyseur F-T présentant de meilleures activité et sélectivité a également été synthétisé par dépôt sélectif d'une fine couche de TiO_2 dans les larges pores de la structure hôte de SiC, puis de la phase active de cobalt. La couche homogène de TiO_2 sur la surface du SiC permet une grande dispersion des nanoparticules de cobalt, conduisant ainsi à un catalyseur très actif et sélectif pour la réaction de F-T. Le catalyseur présente également une grande stabilité en fonction du temps sous flux réactionnel pour des températures de réaction et des vitesses de gaz relativement élevées.

La combinaison de différentes techniques de caractérisations classiques telles que MET à haute résolution, DRX, TPR, etc, et de techniques de caractérisations de pointe telles que EFTEM et RMN ^{59}Co à champs nul nous permettent de corréler les propriétés physiques des nanoparticules de cobalt déposées avec les performances F-T et la stabilité des catalyseurs.

Les études ultérieures seront axées sur l'influence des charges en dopant et en cobalt sur les performances en F-T. La localisation du dopant par rapport au support SiC étudiée par la technique tomographique MET à haute résolution. On introduira également le développement d'un nouveau type de support à base de matériaux nanocarbonés, i.e. nanotubes de carbone et graphène multi-feuillets ("Few Layer Graphene", FLG), de tailles et

de formes bien contrôlées. Ces matériaux nanocarbonés autosupportés seront ensuite caractérisés par différentes techniques et testés dans la réaction de F-T.

Références

[1] G. W. Huber, S. Iborra, A. Corma, *Chemical Reviews* **2006**, *106*, 4044-4098.

[2] J. R. Rostrup-Nielsen, *Science* **2005**, *308*, 1421-1422.

[3] F. Fischer, H. Tropsch, *Brennstoff Chem* **1923**, *4*, 276-285.

[4] F. Fischer, H. Tropsch, *Brennstoff Chem* **1926**, *7*, 97-104.

[5] A. Y. Khodakov, W. Chu, P. Fongarland, *Chemical Reviews* **2007**, *107*, 1692-1744.

[6] E. de Smit, B. M. Weckhuysen, *Chem Soc Rev* **2008**, *37*, 2758-2781.

[7] A. M. Saib, D. J. Moodley, I. M. Ciobica, M. M. Hauman, B. H. Sigwebela, C. J. Weststrate, J. W. Niemantsverdriet, J. van de Loosdrecht, *Catal Today* **2010**, *154*, 271-282.

[8] N. E. Tsakoumis, M. Ronning, O. Borg, E. Rytter, A. Holmen, *Catal Today* **2010**, *154*, 162-182.

[9] Q. H. Zhang, J. C. Kang, Y. Wang, *ChemCatChem* **2010**, *2*, 1030-1058.

[10] J. C. Kang, K. Cheng, L. Zhang, Q. H. Zhang, J. S. Ding, W. Q. Hua, Y. C. Lou, Q. G. Zhai, Y. Wang, *Angew Chem Int Edit* **2011**, *50*, 5200-5203.

[11] R. Luque, A. R. de la Osa, J. M. Campelo, A. A. Romero, J. L. Valverde, P. Sanchez, *Energ Environ Sci* **2012**, *5*, 5186-5202.

[12] S. T. Sie, M. M. G. Senden, H. M. H. Van Wechem, *Catal Today* **1991**, *8*, 371-394.

[13] B. H. Davis, *Top Catal* **2005**, *32*, 143-168.

[14] S. T. Sie, R. Krishna, *Appl Catal a-Gen* **1999**, *186*, 55-70.

[15] B. de Tymowski, Y. F. Liu, C. Meny, C. Lefevre, D. Begin, P. Nguyen, C. Pham, D. Edouard, F. Luck, C. Pham-Huu, *Appl Catal a-Gen* **2012**, *419*, 31-40.

[16] M. Lacroix, L. Dreibine, B. de Tymowski, F. Vigneron, D. Edouard, D. Begin, P. Nguyen, C. Pham, S. Savin-Poncet, F. Luck, M. J. Ledoux, C. Pharn-Huu, *Appl Catal a-Gen* **2011**, *397*, 62-72.

[17] H. F. Xiong, Y. H. Zhang, S. G. Wang, J. L. Li, *Catal Commun* **2005**, *6*, 512-516.

[18] A. Y. Khodakov, *Catal Today* **2009**, *144*, 251-257.

[19] E. Iglesia, S. L. Soled, R. A. Fiato, *J Catal* **1992**, *137*, 212-224.

[20] E. Iglesia, *Stud Surf Sci Catal* **1997**, *107*, 153-162.

[21] E. Iglesia, *Appl Catal a-Gen* **1997**, *161*, 59-78.

[22] R. Oukaci, A. H. Singleton, J. G. Goodwin, *Appl Catal a-Gen* **1999**, *186*, 129-144.

[23] S. Storsaeter, B. Totdal, J. C. Walmsley, B. S. Tanem, A. Holmen, *J Catal* **2005**, *236*, 139-152.

[24] S. Storsaeter, O. Borg, E. A. Blekkan, B. Totdal, A. Holmen, *Catal Today* **2005**, *100*, 343-347.

[25] A. Y. Khodakov, A. Griboval-Constant, R. Bechara, V. L. Zholobenko, *J Catal* **2002**, *206*, 230-241.

[26] A. Y. Khodakov, R. Bechara, A. Griboval-Constant, *Appl Catal a-Gen* **2003**, *254*, 273-288.

[27] E. Rytter, S. Eri, T. H. Skagseth, D. Schanke, E. Bergene, R. Myrstad, A. Lindvag, *Ind Eng Chem Res* **2007**, *46*, 9032-9036.

[28] O. Borg, P. D. C. Dietzel, A. I. Spjelkavik, E. Z. Tveten, J. C. Walmsley, S. Diplas, S. Eri, A. Holmen, E. Ryttera, *J Catal* **2008**, *259*, 161-164.

[29] S. Rane, O. Borg, J. Yang, E. Rytter, A. Holmen, *Appl Catal a-Gen* **2010**, *388*, 160-167.

[30] H. Zhang, C. Lancelot, W. Chu, J. P. Hong, A. Y. Khodakov, P. A. Chernavskii, J. Zheng, D. G. Tong, *J Mater Chem* **2009**, *19*, 9241-9249.

[31] M. Trepanier, A. Tavasoli, A. K. Dalai, N. Abatzoglou, *Appl Catal a-Gen* **2009**, *353*, 193-202.

[32] M. Trepanier, A. K. Dalai, N. Abatzoglou, *Appl Catal a-Gen* **2010**, *374*, 79-86.

[33] J. Lv, X. B. Ma, S. L. Bai, C. D. Huang, Z. H. Li, J. L. Gong, *Int J Hydrogen Energ* **2011**, *36*, 8365-8372.

[34] A. Tavasoli, R. M. M. Abbaslou, M. Trepanier, A. K. Dalai, *Appl Catal a-Gen* **2008**, *345*, 134-142.

[35] L. Guczi, G. Stefler, O. Geszti, Z. Koppany, Z. Konya, E. Molnar, M. Urban, I. Kiricsi, *J Catal* **2006**, *244*, 24-32.

[36] M. C. Bahome, L. L. Jewell, D. Hildebrandt, D. Glasser, N. J. Coville, *Appl Catal a-Gen* **2005**, *287*, 60-67.

[37] M. C. Bahome, L. L. Jewell, K. Padayachy, D. Hildebrandt, D. Glasser, A. K. Datye, N. J. Coville, *Appl Catal a-Gen* **2007**, *328*, 243-251.

[38] W. Chen, Z. L. Fan, X. L. Pan, X. H. Bao, *J Am Chem Soc* **2008**, *130*, 9414-9419.

[39] R. M. M. Abbaslou, A. Tavasoli, A. K. Dalai, *Appl Catal a-Gen* **2009**, *355*, 33-41.

[40] R. M. M. Abbaslou, J. Soltan, A. K. Dalai, *Appl Catal a-Gen* **2010**, *379*, 129-134.

[41] H. J. Schulte, B. Graf, W. Xia, M. Muhler, *ChemCatChem* **2012**, *4*, 350-355.

[42] A. Tavasoli, M. Trepanier, A. K. Dalai, N. Abatzoglou, *J Chem Eng Data* **2010**, *55*, 2757-2763.

[43] H. F. Xiong, M. A. M. Motchelaho, M. Moyo, L. L. Jewell, N. J. Coville, *J Catal* **2011**, *278*, 26-40.

[44] X. W. Zhu, X. J. Lu, X. Y. Liu, D. Hildebrandt, D. Glasser, *Ind Eng Chem Res* **2010**, *49*, 10682-10688.

[45] R. Myrstad, S. Eri, P. Pfeifer, E. Rytter, A. Holmen, *Catal Today* **2009**, *147*, *Supplement*, S301-S304.

[46] Y.-h. Chin, J. Hu, C. Cao, Y. Gao, Y. Wang, *Catal Today* **2005**, *110*, 47-52.

[47] J. J. Delgado, R. Vieira, G. Rebmann, D. S. Su, N. Keller, M. J. Ledoux, R. Schlögl, *Carbon* **2006**, *44*, 809-812.

[48] K. Chizari, A. Deneuve, O. Ersen, I. Florea, Y. Liu, D. Edouard, I. Janowska, D. Begin, C. Pham-Huu, *Chemsuschem* **2012**, *5*, 102-108.

[49] S. Zarubova, S. Rane, J. Yang, Y. Yu, Y. Zhu, D. Chen, A. Holmen, *Chemsuschem* **2011**, *4*, 935-942.

[50] Y. Liu, T. Dintzer, O. Ersen, C. Pham-Huu, *Journal of Energy Chemistry* **2013**, *22*, 279-289.

[51] Y. Liu, B. de Tymowski, F. Vigneron, I. Florea, O. Ersen, C. Meny, P. Nguyen, C. Pham, F. Luck, C. Pham-Huu, *ACS Catalysis* **2013**, *3*, 393-404.

[52] S. J. Park, S. M. Kim, M. H. Woo, J. W. Bae, K. W. Jun, K. S. Ha, *Appl Catal a-Gen* **2012**, *419*, 148-155.

[53] S. Hinchiranan, Y. Zhang, S. Nagamori, T. Vitidsant, N. Tsubaki, *Fuel Process Technol* **2008**, *89*, 455-459.

[54] M. Lualdi, G. Di Carlo, S. Logdberg, S. Jaras, M. Boutonnet, V. La Parola, L. F. Liotta, G. M. Ingo, A. M. Venezia, *Appl Catal a-Gen* **2012**, *443*, 76-86.

[55] A. M. Venezia, V. La Parola, L. F. Liotta, G. Pantaleo, M. Lualdi, M. Boutonnet, S. Järås, *Catal Today* **2012**, *197*, 18-23.

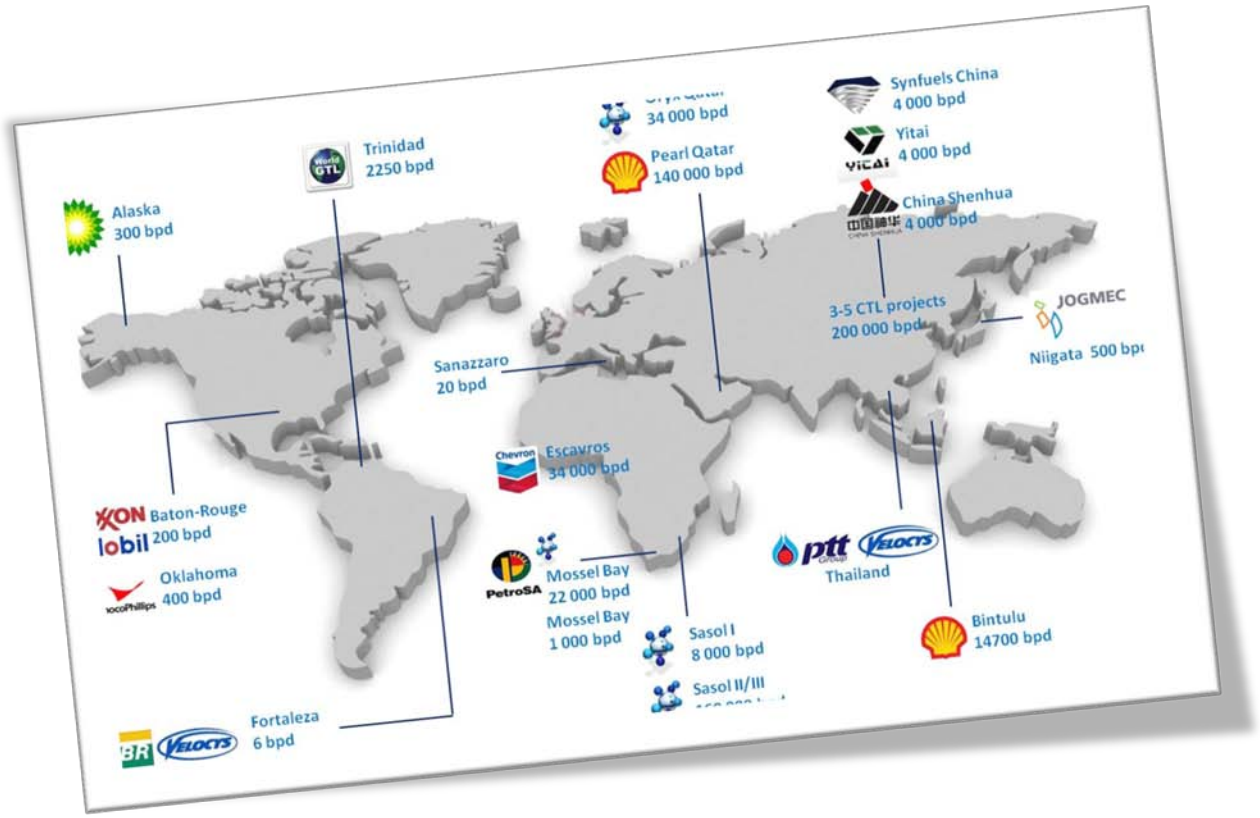

Chapter I

Introduction

Chapter I Introduction

1.1 General introduction of Fischer-Tropsch Synthesis

The demands for energy and goods go sharply upward during the last decades due to the fast industrial growth of the emergent countries like China and India and also to the increase of the world population while the oil reserves are decreasing and their production rate is close to reaching the maximum before facing a decline.[1-2] Thus, sustainable and environment friendly energy production and consumption are among the key challenges in this ongoing century. The new developments of promoting low-CO_2 footprint technologies need to consider the alternative feedstock, such as natural gas, charcoal and biomass.[3-4] It is worthy to note that no pressure will come from natural gas and coal in the near future, since large resources of these raw materials still exist. The synthesis gas ($CO + nH_2$), is generated by the steam reforming of natural gas or gasification of coal and biomass. It is further processed via the Fischer-Tropsch (F-T) reaction which has been firstly developed in the early of 1920s by Franz Fischer and Hans Tropsch[5-6] and has received an over increasing scientific and industrial interest during the last decades.[7-10] The Fischer-Tropsch synthesis (FTS) is a key technology in the global Gas-To-Liquids (GTL) and Coal-To-Liquids (CTL) processes which allow the transformation of synthesis gas ($2H_2$+CO), into liquid hydrocarbons following by a hydrocracking of the heavy fraction into useful compounds such as naphtha, diesel, jet fuel and lubricants.[11-12]

The Fischer-Tropsch process is generally regarded as a polymerization reaction and the main reactions can be summarized as following:

Olefin formation

$$n\,CO + 2nH_2 \rightarrow C_nH_{2n} + n\,H_2O \qquad (1\text{-}1)$$

Paraffin formation

$$nCO + (2n+1)\,H_2 \rightarrow C_nH_{2n+2} + n\,H_2O \quad \Delta H = -165\ kJ\cdot mol^{-1} \quad (1\text{-}2)$$

Meanwhile, methane is also the product obtained during the FTS, and organic oxygenates may also be formed. Moreover the water-gas shift (WGS) reaction leading to the formation of CO_2, also occurs over most of the FTS catalysts.

Methane formation

$$CO + 3H_2 \rightarrow CH_4 + H_2O \qquad \Delta H = -206\ kJ\cdot mol^{-1} \qquad (1\text{-}3)$$

Oxygenated compound formation

$$n\,CO + 2nH_2 \rightarrow C_nH_{2n+1}OH + (n-1)\,H_2O \qquad (1\text{-}4)$$

Water-gas shift (WGS) reaction

$$CO + H_2O \rightarrow CO_2 + H_2 \qquad \Delta H = -39\ kJ\cdot mol^{-1} \qquad (1\text{-}5)$$

The FTS process became fairly popular over years, and currently the term FTS applies to wide varieties of processes that deal with the production of clean synthetic fuels (hydrocarbon) from the synthetic gas.[13]

1.2 Ficher-Tropsch Synthesis technology

1.2.1 Synthesis gas generation

The synthesis gas preparation section is an important part and also the most expensive part of XTL (Coal, gas or biomass to liquid) plant. Synthesis gases are prepared from a carbonaceous feedstock. The feedstock should also contain hydrogen that is needed to produce hydrocarbons. For the preparation of synthesis gas there are two main technologies, gasification and reforming. Gasification is used to convert solid or heavy liquid feedstocks into synthesis gas while reforming is used to describe the conversion of gaseous or light liquid feedstocks. The most common feeds are coal and natural gas.

Gasification involves the reaction of a carbon source, with a source of hydrogen which is usually steam. The solid will be converted into raw synthesis gas containing hydrogen, carbon oxide, carbon dioxide, methane and other undesired products. Once the feedstock has been converted into gas, undesirable impurities like sulfur, mercury, arsenic, etc. will be removed from the gas by different techniques.

In an oxygen and steam fed gasifier the reactions are summarized below: (1-6) steam/carbon reaction and (1-7) partial oxidation.

$$C + H_2O \rightarrow CO + H_2 \qquad \Delta H = 119\ kJ\cdot mol^{-1} \qquad (1\text{-}6)$$

$$C + \tfrac{1}{2}\ O_2 \rightarrow CO \qquad \Delta H = -123\ kJ\cdot mol^{-1} \qquad (1\text{-}7)$$

In addition to these reactions total combustion can also occur, and together with other reactions such as methanation (1-3) and water gas shift (WGS) reaction (1-5). The WGS reaction can tune the H_2/CO ratio.

Before reforming, the natural gas must be treated to remove or recover higher hydrocarbons and also to remove sulfur compounds, since sulfur is a poison for both synthesis gas catalyst and the F-T synthesis catalyst. The synthesis gas can be prepared in various ways, steam reforming or autothermal reforming.

Steam reforming involves the reaction of methane with vapor. This reaction is most frequently catalyzed by nickel on alumina, although other metals can be used.

$$CH_4 + H_2O \leftrightarrow CO + 3H_2 \qquad \Delta H = -206\ kJ\cdot\ mol^{-1} \qquad (1\text{-}8)$$

Steam can be partially substituted by carbon dioxide to perform CO_2 reforming.

$$CH_4 + CO_2 \leftrightarrow 2CO + 2H_2 \qquad \Delta H = -247\ kJ\cdot\ mol^{-1} \qquad (1\text{-}9)$$

Steam and CO_2 reforming are accompanied by the WGS reaction. The steam reforming of methane is highly endothermic and thus a high temperature is needed, i.e. from 600 to 1000°C. This process produces a synthesis gas rich in hydrogen which is subsequently adjusted for the Fischer-Tropsch process.

Autothermal reforming (ATR) is a catalytic process combining combustion. The first part of ATR is the combustion at fuel-rich conditions of a natural gas mixture and steam. The finally convert into syngas over a catalytic fixed bed. The reactions are consisted of combustion (1-10), reforming (1-8) and (1-9) and WGS (1-5).

$$CH_4 + ½\ O_2 \rightarrow CO + 2H_2O \qquad \Delta H = +519\ kJ\cdot mol^{-1} \qquad (1\text{-}10)$$

ATR can produce H_2/CO within a wide range of ratio which could find use in different processes.

1.2.2 FTS reactors

There are three main kinds of F-T reactors in commercial usage at present: fixed bed reactor, fluidized bed reactor and slurry phase reactors (turbulent or fixed fluidized bed reactor and circulating fluidized bed reactor).[14] The FTS reaction is a strongly exothermic reaction and the heat in the reaction needs to be removed rapidly in order to avoid the temperature run away which would result in the undesired formation of methane and light hydrocarbons as well as in catalyst deactivation due to coking and sintering. Therefore, in order to maintain near-isothermal conditions inside the catalyst beds, the key property and evaluation in each reactor is the rate of the heat transfer from the catalyst particles to the heat exchanger surface in the reactor.

1.2.2.1 Fixed bed reactor

The preferred fixed bed reactor type are multitubular reactor (Figure 1-1A) which consist of thousands of long narrow tubes containing the catalyst and cooling medium (water or silicone oil) on the shell sides.

The advantages of the fixed-bed reactor are the following:

- Easily operate: there is no equipment required to separate the heavy wax products from the catalyst bed because of the waxes simply trickle down the bed. There is no need to separate the wax from the catalyst.

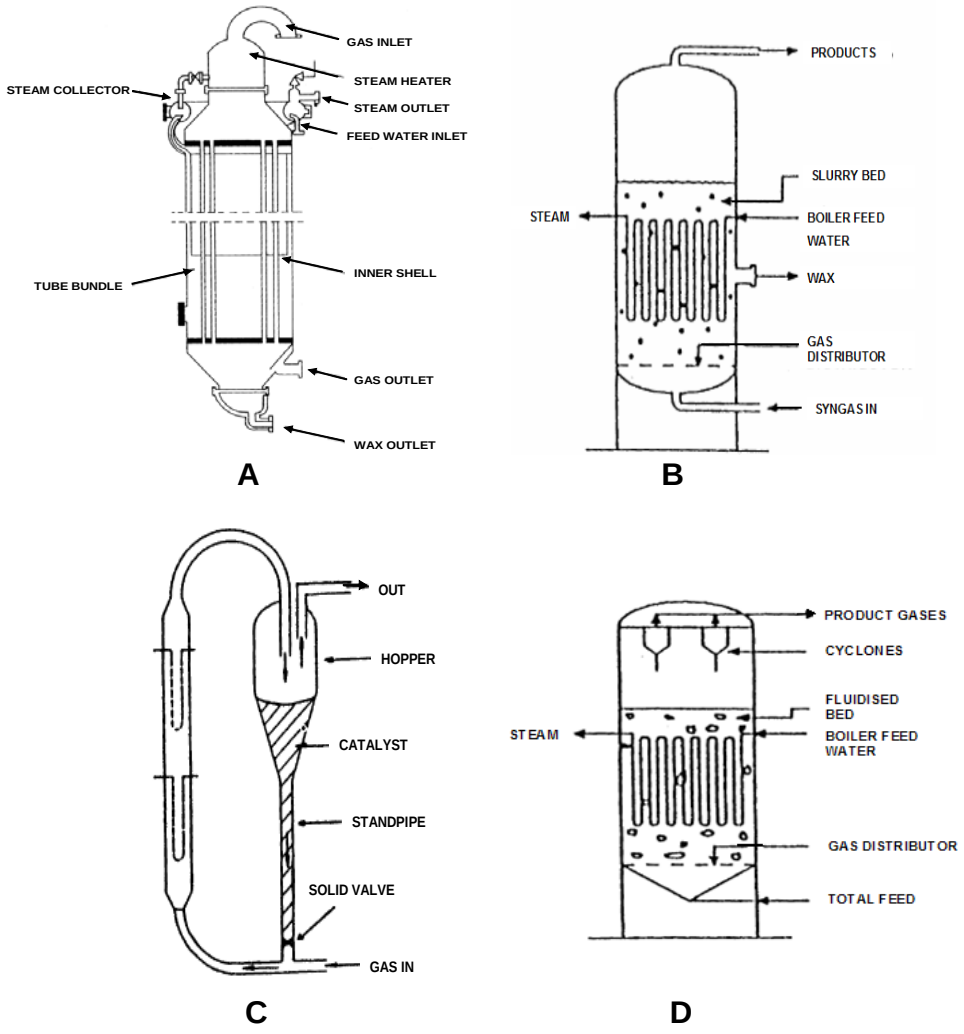

Figure 1-1. Three main kinds of Fishcer-Tropsch reactor. [14]

- Large scale commercial reactor performance can easily be extrapolated starting from pilot consisting of one single reactor tube.
- Catalyst poisons such as H_2S in some case like in the coal derived syngas, the purification process needs only to be added on the top of the catalyst bed.

For the fixed bed reactor, the operating conditions are easier but there are some disadvantages.Vertical spaced packed bed and radial flow reactors with cooling between the beds are not satisfactory because of the negative effects of temperature rise within each individual adiabatic bed. To achieve higher conversion small catalyst pellets or extrudates

are needed but it increases the pressure drop along the tubes so that compromises are needed between the sizes of the particle and the activity of the catalyst. However, multi-tubular reactors consist of thousands of tubes and thus, result in high construction cost.

1.2.2.2 Slurry phase reactor

Various size slurry reactors were tested in Germany, England and the USA in the 1950's and 1960', however the space velocities used were all very low so that could not be jaded in the commercial situations.[14] The slurry reactor of diameter of 1.5 m and bed height of 7.7 m and 10 m^3 working volume were developed by Kolbel, which was one of the largest reactor units.[15] The representative slurry phase reactor is presented in Figure 1-1B. Slurry phase reactor is the same as the tubular fixed-bed reactors operated in the temperature range from 220 to 250 °C; hence they are called low temperature Fischer-Tropsch (LTFT) reactor. In this type of reactor, heavy hydrocarbons in the form of liquid waxes are obtained and can be further upgraded to yield the valuable fractions. Both iron and cobalt are used as catalyst active sites in those reactors. The main advantages of slurry phase reactors are (i) cost of the reactor, i.e. 25 % of a multi-tubular reactor, (ii) absence of pressure drop, and (iii) easy control of the reaction temperature due to the high heat exchange between the catalyst particles and the liquid medium.

1.2.2.3 Fluidized bed reactor

There are two types of industrial fluidized bed reactors: CFB (circulating fluidized bed) reactor (Figure 1-1C) and FFB (fixed fluidized bed) reactor (Figure 1-1D). Both of them are two-phase reactors and only available for iron-based catalysts at high temperatures, 320-350 ^oC. These two kinds of reactors are geared at producing linear 1-alkenes, gasoline and diesel fuel. They cannot be used for wax production due to the fact that the wax is liquid under FT conditions, which may result in agglomeration of the catalyst and hence de-fluidization. The operation of CFB reactor is similar to that of catalytic crackers, with fluidized catalyst moving down the standpipe in dense phase mode, and then being transported at high gas

velocities by the incoming syngas up the reaction zone side in lean phase mode. The CFB operates as a dense phase turbulent bed reactor.

The formation of a liquid phase in the fluidized bed will lead to particle agglomeration and loss of fluidization, the fluidized bed reactors are used for high temperature Fischer-Tropsch synthesis (HTFT). Indeed, the temperature level of fluidized bed is in the range 320-350 °C. The catalysts generally iron in a metallic state and operating conditions are selected to obtain the desired products. HTFT reactors are generally used to produce light alkenes or gasoline.

1.2.3 FTS catalyst

1.2.3.1 Active Phase

It is a well known fact that Group 8 transition metals are active for the FTS reaction.[16] However the CO hydrogenation activity is a key parameter for a commercial application and only Ni, Co, Fe and Ru have a sufficient activity. Unfortunately, Ni has a high selectivity toward methane and for this reason it is not a suitable catalyst to produce long chain hydrocarbon. Ruthenium is the most active metal for FTS and is also working at the lowest temperature. However the scarce availability and the high cost of Ru prevent its commercial use in large scale FT applications. The choice of active metal, between iron and cobalt for commercial application, depends on parameters including the source of carbon used for syngas and the end-product. For syngas deficient in hydrogen, as those obtained from coal and biomass, iron is generally preferred because of its high WGS activity reaction, the lack of hydrogen is compensated by the WGS but more CO_2 is produced in turn. But with new environmental concerns, including the greenhouse effect, carbon dioxide is becoming an undesired byproduct and the high WGS is becoming a major drawback for iron.

Cobalt is preferred for performing FTS with an almost stoechiometric ratio of hydrogen and carbon monoxide, i.e. syngas produced from natural gas. Because of the relatively high cost of cobalt, the use of bulk cobalt as a catalyst is not economically viable.

To obtain a high exposed cobalt metal surface per mass unit of cobalt, cobalt needs to be dispersed on an appropriate support. To have the well dispersed metal particles, a suitable porous material with high surface area is required. The supported cobalt catalysts are well known to be the best candidates for FTS towards higher hydrocarbons (C_{5+}).[17] The catalyst productivity can be directly predicted from the number of cobalt atoms exposed on the surface of small cobalt particles. These small cobalt particles responsible for the significant enhancement of the FTS performance compared to that obtained on the undoped catalyst with much bigger active phase particle size. Indeed, such metal particles with appropriate size (6 - 20 nm) possessing large fraction of surface atoms significantly contribute to enhancing conversion rate of reactants into products. Besides, the characteristics of the surface atoms are greatly different from atoms in deeper layers such as bond distances, geometries and bonding energies that are altered by the reduced local coordination on the surface. Iglesia et al.[18-20] found a constant site-time yield over the cobalt particle with size range of 10-210 nm, which included most of the typical low-dispersion cobalt Fischer-Tropsch catalysts. De Jong and co-workers[21-22] found that small cobalt particles (< 6 nm) led to low FTS activity and high methane selectivity. Bezemer et al.[21] studied the influence of the cobalt particles size on the FTS reaction using carbon nanofibers as support. The highest CoTY (cobalt time yield) was observed with cobalt particle size centered at about 8 nm under severe reaction conditions, i.e. 35 bar and 250 °C.

1.2.3.2 Supports

Generally, active phase is typically employed in a supported form for the FTS process. The ideal support for the Fischer-Tropsch synthesis should have the following properties: (1) Appropriate specific surface area. (2) Adequate mean pore diameter, preferentially large mesopores. (3) Medium metal-support interactions. (4) High attrition resistance and bulk crush strength. (5) Chemical inertness. (5) Moderate and/or high thermal conductivity. (6) Appropriate size and shape regarding the scaling up to industrial process.

In these case, the support should display a relatively high specific surface area in order to achieve a high dispersion of the metal particles, good mechanical and hydrothermal resistance and a medium level of metal-support interaction in order to allow a complete reduction of the active phase and to prevent sintering of the active sites. The most studied supports for the FTS are alumina, silica, titania and carbon-based materials such as activated carbon, carbon nanotubes and nanofibers.[21, 23-29] Among these supports, alumina, either pure or promoted, is the most employed as commercial catalysts support. However, on traditional supports such as alumina and silica, small particles of metal oxide precursor are difficult to be reduced due to the presence of high metal-support interactions which prevent the complete reduction of the active phase oxide precursor at moderate temperatures.[30-32] In addition, the low thermal conductivity of alumina could lead to the formation of local hot spots during FTS, which compromise the selectivity of the reaction and the plant safety, especially at high CO conversion. In this thesis, the main aim would be developing and designing the suitable carrier for supporting active sites (i.e. Cobalt) as the effcient FTS catalyst.

1.2.4 Recent FTS technology developments

During the last decade a large number of FT plants, operated with syngas gas from either natural gas or coal, have been developed around the world in order to valorize in a better manner the natural gas or coal resources and also to fulfill the environmental legislations which are becoming more and more stringent (Figure 1-2). The total production of the different FT plants is amounted to about 400,000 barrels per day from the operated FT plants nowadays.[13] It is worthy to note that such production remains relatively low compared to the total crude oil production of about 85 million barrels per day. However, taken into account the huge demand of clean fuel for transportation one should expected that the FT plants development will strongly growth up in the near future. In addition, these liquid hydrocarbons also have an advantage to prevent the current infrastructure of the energy supply in many industrial sectors and will remain the most important mean for energy

storage and use for many years to come. The interest in the FT technology is also linked with the extensive exploitation of shale gas during the last decade which significantly modify the natural gas resource supply and as a consequence, its price.

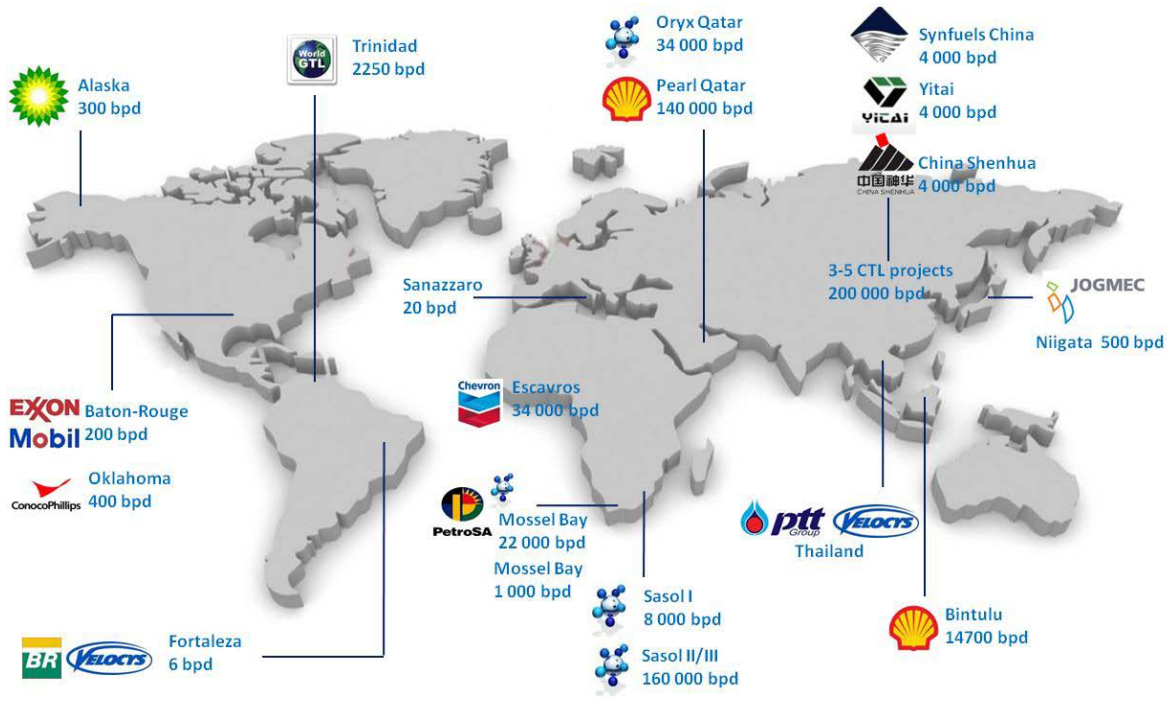

Figure 1-2. Worldwide implantations of the Fischer-Tropsch plants on operation or under way to be constructed. Source TOTAL.

The large proven resources of natural gas and coal emphasize the continuous development of the FT reaction for the next decades for the transportation and chemical fields. In addition, the large development dealing with the shale gas exploitation in the USA during the last decade also significantly impacted the contribution of this later in the energy mix nowadays. The FT reaction should be operated with a highest conversion and selectivity per pass in order to reduce the recycling operation. However, as the FT reaction is a highly exothermic reaction (-165 kJ· mol^{-1}) high conversion leads to the formation of temperature gradient within the catalyst bed which is detrimental for the overall selectivity of the process by favoring intermediate hydrogenation and cracking reactions at the depend of long chain hydrocarbon formation. Multi-tubular fixed bed reactor (MTFB) shows better performance

and is mostly employed in the FT plants.[33-34] The catalyst is in the form of pellets or extrudates with millimeter size in order to reduce the pressure drop across the catalyst bed. In the MTFB reactor the tube diameter is limited to about few centimeters and the CO conversion is kept below 70 % in order to avoid the problem linked with the hot spot formation and temperature runaway which is detrimental for the reaction selectivity and also for the safety of the operated plant. In general, part of the liquid reaction products needs to be recycled inside the reactor in order to remove part of the heat of the reaction.[35] All the drawbacks listed above lead to more investigations dealing with the development of the FT reactor technologies and also to the search of new thermal conductive supports with adequate pore size distribution. It is expected that new improvement on the FT reaction goes closely to the development of new support materials with better physical and chemical properties in order to reduce as much as possible the loss of the selectivity at high CO conversion.

1.3. Insulator macroscopic supports

1.3.1 Key factors of the insulator supports on FTS reaction

The low temperature Fischer-Tropsch reaction is mostly performed nowadays on insulator oxide supports such as alumina, silica and titania, pure or doped with different promoters, which provide high dispersion and stabilization of the active phase consisted with cobalt nanoparticles[23-25]. Alumina is the most used support for FT catalysts, thanks to a reasonably good mechanical properties such as its thermal stability and resistance to attrition at Fischer-Tropsch reaction conditions.[7, 36] The maintain of small cobalt crystallites during the F-T reaction requires a strong metal-support interaction to stabilise the metal particles and prevent sintering.[18] But strong metal interactions induce formation of hardly reducible species that need high reduction temperature which lead to extensive sintering of the active phase particles. According to Jacobs[30] the extent of reduction follows the trend Al_2O_3 < TiO_2 < SiO_2 and increases with the cobalt loading while the average particle size increase follows the reverse trend. There is a competition between dispersion and extent of reduction

of the cobalt crystallite. Among the different supports cited above, alumina has the strongest interaction with cobalt, resulting in a good dispersion of the metal particles but a lower reducibility due to the diffusion of cobalt ions into the alumina structure, while the interaction with silica is lower resulting in larger particles but a higher degree of reduction.[31-32] It has been reported by Biz and Occeli[37] that the water formed during the course of the F-T reaction could induce the formation of the cobalt aluminates with lower F-T activity. Such phenomenon could be partly reduced by depositing a layer of silica on the alumina surface which prevents the formation of the cobalt aluminates during the F-T reaction.

The comparative advance and development of various insulator supported catalysts have also been reviewed by several groups recently.[7, 11, 18] The development of typical insulator supports for enhancing catalytic performance of FTS catalysts can be listed for short as follows:

- Promotion with noble metals and oxides. Introduce the noble promoter (Re, Rh, Rh, Pt and Pd, etc) and oxide-type promoter (ZrO_2, MgO, MnO, La_2O_3, alkalis, etc) for enhancing the dispersion of active sites, obtaining much easier reduction of active components, and even adjust the product selectivity and increasing the FTS reaction. [11, 38-40]

- Investigation of the porosity of the insulator support on the dispersion and sintering of the active phase.[41-44] It has been reported that supports with different pore sizes could led to the formation of active phase nanoparticles with different sizes and sintering behavior which directly impact the F-T performance of the catalyst;[45] In addition, porous structure of the supports strongly affects the extent of cobalt reduction.

- Mastering and adjusting the textural properties by special techniques (Sol-Gel, Colloidal, surfactant added, microemulsion, etc.).[46-48] Martinez et al[47] has developed a hierarchical macro-mesoporous fiber-like γ-Al_2O_3 by a surfactant template method showing the significant effects of diffusion and dispersion during the FTS process.

- Support phase transferred especially for alumina support: γ-Al_2O_3 show high F-T activity but with lower C_{5+} selectivity which is linked with the pore plugging during the reaction leading to the local enrichment of CO versus H_2. On the other hand, α-Al_2O_3 with large pore and low specific surface area shows higher C_{5+} selectivity but low F-T activity due to the problem linked with the active phase dispersion. Holmen's group has also reported the same behaviours on the influence of the alumina-based catalysts on the F-T performance.[25, 38, 49] Rane et al.[49] prepared catalysts supported on several alumina with different phases, i.e. α-, β-, γ-, δ-Al_2O_3 by heat treatment and supported Co as catalysts for FTS. It was observed that α- and δ-Al_2O_3 gave higher C_{5+} selectivity.

1.3.2 Challenges and drawbacks of insulator supports

The formation of cobalt phase which strongly interacts with the insulator support represents a major drawback because of the difficulty in the reduction of the cobalt nanoparticles in strong interaction with the support and thus, leads to the low cobalt active sites available for the F-T reaction.[50-51] In order to ease the reduction of the deposited cobalt phase on these oxide supports, trace amount of noble metals was added to the catalyst which allows the achievement of a higher degree of reduction of the cobalt phase.[52-55] The strong metal-support interactions between the deposited phase and the oxide supports, i.e. Al_2O_3 and SiO_2, and the chemical reactivity of these later also complicate the recovery of the metal and the support after the end-life of the catalyst. On the other hand, carbon-based catalysts are more sensitive to oxidation during the regeneration process. Moreover, the low thermal conductivity of oxide form insulator supports render it more sensitive to the problems of temperature runaway and hot spots formation, which compromise the plant security and decrease the selectivity towards liquid hydrocarbons. Wang et al.[56] have reported that the heat release by the FTS reaction cannot be properly evacuated to the entire body of the alumina support, even with a recycling of part of the liquid reaction products, and thus, leads to the formation of hot spots on the catalyst surface which favors the light product formation.

In addition, the FTS is generally carried out with a relatively low space velocity in order to increase the α-olefins intermediate insertion to improve chain growth. The low space velocity favours the catalyst temperature runaway as generally the hot spot extent is unlikely to appear at high space velocity which causes high turbulence that ensures high heat transfer between the catalytic bed, the gas medium and the reactor wall. One should also note that in some cases the hot spots which are generated on the catalyst surface are at a nanometer size and thus, the extra-heat removal by the gas phase is not sufficient compared to that generated by the reaction itself, i.e. nanoscopic hot spot.

1.4 Thermal conductive supports

1.4.1 Conductive structured metal supports.

Conductive structured metal-based supports such as metal monolith catalyst structures, metallic foams[57-58] and structured packing with open and close cross flow structures, knitted wires, cross flow structure, and finally microstructured reactor[59] have been developed to improve the heat transfer and pressure drop within the FT reactor and also to allow one to ease the catalyst-product recovery. These structured reactors could also be operated in a smaller scale for new developments of F-T plants. By using these conductive supports a relatively high heat transfer improvement has been observed, however, they are still some disadvantages that need to be addressed.

Honeycomb monoliths have been developed as supports for cobalt phase in the F-T reaction by several groups for the F-T process.[60-62] In these reactors, part of the reaction heat was removed by recycling part of the liquid reaction products which were pre-cooled in an external heat exchanger. The results obtained were satisfactory at the lab scale and simulations have confirmed their advantages for the industrial scale development but unfortunately, the later is still at an infancy state due to the lack of industrial interest. Recently, new developments have been reported on the monolith reactors, based on the use of a high thermal conductive material, by the group of Tronconi.[63-64] The metallic monolith and/or foams surface is not efficient for dispersing the catalyst nanoparticles and thus a layer

of wash-coat is needed to ensure the anchorage and dispersion of the active phase. The simulation experiments performed on such system have shown that the radial thermal conductivity reached about 48 W/m/K which is significantly higher than that reported for a fixed-bed constituted by SiO_2 beads of 0.9 mm, i.e. 3-7 W/m/K.[65] The problem linked with the washcoated monolith catalysts is that during the heat treatment part of the interface between the oxide washcoat layer and the metallic structure could be damaged leading to the loss of the active phase.

Ceramic foam, which could be an alternative to ceramic monoliths, has also been extensively developed for the F-T reaction.[66-68] The advantage of foam versus straight channel monolith is the high degree of radial mixing which improve the reactant distribution and also the convective heat transfer. These advantages have been intensively exploited by the group of Schouten in several solid-liquid phase reactions.[69-71] However, in the case of the F-T reaction the low catalytic loading per effective volume of the catalyst leads to a relatively low reaction yield per volume of the reactor.

Microstructured reactors (MR) have been extensively developed during the last decade to operate F-T technology with better heat control and reactant accessibility.[56, 58, 72] The high heat transfer through the small reactor channel wall allows one to operate the exothermic reaction with isothermal gradient even at a relatively high conversion level. The industrial development of such reactor is linked with its cost and the relative complexity of the scale-up. Nowadays only a very few F-T plants have been operated with such microstructured reactors and the overall production is marginal: Petrobras/Velocys plant in Brazil with a production of 6 bpd and a planned F-T laboratory scale in Thailand.

Recent structured conductive catalyst support has been developed by Tatarchuk and co-workers[73-74] which is based on the macroscopic assembly of microfibrous entrapped catalyst (MFEC) with enhanced heat transfer. The cobalt catalyst was deposited on the alumina support which was subsequently entrapped in the copper MFEC. In such catalyst the problem linked with the reduction of the cobalt phase in strong interaction with the alumina represents a main drawback. On such MFEC system the selectivity to methane remains

extremely low even at high reaction temperature which confirms the strong influence of the heat transfer in keeping the selectivity in the F-T reaction.

Another main drawback of these structured catalysts is their relatively low weight per unit volume due to the presence of high voidage which cannot fulfill the high catalytic loading for a given reactor volume to reach an acceptable capacity of production. For these structured catalysts to be efficiently employed in the F-T reaction a much higher activity per weight compared to that reported nowadays is needed.

1.4.2 Nanocarbon materials for F-T synthesis

The last decade has also witnessed a huge development of thermal conductive and high effective surface area nanocarbon supports for the F-T reaction. These nanoscopic supports significantly contribute to reduction of the problem linked with thermal runaway within the catalyst bed and also to improve the mass transfer within catalysts. Nanocarbon materials support, i.e. carbon nanotubes (CNTs), nanofibers (CNFs) and mesoporous carbons have recently attracted much attention as catalyst supports in FT synthesis because of their unique properties, such as high purity, high mechanical strength, high electrical conductivity, high thermal stability, and high surface area.[27, 75-87] Nanocarbons possess high external surface areas without micropores, which may be beneficial to F-T reactions by reducing the problem linked with mass transfer. These thermal conductive supports have been faced an unprecedented investigation during the last decades.[88-89] Recent reports have shown that these supports allow one to improve in a relative manner the selectivity towards long-chain hydrocarbons in the F-T reaction, probably by improving the escaping of the intermediate products.

1.4.2.1 Surface functionalization and confinement effects

Carbon nanotubes show an excellent catalytic performance as catalyst support in Fischer-Tropsch synthesis thanks to their exceptional properties such as thermal, functional groups on the surface, electric conductivity, and relative higher effective surface area with

unique and open structure.[27, 77-87] Many previous works were focused on the role of the active phase particles localized on inner or outer CNTs walls[27, 90], particle size [79, 91], and the diameter and pore size of nanotubes[77, 86] on the catalytic performance. Different functional groups can be introduced onto the surface of nanocarbon materials, which are useful for immobilization of the catalytic actives sites or induce the additional catalytic functional groups. The influence of acid treatment of CNTs on the catalytic performance over the supported Co catalysts was investigated by Dailai and other researchers.[92-93] The caps of the closed carbon nanotubes support was opened by HNO_3 treatment, the capillary force led to the homogeneous dispersion of a larger fraction of particles within the tubes.The smaller cobalt particle size and higher reducibility Co species are obtained with significantly increased CO conversion.[92] However, the C_{5+} selectivity became lower and the CH_4 selectivity became higher. These tendencies are unlike those of the CNT-supported Fe catalyst, with which a higher C_{5+} selectivity was achieved over the confined Fe particles.[85] Another study showed that the Co species had irregular shape and were mainly anchored on the outer surface of the acid-pretreated CNTs.[77] The average size of cobalt oxide particles before reduction was about 11-15 nm, slightly depending on the outer diameter of the CNTs. The catalysts also displayed high cobalt reducibility. Besides, acid pretreatment resulted in a 25% increase of selectivity in hydrocarbon. Nitrogen doping CNTs (N-CNTs) was also achieved by means of a gas-phase treatment using nitric acid vapor at 400 ^{o}C.[94] This nitrogen functionalization CNTs was used as a support for Fe and showed a good intrinsic FTS activity. For the 40 % mass content of Fe on N-CNTs, high and constant stabilized CO conversion was obtained over a period of 80 h time on stream under industrially relevant conditions. Trepanier et al.[79] used microemulsion technique (Figure 1-3) to synthesis cobalt particles on CNTs catalysts with a narrow particle size distribution. Comparing to those prepared by incipient wetness impregnation, the controllable cobalt nanoparticles synthesized by the microemulsion technique lead to a significant improvement of the CO conversion without losing C_{5+} selectivity. In this research, the Co particles at the range of 2 - 6 nm, which were smaller than the theoretical particle size to obtained high C_{5+} selectivity,

i.e. > 6- 8nm, were almost confined inside the CNTs and also performed a high C_{5+} selectivity, i.e. 89%,[21-22] revealing the electron deficiency in the inside surface changed the commonly expected results.

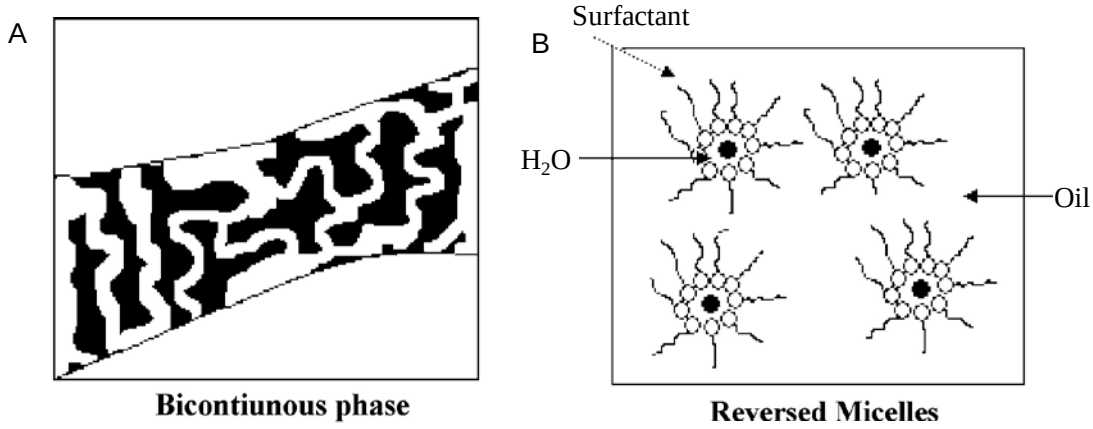

Figure 1-3. Microemulsion structure at a given concentration of surfactant: (a) Water-in-oil phase, (b) formation of cobalt particles (black dots) within the reversed micelles with the addition of surfactant. [79]

Besides, carbon nanotubes consisted by concentric graphene layers with well-defined hollow interiors that causes π-electron density shifting from the concave inner surface to the convex outer surface have confinement effect to influence the structural and catalytic properties of metallic based catalysts.[95-97] This confinement was efficiently applied by several research groups for enhancing the FTS performance on these carbon-based catalysts (Figure 1-4A).[27, 90, 98] Chen et al.[27] found that the reducibility of the iron species is significantly delayed when they were encapsulated inside CNTs (Fe-in-CNT), even the particle size of Fe-in-CNT was in the range of 4-8 and smaller than that outside of CNTs walls (Fe-out-CNT), i.e. 6-10 nm (Figure 1-4B)[21-22]. The enhancement of FTS catalytic performance can be attributed to the confinement effect of the iron catalyst within the CNTs hollow interiors. The C_{5+} hydrocarbons production over Fe-in-CNT was almost 200% of that obtained over Fe-out-CNT and even 6 times more than that over iron deposited on activated

carbon (Fe/AC) catalyst. The Fe-in-CNT was also very stable as a function of time on stream and the Fe particle size was not significantly changed after 200 h of reaction. In contrast, the Fe particle size for the Fe-out-CNT catalyst grew significantly during the reaction. However, the same results have not been found in the case of cobalt. Indeed, no obvious difference between the of C_{5+} hydrocarbons selectivity through FTS on cobalt species encapsulated inside CNTs (Co-in-CNTs) and sited outside of CNTs walls (Co-on-CNTs) when cobalt nanoparticles are completely reduced by pretreatment at 400 °C in pure H_2.[98] The absence of significant differences in the catalytic selectivity of active site Co-in-CNTs and active site Co-on-CNTs suggests that the different electronic densities between the internal concave and external convex surfaces of CNTs do not significantly affect the catalytic selectivity for C_{5+} hydrocarbon over cobalt on CNTs.

1.4.2.2 Hierarchically structured composites

The FTS is one of the most complex three-phase reaction processes, regarding the highly exothermic reaction and various reactions taking place during the gas- to- liquid transformation. The selectivity of long chain hydrocarbons (C_{5+}) depends significantly on the reactor temperature profile. The selection of the appropriate catalysts and carriers for the F-T reaction should obey several roles: good thermal conductivity of the support and the liquid hydrocarbon film formed on the catalyst surface;[99] relatively lower pressure drop along the catalyst bed if used in fixed-bed reactors;[100] effective utilization of all active sites presented on nanoparticles on a macroscopic level; and the structure of the support that favors the evacuation of the products along with satisfied accessibility to the reactants.[100] Thus, it is interesting to apply the structured, thermally conductive nanocarbon composites catalysts in the highly exothermal Fischer-Tropsch synthesis. Chin et al.[101] explored the FeCrAlY foam decorated with aligned multiwall carbon nanotube arrays as microchannel support, and then Co-Re active phase was loaded on this hierarchical structure for subsequence FTS evaluation. The catalyst with such structure, especially resulting from the hierarchical CNTs, provided larger surface area for anchoring active sites, high thermal conductivity and enhances mass transfer. The CH_4 selectivity remained at stable value (~ 20%) at reaction temperature as

high as 290 ^{o}C which indicates that no temperature gradient was presented in the catalyst bed.

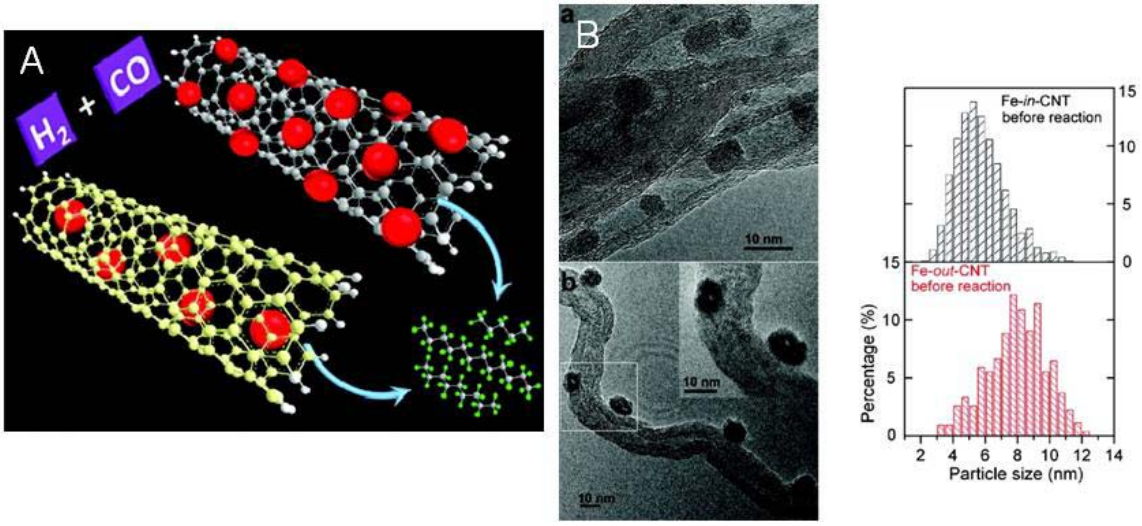

Figure 1-4. (A) Schematic showing the location-specific carbon-nanotube-supported catalysts for Fischer–Tropsch synthesis. (B)TEM images and iron particle size distribution of (a) Fe-in-CNT and (b) Fe-out-CNT. [27, 98]

Many studies have demonstrated that the growth of carbon nanotubes/nanofibers on the macroporous body could provide efficient contact between activate sites and reactants, higher thermal conductivity and better mass transfer.[102-104] The carbon nanofibers were for the first time grown onto carbon synthesized by Zarubova et al.[103] using the method of chemical vapor deposition (CVD) with higher BET surface area (> 280 $m^2 \cdot g^{-1}$) and unique hierarchical structure. The cobalt supported on the hierarchically structured composite (Co/FB-CNF/carbon-felt) was further tested in the FTS without any dilution. The catalyst shows a very stable reaction temperature which indicates that temperature runaway was not occurred within the catalyst bed. In the same time, platelet structured (Co/P-CNF/ carbon-felt) similar with CNF powder catalysts, had a temperature runaway during the FTS reaction (Figure 1-5). The turnover frequency (TOF) of Co/FB-CNF/carbon-felt was 42 s^{-1} compared to 24 s^{-1} of Co/P-CNF/carbon-felt with similar C_{5+} selectivity, i.e. 78.2% and 81.4%,respectively, at the same CO conversion of 40%.[103] These results indicate that the

structure of the support is of primary important to avoid the problem linked with temperature runaway in the FTS reaction.

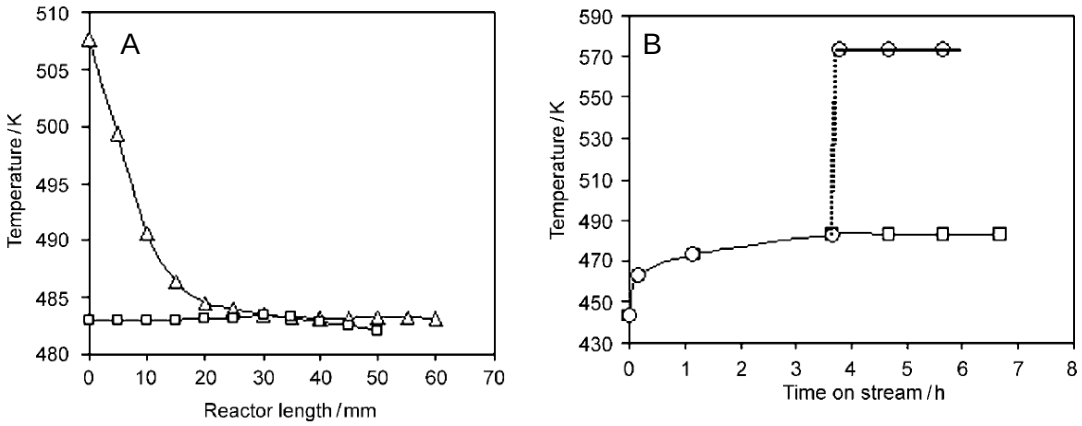

Figure 1-5. Temperature profile along the catalyst bed at 4 h time on stream (A) and change in temperature with time on stream at the reactor inlet (B) of Co/FB-CNF/carbon-felt and Co/P-CNF/carbon-felt. [103]

1.4.2.3 Porous nanocarbons

Some early investigations in the 1980s demonstrated that iron with high dispersion on porous carbons displayed moderate activity and relatively high stability at 1 atm for the FTS reaction.[105-108] Unfortunately, the FTS specific activity decreased with reducing iron crystallite size and iron metal loading in the Fe/C system.[106-107] It is expected that the presence of microporous in the carbon support probably led to the worse FTS activity and the lower operating pressure in these researches, which was hard to meet the industrial requirements. Recently, Coville and co-works[91, 109] prepared carbon spheres (CS) which were composed of random curling graphitic flakes by chemical vapor deposition method to supported cobalt and iron actives sites for FTS. Catalytic performance of catalysts based on CS support was similarly with that of CNTs, and providing an adequate carbon model supports to investigated metal-carbon interactions. However, the disadvantage of the above-mentioned CS was the relatively lower surface area (< 5 $m^2 \cdot g^{-1}$).[16]

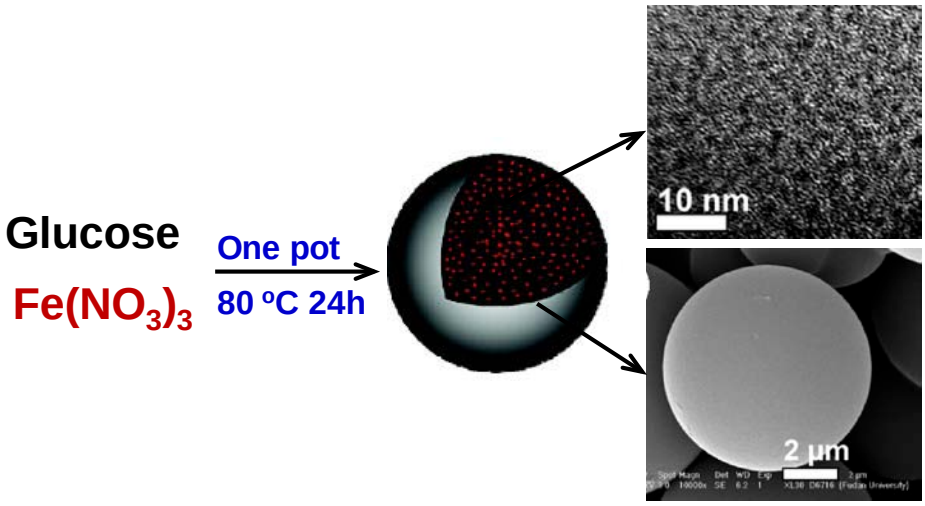

Figure 1-6. Schematic illustrations of Fe*x*O*y*@C sphere with iron oxide nanoparticles highly dispersed inside. [110]

Yu et al.[110] prepared carbonaceous spheres embedded with iron oxide nanoparticles (Fe_xO_y@CS) by using one-pot hydrothermal cohydrolysis -carbonization process involving glucose and iron nitrate (Figure 1-6). This confinement of the carbonaceous matter on iron oxide nanoparticles restrained the particles aggregation during the severe FTS reaction. In such catalysts, the high FTS stability and activity, along with a high selectivity towards the C_{5-12} fraction, i.e.40%, were obtained which were much better than the values reported to date over iron catalysts without promotor.[110] The TEM analysis performed on catalyst, before and after 108 h of reaction, indiacted that the particle sizes of the iron species only slightly enlarged from around 7 to 9 nm, which indicates an advantage of the confinement effect of the carbonaceous matter on the sintering of the iron carbide nanoparticles during the FTS test.

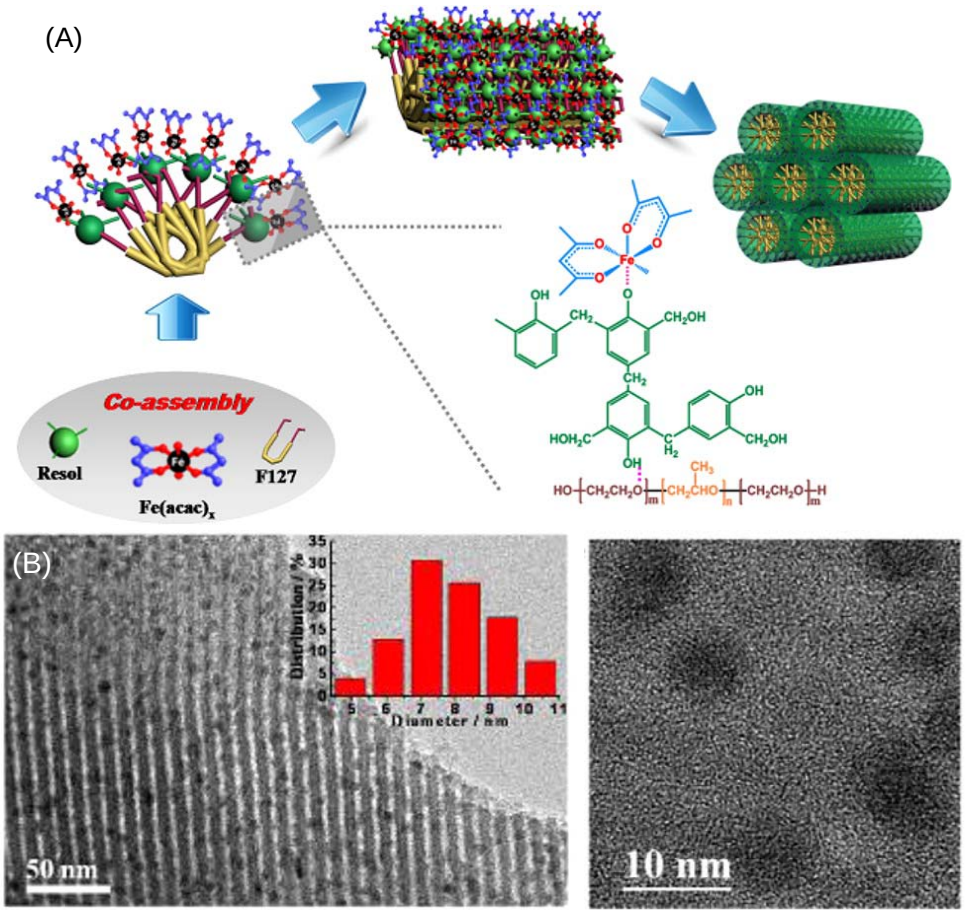

Figure 1-7. (A) Schematic illustrations of the Chelate-Assisted Co-Assembly Route for the Synthesis of Ordered Mesoporous Carbon Nanocomposites Incorporated with Size-Tunable Metallic Nanoparticles. (B) TEM and HRTEM images of the iron-oxide nanoparticles-incorporated ordered mesoporous carbon nanocomposites (Fe–C-8) Inset in (B) is the corresponding particle size distributions of the iron-oxide nanoparticles in the samples Fe-C-8. [111]

A chelate-assisted coassembly route for the synthesis of high-quality ordered mesoporous carbons incorporated with highly dispersed uniform Fe_2O_3 nanoparticles, was reported by Sun et al.[111] The synthesis was based on a multicompoment coassembly process which was accomplished by slow evaporation of an ethanol solution containing soluble resol as carbon source, iron nitrate as metallic precursor, acetylacetone (acac) as chelating agent, and Pluronic F127 as template (Figure 1-7A). The obtained nanocomposites have 2-D hexagonally arranged pore structure, homogeneous pore size (~4.0 nm), high surface area (~500 m^2/g), uniform and highly dispersed Fe_2O_3 nanoparticles with readily controllable

size in the range of 8.3-22.1 nm, and constant Fe_2O_3 contents around 10 wt %. It was moreover found that the Fe_2O_3 nanoparticles were partially embedded in the carbon framework with the remaining part exposed in the mesopore channels (Figure 1-7B). This unique semiexposed structure not only provided an excellent confinement effect and exposed surface for catalysis but also helped to tightly trap the nanoparticles and thus prevented aggregating during catalysis. Owing to the high porosity of the carbon matrix and the unique semiexposed structure of iron-oxide nanoparticles, the mesoporous Fe/carbon nanocomposite catalyst (Fe-C-8) with a small Fe particle size (~8 nm) showed an excellent catalytic performance with a remarkable stability and C_{5+} selectivity (> 68%) in FTS.

1.4.3 Challenges and drawback of thermal conductive supports

The results reported above have highlighted the fact that the improvement of the liquid hydrocarbon selectivity is mostly linked with the thermal conductive character of the support which prevents the local hot spot formation and also to the nanoscopic dimension of the supports which could favor the access of the reactant and the escaping of the intermediate product. However, the main drawback of these thermal conductive carbon-based supports is linked with their nanoscopic size which generates a large pressure drop across the catalyst bed in a fixed-bed configuration compared to the traditional macroscopic size suppots (Figure 1-8). In addition, the problem linked with the transport and handling of these nanomaterials also represents a healthy issue concern.[112]

The problem of pressure drop can be partly avoided by supporting these nanoscopic carbons on a macroscopic host matrix.[113-114] However, another drawback with the use of these nanoporous carbon materials, even in a macroscopic shape, is their high reactivity with oxygen which could lead to the problem of material deterioration during the repeated oxidative regeneration of the spent catalyst. Optimization study on the improvement of the oxidative resistance of these materials is still in progress. In addition, depending to the microstructure of the support, basal or prismatic planes, with difference graphitic arrangement, exposure, a large difference in terms of the heat removal has been reported.[29]

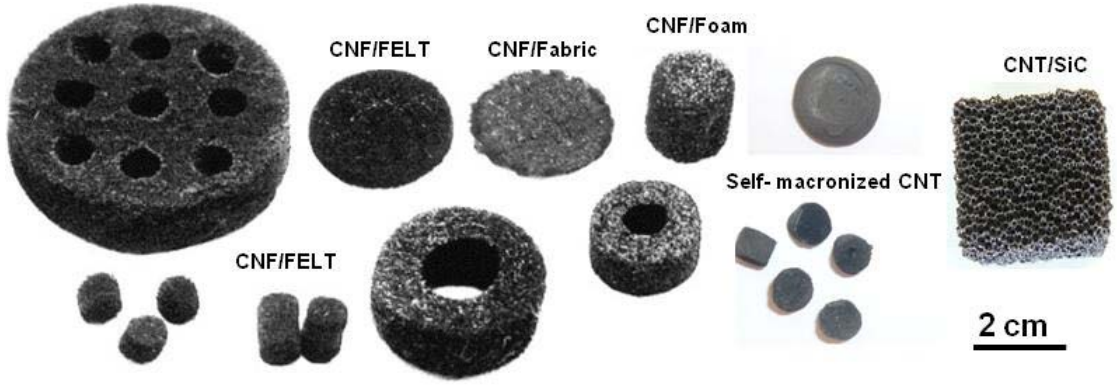

Figure 1-8. Representative SEM micrographs of the CNT and CNF supported on macroscopic host structures (grains, extrudates, foam and monolith, ect).[115-116]

1.5. Strategies in the designing of carbide hybrid materials for FTS catalysts

Carbides were consisted of carbon and less electronegative elements, which can be classified as covalent (e.g. SiC, BC), transition metal carbide (e.g. TiC, WC) or salt-like (e.g. CaC_2). Nowadays, carbides are used in more advanced applications such as catalytic supports, filters, radiant burners, biomedical or electronic devices thanks to extreme hardness of covalent solids, the high melting temperature of ionic crystals, and the excellent electric and thermal conductivity of transition metals. However, all these carbides display a relatively low specific surface area which hinders their use as catalyst support, and thus, a key issue to be optimized is dealt with the development of new synthesis methods for improving the surface area of these materials. Hence, a multiplicity of papers has been published over the last few decades dealing with different porous carbide materials, their preparation, characterization and applications.[117-119] This is even more surprising as many have underlined important roles of transition metal carbide and covalent carbide for F-T process. In this section, we will focus our attention on the synthesis and use of the carbide materials either as active phase or as catalyst support in the F-T reaction. The most part will

be focused on the synthesis and use of silicon carbide as thermal conductive support for the F-T reaction.

1.5.1 Carbide as catalysts

Transition metal carbide, such as molybdenum carbide,[120-121] iron carbide[122-127] can be employed as catalysts for F-T reaction. Saito et al.[39] investigated unsupported molybdenum oxides, sulfide, carbide, and nitride compounds. They found that initial specific activities of these compounds (rates per unit surface area of catalyst) were comparable to the best metallic and oxide catalysts. However, most of molybdenum-based materials show a low F-T activity compared to iron-based catalyst. Iron carbides consist of iron atoms occupied by the carbon atom can adopt various structures which can be classified according to the sites replaced by the carbon atoms: structures with carbon atoms in trigonal prismatic (TP) interstices and structures with carbon atoms in octahedral interstices. (Pseudo-) cementite (θ-Fe_3C), Hägg carbide (χ-Fe_5C_2) and Fe_7C_3 have been well known carbides in F-T of the former class since the first characterization studies. These carbides usually have stable and clearly established structures. Most iron carbide catalysts reported are synthesized during the activation treatment or under F-T reaction conditions from iron oxide precursor.[8] The direct synthesis of iron carbide for being employed as FTS catalyst has appeared in recent years. Yang et al.[127] explored one-pot wet chemistry strategy to synthesize Fe_5C_2 nanoparticles by using iron carbonyl, $Fe(CO)_5$, with octadecylamine in the presence of bromide under mild temperatures, i.e. 350 ^oC (Figure 1-9). The as-synthesized Fe_5C_2 as an FTS catalyst demonstrated higher activity and selectivity than a conventional reduced-hematite catalyst. However, Fe_5C_2 NPs deactived rapilly during the FTS reaction with the initial 30 h time on stream. The Fe_5C_2 NPs catalyst deactivation mostly due to the partial oxidation of the Fe_5C_2 leading the reaction between the carbide and the H_2O and CO_2 formed in the FTS reaction. It is interesting to observed the single phase iron carbide play a role as catalytic activity in FTS from the point of this research.

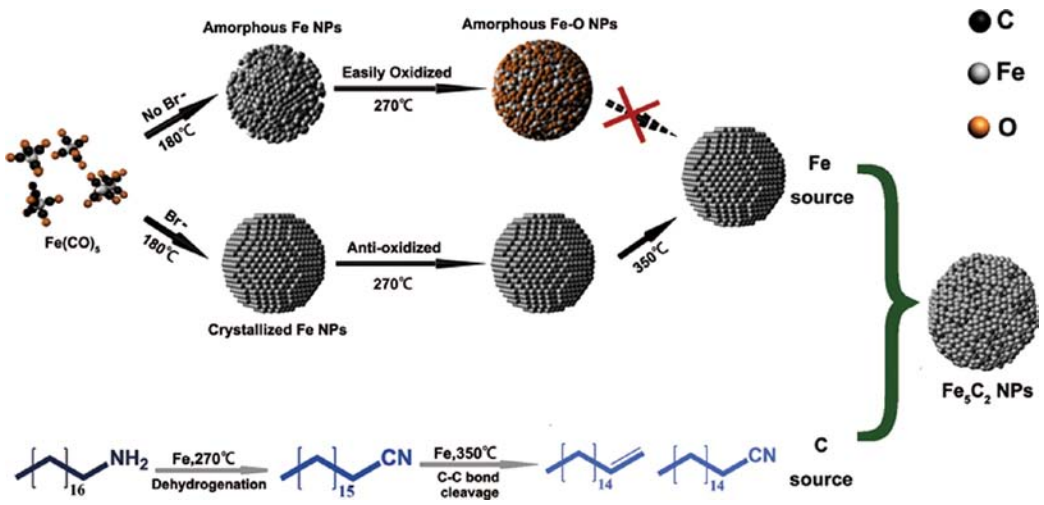

Figure 1-9. Schematic illustration of the formation mechanism of Fe_5C_2 nanoparticles.[127]

1.5.2 Beta-SiC as efficient catalysts supports on F-T reaction

The development of thermal conductive supports with macroscopic shaping and adequate pore size (meso- and macropores) is of interest to improve the F-T performance, especially the long-chain hydrocarbon selectivity at high CO conversion by reducing the problem of hot spot formation, and the one linked with the pore size plugging by liquid hydrocarbons which significantly hinder the accessibility of the reactants to the active site.

Silicon carbide possesses all the physical properties required for being used as catalyst support namely: high mechanical strength, high thermal conductivity (which allow a rapid homogenization of the temperature within the catalyst bed), high oxidative resistance, and chemically inertness (which facilitate the recovery of the active phase and the support for subsequence re-uses and to reduce the problem of solid waste storage).[128-132] However, the extensive use of silicon carbide as support in the field of heterogeneous catalysis is still hampered due to the low specific surface area of the material produced via the Acheson process operated at high temperature, i.e. 1800 °C. In order to circumvent such drawback silicon carbide (β-SiC) with medium to high specific surface area (10 to > 100 m^2/g) has

been synthesized according to the gas-solid Shape Memory Synthesis (SMS) method developed by Ledoux et al. [133-134] in the early of 1990s. The synthesis was further extensively developed by Pechiney Cy. before being transferred to SICAT SARL which continues to develop and optimize the synthesis process nowadays.[135]

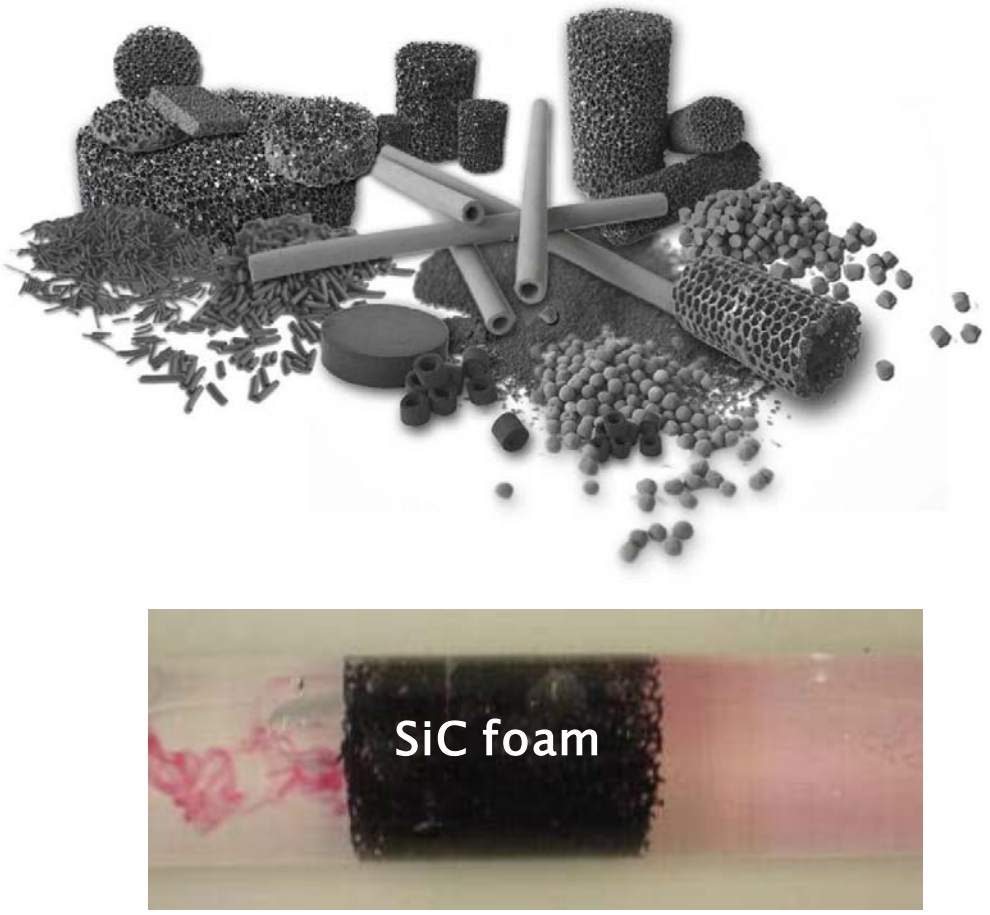

Figure 1-10. (**A**) Optical photo of the medium to high specific surface area (from 10 to 100 $m^2 \cdot g^{-1}$) porous silicon carbide support with different macroscopic shapes ranged from 10^{-6} m to 10^{-1} m. (**B**) Flow mixing through a SiC foam which acting as a static mixer. Courtesy by SICAT SARL. [136]

The synthesis was carried out by carbonizing a solid mixture containing silicon particles, carbon black and a solid resin containing oxygenated groups at a temperature of around 1300 °C under argon atmosphere to produce porous silicon carbide with medium to high specific surface area.[137] The reaction sequences are detailed below:

$$2\ Si + O_2 \rightarrow 2\ SiO \qquad (1\text{-}11)$$

$$SiO + C \rightarrow SiC + CO\uparrow \qquad (1\text{-}12)$$

Figure 1-11. Pilot plant used for the industrial production of β-SiC according to the gas-solid reaction between SiO and solid carbon with a production capacity of 50 tons/year. Courtesy by SICAT SARL (www.sicatcatalyst.com).

The gaseous CO formed during the reaction was continuously removed by the argon stream in order to shift the reaction towards the right hand side. The reaction temperature is kept low enough to avoid the excessive sintering of the formed SiC for different catalytic applications. The synthesis method allows one to produce SiC with different size and shapes (grains, spheres, extrudates, tubes, discs and foams) for various catalytic downstream applications going from the Fischer-Tropsch synthesis to selective hydrogenation and/or oxidation processes (Figure 1-10A). The SiC foam with periodical windows arranged in a 3D model can be also used as a static mixer for performing a well mixing of the reactant before entering the reaction zone as illustrated in Figure 1-10B.

The β-SiC synthesis was carried out nowadays at a pre-industrial scale (> tons per year) by the SICAT SARL.[136] A pilot for the SiC synthesis with a capacity of 50 tons/year is presented in Figure 1-11**.** The synthesis conditions are well optimized allowing the industrial production of the SiC material with controlled pore size for various catalytic applications.

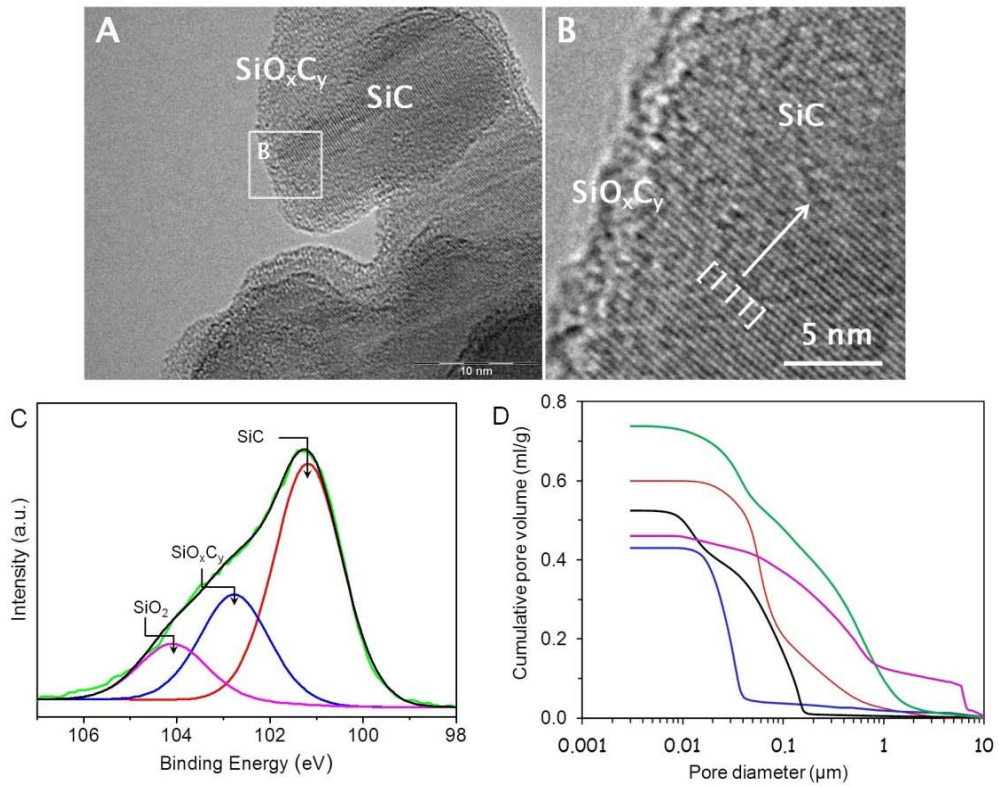

Figure 1-12. (**A, B**) High-resolution TEM micrographs of the SiC surface showing the presence of an amorphous layer (natural wash-coat). (**C**) XPS Si*2p* spectrum of the amorphous layer evidencing the presence of a SiO_xC_y and SiO_2 mixture. (**D**) Mercury pore size measurements of the different SiC support which are consisted by a meso- and macropores network.

The SiC surface, after synthesis and decarbonization at 800 °C in air to remove the residual unreacted carbon, was homogeneously covered with a thin layer of amorphous phase, which is consisted by a mixture of SiO_xC_y and SiO_2, according to the high-resolution TEM and XPS analysis (Figure 1-12).[137-139] Such a natural wash-coat layer allows the good wetting of the support by the impregnated solution and provides anchorage sites for

dispersing the metal nanoparticles on the support surface. In addition, the SiO_xC_y/SiO_2 layer is covalently bonded with the SiC matrix underneath and thus, problem linked with wash-coat breaking, as observed in the case of wash-coated honeycome monoliths, is unlikely to occur. The synthesis method also allows one to produce SiC with controlled meso- and macropore distribution according to the mercury pore size measurements and to the TEM tomography analysis (Figure 1-12). It is worthy to note that the SiC synthesized by the gas-solid reaction typically contains large pore network as evidenced by the TEM tomography presented in Figure 1-13. Such pores will speed-up the mass transfer of the liquid hydrocarbons from the inner to the outer surface of the catalyst during the F-T reaction and prevent gradient concentration of the reactant within the pore which ultimately leads to a higher selectivity towards light products.

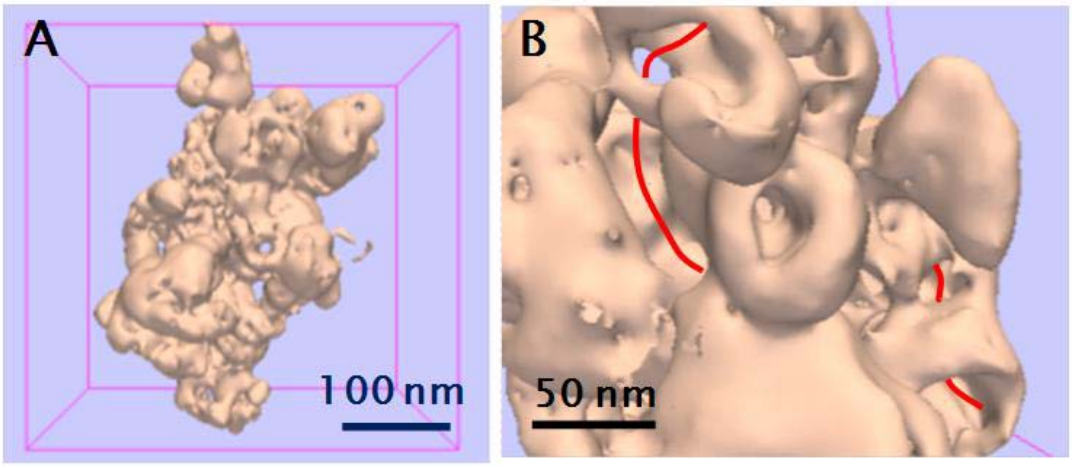

Figure 1-13 TEM tomography micrographs showing the presence of the interconnected meso- and macropores within the SiC sample (indicated by a red line).

The Fischer-Tropsch results obtained on the different SiC-based supports and under various reaction conditions are summarized in Table 1-1. The SiC-based catalysts, with foam or grains morphology, exhibit a moderate activity for the F-T with however, a relatively high selectivity toward the liquid hydrocarbons.[140-141] The F-T activity was strongly influenced by the nature of the impregnated solvent, i.e. ethanol versus water.[139] The SiC also gives

higher reducibility compared with commercial supports (Al_2O_3 and SiO_2) which could enhance catalytic activity as well as promote the chain growth. With the CoOx crystal size decreases, the significant higher reducibility was observed on the SiC supported cobalt catalysts (Figure 1-14).

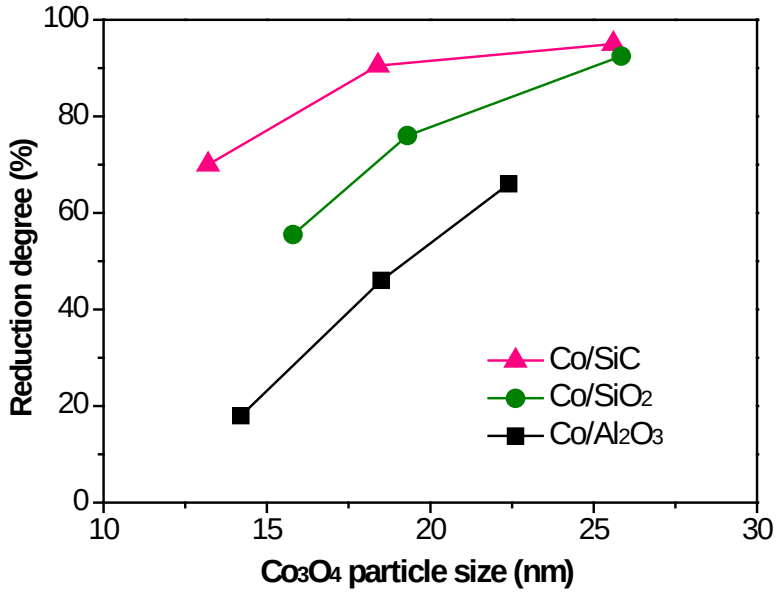

Figure 1-14. Relationship between Co_3O_4 particle size and its reducibility on SiC, SiO_2 and Al_2O_3.[142]

According to the results the FT performances on the SiC-based catalysts is significantly improved by introduction of a doping inside the SiC matrix.[140] The TiO_2 phase provides anchorage site for the dispersion of the cobalt active phase leading to an improved FT activity while the SiC conductive support allows a better heat transfer keeping the C_{5+} selectivity as high as 90 % even at a relatively high CO conversion. It is also worthy to note that the SiC is mainly constituted by meso- and macro-pores (according to the pore size distribution reported above) which significantly enhance the mass transfer for the FT reaction and prevent the formation of a concentration gradient between the two reactants within the catalyst pores. Indeed, during the FTS reaction the catalyst pores were mostly

filled with liquid waxes and thus, both the gaseous reactants and the products must diffuse through a liquid layer before reaching or leaving the active site. Such gas-liquid diffusion layer causes more severe concentration gradients for CO than for H_2 due to the higher diffusivity of the later. The difference in term of reactants diffusivity leads to the formation of high local concentration of H_2 versus CO and as a consequence, a higher selectivity toward light products formation and especially methane. [139, 141, 143-144]

Table 1-1 FTS catalytic performance on the SiC-supported catalysts

Catalyst	Promoter	Reaction conditions	X_{CO} (%)	S_{C5+} (%)	CoTY[a]	Ref.
10Co/SiC	-	235 °C, H_2/CO=2, 6000 $Ncm^3g^{-1}h^{-1}$, 20 bar	67.2	94.1	14.8	[141]
30Co/SiC(foam)	-	220 °C, H_2/CO=2, 330 h^{-1}, 40 bar	71	85	0.58	[131]
30Co/Al_2O_3-SiC (foam)	-	220 °C, H_2/CO=2, 330 h^{-1}, 40 bar	75	79	0.46	[131]
20Co-2Ca/SiC	Ca	235 °C, H_2/CO=2, 6000 $Ncm^3g^{-1}h^{-1}$, 20 bar	39.4	99.6	2.1	[144]
12.5Co-2Ca/SiC	Ca	250 °C, H_2/CO=2, 6000 $Ncm^3g^{-1}h^{-1}$, 20 bar	59.3	98.5	4.7	[144]
30Co-0.5Ru/SiC	Ru	230 °C, H_2/CO=2, 3800 h^{-1}, 40 bar	47	91.6	-	[139]
10Co/SiC	-	230 °C, H_2/CO=2, 3800 h^{-1}, 40 bar	35.4	91.6	5.3	[140]
10Co/TiO_2-SiC	TiO_2	230 °C, H_2/CO=2, 3800 h^{-1}, 40 bar	50.5	91.7	7.5	[140]

[a] Cobalt Time Yield (10^{-5} $mol_{co}\cdot g_{Co}^{-1}s^{-1}$, molar CO conversion rate per gram of Co per hour).

1.6 Scope and outline of this thesis

Fischer-Tropsch synthesis is a method for production of clean synthetic fuels which converts syngas (CO and H_2) into liquid fuels. According to the previous work in the

reported literatures and patents, it can be found that the cobalt active sites supported on the materials with high thermal conductivity (which allows a rapid homogenization of the temperature within the catalyst bed), opened structure (which have macro- and mesoporosity or hierarchical structure) is necessary to accelerate Fischer-Tropsch synthesis process in the development of commercial catalysts. The aim of the present work deals with the thermal conductive supports with macroscopic shaping in the Fischer-Tropsch reaction.

In this thesis, materials like silicon carbide (β-SiC) and alpha alumina (α-Al_2O_3), that perform a medium FTS activity and high long-chain hydrocarbon (C_{5+}) selectivity owing to the properities listed above, are selected as the materials to be improved and applied as the novel supports. We will explore several types of cobalt-based catalysts supported on a large pore alpha-alumina decorated with carbon nanotubes and silicon carbide, doped and decorated with TiO_2, for the FTS. The results obtained will be bench-marked with the state-of-the-art FTS catalysts. The detailed research in this thesis contains the following aspects:

In chapter 1, the development of Fischer-Tropsch technology and efficient thermal conductive supports are reviewed according to the presented literatures.

In chapter 2, the experimental details of materials (supports and catalysts), preparation, characterization techniques and Fischer Tropsch synthesis reaction are displayed.

In chapter 3, we will investigate the FTS performances on a new type of hierarchical support consisting of CNT-α-Al_2O_3 coated with a thin layer of TiO_2 for cobalt active phase. It concerns the synthesis of a new hierarchical composite consisted by multi-walled carbon nanotubes (CNT) layer anchored on macroscopic α-Al_2O_3 host matrix and its use as support for the Fischer-Tropsch synthesis. The composite is constituted by a thin shell of a homogeneous, highly entangled, and structure-opened carbon nanotubes network and exhibits a relatively high and fully accessible specific surface area of 76 $m^2 \cdot g^{-1}$, compared to the origin support, i.e. 5 $m^2 \cdot g^{-1}$. The higher metal-support interaction between the carbon nanotubes surface and the cobalt precursor lead to a relatively high dispersion of the cobalt

nanoparticles. The intrinsic thermal conductivity of decorating CNT could also help the heat dissipating throughout the catalyst body and thus, avoids the formation of local hot spots that may appear in the high CO conversion under the pure syngas feed in FTS reaction.

The TiO_2 is successfully introduced into the hierarchical support during the synthesis process which strongly interacts with cobalt active site, leading to high dispersion of cobalt, accounting for the better activity and stability in FTS reaction. The catalyst also exhibits a highest activity among the all catalysts containing TiO_2 reported nowadays in the literature. This homogeneous TiO_2 layer plays a key role to anchor smaller cobalt particles (< 6 nm) with high dispersion and better resistance towards sintering. The obtained catalysts perform excellent catalytic performance with high C_{5+} selectivity (> 85%) in the FTS reaction.

In chapter 4, we are exploring the metal-support interactions of titanium dioxide decorated silicon carbide (β-SiC) supported cobalt catalyst for Fischer-Tropsch synthesis (FTS) with a combination of energy-filtered transmission electron microscopy (EFTEM), ^{59}Co zero field nuclear magnetic resonance (^{59}CoNMR) and other conventional characterization techniques. From the 2D elemental maps deduced by EFTEM tomography and ^{59}Co NMR analyses, it can be concluded that the nanoscale introduction of the TiO_2 into the β-SiC matrix significantly enhances the formation of small and medium-size cobalt particles. The results reveal that the proper metal-support interaction between cobalt nanoparticles and TiO_2 leads to the formation of smaller cobalt particles, which possess a large fraction of surface atoms, thus significantly contributes to the great enhancement of conversion and reaction rate. Besides, in the industrial process the metal loading is generally high at around 30 wt. % in order to ensure a highest CO conversion per pass and to avoid costly recycling of the unreacted products. The higher cobalt mass loading is also introduced to obtain higher hydrocarbon productions per weight of catalyst in FTS reaction.

In chapter 5, we will report on the development of a highly activity Fischer-Tropsch catalyst based on single crystalline titanium dioxide coated high porosity β-SiC. To date, there has been no report on the utilization of TiO_2 coated on high porosity, thermal

conductivity support such as SiC for FT synthesis. The influence of the TiO_2 loading on the FTS performance is also investigated. The relationship between the cobalt particles dispersion and the FTS performance is investigated using a ^{59}Co zero field NMR and EFTEM characterization techniques.

In chapter 6, the conclusive information obtained during my work, and the concerned indicate novel strategies for the enhancement of catalytic performance of supported cobalt catalysts in FT synthesis are summarized.

1.7 References

[1] K. Aleklett, M. Hook, K. Jakobsson, M. Lardelli, S. Snowden, B. Soderbergh, *Energ Policy* **2010**, *38*, 1398-1414.

[2] G. Centi, S. Perathoner, *Chemsuschem* **2011**, *4*, 913-925.

[3] G. W. Huber, S. Iborra, A. Corma, *Chemical Reviews* **2006**, *106*, 4044-4098.

[4] J. R. Rostrup-Nielsen, *Science* **2005**, *308*, 1421-1422.

[5] F. Fischer, H. Tropsch, *Brennstoff Chem* **1923**, *4*, 276-285.

[6] F. Fischer, H. Tropsch, *Brennstoff Chem* **1926**, *7*, 97-104.

[7] A. Y. Khodakov, W. Chu, P. Fongarland, *Chemical Reviews* **2007**, *107*, 1692-1744.

[8] E. de Smit, B. M. Weckhuysen, *Chem Soc Rev* **2008**, *37*, 2758-2781.

[9] A. M. Saib, D. J. Moodley, I. M. Ciobica, M. M. Hauman, B. H. Sigwebela, C. J. Weststrate, J. W. Niemantsverdriet, J. van de Loosdrecht, *Catal Today* **2010**, *154*, 271-282.

[10] N. E. Tsakoumis, M. Ronning, O. Borg, E. Rytter, A. Holmen, *Catal Today* **2010**, *154*, 162-182.

[11] Q. H. Zhang, J. C. Kang, Y. Wang, *ChemCatChem* **2010**, *2*, 1030-1058.

[12] J. C. Kang, K. Cheng, L. Zhang, Q. H. Zhang, J. S. Ding, W. Q. Hua, Y. C. Lou, Q. G. Zhai, Y. Wang, *Angew Chem Int Edit* **2011**, *50*, 5200-5203.

[13] R. Luque, A. R. de la Osa, J. M. Campelo, A. A. Romero, J. L. Valverde, P. Sanchez, *Energ Environ Sci* **2012**, *5*, 5186-5202.

[14] A. P. Steynberg, M. E. Dry, B. Davis, B. B. Breman, in *Studies in surface science and catalysis, Vol. 15* (Eds.: A. P. Steynberg, M. E. Dry), Elsevier, **2004**, pp. 64-173.

[15] H. Kolbel, P. Ackermann, F. Engelhardt, *Erdol u. Kohel* **1956**, *9*, 153.

[16] M. E. Dry, in *Studies in Surface Science and Catalysis, Vol. 152* (Eds.: A. P. Steynberg, M. Dry), **2004**, pp. 533-593.

[17] Q. Zhang, J. Kang, Y. Wang, *ChemCatChem* **2010**, *2*, 1030-1058.

[18] E. Iglesia, *Appl Catal a-Gen* **1997**, *161*, 59-78.

[19] E. Iglesia, *Stud Surf Sci Catal* **1997**, *107*, 153-162.

[20] E. Iglesia, S. L. Soled, R. A. Fiato, *J Catal* **1992**, *137*, 212-224.

[21] G. L. Bezemer, J. H. Bitter, H. P. C. E. Kuipers, H. Oosterbeek, J. E. Holewijn, X. D. Xu, F. Kapteijn, A. J. van Dillen, K. P. de Jong, *J Am Chem Soc* **2006**, *128*, 3956-3964.

[22] J. P. den Breejen, P. B. Radstake, G. L. Bezemer, J. H. Bitter, V. Froseth, A. Holmen, K. P. de Jong, *J Am Chem Soc* **2009**, *131*, 7197-7203.

[23] R. Oukaci, A. H. Singleton, J. G. Goodwin, *Appl Catal a-Gen* **1999**, *186*, 129-144.

[24] S. Storsaeter, O. Borg, E. A. Blekkan, B. Totdal, A. Holmen, *Catal Today* **2005**, *100*, 343-347.

[25] O. Borg, P. D. C. Dietzel, A. I. Spjelkavik, E. Z. Tveten, J. C. Walmsley, S. Diplas, S. Eri, A. Holmen, E. Ryttera, *J Catal* **2008**, *259*, 161-164.

[26] G. L. Bezemer, P. B. Radstake, V. Koot, A. J. van Dillen, J. W. Geus, K. P. de Jong, *J Catal* **2006**, *237*, 291-302.

[27] W. Chen, Z. L. Fan, X. L. Pan, X. H. Bao, *J Am Chem Soc* **2008**, *130*, 9414-9419.

[28] G. L. Bezemer, T. J. Remans, A. P. van Bavel, A. I. Dugulan, *J Am Chem Soc* **2010**, *132*, 8540-+.

[29] S. Zarubova, S. Rane, J. Yang, Y. D. Yu, Y. Zhu, D. Chen, A. Holmen, *Chemsuschem* **2011**, *4*, 935-942.

[30] G. Jacobs, Y. Y. Ji, B. H. Davis, D. Cronauer, A. J. Kropf, C. L. Marshall, *Appl Catal a-Gen* **2007**, *333*, 177-191.

[31] A. Voss, D. Borgmann, G. Wedler, *J Catal* **2002**, *212*, 10-21.

[32] G. Jacobs, T. K. Das, Y. Q. Zhang, J. L. Li, G. Racoillet, B. H. Davis, *Appl Catal a-Gen* **2002**, *233*, 263-281.

[33] S. T. Sie, M. M. G. Senden, H. M. H. Van Wechem, *Catal Today* **1991**, *8*, 371-394.

[34] B. H. Davis, *Top Catal* **2005**, *32*, 143-168.

[35] S. T. Sie, R. Krishna, *Appl Catal a-Gen* **1999**, *186*, 55-70.

[36] C. Perego, R. Bortolo, R. Zennaro, *Catal Today* **2009**, *142*, 9-16.

[37] S. Biz, M. L. Occelli, *Catalysis Reviews* **1998**, *40*, 329-407.

[38] B. C. Enger, A. L. Fossan, O. Borg, E. Rytter, A. Holmen, *J Catal* **2011**, *284*, 9-22.

[39] J. S. Girardon, E. Quinet, A. Griboval-Constant, P. A. Chernavskii, L. Gengembre, A. Y. Khodakov, *J Catal* **2007**, *248*, 143-157.

[40] A. M. Venezia, V. La Parola, L. F. Liotta, G. Pantaleo, M. Lualdi, M. Boutonnet, S. Järås, *Catal Today* **2012**, *197*, 18-23.

[41] A. Y. Khodakov, A. Griboval-Constant, R. Bechara, V. L. Zholobenko, *J Catal* **2002**, *206*, 230-241.

[42] A. M. Saib, M. Claeys, E. van Steen, *Catal Today* **2002**, *71*, 395-402.

[43] A. Y. Khodakov, A. Griboval-Constant, R. Bechara, F. Villain, *J Phys Chem B* **2001**, *105*, 9805-9811.

[44] D. C. Song, J. L. Li, *J Mol Catal a-Chem* **2006**, *247*, 206-212.

[45] O. Borg, S. Erib, E. A. Blekkan, S. Storsaeter, H. Wigum, E. Rytter, A. Holmen, *J Catal* **2007**, *248*, 89-100.

[46] J. S. Jung, S. W. Kim, D. J. Moon, *Catal Today* **2012**, *185*, 168-174.

[47] A. Martinez, G. Prieto, J. Rollan, *J Catal* **2009**, *263*, 292-305.

[48] X. H. Zhang, H. Q. Su, X. Z. Yang, *J Mol Catal a-Chem* **2012**, *360*, 16-25.

[49] S. Rane, O. Borg, J. Yang, E. Rytter, A. Holmen, *Appl Catal a-Gen* **2010**, *388*, 160-167.

[50] D. J. Kim, B. C. Dunn, P. Cole, G. Turpin, R. D. Ernst, R. J. Pugmire, M. Kang, J. M. Kim, E. M. Eyring, *Chemical Communications* **2005**, 1462-1464.

[51] P. Concepcion, C. Lopez, A. Martinez, V. E. Puntes, *J Catal* **2004**, *228*, 321-332.

[52] G. E. Batley, A. Ekstrom, D. A. Johnson, *J Catal* **1974**, *34*, 368-375.

[53] H. F. J. van 't Blik, D. C. Koningsberger, R. Prins, *J Catal* **1986**, *97*, 210-218.

[54] M. Reinikainen, M. K. Niemelä, N. Kakuta, S. Suhonen, *Applied Catalysis A: General* **1998**, *174*, 61-75.

[55] J. S. Girardon, A. Constant-Griboval, L. Gengembre, P. A. Chernavskii, A. Y. Khodakov, *Catal Today* **2005**, *106*, 161-165.

[56] Y. V. Wang, D.P.; Tonkovich A.L.Y.; Gao,Y.; Eddie G. Baker E.G., (Ed.: B. M. Institute), US, **2006**.

[57] J. I. Yang, J. H. Yang, H. J. Kim, H. Jung, D. H. Chun, H. T. Lee, *Fuel* **2010**, *89*, 237-243.

[58] Y. H. Chin, J. L. Hu, C. S. Cao, Y. F. Gao, Y. Wang, *Catal Today* **2005**, *110*, 47-52.

[59] R. Myrstad, S. Eri, P. Pfeifer, E. Rytter, A. Holmen, *Catal Today* **2009**, *147*, S301-S304.

[60] R. de Deugd, F. Kapteijn, J. Moulijn, *Top Catal* **2003**, *26*, 29-39.

[61] A. M. Hilmen, E. Bergene, O. A. Lindvåg, D. Schanke, S. Eri, A. Holmen, *Catal Today* **2005**, *105*, 357-361.

[62] R. Guettel, J. Knochen, U. Kunz, M. Kassing, T. Turek, *Ind Eng Chem Res* **2008**, *47*, 6589-6597.

[63] C. G. Visconti, E. Tronconi, G. Groppi, L. Lietti, M. Iovane, S. Rossini, R. Zennaro, *Chem Eng J* **2011**, *171*, 1294-1307.

[64] G. Groppi, E. Tronconi, *Chem Eng Sci* **2000**, *55*, 2161-2171.

[65] K. Pangarkar, T. J. Schildhauer, J. R. van Ommen, J. Nijenhuis, J. A. Moulijn, F. Kapteijn, *Catal Today* **2009**, *147, Supplement*, S2-S9.

[66] M. V. Twigg, J. T. Richardson, *Chem Eng Res Des* **2002**, *80*, 183-189.

[67] R. Philippe, M. Lacroix, L. Dreibine, C. Pham-Huu, D. Edouard, S. Savin, F. Luck, D. Schweich, *Catal Today* **2009**, *147*, S305-S312.

[68] G. I. Garrido, F. C. Patcas, S. Lang, B. Kraushaar-Czarnetzki, *Chem Eng Sci* **2008**, *63*, 5202-5217.

[69] R. Tschentscher, R. J. P. Spijkers, T. A. Nijhuis, J. van der Schaaf, J. C. Schouten, *Ind Eng Chem Res* **2010**, *49*, 10758-10766.

[70] M. A. Leon, R. Tschentscher, T. A. Nijhuis, J. van der Schaaf, J. C. Schouten, *Ind Eng Chem Res* **2011**, *50*, 3184-3193.

[71] M. A. Leon, T. A. Nijhuis, J. van der Schaaf, J. C. Schouten, *Chem Eng Sci* **2012**, *73*, 412-420.

[72] J. Knochen, R. Guttel, C. Knobloch, T. Turek, *Chem Eng Process* **2010**, *49*, 958-964.

[73] M. Sheng, H. Y. Yang, D. R. Cahela, W. R. Yantz, C. F. Gonzalez, B. J. Tatarchuk, *Appl Catal a-Gen* **2012**, *445*, 143-152.

[74] L. L. Murrell, F. M. autzenberg, R. A. Overbeek, B. J. Tatarchuk, *Vol. Patent 2002/20068026*, US, **2002**.

[75] A. Moisala, Q. Li, I. A. Kinloch, A. H. Windle, *Compos Sci Technol* **2006**, *66*, 1285-1288.

[76] A. P. Yu, M. E. Itkis, E. Bekyarova, R. C. Haddon, *Appl Phys Lett* **2006**, *89*.

[77] H. Zhang, C. Lancelot, W. Chu, J. P. Hong, A. Y. Khodakov, P. A. Chernavskii, J. Zheng, D. G. Tong, *J Mater Chem* **2009**, *19*, 9241-9249.

[78] M. Trepanier, A. Tavasoli, A. K. Dalai, N. Abatzoglou, *Appl Catal a-Gen* **2009**, *353*, 193-202.

[79] M. Trepanier, A. K. Dalai, N. Abatzoglou, *Appl Catal a-Gen* **2010**, *374*, 79-86.

[80] J. Lv, X. B. Ma, S. L. Bai, C. D. Huang, Z. H. Li, J. L. Gong, *Int J Hydrogen Energ* **2011**, *36*, 8365-8372.

[81] A. Tavasoli, R. M. M. Abbaslou, M. Trepanier, A. K. Dalai, *Appl Catal a-Gen* **2008**, *345*, 134-142.

[82] L. Guczi, G. Stefler, O. Geszti, Z. Koppany, Z. Konya, E. Molnar, M. Urban, I. Kiricsi, *J Catal* **2006**, *244*, 24-32.

[83] M. C. Bahome, L. L. Jewell, D. Hildebrandt, D. Glasser, N. J. Coville, *Appl Catal a-Gen* **2005**, *287*, 60-67.

[84] M. C. Bahome, L. L. Jewell, K. Padayachy, D. Hildebrandt, D. Glasser, A. K. Datye, N. J. Coville, *Appl Catal a-Gen* **2007**, *328*, 243-251.

[85] R. M. M. Abbaslou, A. Tavasoli, A. K. Dalai, *Appl Catal a-Gen* **2009**, *355*, 33-41.

[86] R. M. M. Abbaslou, J. Soltan, A. K. Dalai, *Appl Catal a-Gen* **2010**, *379*, 129-134.

[87] H. J. Schulte, B. Graf, W. Xia, M. Muhler, *ChemCatChem* **2012**, *4*, 350-355.

[88] J. P. Tessonnier, D. S. Su, *Chemsuschem* **2011**, *4*, 824-847.

[89] Q. Zhang, J. Q. Huang, M. Q. Zhao, W. Z. Qian, F. Wei, *Chemsuschem* **2011**, *4*, 864-889.

[90] A. Tavasoli, M. Trepanier, A. K. Dalai, N. Abatzoglou, *J Chem Eng Data* **2010**, *55*, 2757-2763.

[91] H. F. Xiong, M. A. M. Motchelaho, M. Moyo, L. L. Jewell, N. J. Coville, *J Catal* **2011**, *278*, 26-40.

[92] M. Trepanier, A. Tavasoli, A. K. Dalai, N. Abatzoglou, *Fuel Process Technol* **2009**, *90*, 367-374.

[93] M. A. M. Motchelaho, H. Xiong, M. Moyo, L. L. Jewell, N. J. Coville, *Journal of Molecular Catalysis A: Chemical* **2011**, *335*, 189-198.

[94] H. J. Schulte, B. Graf, W. Xia, M. Muhler, *ChemCatChem* **2012**, *4*, 350-355.

[95] D. Ugarte, A. Chatelain, W. A. deHeer, *Science* **1996**, *274*, 1897-1899.

[96] X. L. Pan, Z. L. Fan, W. Chen, Y. J. Ding, H. Y. Luo, X. H. Bao, *Nat Mater* **2007**, *6*, 507-511.

[97] W. Chen, X. L. Pan, X. H. Bao, *J Am Chem Soc* **2007**, *129*, 7421-7426.

[98] Y. Zhu, Y. C. Ye, S. R. Zhang, M. E. Leong, F. Tao, *Langmuir* **2012**, *28*, 8275-8280.

[99] X. W. Zhu, X. J. Lu, X. Y. Liu, D. Hildebrandt, D. Glasser, *Ind Eng Chem Res* **2010**, *49*, 10682-10688.

[100] R. Myrstad, S. Eri, P. Pfeifer, E. Rytter, A. Holmen, *Catal Today* **2009**, *147*, *Supplement*, S301-S304.

[101] Y.-h. Chin, J. Hu, C. Cao, Y. Gao, Y. Wang, *Catal Today* **2005**, *110*, 47-52.

[102] K. Chizari, A. Deneuve, O. Ersen, I. Florea, Y. Liu, D. Edouard, I. Janowska, D. Begin, C. Pham-Huu, *Chemsuschem* **2012**, *5*, 102-108.

[103] S. Zarubova, S. Rane, J. Yang, Y. Yu, Y. Zhu, D. Chen, A. Holmen, *Chemsuschem* **2011**, *4*, 935-942.

[104] J. J. Delgado, R. Vieira, G. Rebmann, D. S. Su, N. Keller, M. J. Ledoux, R. Schlögl, *Carbon* **2006**, *44*, 809-812.

[105] H. J. Jung, P. L. Walker, M. A. Vannice, *J Catal* **1982**, *75*, 416-422.

[106] H. J. Jung, M. A. Vannice, L. N. Mulay, R. M. Stanfield, W. N. Delgass, *J Catal* **1982**, *76*, 208-224.

[107] V. K. Jones, L. R. Neubauer, C. H. Bartholomew, *The Journal of Physical Chemistry* **1986**, *90*, 4832-4839.

[108] A. P. B. Sommen, F. Stoop, K. Van Der Wiele, *Appl Catal* **1985**, *14*, 277-288.

[109] H. F. Xiong, M. Moyo, M. A. M. Motchelaho, L. L. Jewell, N. J. Coville, *Appl Catal a-Gen* **2010**, *388*, 168-178.

[110] G. B. Yu, B. Sun, Y. Pei, S. H. Xie, S. R. Yan, M. H. Qiao, K. N. Fan, X. X. Zhang, B. N. Zong, *J Am Chem Soc* **2010**, *132*, 935-+.

[111] Z. K. Sun, B. Sun, M. H. Qiao, J. Wei, Q. Yue, C. Wang, Y. H. Deng, S. Kaliaguine, D. Y. Zhao, *J Am Chem Soc* **2012**, *134*, 17653-17660.

[112] P. Wick, M. J. D. Clift, M. Rosslein, B. Rothen-Rutishauser, *Chemsuschem* **2011**, *4*, 905-911.

[113] M. J. Ledoux, C. Pham-Huu, *Catal Today* **2005**, *102*, 2-14.

[114] C. Pham-Huu, R. Vieira, B. Louis, A. Carvalho, J. Amadou, T. Dintzer, M. J. Ledoux, *J Catal* **2006**, *240*, 194-202.

[115] R. Vieira, M. J. Ledoux, C. Pham-Huu, *Appl Catal a-Gen* **2004**, *274*, 1-8.

[116] Y. F. Liu, L. D. Nguyen, T. H. Tri, Y. Liu, T. Romero, I. Janowska, D. Begin, C. Pham-Huu, *Mater Lett* **2012**, *79*, 128-131.

[117] H. H. Hwu, J. G. G. Chen, *Chemical Reviews* **2005**, *105*, 185-212.

[118] L. Borchardt, C. Hoffmann, M. Oschatz, L. Mammitzsch, U. Petasch, M. Herrmann, S. Kaskel, *Chem Soc Rev* **2012**, *41*, 5053-5067.

[119] H. Pedersen, S. Leone, O. Kordina, A. Henry, S. Nishizawa, Y. Koshka, E. Janzen, *Chemical Reviews* **2012**, *112*, 2434-2453.

[120] M. Saito, R. B. Anderson, *J Catal* **1980**, *63*, 438-446.

[121] J. W. Dun, E. Gulari, K. Y. S. Ng, *Appl Catal* **1985**, *15*, 247-263.

[122] H. H. Podgurski, J. T. Kummer, T. W. DeWitt, P. H. Emmett, *J Am Chem Soc* **1950**, *72*, 5382-5388.

[123] D. B. Bukur, K. Okabe, M. P. Rosynek, C. P. Li, D. J. Wang, K. R. P. M. Rao, G. P. Huffman, *J Catal* **1995**, *155*, 353-365.

[124] D. B. Bukur, L. Nowicki, R. K. Manne, X. S. Lang, *J Catal* **1995**, *155*, 366-375.

[125] S. Janbroers, J. N. Louwen, H. W. Zandbergen, P. J. Kooyman, *J Catal* **2009**, *268*, 235-242.

[126] E. de Smit, F. Cinquini, A. M. Beale, O. V. Safonova, W. van Beek, P. Sautet, B. M. Weckhuysen, *J Am Chem Soc* **2010**, *132*, 14928-14941.

[127] C. Yang, H. B. Zhao, Y. L. Hou, D. Ma, *J Am Chem Soc* **2012**, *134*, 15814-15821.

[128] M. Benaissa, J. Werckmann, G. Ehret, E. Peschiera, J. Guille, M. J. Ledoux, *J Mater Sci* **1994**, *29*, 4700-4707.

[129] J. M. Nhut, R. Vieira, L. Pesant, J. P. Tessonnier, N. Keller, G. Ehret, C. Pham-Huu, M. J. Ledoux, *Catal Today* **2002**, *76*, 11-32.

[130] P. Leroi, E. Madani, C. Pham-Huu, M. J. Ledoux, S. Savin-Poncet, J. L. Bousquet, *Catal Today* **2004**, *91-2*, 53-58.

[131] M. Lacroix, L. Dreibine, B. de Tymowski, F. Vigneron, D. Edouard, D. Begin, P. Nguyen, C. Pham, S. Savin-Poncet, F. Luck, M. J. Ledoux, C. Pharn-Huu, *Appl Catal a-Gen* **2011**, *397*, 62-72.

[132] A. Deneuve, I. Florea, O. Ersen, P. Nguyen, C. Pham, D. Begin, D. Edouard, M. J. Ledoux, C. Pham-Huu, *Appl Catal a-Gen* **2010**, *385*, 52-61.

[133] M. J. Ledoux, C. Pham-Huu, *Cattech* **2001**, *5*, 226-246.

[134] M. J. Ledoux, S. Hantzer, C. Pham-Huu, J. Guille, M. P. Desaneaux, *J Catal* **1988**, *114*, 176-185.

[135] P. Nguyen, C. Pham, *Appl Catal a-Gen* **2011**, *391*, 443-454.

[136] http://www.sicatcatalyst.com.

[137] N. Keller, C. Pham-Huu, M. J. Ledoux, C. Estournes, G. Ehret, *Appl Catal a-Gen* **1999**, *187*, 255-268.

[138] R. Moene, M. Makkee, J. A. Moulijn, *Appl Catal a-Gen* **1998**, *167*, 321-330.

[139] B. de Tymowski, Y. F. Liu, C. Meny, C. Lefevre, D. Begin, P. Nguyen, C. Pham, D. Edouard, F. Luck, C. Pham-Huu, *Appl Catal a-Gen* **2012**, *419*, 31-40.

[140] Y. Liu, B. de Tymowski, F. Vigneron, I. Florea, O. Ersen, C. Meny, P. Nguyen, C. Pham, F. Luck, C. Pham-Huu, *ACS Catalysis* **2013**, *3*, 393-404.

[141] A. R. de la Osa, A. De Lucas, A. Romero, J. L. Valverde, P. Sanchez, *Catal Today* **2011**, *176*, 298-302.

[142] L. Yu, X. Liu, Y. Fang, C. Wang, Y. Sun, *Fuel* **2013**, *112*, 483-488.

[143] A. R. de la Osa, A. De Lucas, J. Diaz-Maroto, A. Romero, J. L. Valverde, P. Sanchez, *Catal Today* **2012**, *187*, 173-182.

[144] A. R. de la Osa, A. de Lucas, L. Sanchez-Silva, J. Diaz-Maroto, J. L. Valverde, *Fuel* **2012**, *95*, 587-598.

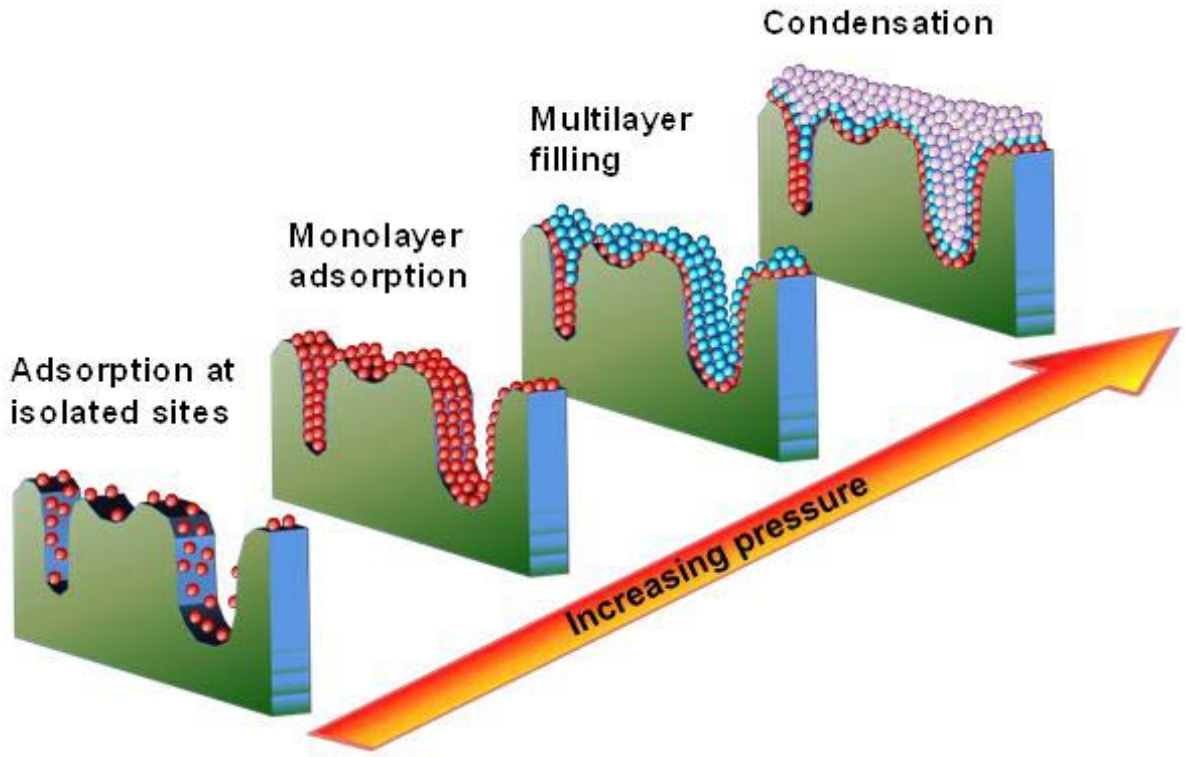

Chapter II

Catalysts preparation, characterization and FTS reaction

Chapter II Catalysts preparation, characterization and FTS reaction

2.1 Brief catalyst preparation and catalytic reaction illustration

In this chapter, the synthesis of thermal conductive macroscopic materials & FTS catalyst preparation, characterization techniques and catalytic tests for evaluating the catalytic performances are described in detail. The important stages for the catalyst preparation and catalytic reaction are presented in Figure 2-1. Characterizations at different steps of catalyst were used to gather useful information of catalyst structure, cobalt reducibility, dispersion, regeneration and performance in F-T synthesis.[1]

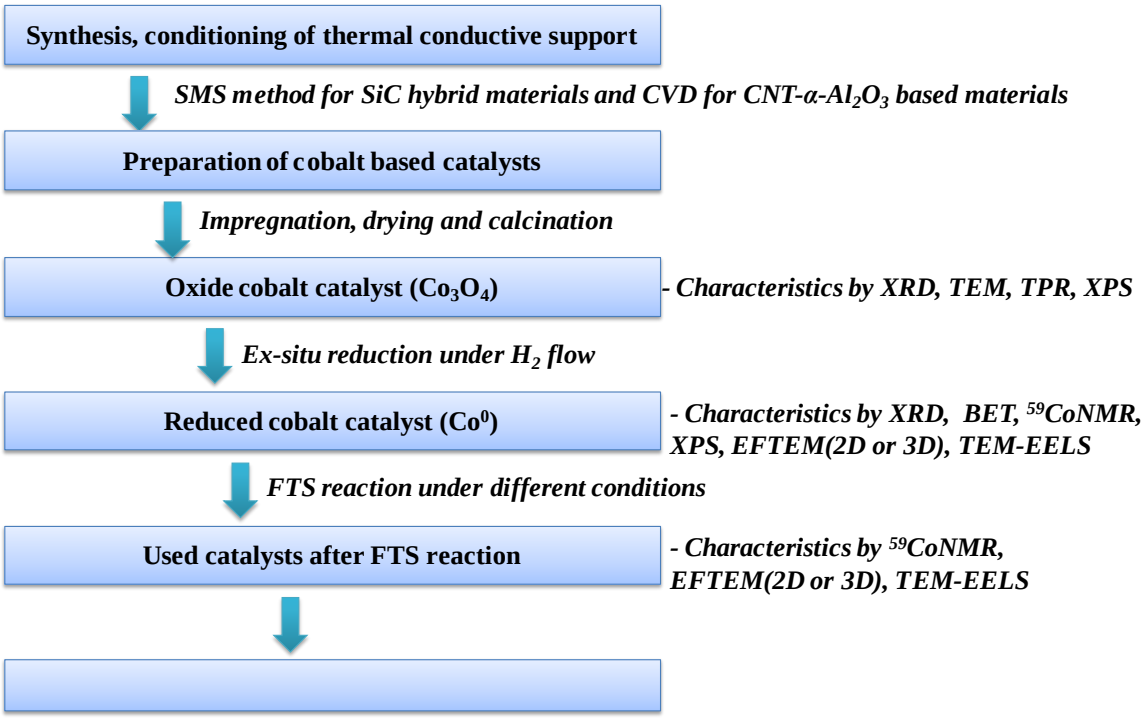

Figure 2-1. Principal stages for the preparation and catalytic performance of Co-supported FTS catalysts.

2.2 Thermal conductive macroscopic materials synthesis

2.2.1 Synthesis of SiC-based hybride materials

Silicon carbide (*β*-SiC) was synthesized via a gas-solid reaction between SiO vapour and dispersed solid carbon. The detailed synthesis of the SiC-based materials was summarized in a recent review.[2] Silicon carbide (β-SiC) with medium to high specific surface area (10 to > 100 m^2/g) has been synthesized according to the Shape Memory Synthesis (SMS) method developed by Ledoux et al.[3-4] in the early of 1990s. The synthesis was further extensively developed by Pechiney Cy. before being transferred to the SICAT SARL which continues to develop the synthesis process nowadays.[2] The synthesis method allows one to produce SiC with different size and shapes (grains, spheres, extrudates, tubes and foams) for various catalytic downstream applications (Figure 2-2).

The titania decorated *β*-SiC was synthesized by mixing microsized silicon powder and TiO_2 nanoparticles with a carbon-containing resin.[5] The carbidization process was carried out under flowing argon at temperatures around 1350 °C during one hour. The argon flow allows to remove the CO formed during the reaction from the reactor and thus, to shift the reaction towards the formation of SiC. The resulting composite contains SiC intimately mixed with TiC. The TiC-to-TiO_2 transformation was carried out by treating the composite at 550 °C in air for 2 h.

The titanium dioxide coated *β*-SiC was prepared by pore volume impregnation of the high porous SiC with ethanol solution of $Ti(iOC_3H_7)_4$. After impregnation, the samples were allowed to dry at room temperature for 4 h and then were dried at 110 ^oC in air for 8 h. The transformation of TiO_2 crystalline phase from the precursor is performed by calcination in air at 600 °C for 5 h with temperature increase rate of 2 °C/min. The supports are then noted *x*TiO_2-SiC with *x* representing the loading of TiO_2 on the SiC carrier (5 wt. %, 10 wt. % and 15 wt. %) and marked as 5TiO_2-SiC, 10TiO_2-SiC and 15TiO_2-SiC.

Figure 2-2. Optical photo of the medium to high specific surface area silicon carbide support with different macroscopic shapes. [2]

2.2.2 Structured materials synthesis

√ ***Synthesis of hierarchically structured composite materials***

The α-alumina support (Sasol) was crushed and sieved and a fraction of 150 - 400 µm was retained for catalyst preparation. The catalyst was prepared using an aqueous solution of Fe ($Fe(NO_3)_3 \cdot 9H_2O$) and Co ($Co(NO_3)_2 \cdot 6H_2O$), with the Fe and Co concentration fixed at 2 wt.%, respectively. The wet solid was dried in an oven at 110 ^oC and then calcined in air at 350 °C for 2 h. Multi-walled carbon nanotubes (CNTs) were synthesized by a chemical vapour deposition (CVD) method using a mixture of C_2H_6/H_2 and the 2 wt% Fe-2 wt % $Co/\alpha\text{-}Al_2O_3$ as growth catalyst.[6-7] The catalyst in its oxide form was placed in a ceramic boat inside a quartz tube (Figure 2-3A), located in a horizontal electrical furnace, and flushed for 30 min in pure hydrogen flow at room temperature and finally reduced at 400 °C for 2 h. After this treatment the hydrogen flow was directly replaced by a mixture of ethane and hydrogen (40 $ml \cdot min^{-1}$:60 $ml \cdot min^{-1}$) and the temperature of the furnace was rapidly increased (20 $^oC \cdot min^{-1}$) to 750 °C (Figure 2-3B). The reaction temperature was fixed at

750 °C and the synthesis lasted for 2 h. After the synthesis the temperature was stopped and the reactor was cooled down under the reactant mixture from 750 °C to ambient temperature.

The single crystal TiO_2 layer was introduced on the structured materials by pore volume impregnation with ethanol solution of $Ti(iOC_3H_7)_4$. After impregnation, the samples were allowed to dry at room temperature for 4 h and then were dried at 110 ^oC in air for 8 h. The transformation of TiO_2 crystalline phase from the precursor is performed by calcination in helium at 600 °C for 5 h with temperature increase rate of 2 $°C \cdot min^{-1}$.

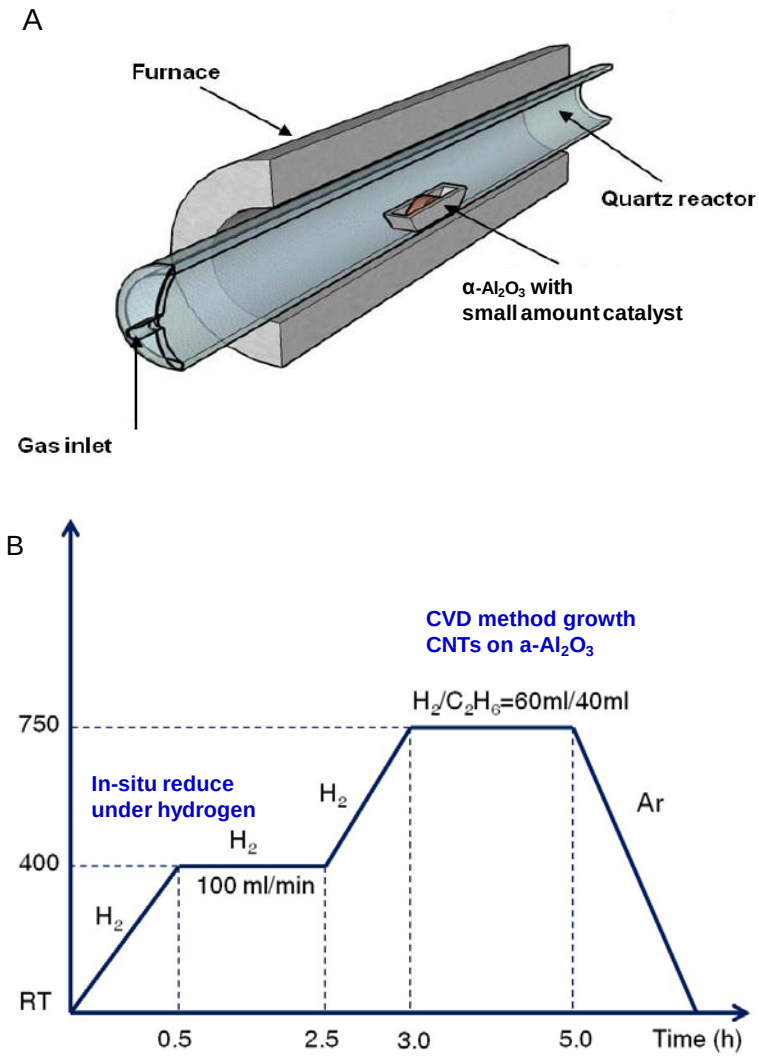

Figure 2-3. Setup (A) and temperature program (B) for the synthesis hierarchically structured composites.

√ ***Catalysts preparation***

A cobalt loading was set at 10 wt. % for all catalysts, the real cobalt mass content was analyzed by inductively coupled plasma (ICP) techniques. In this process, the cobalt phase was deposited onto the supports via an incipient wetness method using an ethanol-water (50:50 v:v) solution containing cobalt nitrate (Acros, ≥ 99.0%). After impregnation the solid was allowed to dry at room temperature for 2 h and then oven-dried at 110 °C for 2 h. The solid was calcined in air at 300 °C for 2 h in order to decompose the nitrate into its corresponding oxide. And then the oxide form was further reduced in flowing hydrogen (30 $mL \cdot g_{cat}^{-1} \cdot min^{-1}$) at 350°C for 6 h. The obtained reduced catalysts noted as CoTiCNTA and CoCNTA for the one supported on the TiO_2-promoted and TiO_2-free hierarchical structure alumina decorated with carbon nanotubes, respectively, and CoTiA and CoA for the one supported on TiO_2-added or pure alumina, respectively. In order to prevent excessive air oxidation during the exposure of the catalyst a passivation process was performed before discharging of the catalyst (surface passivation was carried out with a mixture of 1 vol. % O_2 diluted in helium at room temperature).

2.3 Catalyst characterization

2.3.1 N_2 adsorption/desorption measurement

The different pores in the porous materials can be divided into micropore (< 2 nm), mesopore (2 to 50 nm) and macropore (> 50 nm) according to the pore sizes. The pores such as the inter-connected open channel, the channel with one dead end, and the fully opened passing channel can be measured, while there also exist some closed cavity that are not connected with the outside surface and cannot be detected by the N_2 adsorption/desorption measurement. Figure 2-4 also illustrates some normal shapes that frequently appeared in the material, which include the cylindrical pore such as in SBA-15,[8] the slits such as in the coal mine,[9] the conical pore such as in poly(ethylene terephthalate) (PET) membranes,[10] the spherical or ink bottle,[11] and the interstices.

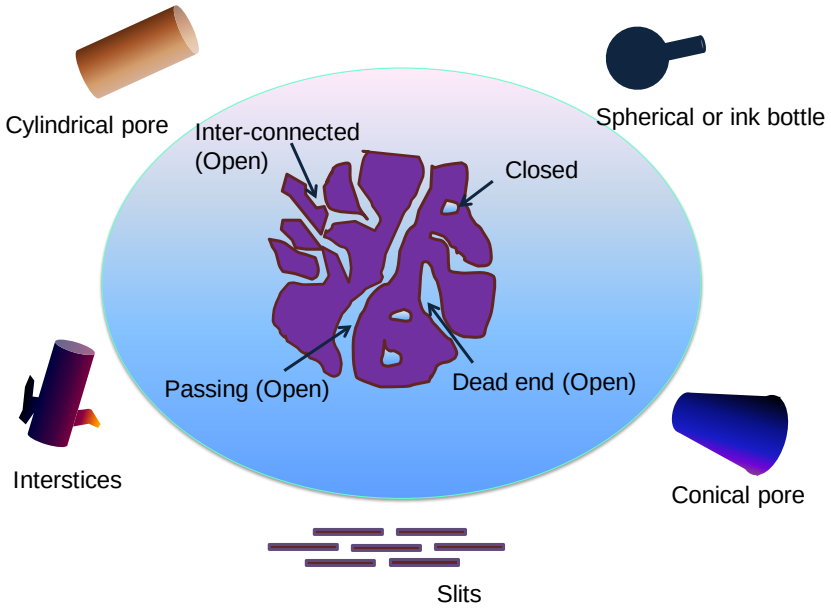

Figure 2-4. The formation of inner porosity of materials and the possible shapes of pores.

The porous structure parameters including surface area, pore size distribution and average pore volume are important for estimating the textures of materials. The specific surface area is consisted by the internal irregular opening and small holes, and cannot be calculated directly from the size of bulk particles. The specific surface area is an important parameter for estimating the thermal properties, chemical stability, and adsorption capacity. The adsorption of inert gases over the atoms in the tested materials can help understanding the surface area. The adsorbed amount is defined as X, which is not only a function of exposed surface but also related to the temperature, gas pressure and the interaction intensity between gas and solid. Since the interaction between most of the gas and solid is very weak, the low temperature is necessary for the sufficient adsorption to occur and cover the entire surface. The surface adsorption is generally increased with the raise of pressure as a linear relationship. However, when the adsorbed gas covers the entire surface with the thickness of one atom (the adsorption amount of monolayer is named as X_m), the gas adsorption do not finished but then adsorbed as multilayer adsorption with pressure as shown in Figure 2-5.

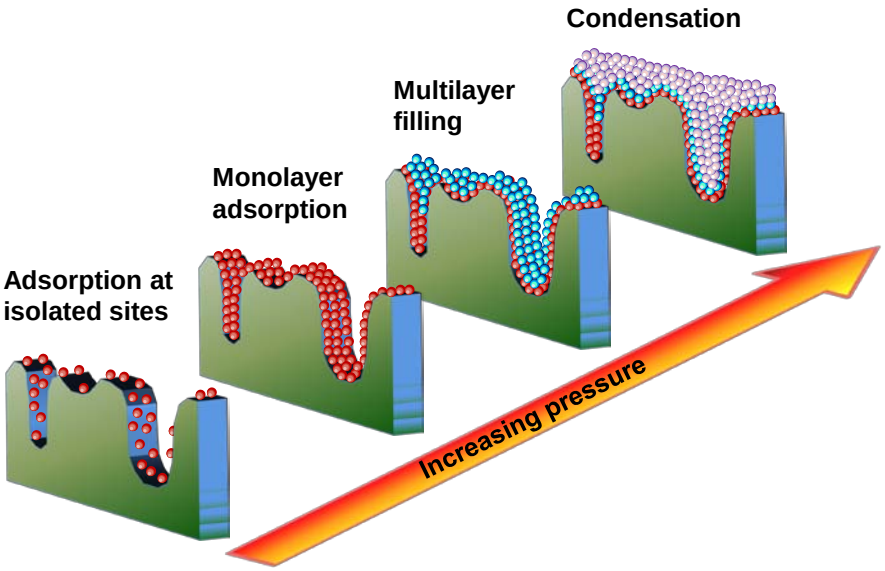

Figure 2-5 Illustration of the adsorption of N_2 gas on porous structured materials.

The surface area of tested material can be related to the adsorption amount of gas and calculated by an appropriate mathematical model. The BET formula is thus utilized which is defined by the names of three persons (Brunauer, Emmett and Teller). The BET model is based on the assumptions: I. The surface of solid is uniform and monolayer adsorption occurred on the surface; II. The adsorption heat of each layer (except the first adsorption layer) is equal to the heat of liquefaction of adsorbate. The equation is as below:

$$\frac{1}{X[(P_0/P)-1]} = \frac{1}{X_m C} + \frac{C-1}{X_m C}\left(\frac{P}{P_0}\right) \qquad (2\text{-}1)$$

In the above equation, the P/P_0 is relative pressure; C is a parameter corresponding to the interaction between gas and solid. The X and P/P_0 can be measured directly by the machine, while X_m is related to the surface area.

For the total surface area S_t, the calculating process will be easy if the accounted surface area of each molecule is known. The S_t can be estimated as following:

$$S_t = \frac{V_m L_{Av} A_m}{M_V} \qquad (2\text{-}2)$$

The L_{Av} is the Avogadro's constant; the A_m is the area of the cross-section; the V_m is the monomolecular layer capacity; and the M_v is the molar volume. The parameter V_m can be obtained by the linear regression of least square method of the following equations (2-5) to (7):

$$s = \frac{c-1}{V_m C} \qquad (2\text{-}2)$$

$$i = \frac{1}{V_m C} \qquad (2\text{-}4)$$

$$V_m = \frac{1}{s+i} \qquad (2\text{-}5)$$

In this thesis, the specific surface area, average pore volume and the average pore size of the support and the catalyst, after reduction, were determined in a Micromeritics sorptometer. The sample was outgassed at 250 °C under vacuum for 14 h in order to desorb moisture and adsorbed species on its surface. The measurements were carried out using N_2 as adsorbent at liquid N_2 (-196 ^oC) temperature at relative pressures between 0.06 and 0.99.

2.3.2 Superficial detection by XPS

The X-ray photoelectron spectroscopy (XPS) is a quantitative technique for measuring the composition of surface elements, the ratio and homogeneity between element, and their corresponding valence states. This technique should be carried out under ultrahigh vacuum condition and can generally detect the 1-10 nm subsurface. The basic theory of the XPS is that the inner electrons or valence electron in the atoms or molecules are excited as photo-emitted electrons. The focused beam of light of X-ray is usually the monochrome Al Kα (1486.6 eV, the X-ray for this work) with 20-200 μm beam of light or Mg Kα (1253.6 eV) with 10-30 μm beam of light.

The surface sensitivity of analysis depends on the detected radiation. The characteristic electrons are emitted from the electron beam or the X-ray irradiation and arrive to the electron energy analyzer and detector. Although the X-ray photons or the high-energy electrons bombarding the surface can permeate as deep as ~ 1 μm, only small amount of

electrons overflow the surface maintaining the initial energy. The detectable emergent electrons without energy loss can be only from about 1-8 nm on the surface. In fact, the electrons in the deep of the solid also have chances to be overflowed, however the energy of which will be lost because of the collision with other electrons during the overflow path. The experimental results suggested that the inelastic scattering cross section of electrons in the solid is huge, and the inelastic mean free path (IMFP, the average distance of the paths between two times of valid inelastic collision of electrons possessing certain energy) is short for only lower than 10 nm. In this case, only small amount of electrons at the superficial surface can escape from the surface with unchanged characteristic energy. The XPS is really sensitive to the surface contamination, and this is also why the ultra high vacuum is in use- to remove the contamination from the surface.

2.3.3 X-ray diffraction

The phenomenon is called X-ray diffraction. The X-ray diffraction is a useful technique for measuring the average distance between layers or atoms, determine the orientation of single crystal, detect the structure of novel material, and find out the sizes and shapes of grains. The XRD analysis in this work was carried out on a Bruker D-8 Advance diffractometer with a Cu Kα radiation in the range of $2\theta = 10 - 80^{o}$.The sample was crushed into powder and deposited on a glass plate for analysis. The average size of crystalline grains is calculated by Scherrer Equation:

$$d = \frac{0.89\lambda}{B\cos\theta} \times \frac{180^{o}}{\pi} \qquad (2\text{-}6)$$

In which d is the average size of crystalline grains, λ is the wavelength of incipient X-ray, and B is the full width at half maximum of the diffraction peak.

The X-ray diffraction (XRD) measurement was carried out in a Bruker D-8 Advance diffractometer equipped with a Vantec detector. The powdered sample was packed onto a glass slide. ASTM powder diffraction files were used to identify the phase present in the sample. Crystallite sizes were calculated from line broadening using the Scherrer equation.

When the metallic cobalt (Co^0) crystallite size was estimated from the size of cobalt oxide form (Co_3O_4) in the oxide catalysts, the following formula (2-7) was used according the relative molar volumes of Co^0 and Co_3O_4.[12]

$$d(Co^0) = 0.75 \times d(Co_3O_4) \qquad (2\text{-}7)$$

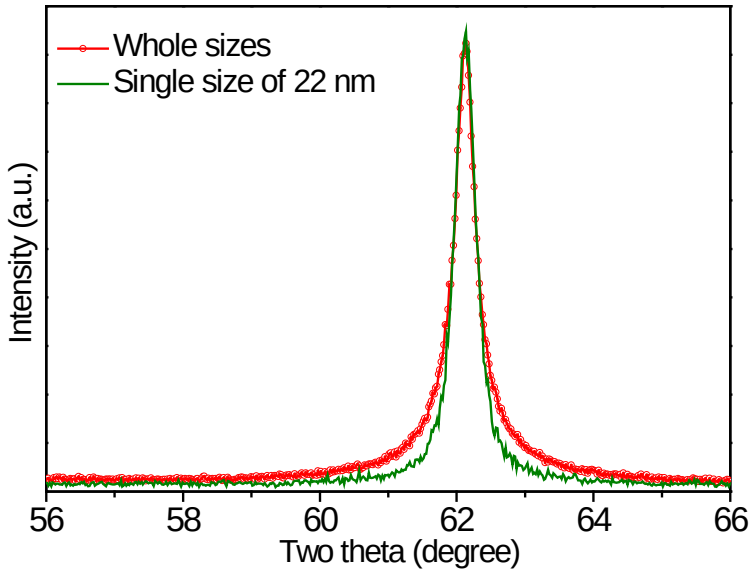

Figure 2-6. XRD patterns of (A) whole particle sizes range from 1nm to 28 nm and (B) single particle size in 22 nm.

The problem when determining particle size by XRD is that the line shape is dominated by the few biggest particles existing in the sample. To exemplify this effect we have constructed a diffraction pattern for a wide distribution of hcp Co particles. Indeed we have chosen a flat atomic distribution from 1 to 28 nm of particles diameter (D). In other words in each size range the same total mass of Co is considered. In term of size distribution it means that the number of particles decreases with increasing size like $1/D^3$. For examples it means that for such distribution there is about twenty thousand (20000) time more particles with a diameter of 1 nm than particles with a diameter of 28 nm. From this simulated diffraction pattern we computed the averaged particle size as it is usually performed experimentally by using the Scherrer equation. The computed average size is 22 nm while the average size

obtained from the distribution should obviously be of 14.5 nm. To explain this difference Figure 2-6 compares the diffraction pattern for the distribution of particles with the diffraction pattern of particles with a single size of 22 nm. As can be seen the overall shape is very similar, the only differences are found into the tails of the line shape. The FWHM is mostly determined by the very big particles. Therefore when the particle size distribution is wide the particle size computed from XRD line width has to be considered with care, it is really accurate only when the size distribution is narrow.

2.3.4 Thermo-gravimetric analysis

Thermal gravimetry analysis (TGA) was carried out under air flow (25 $mL \cdot min^{-1}$) with a heating rate of 10 $°C \cdot min^{-1}$ using Setaram apparatus. The sample loading was typically 20-30 mg.

2.3.5 H_2-temperature programmed reduction

Temperature-Programmed Reduction (TPR) was determined using a Micromeritics ASAP-2100 setup under diluted hydrogen flow (5 or 10 vol. % in argon) with a heating rate of 10 or 15$°C \cdot min^{-1}$. The hydrogen consumption was continuously monitored with a thermal conductivity detector (TCD). The steam formed during the reduction was trapped at -88 °C using liquid-solid mixed acetone obtained by liquid nitrogen.

Cobalt species reduced from Co_3O_4 to metallic Co^0 generally passes through an intermediate phase, CoO. It means that the first oxide reduction peak is typically assigned to the reduction of Co_3O_4 to CoO, although a fraction of the peak are likely to comprise the reduction of the larger, bulk-like CoO species to Co. The second reduction step is composed of overlapping peaks which is due to the reduction of CoO to Co. These peaks also include the reduction of cobalt species that interact with the support. Therefore, the two-steps reduction is utilized to simplify the processes which are listed as follows:

$$H_2 + Co_3O_4 \rightarrow H_2O + 3\,CoO \qquad (2\text{-}8)$$

$$H_2 + CoO \rightarrow H_2O + Co^0 \qquad (2\text{-}9)$$

It can be seen from the equations that in producing 1 mol of Co^0, one-third mole of H_2 is first consumed to produce CoO, and 1 mol of H_2 is consumed to produce the metal.

2.3.6 Scanning electron microscopy

The morphology of the solid was examined by scanning electron microscopy (SEM) on a JEOL 6700-FEG microscope. The solid was fixed on the sample holder by a graphite paste for examination. Before analysis the sample was covered by a thin layer of gold in order to avoid the problem of charge effect.

2.3.7 Transmission electron microscopy

In the transmission electron microscope (TEM), electron beam after speed-up is cast onto a very thin layer of sample. The electros collide with the atoms in the sample and then change the moving orientation and perform the solid angle scattering. The scattering angle depends on the density and thickness of the sample, which forms the images with different intensity. The images can be modified and focused on the image device. The distinguish ability of the TEM is much higher than the optical microscope due to the very short De Broglie wavelength of electrons, which can be modified to about 0.1-0.2 nm. Therefore, the fine structure or even a series of atoms in the target sample can be observed by this technique. The TEM is an important technique in many disciplines corresponding to physics, chemistry, and biology.

The sample preparation for classical and tomography transmission electron microscopy (TEM) was done according to the following process: the solid was crushed in a mortar into a very fine powder. The powder was then dispersed in ethanol by sonication during 5 min. After sonication a drop of the solution was deposited on a holey carbon copper grid supporting the gold beads used as fiducial markers, and the solvent was evaporated at room temperature before introducing of the sample holder in the microscope. The classical TEM images in this work are operated on a Topcon EM002B microscope (accelerating voltage of

200 kV) as shown in Figure 2-7, using a 2048 × 2048 pixels Ultrascan cooled CCD array detector, and a high tilt sample holder.

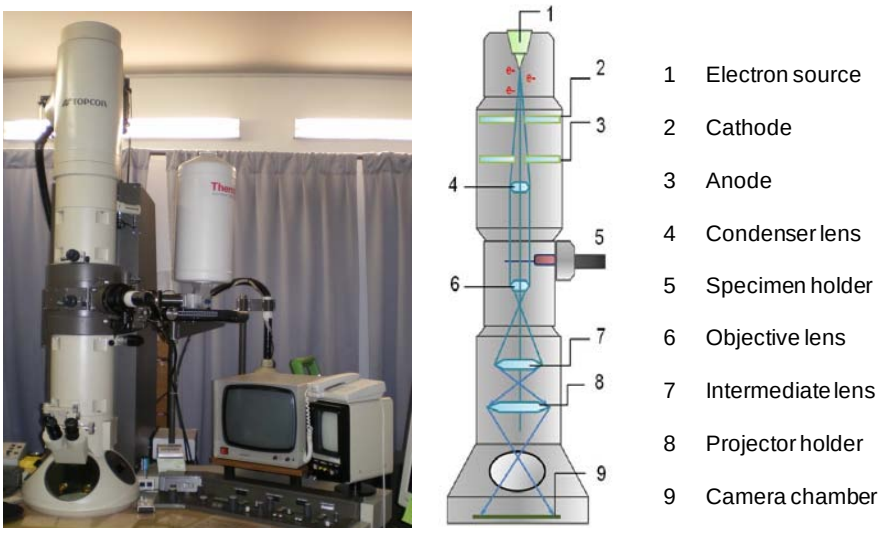

Figure 2-7. Optical photos of Transmission electron microscopy apparatus in IPCMS (UMR 7504 CNRS - UdS) and its illustration.

2.3.8 Energy-filtered TEM and TEM-EELS

EFTEM tomography and high-resolution TEM and were performed on a JEOL 2100F electron microscope operating at 200 kV, equipped with a Cs corrector and a GIF Tridiem energy filter. The TEM/EFTEM images and the EELS spectra were recorded on a 2048 × 2048 pixels Ultrascan CCD array detector. Before analysis, the preparation of the samples was done according to the following process: the solid was crushed in a mortar into a very fine powder. The powder was then dispersed in ethanol by ultrasonication during 5 min. After ultrasonication a drop of the solution was deposited on a holey carbon copper grid and the solvent was evaporated at room temperature before introducing of the sample holder in the microscope.

For the sample analyzed by 3D EFTEM, the EFTEM tomographic tilt series were recorded by using the GATAN acquisition software for tomography, which allows varying systematically the tilt angle step by step, to correct for defocusing, to maintain the object under study within the field of view and to record and store the object projections. Seven energy-filtered images were recorded at each tilt angle: a Zero-Loss image, three images at the L_{23} ionization edge of Si (at energy positions of 79, 93, and 105 eV), and finally three images at the L_{23} ionization edge of Ti (424, 446, and 468 eV). The slit width used to record the ZL images was 10 eV whereas for the core-loss energy-filtered images slit widths of 12 and 24 eV were considered for Si and Ti, respectively. The acquisition time was 2 s for the images over the Si - L_{23} edge, 10 s for the images over the Ti - L_{23} edge, and 0.3 s for the Zero-Loss images. All of the EFTEM images have a size of 512 × 512 pixels with a pixel size of 0.56 nm. The seven series of energy-filtered images were obtained by varying the tilt angle from +72.5° to -72.5° with a tilt increment agreeing with a 4° Saxton scheme,[13] and then a total of 55 images were obtained. No visible irradiation damages were observed during the whole acquisition process (about 90 min). During the analysis, the incident electron beam density was constant for the acquisition of filtered images, which requires a specific adjustment of the illumination conditions when going from an ionization edge to the other. Furthermore, the validity of the projection is satisfied, giving that the global contribution of the diffraction contrast to the series of energy-filtered images can be considered as negligible in first approximation. In addition, the specimen thickness is constant over the whole angular range, and its value is largely below the inelastic mean free path of the electrons. Thus, multiple inelastic scattering effects are negligible, and the dynamical multiple elastic scattering is not too high. Because of their high contrast and SNR, the standard alignment tools of the IMOD software [14-15] (a cross-correlation algorithm followed by a fine alignment using gold fiducial markers) were used to align the Zero-Loss tilt series.

A thorough work was to calculate the series of Si and Ti 2D elemental maps from the series of energy-filtered projections. First, the energy filtered images recorded at a given tilt

angle were aligned to the corresponding Zero-Loss image. This additional step allows then applying the alignment parameters obtained for the Zero-Loss tilt series to the tilt series of energy filtered images, leading thus to six spatially correlated tilt series of EFTEM images. Using these series as input; the three windows method was applied for Si and Ti and two tilt series of Si and Ti elemental images were finally obtained, both correlated to the ZL tilt series. A shape-sensitive and two elemental (Si and Ti) reconstructions have been computed using iterative algorithms from the tilt series of Zero-Loss and Si and Ti 2D elemental projections. Once the three tomographic reconstructions were computed, the external borders and the internal structure of the system were extracted from the shape-sensitive volume by using a segmentation procedure based on the gray-level intensities of the voxels.[16] The knowledge of the external morphology and porous structure of the object is useful to determine accurately the voxels representing the material, thus simplifying the data segmentation process of the elemental volumes, a step difficult to realize otherwise owing to their low SNR. Once the inner part of the specimen extracted from the two elemental reconstructions, a simple selection criterion is used to attribute a given voxel to one of the two elements. It is based on the direct comparison of the two intensities, voxel by voxel, which were averaged over a 5 voxel diameter sphere, in order to reduce the statistical noise. For the other catalysts analyzed in this work, the 2D chemical maps of the selected grains were obtained by using the three windows method from EFTEM images recorded at 0° tilt with the same parameters as previously.

2.3.9 ^{59}Co zero field nuclear magnetic resonance

(1) Principles

The typical design of a Nuclear Magnetic Resonance (NMR) experiment is presented in Figure 2-8. As the sample is placed in a magnetic field H_0 the degeneracy of the nuclear spin ground state is removed by the Zeeman interaction.[17] NMR refers to the resonant absorption of photons by the nuclear spin system through dipolar transitions between adjacent spin levels. Actually owing to the very low Zeeman energy the photons simply consist of a radio

frequency field H_1, perpendicular to H_0, which is produced by a radio frequency (RF) generator in the sample coil. Therefore it is more convenient to consider the photons as a coherent classical electromagnetic field which is part of the experimental setup. The NMR spectrum consists of a plot the energy absorption as a function of either the RF field frequency at a constant H_0 or as a function of H_0 at a constant frequency (ω_0).

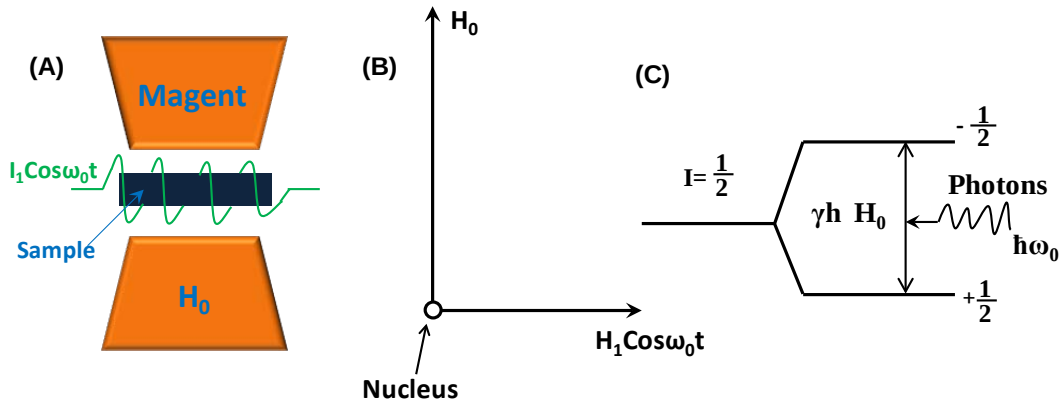

Figure 2-8. The typical design of NMR expermiment. (A) Laboratory scale, (B) microscopic scale, (C) nuclear energy levels (I= 1/2)

When applied in the study of ferromagnetic samples the application of an external magnetic field H_0 is not needed. Indeed in ferromagnets the nuclei already experience a static magnetic field originating from the magnetization of the sample that is called the hyperfine field (HF). In bulk Co the hyperfine field is typically of the order of 20 Tesla. Therefore the easiest way to perform NMR measurements in ferromagnets is to perform frequency sweeps measurements without applying any external static field. Therefore it is often called zero field NMR. In ferromagnets NMR provides an original insight into the structural and magnetic characterization of composite nanostructured materials. Indeed the yield of NMR experiments is two-fold:[18] (i) The NMR spectrum, usually acquired in zero external field, reflects the distribution of hyperfine fields in the sample, and thus gives information about the different chemical configurations and site symmetries in the sample, the different phases, their structure, and their defects. (ii) The evolution of the spectral shape

against the external field strength and orientation or against the radio frequency field strength probes the magnetic anisotropy or the magnetic stiffness of the electronic moments around the nucleus site, thus providing information comparable to that given by ferromagnetic resonance (FMR) measurements. Therefore, combining both yields makes it possible to correlate the heterogeneous magnetic properties of a composite sample to its different structural components.

(2) Experimental details

^{59}Co zero field nuclear magnetic resonance (^{59}Co NMR) experiments were performed in a home-made zero magnetic field spectrometer. The integrated spin-echo intensity was recorded every 0.32 MHz using a coherent pulsed NMR spectrometer with phase-sensitive detection and automated frequency scanning. The NMR spectra were taken at five different values of the excitation RF field power, covering a range over more than one order of magnitude. Such a procedure allowed us to determine the optimum excitation field power at each frequency and to correct for the variation of the local electronic susceptibility and thus of the NMR enhancement factor as a function of frequency. After this, a further correction for the usual frequency dependence of the NMR signal was applied. The NMR amplitudes obtained in such a way represent the true distribution of nuclei with a given hyperfine field. The measurements were done at 2, 4.2 and 77 K in order to be able to obtain information about crystal microstructure and size distribution of Co particles in the samples. The analysis was performed on the tested catalyst covered with a homogeneous solid wax layer in order to prevent any surface oxidation of the cobalt phase during air exposure.

(3) Identification of cobalt crystal phase and fitting model

To obtain quantitative information about the amount of hexagonal closed packed (hcp) and face centered cubic (fcc) phases of the Co particles, a model has been used in this thesis for reproducing the experimental spectra. According to previous work,[18-19] we used the model developed for the analyses of cobalt films. In this model the NMR signal at 217 MHz corresponds the pure fcc cobalt and the line at 227 MHz corresponds to pure hcp cobalt.

Between, these two lines two additional contributions are considered for stacking faults within the bulk structure (~ 220 MHz and ~ 223 MHz). As described in details in ref [19] (Figure 2-9). The intensities of these stacking faults lines depend on the concentration of stacking faults in the fcc or hcp crystal. In the model a random distribution of stacking faults is assumed: it implies that, in a given phase, the intensities of the bulk line and the two defect lines obey a binomial law which depends only on the concentration of stacking faults in the phase. Hence the model has three main parameters: i) the fraction of hcp phase (in % of the total amount of bulk Co), ii) the concentration of stacking faults in the fcc phase (in % of the fcc fraction) and iii) the concentration of stacking faults in the hcp phase (in % of the hcp fraction). The secondary parameters are the positions and widths of each line but, in order to obtain a consistent description of the continuous structural evolution of the samples over the same blocking temperature, we have fixed the positions and widths of the - less resolved - stacking fault lines. Only a limited shift of the resolved bulk lines has been allowed.

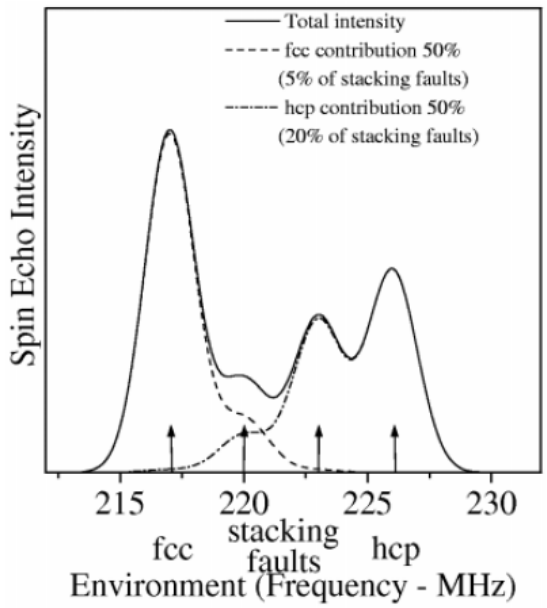

Figure 2-9. Example of shape obtained with the model used to analyze the NMR spectra.[19]

It has to be remarked that all the resonance frequencies given in the previous paragraph are valid for bulk or big particles only (>30 nm). When particles become small, as for most of the samples that have been investigated, the magnetic structure of the particles becomes single domain. In this case an additional magnetostatic field is experienced by the nuclei (in bulk samples this magnetostatic field is canceled by their magnetic multi-domain structure). This will result in a shift of the NMR resonance lines. This shift will depend on the shape of the particles, but for spherical particles, this shift will be of the order of +6MHz.

(4)Temperature dependent ^{59}Co zero field NMR measurements

For sake of sensitivity NMR measurements are usually performed at low temperature because the NMR signal increases as 1/T. However in this work temperature dependent measurement allows getting a deeper insight into the structure and size distribution of the Co particles. Indeed when at a given temperature magnetic particles, because small enough, become super-paramagnetic. For a super-paramagnetic particle,its magnetization direction does not stay fixed in direction in the time scale of the NMR measurement and therefore its contribution to the NMR spectrum vanishes. As a consequence as shown in Figure 2-10, even if the NMR intensity is multiplied by the measurement temperature to take into account the regular temperature dependence of the NMR intensity, the NMR signal decreases with the increase of the measurement temperature (from 2K, 4.2K, to 77 K). When the measurement temperature is increased the super-paramagnetic particles disappear from the NMR spectrum. Since the temperature at which a particle becomes super-paramagnetic (the blocking temperature) increases with the size of the particle, the higher the NMR measurement temperature the larger the size of the particles that are observed in the spectrum. It becomes therefore possible to probe the modification of the structure of the particles with their size. Actually by subtracting the NMR spectra recorded at two subsequent temperatures (Figure 2-10) it is possible to determine the number of Co atoms and the structure of the particles of a given blocking temperature range, or in other word of a given size range. Detailed explanations can be found as follows:

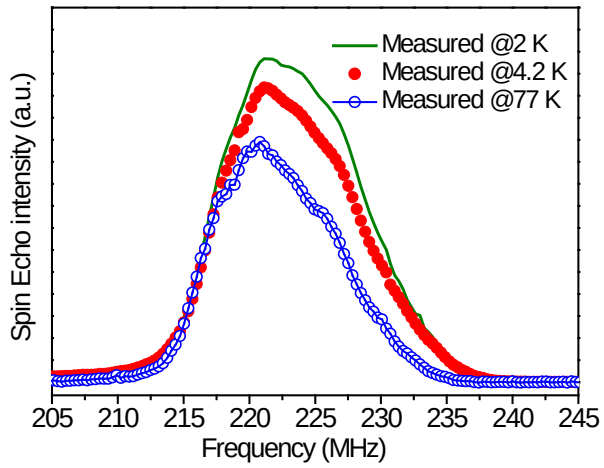

Figure 2-10. Typical ^{59}Co zero field NMR spectra recorded at different temperatures.

√ *Cobalt atoms distribution*

The sensitivity of the NMR measurement to the blocking temperature of the particles allows probing the Co atoms distribution versus the particles blocking temperature. The NMR intensity difference between the spectra taken at different temperatures is directly proportional to the number of Co atoms situated in the respective blocking temperature ranges. This is a distribution of Co atoms and not the Co particle size distribution that would be relevant for the discussion of the properties of the samples.

√ *Cobalt particle sizes distribution*

To compute the particle size distribution we have to determine the blocking temperature of the particles that is given by the following formula:

$$K \times V = \ln(\frac{\tau}{\tau_0}) \times k_B \times T \qquad (2\text{-}10)$$

With:

K: anisotropy constant of Co = 5×10^6 Erg·cm^{-3}

V: volume of the particle

τ: characteristic time of measurement = 20 to 100 micro seconds in NMR

τ_0: Test time for a particul to turn back: between 10^{-9} to 10^{-10} second

k_B: Boltzmann constant = 1.38×10^{-16} Erg·Kelvin^{-1}

T: blocking temperature in Kelvin

Assuming spherical particles, the minimum particle sizes are 1.2, 1.6, and 4.2 nm for measurement temperatures of 2, 4.2, and 77 K respectively. Moreover, a correction factor (k) of ~2.5 can be considered to adjust to the changes of various particle shapes (half cubic, spheres or pan cake like shapes). The resulting adjusted particle sizes are of the order of 3, 4, and 10 nm for measurement temperatures of 2, 4.2, and 77 K respectively.

Once the size of the particles is defined for each blocking temperature range, the amount of particle ($N_{P,T}$) in each temperature range can be calculated as follows:

$$N_{P,T} = N_{A,T} \times \frac{4}{3} \pi R_T^{\,3} \qquad (2\text{-}11)$$

where, R_T is the particle radius, and $N_{A,T}$ is the number of atoms in each blocking temperature range.

The particle size distribution from the different blocking temperature is calculated as follows:

$$\frac{N_{P,T2}}{N_{P,T1}} = \frac{N_{A,T2}}{N_{A,T1}} \times \left(\frac{R_1}{R_2} \right)^3 \qquad (2\text{-}12)$$

In a given series of samples, for sake of comparison, the number of particles is normalized to the number of particles of the sample producing the largest number of particle. Indeed for the same amount of Co atoms the total number of particles will be much larger if the Co atoms are clustered in small particles than in very big ones.

√ *Cobalt surface area distribution*

Since the activity of the samples is a surface effect we considered in this work that the distribution of the developed Co particles surface should be investigated.

The computations are similar to the ones of the previous paragraph, the surface of a spherical particle being given by:

$$S_T = k \times N_{P,T} \times 4\pi R_T^2 \qquad (2\text{-}13)$$

Taking R_1 as reference particle size it becomes:

$$\frac{S_{T2}}{S_{T1}} = \frac{N_{P,T2}}{N_{P,T1}} \times \left(\frac{R_2}{R_1} \right)^2 \qquad (2\text{-}14)$$

2.4 Fischer-Tropsch synthesis

2.4.1 FTS reaction setup

Fischer-Tropsch synthesis was carried out in a tubular fixed-bed stainless steel reactor (I.D. of 6 or 7 mm) with circulating silicon oil as heating source. The schema of catalytic measurements was shown in Figure 2-11.

The reduced catalyst (2.5-5 g catalyst, in form of grains 150-400 µm) was deposited between quartz wool plugs in the middle of the reactor. The reactor pressure was slowly increased from 1 to 40 bar (ramping rate of 10 bar·h^{-1}) under argon. The total pressure was controlled by a back pressure regulator (MFI Ltd.). At 40 bar the reactor temperature was raised from room temperature to the desired reaction temperature (heating rate of 2 °C·min^{-1}). Then, the argon flow was replaced by a 50:50 v:v % mixture of synthesis gas and argon ($CO:H_2$ = 1:2). The catalyst was activated under a synthesis gas-argon mixture with different synthesis gas concentrations during three days before evaluation under pure synthesis gas atmosphere. The catalyst bed temperature was monitored with a thermocouple (Ø 0.3 mm) inserted inside a stainless steel finger (Ø 1 mm) passing through the catalyst bed. The products were condensed in two high pressure traps maintained at 85°C and 15 °C, respectively.

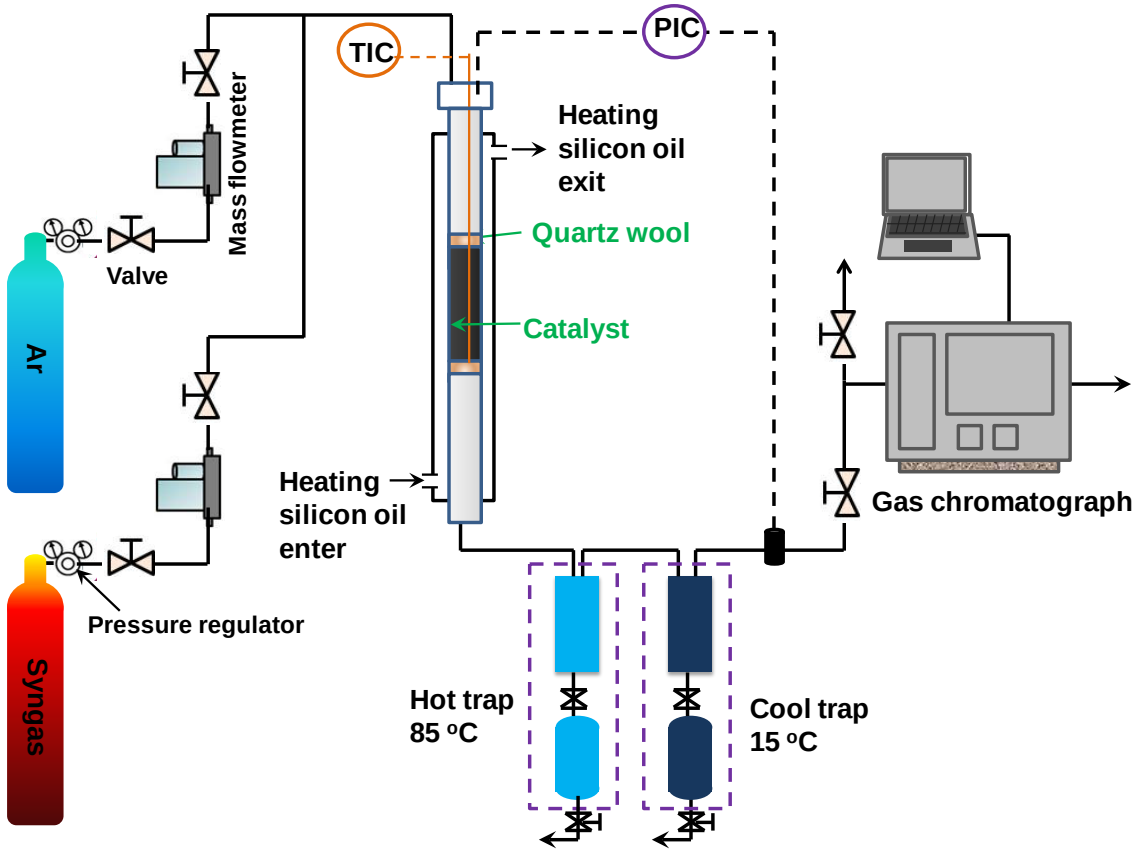

Figure 2-11. Setup of Fischer-Tropsch synthesis reaction on fixed-bed reactor

2.4.2 Products analysis

The exit gas was analyzed on-line, both by Thermal Conductivity Detector (TCD) and Flame Ionization Detector (FID), with a gas chromatograph (GC Varian 3800 equipped with a DP-1 and Carbobond capillary columns).Analysis of H_2, CO, CO_2, and CH_4 was performed by a DP-1 column and a thermal conductivity detector. Light hydrocarbons (C1–C4) were analyzed by a flame-ionization detector with a Carbobond capillary column. The hydrocarbon selectivities were calculated on carbon basis.

2.4.3 Catalytic performances calculations

(1) Calculation of CO conversion

The molar ratio of H_2/CO in the feed gas was 2. The CO conversion (X_{CO}, %) was based on the flow of carbon monoxide entering ($M°_{CO}$, mol/min) and leaving the reactor (M^t_{CO}, mol/min) with the reaction time:

$$X_{CO}(\%) = 100\times(M°_{CO}-M^t_{CO})/M°_{CO} \qquad (2\text{-}15)$$

Where $$M°_{CO} = \frac{F^o{}_{CO} \times R^o{}_{CO}}{24448(ml/mol)} \qquad (2\text{-}16)$$

and $$M^t_{CO} = \frac{F^t{}_{CO} \times R^t{}_{CO}}{24448(ml/mol)} \qquad (2\text{-}17)$$

where $F°_{CO}$ is the initial CO flow rate (ml/min); F^t_{CO} is outlet CO flow rate (ml/min) at a certain reaction time t; $R°_{CO}$ and R^t_{CO} (%) are CO concentration in the inlet and outlet flow, respectively, which are confirmed by TCD.

(2) The product selectivity calculation

The selectivity calculation of each product C_x (CO_2, C_1, C_2, C_3, C_4, C_{5+}) is defined as the ratio of the amount of product with the amount of converted CO at the reaction time t, S_{X^t} (%),

$$S_{X^t} = \frac{X^t \times nC_x}{M^o{}_{CO} - M^t{}_{CO}} \qquad (2\text{-}18)$$

Where X^t is calculated in the same way with reactant which is the different C_x product concentration between the outlet and inlet (mol/min) at the reaction time t; nC_x is a number from the amount mol/min CO transformed to the 1 mol/min C_x.

The selectivity of long-chain hydrocarbon (C_{5+}) is calculated as follows:

$$S_{C_{5+}} = 1 - \sum_{i=1}^{4} S_{c_i} \qquad (2\text{-}19)$$

Table 2-1. Characteristics of GC columns and conditions of online analysis

Column	**Flame-ionization detector (FID):** DB-1 30 m × 0.53 mm Thickness of stationary phase: 1.5 μm **Thermal conductivity detector (TCD):** CP carbobond 30 m × 0.53 mm Thickness of stationary phase: 10 μm
Injector temperature	180 ^{o}C
Dector temperature	FID: 180 ^{o}C TCD: 140 ^{o}C (filament: 170 ^{o}C)
Carrier gas	Argon
Temperature program	38 ^{o}C → 4.5 min From 38 ^{o}C to 100 ^{o}C → 20 ^{o}C /min 100 ^{o}C → 15 min

(3) Cobalt time yield

Cobalt time yield (CoTY, $mol_{co}g_{Co}^{-1}s^{-1}$) is a parameter to performance the FTS catalytic activity which can be identified from the conversion rate molar CO conversion rate per gram atom cobalt per hour. From the following equation can be derived the cobalt time yield :

$$CoTY = \frac{F^{o}_{CO} \times X_{CO}}{60 \times 22400 \times m_{catalyst} \times p_{Co}} \qquad (2\text{-}20)$$

with :

F^{o}_{CO} : initial CO flow rate (ml/min)

X_{CO} : conversion of CO (%)

$m_{catalyst}$: catalyst weight (g)

p_{Co} : cobalt mass loading (%), which is confirmed by ICP technique

(4) FTS conversion rate to C_{5+} hydrocarbons (r_{C5+})

The reaction rate can also represent the FTS conversion rate to C_{5+}, r_{C5+}, which can be defined by the weight of long chain hydrocarbons (C_{5+}) formed per gram of catalyst per hour ($g_{C5+}\ g_{catalyst}^{-1}\ h^{-1}$) :

$$r_{C_{5+}} = \frac{\text{mass of } C_{5+}}{\text{mass of catalyst} \times \text{reaction time}} = \frac{F^{o}_{CO} \times S_{C_{5+}} \times X_{CO} \times 60 \times 14}{22400 \times m_{catalyst}} \qquad (2\text{-}21)$$

with :

F^{o}_{CO} : initial CO flow rate (ml/min)

X_{CO} : conversion of CO (%)

$S_{C_{5+}}$: selectivity oflong-chain hydrocarbon (C_{5+})

$m_{catalyst}$: catalyst weight (g)

2.4.4 Liquid hydrocarbons product selectivity

The liquid phase and water were condensed in the traps and analyzed off-line at the end of the test. The water was removed from the organic phase by decantation of the system. A known amount (100 mg) of the organic phase, liquid hydrocarbons and waxy products, was dissolved in 3 ml of dichloromethane under sonication during 30 minutes. Then, 20 ml of CS_2 were further added to the solution in order to ensure complete dissolution of the organic phase. For analysis, 1 µL of the solution was injected in a GC apparatus with a flame ionization detector equipped with a Simdist column operated at 400 °C, which allowed the detection of hydrocarbons ranging from C_9 to C_{70}.The details conditions of chromatographic system are presented in Table 2-2.

Table 2-2. Characteristics of the chromatographic system for the analysis of waxes collected after test.

Column	CP-simidist ultimetad (CP7542) 10 m × 0.53 mm Thickness of stationary phase: 0.17 μm
Injector temperature	270 ^{o}C
Dector temperature	FID: 300 ^{o}C
Carrier gas	Argon
Temperature program	40 ^{o}C → 20 min From 40 ^{o}C to 130 ^{o}C → 2 ^{o}C /min From 130 ^{o}C to 400 ^{o}C → 1 ^{o}C /min 400 ^{o}C → 20 min Total 355 min

Indeed, the molar number (Ni) of different chain length hydrocarbon product (i) is given by the following equation:

$$\mathrm{N}i = \frac{\mathrm{A}i}{\alpha \times \mathrm{r}i \times \mathrm{M}i} \qquad (2\text{-}22)$$

where,

A*i* is the peak area corresponding to hydrocarbon (i) detected by chromatography

α is the sensitivity factor of the detector (in counts per gram)

r*i* is the factor Dietz component (dimensionless)

Mi is the molar mass of component i (in grams per mole)

When Dietz factor is close to 1 for all linear hydrocarbons, branched and olefin, and the sensitivity factor is constant, so we have:

$$\mathrm{N}i = C \times \frac{\mathrm{A}i}{\mathrm{M}i} \qquad (2\text{-}23)$$

Where C is constant,

The molar percentage of each product can be obtained:

$$n_i\,(\%) = \frac{\frac{A_i}{M_i}}{\sum_{i=1}^{N}\frac{A_i}{M_i}} \qquad (2\text{-}24)$$

It should be noted that the products are separated into two categories: perfect Linear hydrocarbons and wired and / or olefin hydrocarbons. "

Table 2-3. Representative hydrocarbon products issued from the GTL process (adapted from Leckel et al[20]).

Fraction	**Carbon chain length**
Fuel gas	$C_1 - C_2$
Liquefied petroleum gas	$C_3 - C_4$
Gasoline	$C_5 - C_{12}$
Naptha	$C_8 - C_{12}$
Kerosene (jet fuel)	$C_{11} - C_{13}$
Diesel	$C_{13} - C_{17}$
Middle distillates	$C_{10} - C_{20}$
Soft wax	$C_{19} - C_{23}$
Medium wax	$C_{24} - C_{35}$
Hard wax	C_{35+}

As we all known, the syngas ($2H_2$ + CO) issued from natural gas reforming can be converted into liquid hydrocarbons followed by a hydrocracking of the heavy fraction into different carbon chain length compounds such as naphtha, diesel, lubricants and others. The main products are presented in Table 2-3. The FTS is considered as a polymerization-like reaction based on sequential -CH_2- additions. It is expected that catalyst with large pore will favorize the mass transfer in the catalyst which significantly reduces the light product formation. As a result of the polymerization mechanism, the products of FT synthesis

generally follow a statistical hydrocarbon distribution, which is known as the Anderson-Schulz-Flory (ASF) distribution. The chain growth factor (α) calculated from the linear portion of the hydrocarbons, according to the following equation:

$$Wn/n = (1-\alpha)^2\alpha^{(n-1)} \qquad (2\text{-}20)$$

where

Wn is the weight fraction of hydrocarbon molecules containing n carbon atoms.

α is the chain growth probability. If α is equal to 0 all the CO molecules are converted to CH_4 and when α is equal to 1 all the CO molecules are converted to liquid hydrocarbons (Figure 2-12).

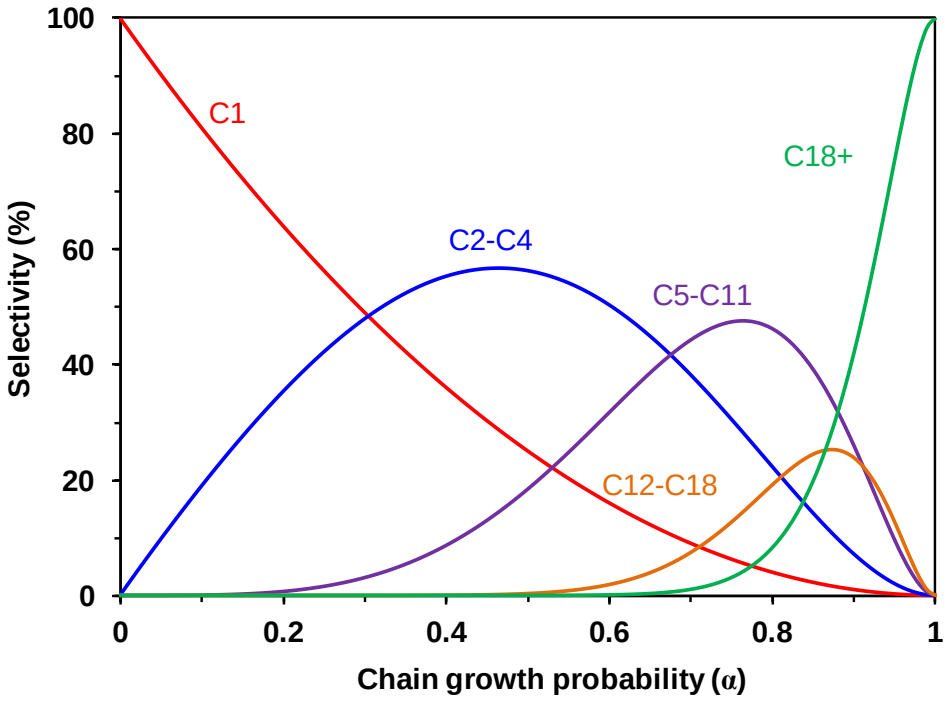

Figure 2-12. Product distribution in FT synthesis as a function of the chain growth probability (α).

2.4.5 Carbon balance

The analysis systems, primarily by gas chromatography, were used to overview the reaction results while the carbon balance, B_C, maintains a satisfactory status, i.e. ≥ 93%.

The carbon balance is the ratio of the molar carbon in inlet, n_C^f, and outlet, where the molar carbon outlet consisted by the carbon in the un-reacted feed gas n_C^u and carbon in the products n_C^n. Normally, the theoretical carbon balance is 1, which is given by:

$$n_C^f = n_C^u + n_C^n \qquad (2\text{-}26)$$

The only carbon source entering in FTS reaction is carbon monoxide; n_C^f corresponds to the entering total molar carbon monoxide injected during the duration of the experiment, that is:

$$n_C^f = n_C^u = F^O_{CO} \times \int_{t=0}^{T} dt \qquad (2\text{-}27)$$

Unlike inlet carbon, the outlet carbon is relative complex which can be described using the equation:

$$n_C^u + n_C^n = n_C^u + n_{CO_2} + n_{CH_4} + \sum_{j=2}^{N} j(C_jH_{2j+2}) + xn_{C_xH_yO_z} \qquad (2\text{-}28)$$

with:

n_C^u the total molar of un-reacted feed gas

n_{CO_2} the total molar of CO_2 products

n_{CH_4} the total molar of CH_4 products

$\sum_{j=2}^{N} j(C_jH_{2j+2})$ the total molar of hydrocarbons products (expect for CH_4)

$xn_{C_xH_yO_z}$ the total molar of oxygenated hydrocarbons

It should be noted that the final carbon balance is ≥ 93% in our reaction system. The discrepancy between the experimental and theoretical carbon balance could be due to several facts: (i) the uncertainty on the CO flow rate, before and after reaction, which leads to a carbon error of 2-5 % in the carbon balance, (ii) the waxes which were lost during the waxes recovery from the different traps accounting for about 2-5 %.

2.5 References

[1] A. Y. Khodakov, W. Chu, P. Fongarland, *Chemical Reviews* **2007**, *107*, 1692-1744.

[2] P. Nguyen, C. Pham, *Appl Catal a-Gen* **2011**, *391*, 443-454.

[3] M. J. Ledoux, C. Pham-Huu, *Cattech* **2001**, *5*, 226-246.

[4] M. J. Ledoux, S. Hantzer, C. Pham-Huu, J. Guille, M. P. Desaneaux, *J Catal* **1988**, *114*, 176-185.

[5] Y. Liu, B. de Tymowski, F. Vigneron, I. Florea, O. Ersen, C. Meny, P. Nguyen, C. Pham, F. Luck, C. Pham-Huu, *ACS Catalysis* **2013**, 393-404.

[6] B. Louis, G. Gulino, R. Vieira, J. Amadou, T. Dintzer, S. Galvagno, G. Centi, M. J. Ledoux, C. Pham-Huu, *Catal Today* **2005**, *102*, 23-28.

[7] G. Gulino, R. Vieira, J. Amadou, P. Nguyen, M. J. Ledoux, S. Galvagno, G. Centi, C. Pham-Huu, *Appl Catal a-Gen* **2005**, *279*, 89-97.

[8] L. Cao, T. Man, M. Kruk, *Chem Mater* **2009**, *21*, 1144-1153.

[9] A. Vishnyakov, E. Piotrovskaya, E. Brodskaya, *Adsorption* **1998**, *4*, 207-224.

[10] H. Mukaibo, L. P. Horne, D. Park, C. R. Martin, *Small* **2009**, *5*, 2474-2479.

[11] D. Chandra, T. Ohji, K. Kato, T. Kimura, *Phys Chem Chem Phys* **2011**, *13*, 12529-12535.

[12] D. Schanke, S. Vada, E. A. Blekkan, A. M. Hilmen, A. Hoff, A. Holmen, *J Catal* **1995**, *156*, 85-95.

[13] W. O. Saxton, W. Baumeister, M. Hahn, *Ultramicroscopy* **1984**, *13*, 57-70.

[14] D. N. Mastronarde, *J Struct Biol* **1997**, *120*, 343-352.

[15] C. Messaoudil, T. Boudier, C. O. S. Sorzano, S. Marco, *Bmc Bioinformatics* **2007**, *8*, 288.

[16] http://www.slicer.org/.

[17] P. Panissord, in *Topics in current physics - Microscopic methods in metals, Vol. 40* (Ed.: P. Gonser), Springer-Verlag, **1986**, pp. 365-407.

[18] P. Panissod, C. Meny, *Appl Magn Reson* **2000**, *19*, 447-460.

[19] J. L. Bubendorff, C. Meny, E. Beaurepaire, P. Panissod, J. P. Bucher, *Eur Phys J B* **2000**, *17*, 635-643.

[20] D. Leckel, *Energ Fuel* **2009**, *23*, 2342-2358.

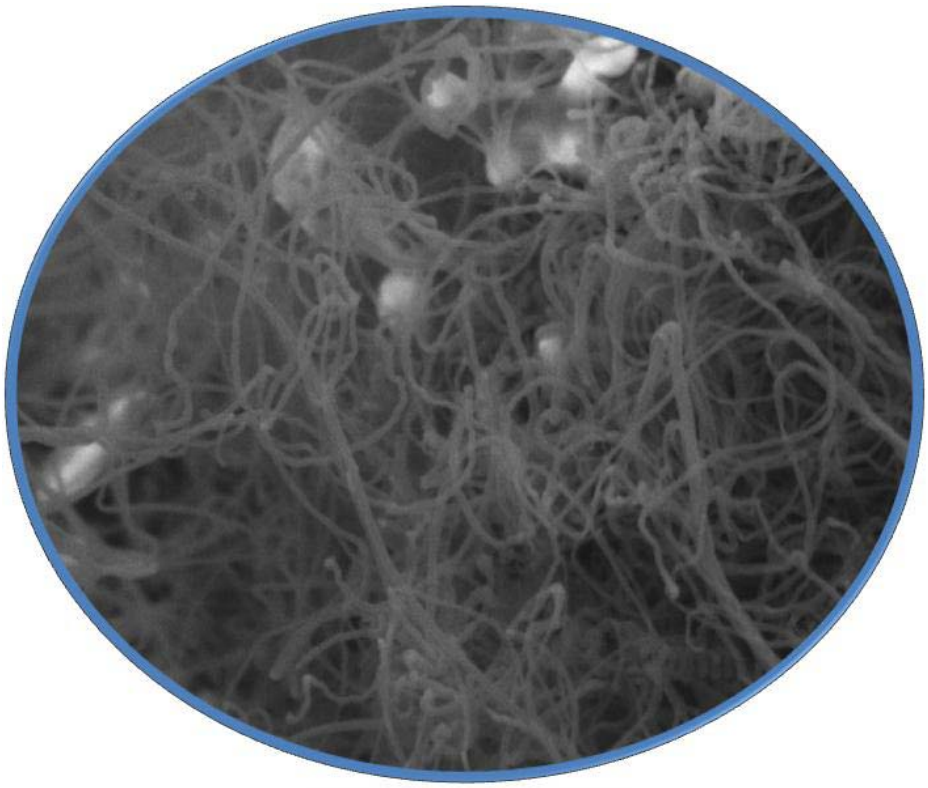

Chapter III

Hierarchical structured conductive carbon nanotubes-based composite supports

Chapter III Hierarchical structured conductive carbon nanotubes-based composite supports

Brief introduction of Chapter III

In this chapter the insulator large pore α-Al_2O_3 is decorated with a homogeneous layer of multi-walled carbon nanotubes (CNT) with better thermal conductivity and high effective surface support for cobalt in the FTS. And then, we will explore the FTS performance on a new type of hierarchical support consisting of CNT-α-Al_2O_3 coated with a thin layer of TiO_2 for cobalt active phase. This chapter is consisted of two sections:

[Part-A] CNT decorated α-Al_2O_3 containing cobalt nanoparticles for the FT Reaction

In this part, a new hierarchical composite consisted by multi-walled carbon nanotubes (CNTs) layer anchored on macroscopic α-Al_2O_3 host matrix was synthesized and used as support for the Fischer-Tropsch synthesis (FTS). The composite is constituted by a thin shell of a homogeneous, highly entangled, and structure-opened carbon nanotubes network and exhibited a relatively high and fully accessible specific surface area of 76 $m^2 \cdot g^{-1}$, compared to the origin support, i.e. 5 $m^2 \cdot g^{-1}$. The relatively high metal-support interaction between the carbon nanotubes surface and the cobalt precursor led to a relatively high dispersion of the cobalt nanoparticles. This hierarchically supported cobalt catalyst exhibited a high FTS activity along with an extremely high selectivity towards liquid hydrocarbons compared to the cobalt-based catalyst supported on the pristine α-Al_2O_3 or on the carbon nanotubes carriers. This improvement was attributed to the high accessibility of the composite surface area compared to the macroscopic host structure alone or to the bulk carbon nanotubes where the nanoscopic dimension induced a dense packing with low mass transfer which favoured the problem of competitive diffusion of the reactants towards the cobalt active site. In addition, the intrinsic thermal conductivity of decorating CNTs could help the heat dissipating throughout the catalyst body and thus, avoid the formation of local hot spots which may appear in the high CO conversion under the pure syngas feed in FTS reaction. The CNTs decorated α-Al_2O_3 catalyst also exhibited satisfactory high stability during more than 200 h on stream under relative severe conditions compared to other catalysts reported in

the literature. Finally, the macroscopic shape of such composite renders easier its usage as catalyst support in a fixed-bed configuration without facing problems of transport and pressure drop as encountered with the bulk carbon nanotubes.

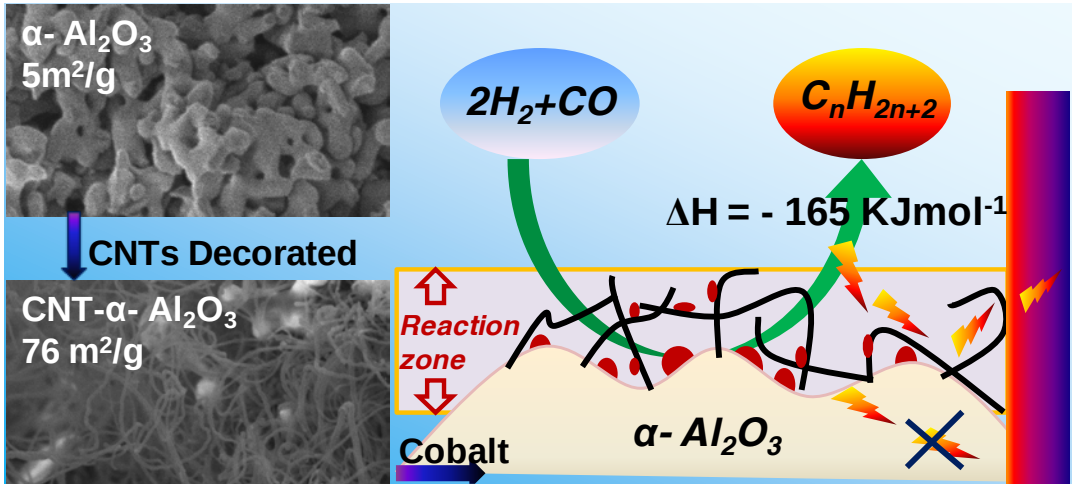

[Part-B] Efficient hierarchically structured composite supported cobalt catalysts for clean synthetic fuel via Fischer-Tropsch

In this section we will explore the FTS performance on a new type of hierarchical support consisting of CNT-α-Al_2O_3 coated with a thin layer of TiO_2 for cobalt active phase. The titanium addition caused a slight change of the surface area and mean pore diameter, i.e. 72 $m^2 \cdot g^{-1}$ and 15 nm for TiO_2-CNT-α-Al_2O_3 instead of 76 $m^2 \cdot g^{-1}$ and 11 nm for CNT-α-Al_2O_3. SEM analysis indicates that the CNTs network is well coated with TiO_2 and almost no pore plugging was observed. The introduction of TiO_2 on the hierarchical support leads to a significant increase of the FTS performance compared to that without TiO_2. The catalyst also exhibits a highest activity among the all catalysts containing TiO_2 reported nowadays in the literature. The TiO_2 promoted hierarchically structured catalyst (CoTiCNTA) exhibited a carbon monoxide conversion of 44.3%, which is higher than that obtained with conventional hierarchically catalyst (28.2%, CoCNTA) and conventional TiO_2 promoted catalysts (33.4%, CoTiA). The TiO_2-promoted hierarchically-structured catalyst gave approximately 84.5% selectivity to C_{5+} at 47.4% CO conversion under severe FTS reaction conditions, i.e. relative high reaction temperature (T= 245 ^oC), high pressure (40 bar) and high flow rate (GHSV (STP) =9600 $ml \cdot g_{cat}^{-1} \cdot h^{-1}$). The FTS rate expressed in the terms of the weight of long chain hydrocarbon formed per gram of catalyst per hour is around 0.80 $g_{C5+} \cdot g_{cat}^{-1} \cdot h^{-1}$.

[Part-A] CNT decorated α-Al_2O_3 containing Co nanoparticles for the FT Reaction

3.1 Introduction

Since the middle of the last century crude oil has been one of the central primary energy carriers compared to other energy sources such as natural gas or charcoal. The crude oil extracted nowadays shows limited availability also with lower quality and thus, new sources of energy supply with better quality need to be developed in order to face the constant increase of the worldwide energy demand. Clean fuels which are free of sulfides, nitrides and aromatics are synthesized from natural gas (Gas-To-Liquids, GTL), coal (Coal-To-Liquids, CTL) or biomass (Biomass-To-Liquids, BTL) via the process of Fischer-Tropsch synthesis (FTS).[1-2] Among these different raw materials natural gas is very likely to become a principal source of energy that is easy to transport and handle and thus, the GTL process will become even more important in the near future. In addition, natural gas also contains higher hydrogen versus carbon ratio that leads to a H_2/CO ratio of 3 after reforming process which is higher than in production processes from other raw materials like crude oil, coal or biomass. The H_2/CO ratio will be further adjusted with the aid of water-gas-shift reaction before admitting to the FTS unit.

Cobalt components are widely applied as active sites in the Fischer-Tropsch synthesis because of their high activity and C_{5+} selectivity, lower water gas shift (WGS) activity and relatively slower deactivation.[3-5] Thus, supported cobalt catalysts are well known to be the best candidates for FTS towards higher hydrocarbons (C_{5+}).[4] The catalyst productivity can be directly predicted from the number of cobalt atoms exposed on the surface of small cobalt particles. These small cobalt particles are responsible for the significant enhancement of the FTS performance compared to that obtained with much bigger active phase particle size. Indeed, such metal particles with appropriate size (6 - 20 nm) possessing a large fraction of surface atoms significantly contribute to the enhancement of the conversion rate of reactants into products. Besides, the characteristics of the surface atoms are greatly different from atoms in deeper layers such as bond distances, geometries and bonding energies that are altered by the reduced local coordination on the surface. Iglesia et al.[5-7] found the constant site-time yield over the cobalt particle with size range of 10-210 nm, which included most of

the typical low-dispersion cobalt Fischer-Tropsch catalysts. Storsæter et al.[8] also found constant site-time yield over cobalt deposited on different metal oxides (γ -Al_2O_3, SiO_2, and TiO_2). For cobalt supported on carbon nanofibers, it has recently been proved that the site-time yield was lower for particles smaller than 8 nm.[9-10]

According to earlier studies, the activity and selectivity are also influenced by catalytic support properties like surface area, pore volume and pore size distribution in addition to the support material itself.[11-12] Because the support is very important for the properties of final Fischer-Tropsch catalyst, the activity is indirectly affected by the support nature. Moreover, at conditions favouring chain-growth, site-time yields on supported cobalt catalysts are traditionally considered independent of cobalt dispersion and of support identity.[5-8, 13-14] The α-Al_2O_3 is found to perform higher C_{5+} selectivity thanks to their large pore structure which significantly reduces the mass transfer limitations; however the FTS activity obtained is a little lower.[15-19] Borg et al.[18] investigated 26 catalysts based on alumina (γ-Al_2O_3 and α-Al_2O_3) carriers supporting various contents of cobalt for FTS, and the result turned out that the selectivity of catalysts supported on α-Al_2O_3 was much higher than those supported on γ -Al_2O_3 among all the tested cobalt particle sizes. Besides, carbon nanotubes show excellent catalytic performances as catalyst support in Fischer-Tropsch synthesis thanks to their exceptional properties such as thermal and electric conductivity, and relative higher effective surface area with unique and open structure.[20-31] Many previous works were focused on the role of particle sited on inner or outer CNTs walls[28, 32], cobalt particle size [22, 33], and the diameter and pore size of nanotubes[20, 30] influencing the catalytic performance. However, the effect of a hierarchical structured support consisted of carbon nanotubes decorating a macroscopic host matrix on FTS activity and C_{5+} selectivity have never been reported according to our knowledge.

In this study, we report a simple method to synthesis multi-walled carbon nanotubes anchored on a macroscopic host structure of α-Al_2O_3 as the catalyst support for highly exothermal Fischer-Tropsch synthesis. The CNTs grown process led to the final composite with a thin shell constituted of homogeneous, highly entangled, and structure-opened carbon nanotubes network. The composite exhibited a relatively high and fully accessible specific surface area for the tri-phasic reaction like the FTS. These composite were further used as a support for the deposition of Co nanoparticles on the FTS reaction. In addition, the intrinsic thermal conductivity of decorated CNTs could help the heat dissipating throughout the catalyst body and thus, avoid the formation of local hot spots which appeared in the high CO

conversion under the pure synthesis gas feed in FTS reaction.[34] The obtained supports and catalysts were characterized by a range of techniques, and the improved catalytic performance discussed in light of the characterization results.

3.2 Results and discussion

3.2.1 Supports characteristics

Results of surface area measurements on the different supports are shown in Table 3-1 and Figure 3-1A. The introduction of the CNTs into the alumina matrix leads to a significant increase of the specific surface area of the composite, i.e. 76 $m^2 \cdot g^{-1}$ for the CNT/Al_2O_3 composite instead of 5 $m^2 \cdot g^{-1}$ for the α-Al_2O_3. Such specific surface area increase is directly attributed to the nanoscopic size of the CNTs with a high intrinsic effective surface area.[35] Indeed, carbon nanotubes possess a relatively high specific surface area, ranged from 80 to 200 $m^2.g^{-1}$, depending on the average diameter of the as-synthesized CNTs. After decorated by CNTs, the sample exhibited bimodal pore size distribution in the range of 3-100 nm diameter region. At the same time, the pore volume of CNT-α-Al_2O_3 increases to 0.20 $cm^3 \cdot g^{-1}$ comparing with α-Al_2O_3 (0.01 $cm^3 \cdot g^{-1}$), and is mostly consisted by meso- and macro-porosity which is linked with the presence of a CNTs entangled network. It is found that the specific surface area of the CNT-α-Al_2O_3 was about 15 times higher than that of α-Al_2O_3. Besides, the macropore volume is approximately 20 times larger than that of α-Al_2O_3.

Table 3-1. BET surface area and pore volume derived from BJH method of the α-Al_2O_3, CNTs decorated α-Al_2O_3, and the corresponding cobalt-based catalysts containing 10 wt. % of cobalt.

Sample	Surface area ($m^2 \cdot g^{-1}$)	Total pore volume ($cm^3 \cdot g^{-1}$)	BJH pore diameter (nm)
α-Al_2O_3	5	0.01	18
CNT-α-Al_2O_3	76	0.20	11
CoA	7	0.02	13
CoCNTA	62	0.25	17

The TGA technique is used to investigate the yield of carbon nanotubes growth on α-Al_2O_3. Figure 3-1B illustrates the results of thermogravimetric analysis over CNT decorated α-Al_2O_3. Result shows that the rapid weight loss starts from 500 ^oC with the maximum centered at 570 ^oC, which display to the oxidation behavior of CNTs.[33] The CNTs yield over α-Al_2O_3 is about 73 wt. %.

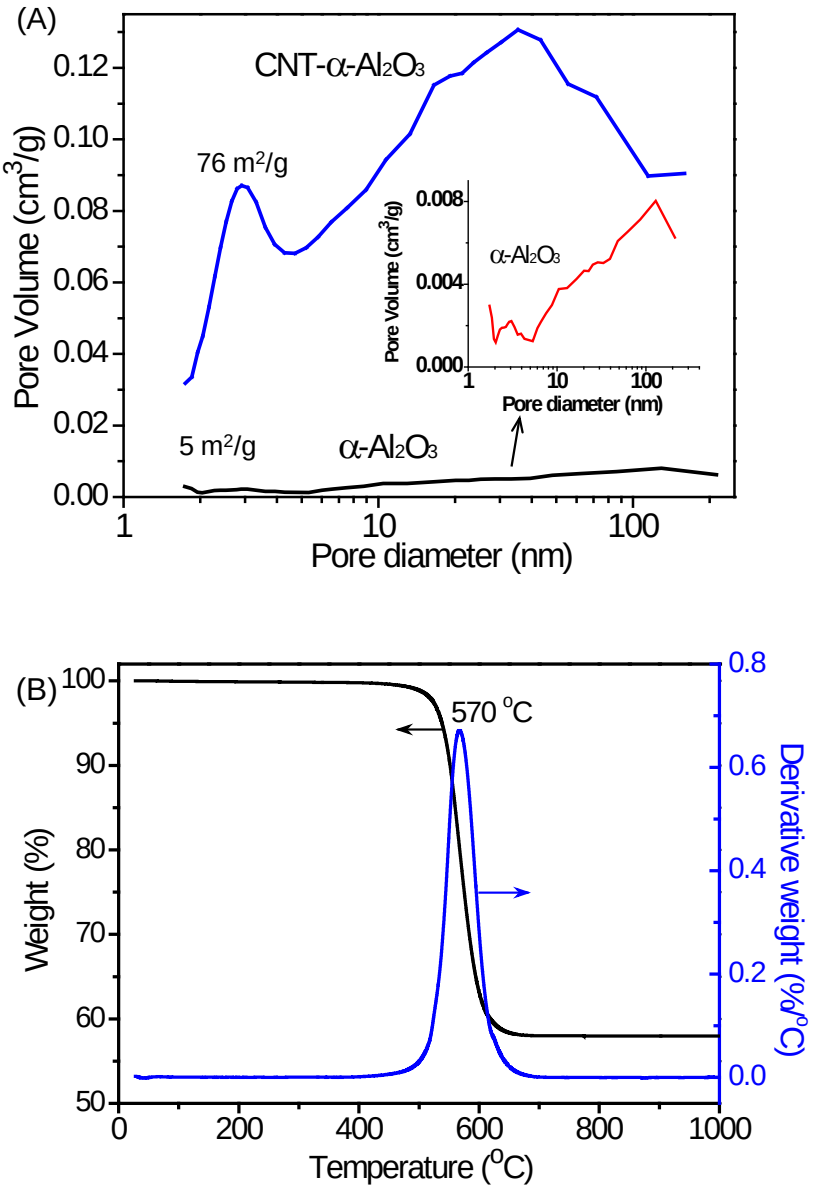

Figure 3-1. (A) Pore size distribution of the α-Al_2O_3 and CNT decorated α-Al_2O_3 supports based on N_2 adsorption using BJH model, the inset image of (A) is a magnified pore size distribution profile of α-Al_2O_3. **(B)** TGA curve of the CNT-α-Al_2O_3.

The representative SEM micrographs of the α-Al_2O_3 and CNT-α-Al_2O_3 supports are displayed in Figure 3-2. The low magnification SEM micrographs (Figure 3-2A and B) highlight the complete morphology conservation of the alumina material after CNTs deposition. As can be seen, the carbon nanotubes cover the α-alumina surface with a homogeneous web-like network (Figure 3-2C). The average diameter of the as-synthesized CNTs is around 20 ± 5 nm according to the high-resolution SEM micrograph (Figure 3-2D). The SEM observation also demonstrates the high entanglement of the CNT that is directly attributed to the relatively low synthesis temperature of the CVD process.[36-37]

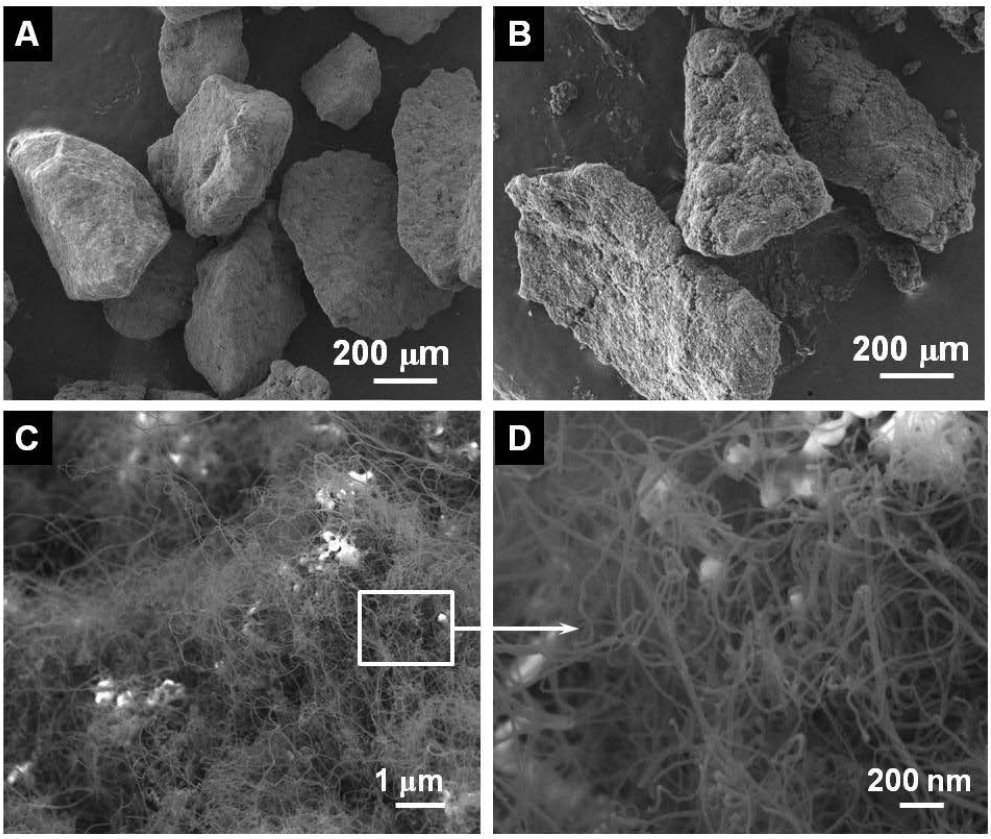

Figure 3-2. (A) Low-magnification SEM image of α-Al_2O_3; **(B,C)** Low-magnification SEM images of CNT-α-Al_2O_3; **(D)** High-magnification SEM image of CNT-α-Al_2O_3

The low-resolution TEM micrograph (Figure 3-3A) demonstrates that the synthesis method allows one to obtain the high selectivity toward carbon nanotube as neither carbon nanoparticles nor amorphous carbon is obtained as observed within the sample according to the statistical TEM observation.[37] High-resolution TEM micrograph shows that the nanotubes are made of parallel graphene planes oriented along the tube axis (Figure 3-3B). An amorphous phase is also observed on the outer surface of the CNTs which could be due

to the incomplete formation of ordered graphene layer during the cooling process from the synthesis temperature to room temperature. TEM micrograph indicates that the CNTs are relatively homogeneous in diameter with an average value of ca. 20 ± 3 nm. TEM analysis also highlights the presence of some iron-cobalt catalyst particles which are embedded within several graphene layers as illustrated in the red box of Figure 3-3A. The energy dispersive spectrometer (EDS) is carried out over this region as shown in Figure 3-3C, and the particles are demonstrated to be composed of Fe-Co. These iron particles were inaccessible, neither to the acid medium during the purification process, nor by any gaseous reactants during the subsequence use of the composite due to the presence of the graphene layer wrapping their surface.[37] Thus, these residual Fe-Co particles barely influence the FTS reaction performance.

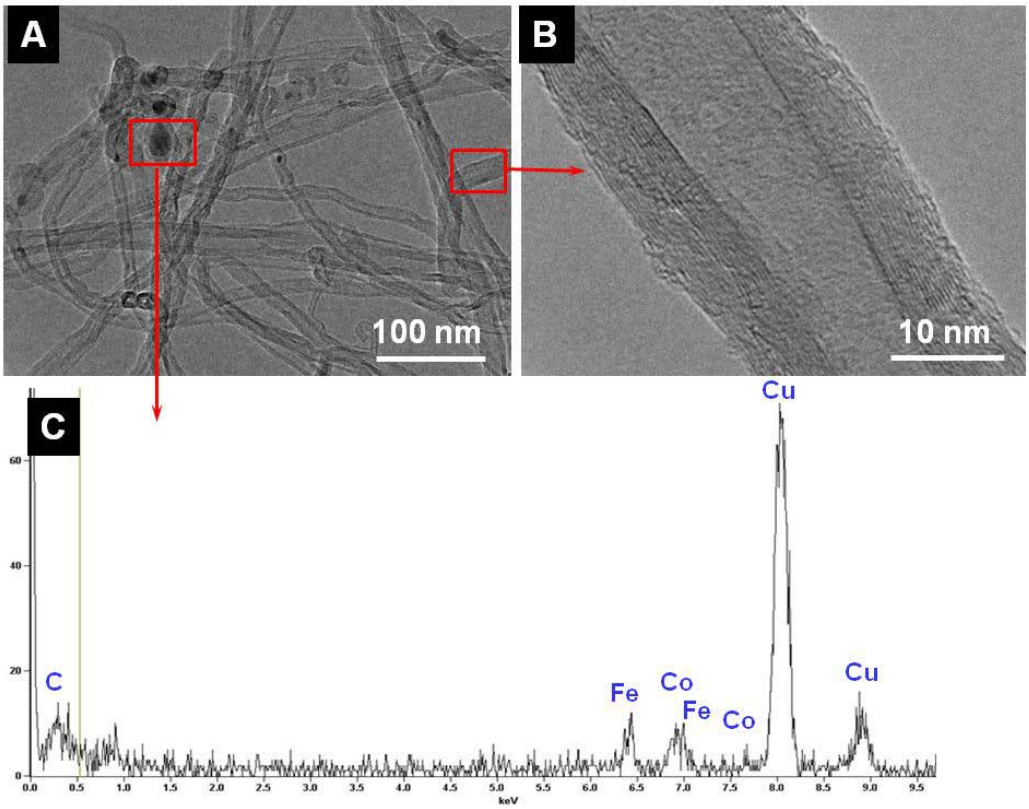

Figure 3-3. (A) TEM image of CNT decorated α-Al_2O_3 catalyst showing the relatively high homogeneous diameter of the as-synthesized CNTs; **(B)** High-resolution TEM micrograph of the CNT with parallel graphene planes running along the tube axis; **(C)** Energy dispersive spectrometer (EDS) analysis of the residual growth catalyst particles encapsulated within graphene layers.

3.2.2 Cobalt containing catalysts characteristics

The specific surface area of the CNT-α-Al_2O_3 catalyst slightly decreases from 76 $m^2 \cdot g^{-1}$ to 62 $m^2 \cdot g^{-1}$ (Table 3-1) after deposition of cobalt active phase. Such relatively low surface area lost could be attributed to the high effective surface area of the CNT network and the complete absence of any ink-bottled pores within the composite material. Indeed, it has been reported that on supports with micropores or small mesopores a large surface area lost has been observed after depositing an active phase due to the problem of pore aperture plugging by the metal active phase.[38] The specific surface area of the alumina-based catalyst remaining almost unchanged after the cobalt deposition, i.e. 7 $m^2 \cdot g^{-1}$ versus 5 $m^2 \cdot g^{-1}$, can be explained by the presence of a large pore inside the support that is hardly affected by the cobalt particles.

The XRD patterns of the ex-situ reduced CoA and CoCNTA catalysts are presented in Figure 3-4. The XRD patterns of the α-Al_2O_3 and the CNT-α-Al_2O_3 supports are also reported in the same figure for comparison. The main and strong peaks (marked as black plenigita circle) in all samples are corresponding to the diffraction lines of the α-Al_2O_3. For the CNT-α-Al_2O_3 and the related supported catalyst, the peaks at 26° and 44° are ascribed to graphite layers for multi-walled carbon nanotubes. On the two cobalt-based catalysts, the XRD patterns show only the presence of a relatively well defined diffraction lines corresponding to the metallic cobalt phase. However, the CNTs and Co^0 diffraction peaks are overlapped in CoCNTA catalyst. The Co_3O_4 particle size is calculated by Scherrer equation from the [311] lattice of Co_3O_4 cubic fcc phase, which is detected at $2\theta = 36.9$ by XRD profile. The average Co^0 particle sizes, deduced from the size of Co_3O_4 by the following formula: d (Co^0) (nm) = 0.75 d (Co_3O_4)[39], are 35 nm and 20 nm over α-Al_2O_3 and CNT-α-Al_2O_3 supports, respectively.

The TPR spectra of the samples after calcination in air are presented in Figure 3-5. The small reduction peak localized at low-temperature region (260 °C) of both samples can be attributed to the reduction of the residual cobalt nitrate in the catalysts after calcination. Indeed, it is expected that some residual cobalt nitrate still remains inside the active phase precursor due to the relatively low calcinations temperature. According to the literature reports the complete decomposition of the supported cobalt nitrate is above 450 ^oC.[39-40] The first reduction peak located at around 355 °C is attributed to the reduction of Co_3O_4 to CoO, although a fraction of the peak is likely comprised the reduction of the larger, bulk-like CoO species to Co^0. This reduction peak of the CoCNTA catalyst presenting at 355 ^oC is about 20

^{o}C lower than the CoA catalyst which could be due to the lower metal-support interaction between the cobalt oxide precursor and the CNT surface. The second reduction peak of CoA catalyst locates at 443 ^{o}C, which is mainly originated from the reduction of CoO to Co^{0}. The relatively low and complete reduction profile observed over the CoA catalyst is attributed to the low interaction between the α-Al_2O_3 support and the deposited cobalt oxide precursor.[41] Different from the CoA sample, the CoCNTA catalyst displays a broader and overlapped peaks, a peak locating at 437 ^{o}C is attributed to the reduction of CoO. The high temperature reduction peak located at around 600 °C could be attributed to the gasification of the carbon nanotubes which is partly catalyzed by the presence of the cobalt particles. Similar results have already been reported by Khodakov and co-workers[20] on the cobalt deposited on multi-walled carbon nanotubes catalyst. It can be seen in the XRD analysis the average particle size on CoA was 1.75 times higher than that on CoCNTA, indicating the higher cobalt dispersion on the CNT-based composite which is in good agreement with the higher metal-support interaction on the carbon nanotube surface.

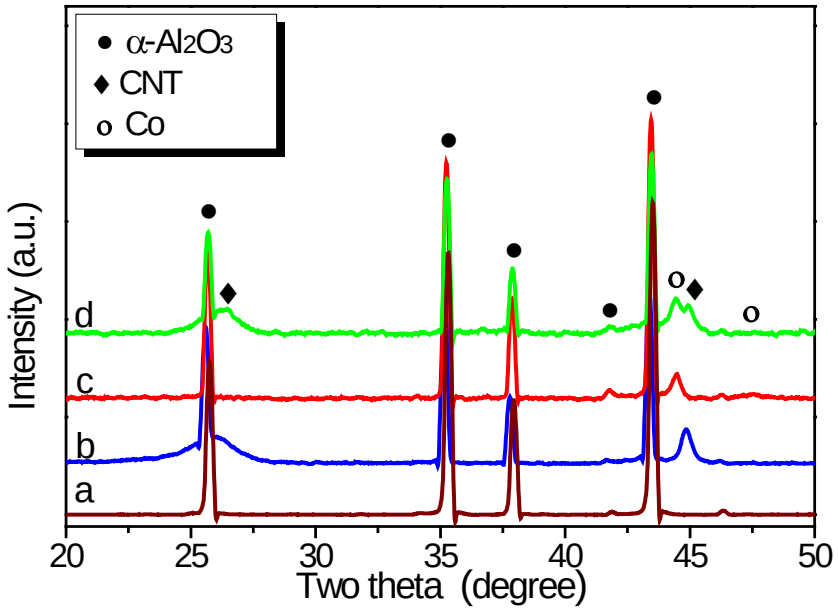

Figure 3-4. XRD patterns of the (a) α-Al_2O_3, (b) CNT-α-Al_2O_3, (c) reduced CoA and (d) reduced CoCNTA catalysts.

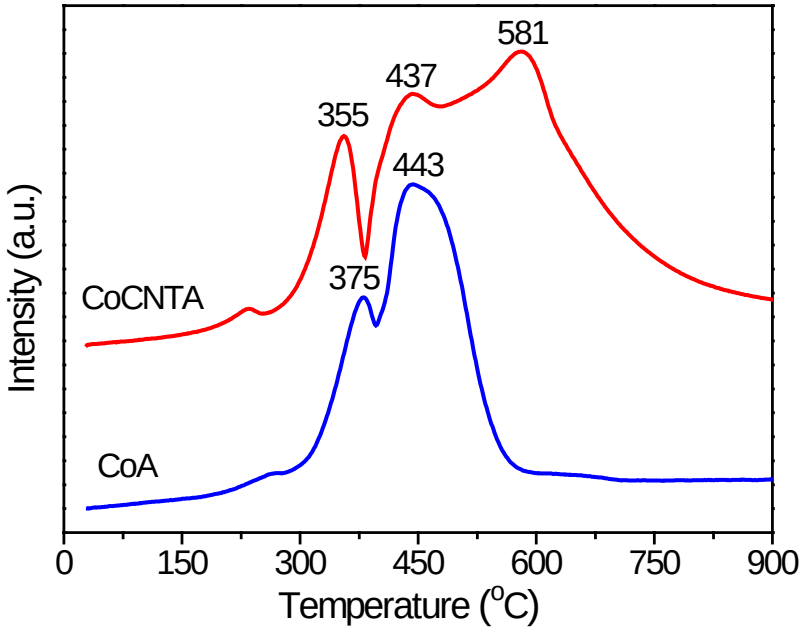

Figure 3-5. TPR spectra of the CoA and CoCNTA catalysts.

The representative TEM images of the CoA and CoCNTA catalysts after reduction under H_2 at 350 °C for 6 h, are presented in Figure 3-6. The condition of cobalt particles dispersion differs very much on the two catalysts: on the CoA catalyst the cobalt phase is present in an aggregate shape (30-40 nm) whereas on the CoCNTA catalyst the cobalt particles are better dispersed with a small cobalt particle size (10-20 nm). However, it is worthy to note that in the CoCNTA catalyst, cobalt particles are both dispersed on the surface of α-Al_2O_3 and the outer surface of the CNTs walls due to the fact that some alumina surface is remain available during the impregnation step. The high-resolution TEM micrograph (Figure 3-6C) indicates that the cobalt particle is almost exclusively deposited on the outer wall of the CNT while no cobalt particles are detected within the nanotube channel. The formation of a thin layer of cobalt oxide, CoO, is observed on the surface of the particle. Such thin oxide layer was expected to be formed during the transfer of the reduced sample in air for analysis. However, it is expected that this cobalt oxide layer will be completely reduced during the activation period under the reactant mixture. Similar results have also been reported in our previous articles.[42-43] Figure 3-6D shows the EDS analysis of deposited cobalt by impregnation method in the CoCNTA sample and confirms that the particles observed are consisted with cobalt active phase but not a residual Co-Fe growth catalyst.

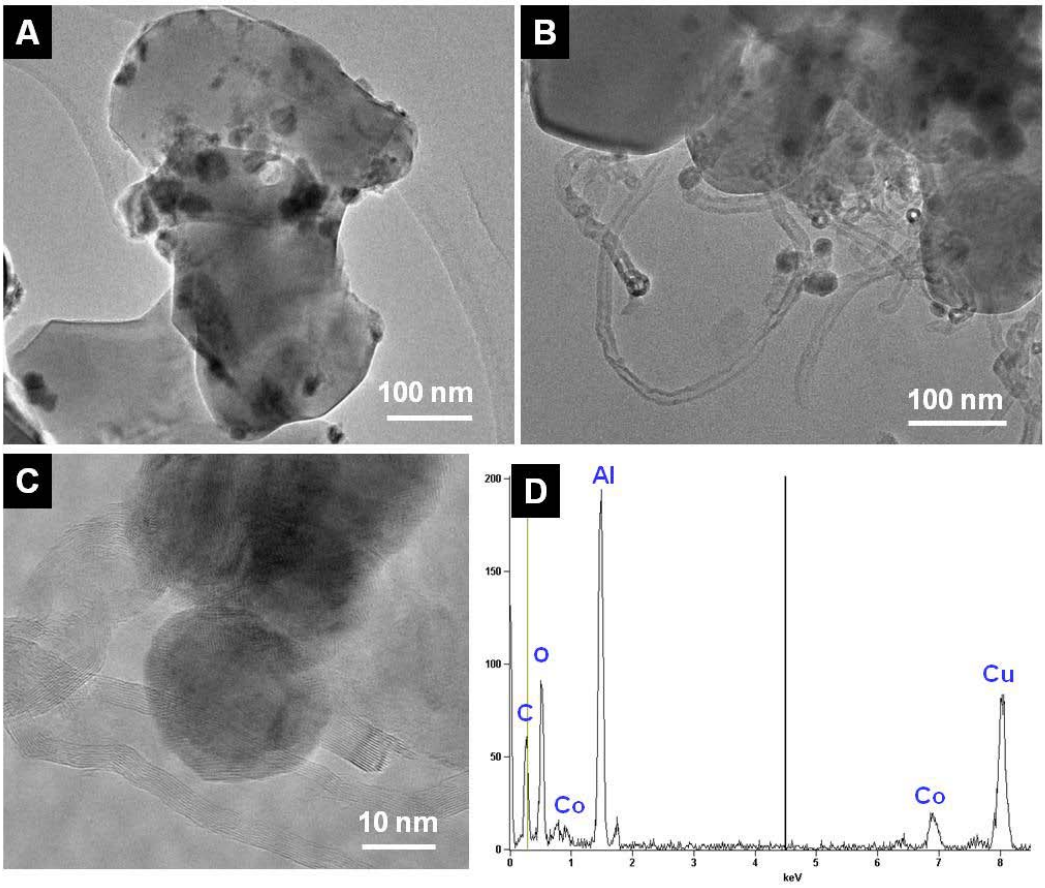

Figure 3-6. Representative TEM tomography of the **(A)** CoA and (**B**) CoCNTA catalyst after reduction under H_2 at 350 °C for 6 h, **(C)** HRTEM image showing the cobalt nanoparticles sited on the CNTs, **(D)** EDS analysis (of the TEM image in B) of the CoCNTA sample.

3.2.3 Fischer-Tropsch synthesis

The FTS catalytic activity and C_{5+} selectivity of the CoA and CoCNTA catalysts as a function of the reaction temperature are presented in Figure 3-7. FTS activity reveals the quasi-steady state after about 2-4 h on both catalysts and no deactivation is observed within the duration of the experiments.[44] A gradual increase of the FTS activity for both catalysts is displayed as a function of reaction temperature, whereas the C_{5+} selectivity remains relatively high at around 89 ± 2 %. The CoCNTA catalyst exhibits a significantly higher FTS activity than the CoA catalyst whatever the reaction temperature. The FTS activity also remains stable for the whole test, i.e. > 120 h, indicating barely deactivation on such catalysts after stabilization.

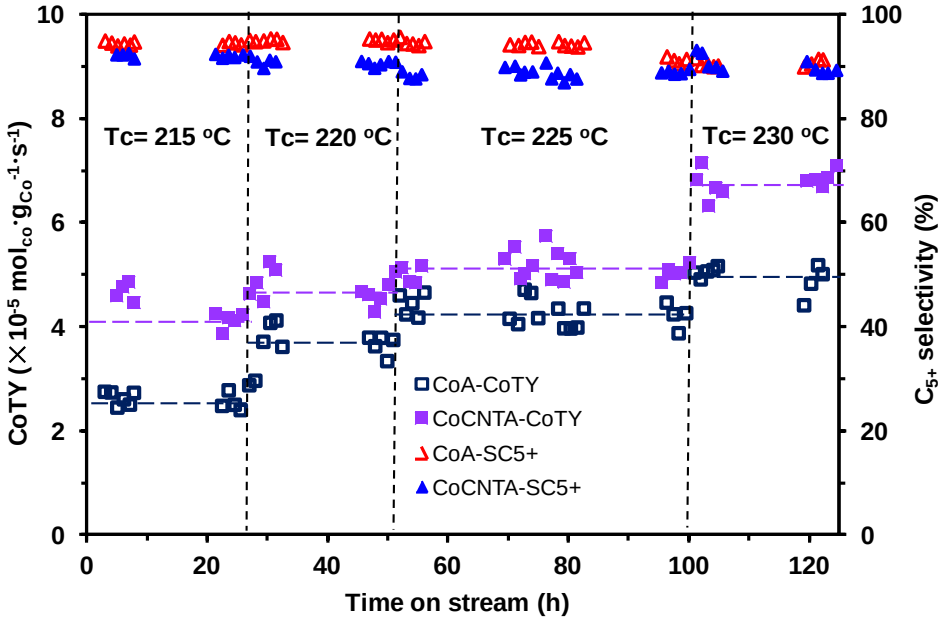

Figure 3-7. FTS activity and C_{5+} selectivity as a function of the reaction temperature on the CoA and CoCNTA catalysts. Reaction conditions: H_2/CO molar ratio = 2, pure syngas, total pressure = 40 bar, GHSV (STP) = 3600 ml·g_{cat}^{-1}·h^{-1}. The catalysts tested have already been evaluated in the FTS reaction at 215 °C during about 80 h on stream (not reported).

The experimental results under steady-state conditions at different temperature over the CoA and CoCNTA catalysts are summarized in Table 3-2. The FTS reaction specific rate and selectivity values reported here correspond to the quasi-steady state behavior. The FTS reaction specific rates are expressed as cobalt time yields (CoTY, mol_{co}·g_{Co}^{-1}·s^{-1}). Over the CoCNTA catalyst, the cobalt time yield at 215 °C reached 4.2 × 10^{-5} mol_{co}·g_{Co}^{-1}·s^{-1}, which was about 60 % higher than that obtained on the CoA catalyst, i.e. 2.6 × 10^{-5} mol_{co}·g_{Co}^{-1}·s^{-1}. The difference of FTS performance slightly decreases when increasing the reaction temperature: the FTS activity on the CoCNTA catalyst is about 40 % at 230 °C higher than that of the CoA catalyst. Such FTS performance could be attributed to the higher cobalt dispersion on the CoCNTA catalyst which leads to higher weight of active sites per active phase and also the higher accessible surface area of the catalyst. The methane selectivity increases a little (from 3.3 to 4.2%) over the CoCNTA catalyst along with a slight decrease of the C_{5+} selectivity from 94.8 to 92.1 % (Table 3-2). The effect of the reaction temperature on methane selectivity was not pronounced either over the α-Al_2O_3-supported catalyst or on the CNTs decorated α-Al_2O_3-supported catalyst. On both catalysts the C_{5+} selectivity

remains superiority at around 89 % regardless of the reaction temperature. Such result is quite surprising compared to the literature results which generally showed relatively low C_{5+} selectivity on the carbon nanotubes-based catalysts.[21, 23] The lower C_{5+} selectivity reported in the literature could be attributed to the densely packed bed when CNTs were used due to their nanoscopic size which induce a large liquid holdup and enhance the problem of reactant diffusion through the liquid film.

Table 3-2. Product distribution on the CoA and CoCNTA catalysts as a function of the reaction temperature. [a]

Catalyst	T(°C)	CO conversion (%)	Product selectivity (%)				CoTY [b] (10^{-5} $mol_{co}\cdot g_{Co}^{-1}\cdot s^{-1}$)
			CO_2	CH_4	C_2-C_4	C_{5+}	
CoA	215	17.7	0	3.3	1.9	94.8	2.6
	220	24.6	0	3.1	1.7	95.2	3.7
	225	29.1	0.1	3.9	2.7	93.3	4.3
	230	33.1	0.1	5.2	3.9	90.8	4.9
CoCNTA	215	28.2	0.1	4.2	3.6	92.1	4.2
	220	31.5	0.1	5.1	4.0	90.8	4.7
	225	34.5	0.2	6.2	4.5	89.1	5.1
	230	45.8	0.3	6.6	3.7	89.4	6.8

[a] Reaction conditions: $H_2/CO = 2$, pure syngas, total pressure = 40 bar, GHSV (STP) = 3600 $ml\cdot g_{cat}^{-1}\cdot h^{-1}$.
[b] Cobalt-Time-Yield (CoTY, molar CO conversion rate per g atom Co per hour)

The high C_{5+} selectivity observed in the present work could be attributed to three main factors: (i) the open structure of the hierarchical catalyst with an evenly distribution of the CNTs on a macroscopic support which provides a high escaping rate of the intermediate products, leading to a thin liquid film layer on the catalyst surface which prevents competitive diffusion of the reactants towards the active sites. In other literature reports, the CNTs were directly packed into the reactor and the nanoscopic size of the support resulted in a dense packed bed which rendered hardly the evacuation of the intermediate liquid products from the catalyst bed. The high liquid retention within the catalyst bed favours the formation

of a H_2-rich environment next to the active site, and as a consequence, to a higher selectivity towards light products, i.e. CH_4 and C_2 to C_4 products; (ii) the high thermal conductivity of the CNTs decorated support significantly enhances the heat transfer among the catalytic bed and reduces the probability of local hot spot formation within the catalyst bed which is detrimental for the C_{5+} selectivity.[34] It is so remarkable to note that the internal reaction temperature measured during reaction is about 1-2 ^{o}C higher than the silicon oil temperature and remains unchanged along the catalyst bed;[43] and (iii) relatively large cobalt particles (> 10 nm) have high potential towards α-olefins re-adsorption and chain initiation which leads to a higher selectivity of heavier molecular weight hydrocarbons, i.e. C_{5+}.[22, 45]

Figure 3-8 illustrate the C_{5+} selectivity as function of the FTS activity, expressed in terms of the cobalt time yield, over the CoA, CoCNTA and other carbon materials and oxide support catalyst. Bezemer et al.[9] studied the influence of the cobalt particle sizes on the FTS reaction using carbon nanofibers as support. The highest CoTY (19.2 $\times 10^{-5}$ $mol_{co} \cdot g_{Co}^{-1} \cdot s^{-1}$) was observed with cobalt particle size centered at about 8 nm under severe reaction conditions, i.e. 35 bar and 250 $^{\circ}$C. However, the large amounts of light products were formed at high temperature. Thus, the C_{5+} selectivity significantly decreased to 74 %. Khodakov and co-workers[20] have reported the CoTY of about 7.0 $\times 10^{-5}$ $mol_{co} \cdot g_{Co}^{-1} \cdot s^{-1}$ on the cobalt supported on carbon nanotubes catalysts with a similar cobalt loading. The catalyst also exhibited a relatively stable FTS activity for a short evaluation test lasted for about 10 h. However, such catalyst is a powder form however it would be hampered in a fixed-bed by a large pressure drop across the catalyst bed according to the results reported elsewhere.[35, 46]. Trépanier et al.[21] have investigated the Co, Ru and K loading effects on the FTS performance of CNTs supported cobalt catalyst. They found that the FTS specific rate was just around 3.88 $\times 10^{-5}$ $mol_{co} g_{Co}^{-1} s^{-1}$ with 15 wt. % of cobalt loading at 220 ^{o}C. The higher FTS specific rate and C_{5+} selectivity was obtained when 0.5 wt. % Ru was introduced by enhancing the reducibility of cobalt surface atoms and availability of the active sites. The special method named micromulsion technique was also used by Delai group[22] to obtained highly dispersed cobalt active sites with the FTS specific rate of 4.2 $\times 10^{-5}$ $mol_{co} g_{Co}^{-1} s^{-1}$ and a C_{5+} selectivity of 92.5%. The α-Al_2O_3 supported catalyst displays medium FTS activity with relativity higher C_{5+} selectivity comparing to those of other supported catalysts.[19] Besides, the reports in the literature evidence that generally carbon nanotubes supported catalyst provides higher cobalt time yield with lower C_{5+} selectivity or lower cobalt time yield with higher C_{5+} selectivity. Here in this work, it is interesting to note that the FTS catalytic

performance of the CNTs-α-Al_2O_3 supported cobalt catalyst displays both high FTS activity and C_{5+} selectivity than other carbon nanotubes-based catalysts. The bench-marking figure highlights the fact that the Co- supported on a CNTs decorated alumina catalyst exhibits a highest FTS activity, expressed in terms of the cobalt time yield, along with a highest C_{5+} selectivity.

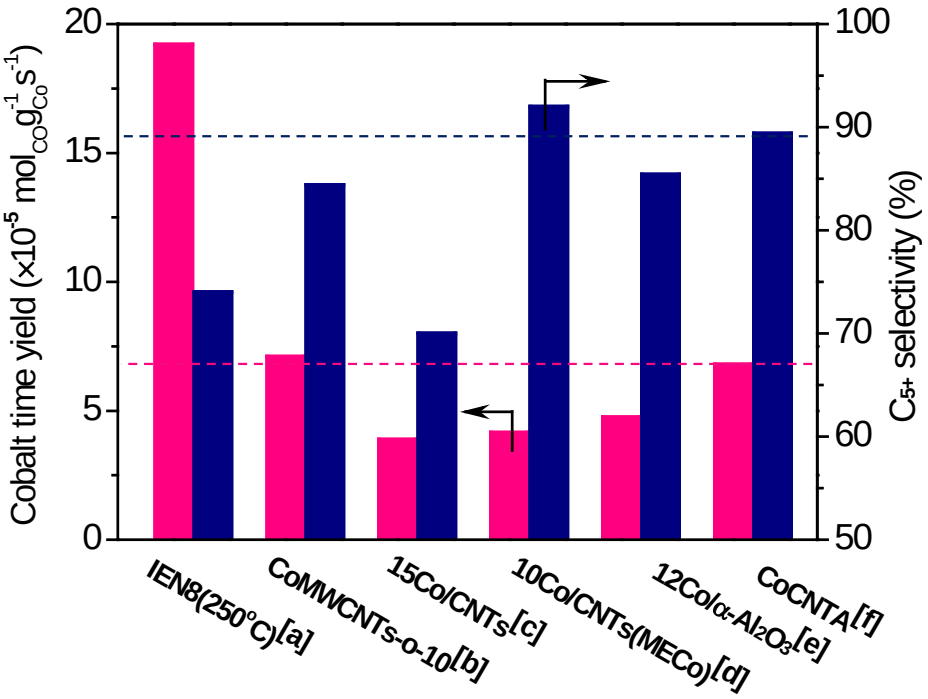

Figure 3-8. Comparison of FTS catalytic performance over different catalysts reported in literatures. [a] Data from ref. [9], reaction conditions: P = 35 bar, H_2/CO = 2, 0.25 g of catalyst. [b] Data from ref.[20], reaction conditions: P = 20 bar, T = 220 ^oC, 10 wt% of cobalt, 0.1 g of catalyst, GHSV = 5000 $ml \cdot g^{-1} \cdot h^{-1}$, H_2/CO = 2, t = 1200 min. [c] Data from ref.[21], reaction conditions: P = 20 bar, T= 220 ^oC, H_2/CO = 2, 15 wt% of cobalt, 1 g of catalyst, Flow rate = 60 $ml \cdot min^{-1}$. [d] Data from ref.[22], reaction conditions: P = 20 bar, T= 220 ^oC, H_2/CO = 2, 10 wt% of cobalt, Flow rate = 30 ml/min. [e] Data from ref.[19], reaction conditions: P = 20 bar, H_2/CO = 2.1, 12% of cobalt, 1.7 g of catalyst. [f] Data from this work, reaction conditions: P = 40 bar, T = 230 ^oC, H_2/CO = 2, GHSV = 3600 $ml \cdot g_{cat}^{-1} \cdot h^{-1}$, 10 wt% of cobalt, 5 g of catalyst.

The selectivity of various hydrocarbons (HCs) and chain growth factor (α) from the linear portion of the HCs over CoA and CoCNTA catalysts are shown in Figure 3-9. The product selectivity of HCs is obtained from mass balance after test and by analyzing the wax

phase products. Normally, higher coverage of olefin on the catalyst surface is an obstacle for CO adsorption, possibly resulting in a lower conversion.[47] The CoCNTA has a higher activity than the CoA catalyst, which is also consistent with the presence of higher olefin concentration inside the liquid phase of CoA catalyst (Figure 3-9A and C). The chain growth factor (α) determined on both catalysts is presented in Figure 3-9B and D. According to the results one can state that the chain growth factor (α) is relatively high for both catalysts, i.e. 0.915 for α-Al_2O_3 supported catalyst and 0.913 for CNTs decorated α-Al_2O_3 support catalyst, which is in accordance with the relatively high C_{5+} selectivity obtained on both catalysts. It is interesting that the introduction of the CNTs on the surface of the α-Al_2O_3 performs no significant influence on the hydrocarbon chain growth. The high α-value observed in the present work ought to be ascribed from the high porosity of both supports which favor the diffusion of the reactant towards the active site.[19, 48] For the relativity low methane selectivity (Table 3-2), it is believed that part of -CH_2- is consumed in the additional chain growth initiated by re-adsorption of olefin and the incorporation of hydroxyl to the -CH_2- and metal bond.[19, 47] It is very clear from the distribution figure of HCs (Figure 3-9A and C) that the most amount of olefin molar fraction is low-carbon-number HCs. From this information, it can be deduced that lower-carbon-number alkenes are reabsorbed onto the active site to initiate a new chain growth reaction by consuming -CH_2-, resulting in an enhanced molar fraction of olefins with higher carbon number. Simultaneously, -CH_2- groups are rapidly consumed by chain growth propagation to form longer carbon chain olefins, as a result of an increased heavier olefin selectivity and decreased methane selectivity with temperature increased, exhibiting much slightly enlarged chain growth probability. Moreover, Holmen and coworkers[19] also found that there is no direct relationship between the cobalt metal dispersion and the C_{5+} selectivity for the Al_2O_3-supported catalyst.

The carbon materials-supported Co catalysts deactivated rapidly as the CO conversion higher than medium conversion level (> 40 %).[34, 49] Catalyst with better activity commonly leads to more rapid deactivation in the first few days' test.[50-51] A better stability in more than 100 h time on stream on the FTS using Fe-Ru bimetallic or Fe supported on CNTs were obtained by Bahome et al.[26-27] However, Dalai and co-workers[29-30] reported that Fe-based catalysts supported CNTs show different deactivation after 120 h stability tests as a function of the structure of CNTs and the position of metal sites. More unfortunately, the commercial oxides supports, i.e. SiO_2 and γ-Al_2O_3, show a poor FTS stability.[8, 14]

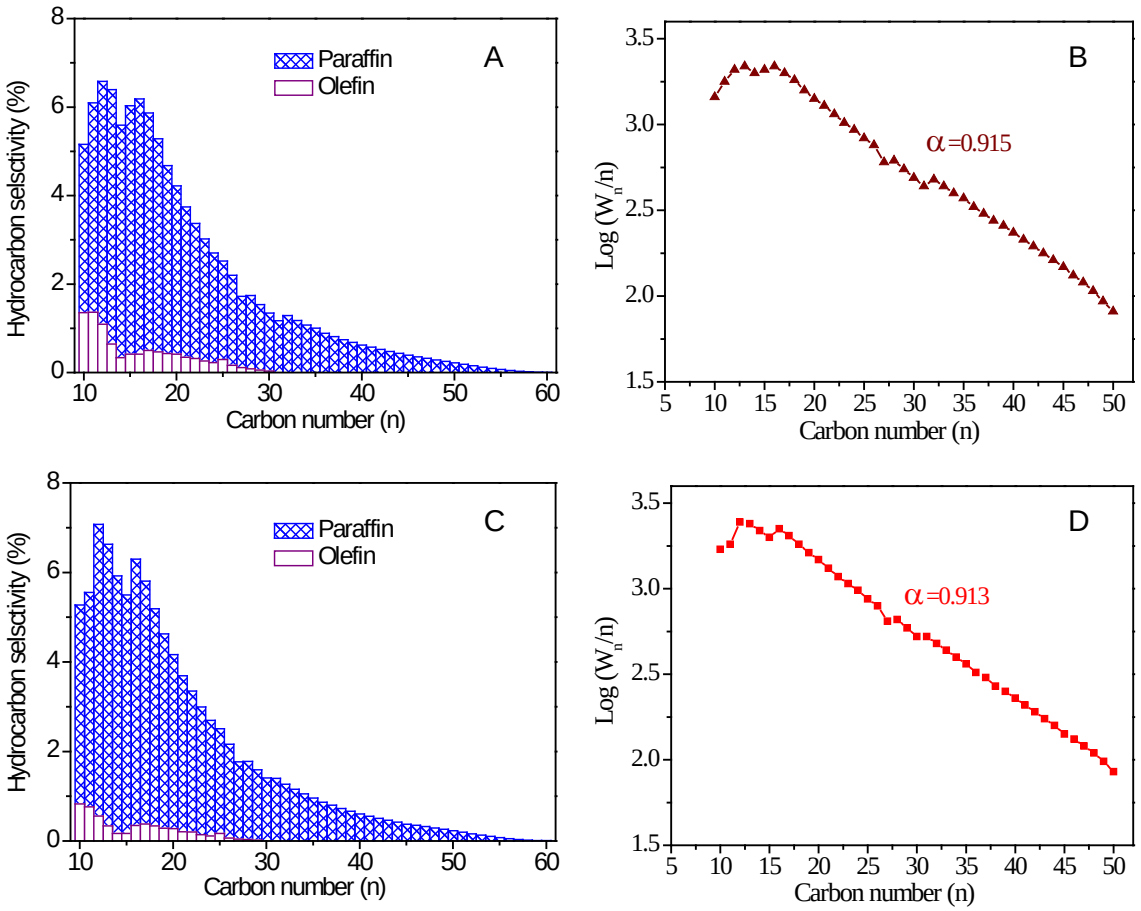

Figure 3-9. Hydrocarbon distributions and chain growth factor (α) from the linear portion of the hydrocarbons over CoA (A, B) and CoCNTA (C, D) catalysts.

The long-term stability of the CoCNTA catalyst is evaluated under relative severe reaction conditions, i.e. high reaction temperature and high space velocity, as presented in Figure 3-10. The tested catalyst has already been run for more than 150 h under different reaction conditions before. According to the results presented in Figure 3-10, CoCNTA catalyst exhibits nearly constant performances during the 100 h on stream, and even no significant deactivation was observed during 250 h for a total test under different reaction conditions. Park et al.[52] reported the FTS deactivation at 220 ^{o}C for the different cobalt size in the range of 4.8 nm to 17.5 nm on γ-Al_2O_3 catalysts. The deactivation of small particles was due to the sintering and oxidization by H_2O formed during the course of the reaction.[34, 52-53] Storsæter et al.[8] showed that the reaction rate dropped about 20 % compared to the initial reaction rate over CoRe/γ-Al_2O_3 catalyst as a result of the reduced partial pressure of H_2 and CO inside the catalyst bed, and to the formation of agglomeration from smaller cobalt particles. On the CoCNTA catalyst, almost no deactivation is observed over the catalyst up

to 100 h on stream at 230 °C, indicating that deactivation linked with cobalt surface oxidation or sintering is unlikely to occur under the reaction conditions used in the present work.

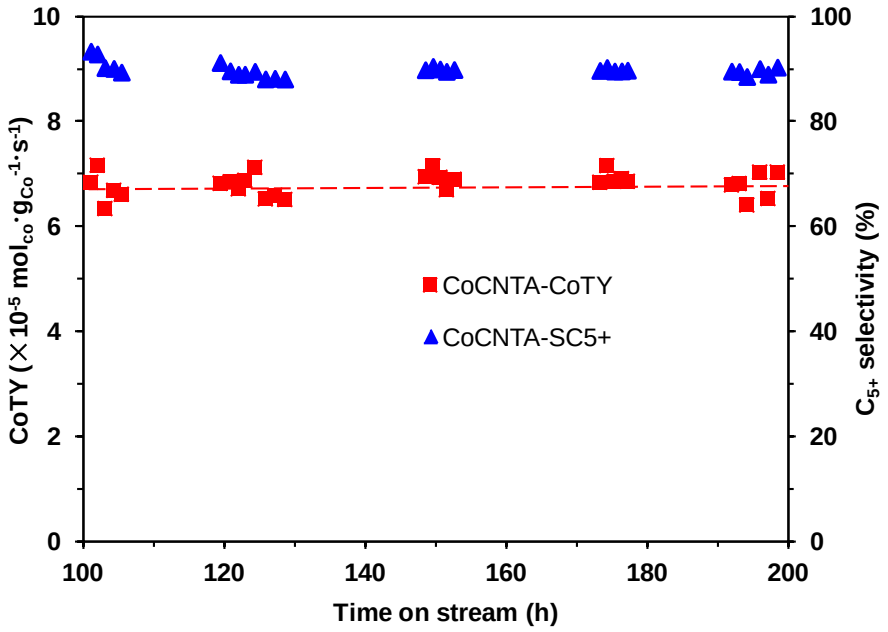

Figure 3-10. FTS performance and stability of the CoCNTA catalyst as a function of time on stream at 230 °C. Reaction conditions: H_2/CO molar ratio = 2, pure syngas, total pressure = 40 bar, GHSV (STP) = 3600 $ml \cdot g_{cat}^{-1} \cdot h^{-1}$.

TEM analysis was also performed on the spent catalyst, covered with solid waxes, in order to check the evolution of the active phase particle size after a long-term test, and the results are presented in Figure 3-11. According to the low magnification TEM micrograph (Figure 3-11A) some small cobalt particles were sintered during the course of the catalytic tests (indicated by arrows) while a large part of the cobalt particles remains small at around 20 nm which explains the relatively high stability of the catalyst as a function of the FTS test. High-resolution TEM micrograph (Figure 3-11B) shows the catalyst area where some small cobalt particles are still present along with some aggregation between small cobalt particles due to the sintering (indicated by arrow).

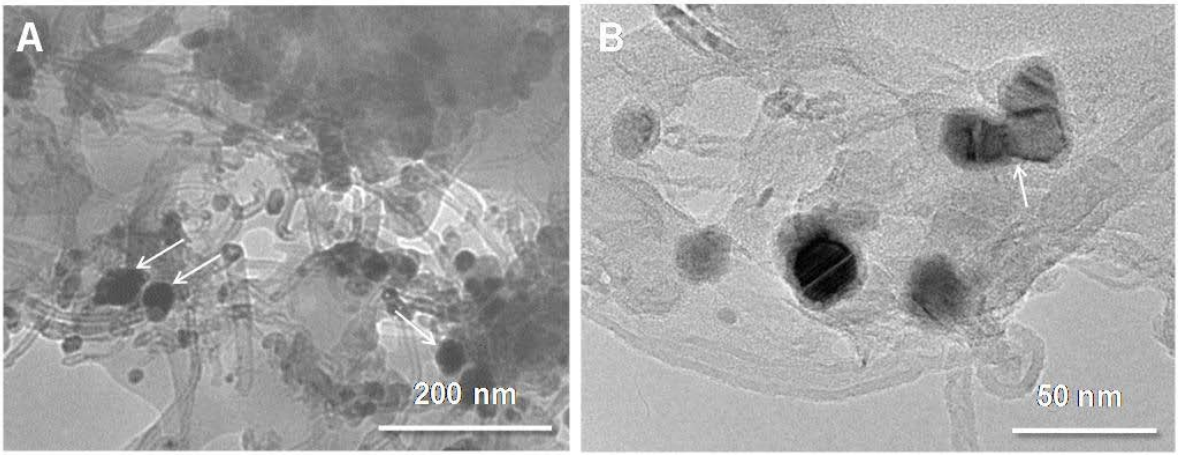

Figure 3-11. TEM micrographs of the CoCNTA catalyst after 250 h of FTS test. The catalyst was covered with solid waxes.

3.4 Conclusion

In summary, we have succeeded in preparing a hierarchical support consisting of a macroscopic shape α-Al_2O_3 homogeneously covered by a layer of carbon nanotubes with high specific surface area (76 $m^2 \cdot g^{-1}$) and fully accessible effective surface due to their nanoscopic size and the complete absence of single entrance pore like for traditional supports. This hierarchical support displayed a high interaction with the deposited cobalt phase leading to the formation of small cobalt particles in the range of 10 to 20 nm. On the other hand, the nanoscopic size of the carbon nanotubes provided short diffusion pathway for the reactant to get access to the active site during the Fischer-Tropsch synthesis process. The introduction of a layer of 1D carbon led to a significant improvement of the FTS activity compared to that of the pristine alumina-based catalyst. The improvement of the FTS activity was attributed to the high accessibility of the composite surface area compared to the macroscopic host structure alone, or to the bulk carbon nanotubes, where the nanoscopic dimension induced a dense packing with low mass transfer which favour the problem of competitive diffusion of the reactants towards the active site. The cobalt supported on CNTs decorated alumina catalyst also exhibits an extremely high stability during the long-term test under high reaction temperature and high space velocity compared to other carbon nanotubes-based catalysts reported in the literature.

Optimization study will be performed in order to anchor a higher amount of cobalt nanoparticles on the carbon nanotubes surface along with the reduction of these metal nanoparticles on the alumina surface with lower FTS activity by either increasing the CNTs

loading or by modifying the impregnation method, i.e. ion exchange method instead of incipient wetness impregnation method. Such hierarchical composite with high effective surface area and macroscopic shape could also be further employed as catalyst support in other reactions where high mass and heat transfer are encountered, i.e. selective oxidation or hydrogenation.

3.5 References

[1] J. R. Rostrup-Nielsen, *Science* **2005**, *308*, 1421-1422.

[2] G. M. Whitesides, G. W. Crabtree, *Science* **2007**, *315*, 796-798.

[3] A. Y. Khodakov, W. Chu, P. Fongarland, *Chem Rev* **2007**, *107*, 1692-1744.

[4] Q. Zhang, J. Kang, Y. Wang, *ChemCatChem* **2010**, *2*, 1030-1058.

[5] E. Iglesia, *Appl Catal a-Gen* **1997**, *161*, 59-78.

[6] E. Iglesia, *Stud Surf Sci Catal* **1997**, *107*, 153-162.

[7] E. Iglesia, S. L. Soled, R. A. Fiato, *J Catal* **1992**, *137*, 212-224.

[8] S. Storsaeter, B. Totdal, J. C. Walmsley, B. S. Tanem, A. Holmen, *J Catal* **2005**, *236*, 139-152.

[9] G. L. Bezemer, J. H. Bitter, H. P. C. E. Kuipers, H. Oosterbeek, J. E. Holewijn, X. D. Xu, F. Kapteijn, A. J. van Dillen, K. P. de Jong, *J Am Chem Soc* **2006**, *128*, 3956-3964.

[10] J. P. den Breejen, P. B. Radstake, G. L. Bezemer, J. H. Bitter, V. Froseth, A. Holmen, K. P. de Jong, *J Am Chem Soc* **2009**, *131*, 7197-7203.

[11] H. F. Xiong, Y. H. Zhang, S. G. Wang, J. L. Li, *Catal Commun* **2005**, *6*, 512-516.

[12] A. Y. Khodakov, *Catal Today* **2009**, *144*, 251-257.

[13] R. Oukaci, A. H. Singleton, J. G. Goodwin, *Appl Catal a-Gen* **1999**, *186*, 129-144.

[14] S. Storsaeter, O. Borg, E. A. Blekkan, B. Totdal, A. Holmen, *Catal Today* **2005**, *100*, 343-347.

[15] A. Y. Khodakov, A. Griboval-Constant, R. Bechara, V. L. Zholobenko, *J Catal* **2002**, *206*, 230-241.

[16] A. Y. Khodakov, R. Bechara, A. Griboval-Constant, *Appl Catal a-Gen* **2003**, *254*, 273-288.

[17] E. Rytter, S. Eri, T. H. Skagseth, D. Schanke, E. Bergene, R. Myrstad, A. Lindvag, *Ind Eng Chem Res* **2007**, *46*, 9032-9036.

[18] O. Borg, P. D. C. Dietzel, A. I. Spjelkavik, E. Z. Tveten, J. C. Walmsley, S. Diplas, S. Eri, A. Holmen, E. Ryttera, *J Catal* **2008**, *259*, 161-164.

[19] S. Rane, O. Borg, J. Yang, E. Rytter, A. Holmen, *Appl Catal a-Gen* **2010**, *388*, 160-167.

[20] H. Zhang, C. Lancelot, W. Chu, J. P. Hong, A. Y. Khodakov, P. A. Chernavskii, J. Zheng, D. G. Tong, *J Mater Chem* **2009**, *19*, 9241-9249.

[21] M. Trepanier, A. Tavasoli, A. K. Dalai, N. Abatzoglou, *Appl Catal a-Gen* **2009**, *353*, 193-202.

[22] M. Trepanier, A. K. Dalai, N. Abatzoglou, *Appl Catal a-Gen* **2010**, *374*, 79-86.

[23] J. Lv, X. B. Ma, S. L. Bai, C. D. Huang, Z. H. Li, J. L. Gong, *Int J Hydrogen Energ* **2011**, *36*, 8365-8372.

[24] A. Tavasoli, R. M. M. Abbaslou, M. Trepanier, A. K. Dalai, *Appl Catal a-Gen* **2008**, *345*, 134-142.

[25] L. Guczi, G. Stefler, O. Geszti, Z. Koppany, Z. Konya, E. Molnar, M. Urban, I. Kiricsi, *J Catal* **2006**, *244*, 24-32.

[26] M. C. Bahome, L. L. Jewell, D. Hildebrandt, D. Glasser, N. J. Coville, *Appl Catal a-Gen* **2005**, *287*, 60-67.

[27] M. C. Bahome, L. L. Jewell, K. Padayachy, D. Hildebrandt, D. Glasser, A. K. Datye, N. J. Coville, *Appl Catal a-Gen* **2007**, *328*, 243-251.

[28] W. Chen, Z. L. Fan, X. L. Pan, X. H. Bao, *J Am Chem Soc* **2008**, *130*, 9414-9419.

[29] R. M. M. Abbaslou, A. Tavasoli, A. K. Dalai, *Appl Catal a-Gen* **2009**, *355*, 33-41.

[30] R. M. M. Abbaslou, J. Soltan, A. K. Dalai, *Appl Catal a-Gen* **2010**, *379*, 129-134.

[31] H. J. Schulte, B. Graf, W. Xia, M. Muhler, *ChemCatChem* **2012**, *4*, 350-355.

[32] A. Tavasoli, M. Trepanier, A. K. Dalai, N. Abatzoglou, *J Chem Eng Data* **2010**, *55*, 2757-2763.

[33] H. F. Xiong, M. A. M. Motchelaho, M. Moyo, L. L. Jewell, N. J. Coville, *J Catal* **2011**, *278*, 26-40.

[34] S. Zarubova, S. Rane, J. Yang, Y. D. Yu, Y. Zhu, D. Chen, A. Holmen, *Chemsuschem* **2011**, *4*, 935-942.

[35] Y. F. Liu, L. D. Nguyen, T. Truong-Huu, Y. Liu, T. Romero, I. Janowska, D. Begin, C. Pham-Huu, *Mater Lett* **2012**, *79*, 128-131.

[36] B. Louis, G. Gulino, R. Vieira, J. Amadou, T. Dintzer, S. Galvagno, G. Centi, M. J. Ledoux, C. Pham-Huu, *Catal Today* **2005**, *102*, 23-28.

[37] G. Gulino, R. Vieira, J. Amadou, P. Nguyen, M. J. Ledoux, S. Galvagno, G. Centi, C. Pham-Huu, *Appl Catal a-Gen* **2005**, *279*, 89-97.

[38] P. Nguyen, C. Pham, B. de Tymowski, C. Pham-Huu, F. Luck, in *France Patent 11-01704, Vol. 11-01704*, France Patent ed., France, **2011**.

[39] O. Borg, S. Erib, E. A. Blekkan, S. Storsaeter, H. Wigum, E. Rytter, A. Holmen, *J Catal* **2007**, *248*, 89-100.

[40] A. Lapidus, A. Krylova, V. Kazanskii, V. Borovkov, A. Zaitsev, J. Rathousky, A. Zukal, M. Jancalkova, *Appl Catal* **1991**, *73*, 65-82.

[41] O. Borg, M. Ronning, S. Storsaeter, W. van Beek, A. Holmen, *Fischer-Tropsch Synthesis, Catalysts and Catalysis* **2006**, *163*, 255-272.

[42] M. Lacroix, L. Dreibine, B. de Tymowski, F. Vigneron, D. Edouard, D. Begin, P. Nguyen, C. Pham, S. Savin-Poncet, F. Luck, M. J. Ledoux, C. Pharn-Huu, *Appl Catal a-Gen* **2011**, *397*, 62-72.

[43] B. de Tymowski, Y. F. Liu, C. Meny, C. Lefevre, D. Begin, P. Nguyen, C. Pham, D. Edouard, F. Luck, C. Pham-Huu, *Appl Catal a-Gen* **2012**, *419*, 31-40.

[44] J. P. Hong, W. Chu, P. A. Chernavskii, A. Y. Khodakov, *J Catal* **2010**, *273*, 9-17.

[45] R. J. Madon, E. Iglesia, *J Catal* **1993**, *139*, 576-590.

[46] R. Philippe, M. Lacroix, L. Dreibine, C. Pham-Huu, D. Edouard, S. Savin, F. Luck, D. Schweich, *Catal Today* **2009**, *147*, S305-S312.

[47] X. J. Zhang, Y. Liu, G. Q. Liu, K. Tao, Q. Jin, F. Z. Meng, D. Wang, N. Tsubaki, *Fuel* **2012**, *92*, 122-129.

[48] A. Martinez, G. Prieto, J. Rollan, *J Catal* **2009**, *263*, 292-305.

[49] Z. X. Yu, O. Borg, D. Chen, E. Rytter, A. Holmen, *Top Catal* **2007**, *45*, 69-74.

[50] T. K. Das, G. Jacobs, P. M. Patterson, W. A. Conner, J. L. Li, B. H. Davis, *Fuel* **2003**, *82*, 805-815.

[51] O. Borg, N. Hammer, S. Eri, O. A. Lindvag, R. Myrstad, E. A. Blekkan, M. Ronning, E. Rytter, A. Holmen, *Catal Today* **2009**, *142*, 70-77.

[52] J. Y. Park, Y. J. Lee, P. R. Karandikar, K. W. Jun, K. S. Ha, H. G. Park, *Appl Catal a-Gen* **2012**, *411*, 15-23.

[53] N. E. Tsakoumis, M. Ronning, O. Borg, E. Rytter, A. Holmen, *Catal Today* **2010**, *154*, 162-182.

[Part-B] Efficient hierarchical structured composite containing cobalt catalyst for clean synthetic fuel production

3.6 Introduction

The demands for energy and goods go upward sharply during the last decades due to the fast industrial growth of the emergent countries like China and India and also to the increase of the world population, while the oil reserves is decreasing and their production rate is close to reaching its maximum before facing a decline.[1-2] Thus, sustainable and environment friendly energy production and consumption is one of key challenges of this ongoing century. The new developments of promoting low-CO_2 footprint technologies need to consider the alternative feedstock, such as natural gas, charcoal and biomass.[3-4] It is worthy to note that no pressure will come from natural gas and coal in the near future as large resources of these raw materials still exist. The synthesis gas ($CO + nH_2$) generated by the steam reforming of natural gas or gasification of coal and biomass will be further processed via the Fischer-Tropsch reaction which has been firstly developed in the early of 1920s by Franz Fischer and Hans Tropsch[5-6] and has received an over increasing scientific and industrial interest during the last decades.[7-10] The Fischer-Tropsch synthesis (FTS) is a key technology in the more global X-To-Liquids (XTL) processes which allow the transformation of synthesis gas ($2H_2$+CO) into liquid hydrocarbons following by a hydrocracking of the heavy fraction into useful compounds such as naphtha, diesel, jet fuel and lubricants.[11-13]

Supported catalyst plays an important role in the FTS process. The development of active, selective and stable catalysts remains one of the main challenges in the FTS process.[7, 13-14] According to earlier studies, the activity and selectivity are also influenced by the support physical properties like specific surface area, pore volume and pore size distribution in addition to the support material itself.[15-16] The nature of the support plays a crucial role on the properties of the final Fischer-Tropsch catalyst; indeed, the activity is indirectly affected by the support nature. Moreover, at conditions favoring chain-growth, site-time yields and stability on supported cobalt catalysts are traditionally considered to be independent of cobalt dispersion and support identity.[17-21] Indeed, the FTS is one of the

most complex three-phase reaction, regarding the highly exothermic reaction and various reactions taking place during the gas-to-liquids transformation. The selectivity of long chain hydrocarbons (C_{5+}) depends significantly on the reactor temperature profile, the selection for appropriate catalysts and carriers should obey several roles: good thermal conductivity of the support;[22] low pressure drop along the catalyst bed;[23-24]effective utilization of all active sites presented in the catalyst, along with the appropriate structure of the support that favors the evacuation of the products and high accessibility to the reactants.[23] Thus, it is of interest to develop new type of carbon-based support with high accessibility and good thermal conductivity in the highly exothermal Fischer-Tropsch synthesis. Chin et al.[25] explored the FeCrAlY foam covered with aligned multiwall carbon nanotube arrays as microchannel support containing Co-Re active sites for FTS. The catalyst with such structure, especially resulting from the hierarchical CNT, provided larger surface area for anchoring active sites, high thermal conductivity and enhances mass transfer by the larger interstitials. Many studies have also demonstrated that the growth of carbon nanotubes/nanofibers on the macroporous host structure could provide efficient contact between active sites and reactants, improving thermal conductivity along with better mass transfer throughout the catalyst body.[26-29] The carbon nanofibers were for the first time grown onto carbon synthesized by Zarubova et al.[28] using the method of chemical vapor deposition (CVD) leading to the formation of carbon composite support with high BET surface area (> 280 m^2/g) and unique hierarchical structure. The cobalt supported on this structured composite (Co/FB-CNF/ carbon-felt) shows a very uniform reaction temperature during the FTS reaction.[28]

We have previously found that thermal conductive support (β-SiC) matrix doped with TiO_2 exhibits a medium metal-support interaction with the cobalt nanoparticles and lead to the formation of small cobalt particles with enhanced FTS activity compared to the same catalyst supported on the undoped SiC support.[30] It is expected that the TiO_2 phase not only participate in the increase of the cobalt dispersion,[30-32] but also interact with the active phase nanoparticles to prevent the particles mobility and thus, deactivation by sintering during FTS test.[33-34] However, to date there has no reports on the utilization of TiO_2 promoted hierarchically-structured composite for the FTS reaction. Herein, we reports on a facile preparation way to synthesis hierarchically-structured composited containing TiO_2 coated on the multi-walled carbon nanotubes (CNT) anchoring on a macroscopic host structure of α-Al_2O_3 acting as support for cobalt-based catalysts in the FTS. The catalyst

exhibits a relatively high FTS activity along with a high selectivity towards long chain hydrocarbons and also displays an extremely high resistance towards deactivation.

3.7 Results and discussion

3.7.1 Synthesis of CNTs on the α-Al_2O_3

The carbon nanotubes (CNTs) were synthesized by a chemical vapour deposition (CVD) method. The α-Al_2O_3 host matrix was previously decorated with a small amount of iron and/or cobalt catalyst which will play a role of growth catalyst. The CNTs growth process was carried out in a fixed-bed reactor with a mixture of ethane and hydrogen. The SEM micrographs of the α-Al_2O_3 loaded with different weight of CNTs are presented in Figure 3-12 A-E. The yield of CNTs on the alumina host matrix is confirmed by the thermogravimetric analysis (Figure 3-12 F). The results indicate that the α-Al_2O_3 surface was not completely covered by the CNTs network when the CNTs yield is below 26 wt. %. As it can be seen, the α-Al_2O_3 composite with CNTs loading of 73 wt. % (Table 3-3) is constituted by a thin shell of a homogeneous, highly entangled, and structure-opened carbon nanotubes network that exhibits fully accessibility and relatively high specific surface area of 76 $m^2 \cdot g^{-1}$.

Table 3-3. Synthesis conditions and physical characteristics of the CNTs decorated α-Al_2O_3 composites with various CNT loading.

Sample	Catalyst	Syn. temp. (^oC)	Yield (%)	Surface area ($m^2 \cdot g^{-1}$)	Total pore volume ($cm^3 \cdot g^{-1}$)	BJH pore diameter (nm)
A	-	-	-	5	0.011	17.7
B	2 wt.% Co	750	4	11.1	0.053	24.8
C	2 wt.% Fe	750	12	18.4	0.051	10.3
D	4 wt.% Fe	750	26	27.0	0.106	15.6
E	2 wt.% Co+ 2 wt.% Fe	750	73	76	0.199	10.5

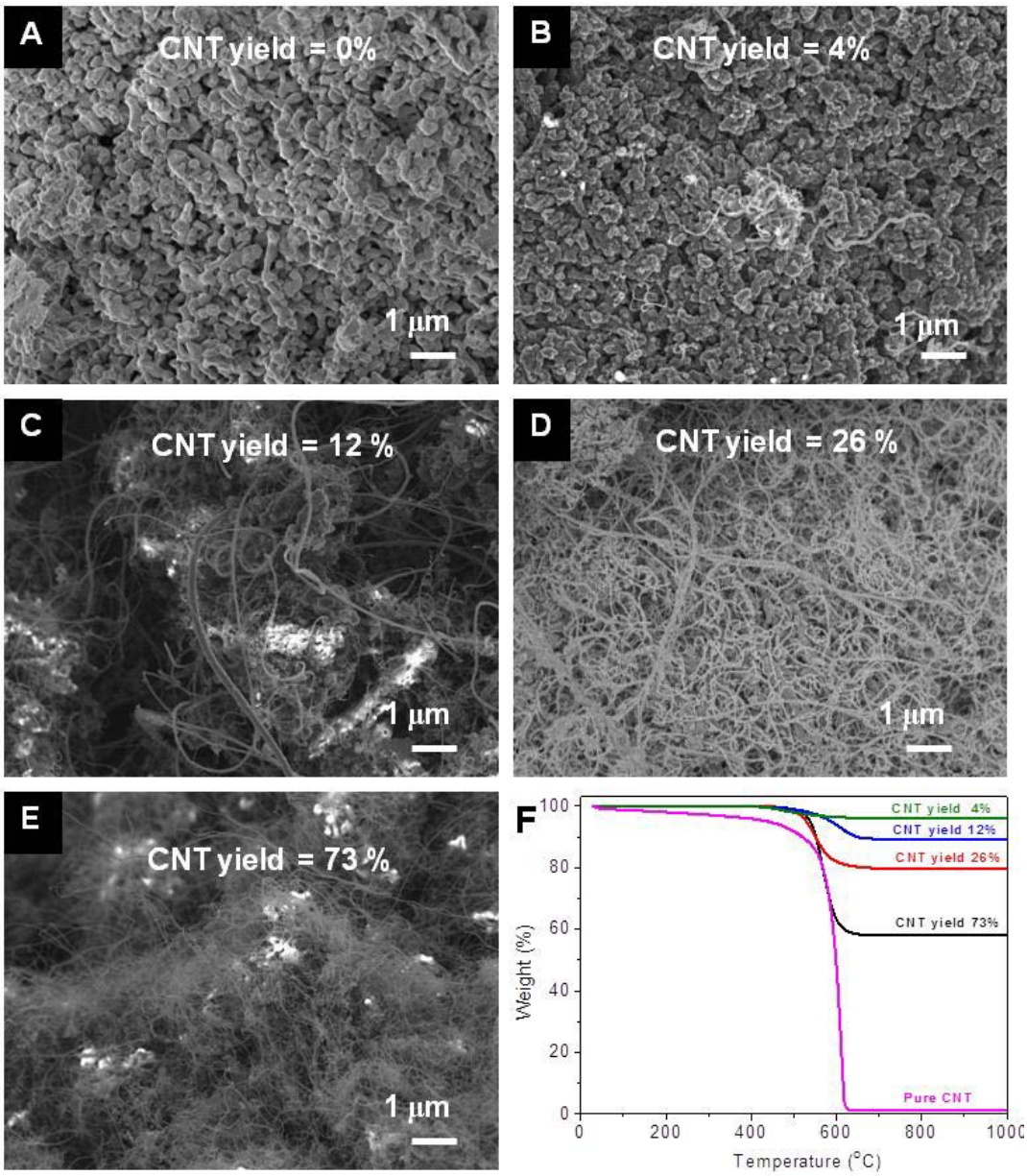

Figure 3-12. SEM micrographs of α-Al_2O_3 and different CNT mass loading on its surface (**A-E**), and corresponding TG curves (**F**).

The corresponding N_2 adsorption-desorption data is listed in Table 3-3. The results show that the BET surface area increases as a function of the CNTs yield. We also found remarkable growth rate of the CNTs on the Co-Fe alloy (2 wt. % Co + 2 wt. % Fe). The CNTs growth rate over this catalyst is almost three times higher than that obtained on the 4 wt. % Fe. The surface area of pure α-Al_2O_3 was only only amounted to about 5 $m^2 \cdot g^{-1}$, and thus it is expected that the CNTs (CNTs surface area is about 189 $m^2 \cdot g^{-1}$ after purification[35]) is the primary contributor to the overall surface area of the final composite. Thus, for the 12 wt. % CNTs yield the surface area associates with the CNTs can be estimated to be 0.11 ×

189 = 20 $m^2 \cdot g^{-1}$, which generally matches the measured value (18.4 $m^2 \cdot g^{-1}$). Similarly, the theoretical value of surface area should be 79.8 $m^2 \cdot g^{-1}$ with 73 wt. % CNTs yield. The difference between the real and estimated specific surface area of the CNTs decorated α-Al_2O_3 composites should be resulted from the closed caps on the synthesised composite, whilst most of them should be opened in the purified CNT during acid treatment.[36]

3.7.2 Preparation of hierarchically-structured TiO_2-CNT-α-Al_2O_3 composites

In our previous work (Part A), the cobalt based catalyst supported on hierarchically-structured material was introduced in the FTS reaction. The higher catalytic activity along with an extremely high selectivity towards liquid hydrocarbons can be obtained compared to the pristine α-Al_2O_3 or traditional CNTs supported cobalt catalysts.[29] In this study, the CNT with 73 wt. % yield, issued from the Co-Fe (2 wt% Co+2 wt% Fe) catalyst is applied as the support for synthesizing the TiO_2 based catalyst. The N_2 adsorption-desorption results are detailed in Figure 3-13 and Table 3-4. The specific surface area of alumina undergoes huge increase after the introduction of CNTs as mentioned above, from 5 $m^2 \cdot g^{-1}$ for α-Al_2O_3 to 76 $m^2 \cdot g^{-1}$ for CNTs-α-Al_2O_3 composite. The titanium addition caused a slight change of the surface area and pore diameter, i.e. 72 $m^2 \cdot g^{-1}$ and 15 nm for TiO_2/CNT-α-Al_2O_3 instead of 76 $m^2 \cdot g^{-1}$ and 11 nm for CNT-α-Al_2O_3, respectively (Table 3-4).

Table 3-4 BET surface area and pore volume of the hierarchically structured composite.

Sample	Surface area ($m^2 \cdot g^{-1}$)	Total pore volume ($cm^3 \cdot g^{-1}$)	BJH pore diameter (nm)
α-Al_2O_3	5	0.01	18
TiO_2-α-Al_2O_3	9	0.03	11
CNT-α-Al_2O_3	76	0.20	11
TiO_2/CNT-α-Al_2O_3	72	0.28	15

X-ray diffraction patterns of the supports are presented in Figure 3-14A and confirm the presence of CNTs and TiO_2, respectively, in the composite. The main diffraction peaks of α-Al_2O_3 were observed in all supports. The XRD pattern presented in Figure 3-14A (b and d) only shows crytalline anatase phase which indicates the high selectivity during the thermal treatment process.

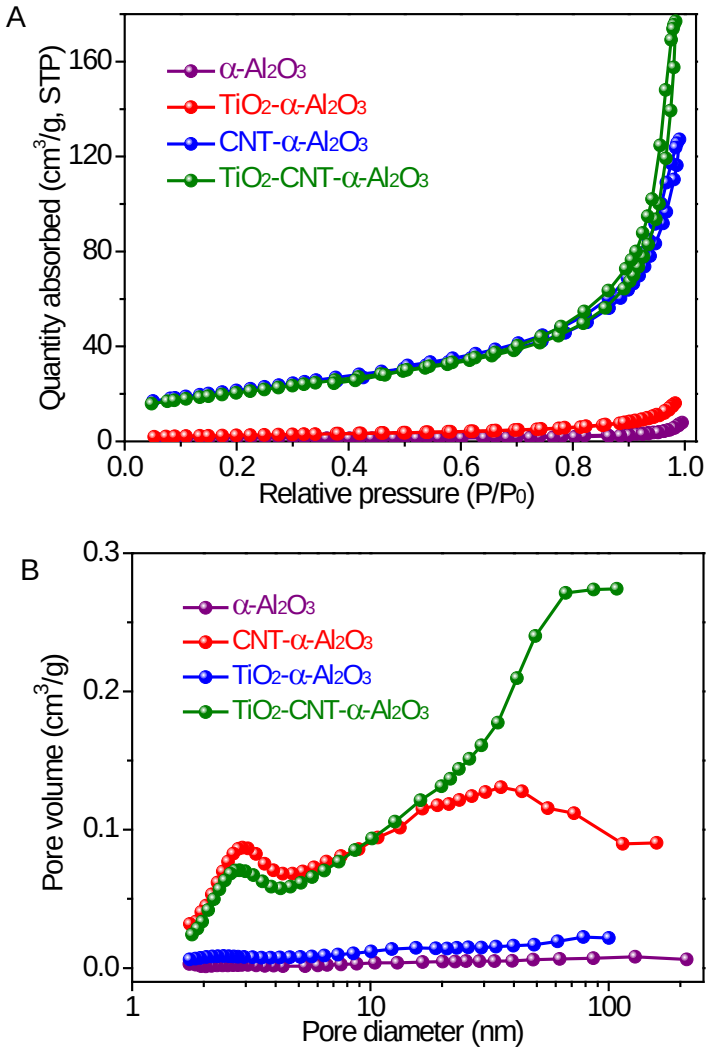

Figure 3-13. N_2 adsorption-desorption isotherms and the corresponding pore size distribution using the BJH methods of the support materials.

X-ray photoelectron spectroscopy (XPS) analysis was also performed on the TiO_2-CNT-α-Al_2O_3 composite. Typical survey and high-resolution spectra of TiO_2 are displayed in Figure 3-14B and C. The survey scan of the TiO_2-CNT-α-Al_2O_3 reveals the existences of elements, Ti, C and Al, corresponding to the different phases in the composite (Figure 3-14B). The photoelectron peak for Ti $2p_{1/2}$ and Ti $2p_{3/2}$ in the hierarchically-structured TiO_2-CNT-α-Al_2O_3 composite locate clearly at binding energies of 465.6 and 459.7 eV, respectively, as presented in Figure 3-14C. The peak separation of 5.9 eV between the Ti $2p_{1/2}$ and Ti $2p_{3/2}$ signals can be assigned to TiO_2 , which is in excellent agreement with the reported literature values.[37]

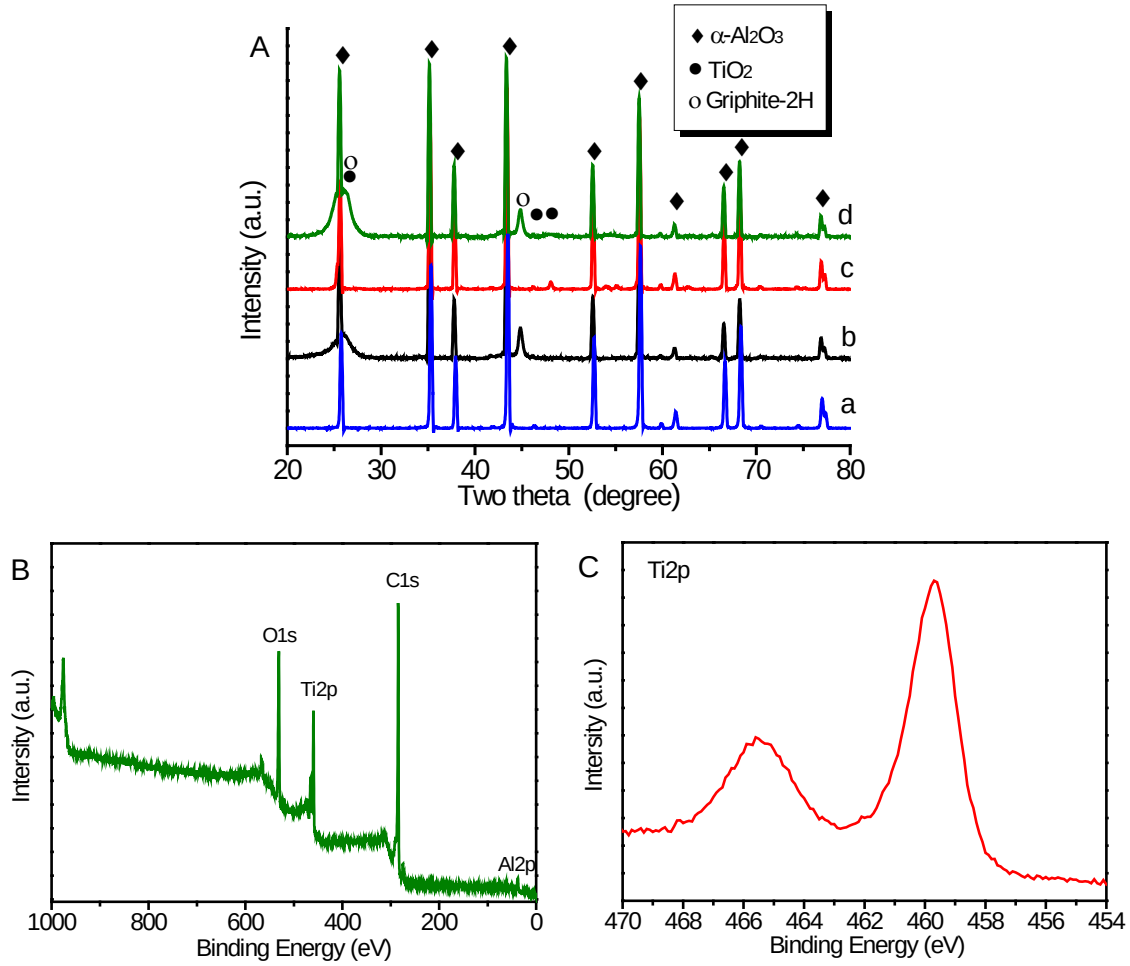

Figure 3-14. (A) XRD patterns of α-Al_2O_3 (a), CNTs-α-Al_2O_3 (b), TiO_2-α-Al_2O_3 (c) and TiO_2-CNTs-α-Al_2O_3. (B) General scanning XPS spectrum and high-resolution XPS spectrum of the Ti 2p peaks of TiO_2-CNT-α-Al_2O_3.

Typical TEM analysis of the CNT-α-Al_2O_3 composite with hierarchical structure is displayed in Figure 3-15. The low-resolution TEM micrograph (Figure 3-15A) demonstrates that the synthesis method was extremely selective towards the formation of carbon nanotubes and neither carbon nanoparticles nor amorphous carbon was observed inside the composite.[38] The α-Al_2O_3 matrix (white arrow) is covered by a highly entangled CNTs network as shown in Figure 3-15A. High-resolution TEM micrograph of CNT-α-Al_2O_3 in Figure 3-15B shows the residual catalyst particles (pointedly the red arrows) which were embedded within several graphene layers. These metallic particles are inaccessible, neither to the acid medium during the purification process, nor to any gaseous reactants during the subsequence use of the composite, due to the presence of the graphene layer wrapping their

surface.[38] Thus, these residual Fe-Co particles are expected to barely influence the FTS reaction performance.[29]

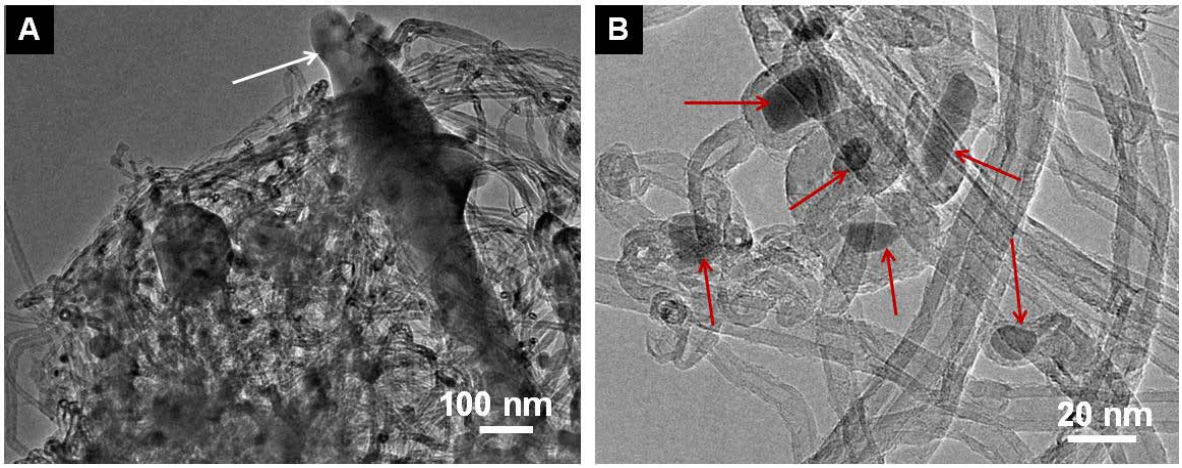

Figure 3-15. TEM images of the hierarchical structure CNT-α-Al_2O_3.

As shown in the SEM image (Figure 3-16A), the as-prepared hierarchical structure TiO_2-CNT-α-Al_2O_3 is composed of bare rock mountain-like α-Al_2O_3 matrix and the thin shell of a homogeneous vegetation-like carbon nanotube. This structure-opened carbon nanotubes network decorated with TiO_2 nanoparticles will play an efficient role to enhance the diffusion of reactant (CO and H_2) towards the active site and also the products evacuation from the catalyst to the gas phase medium. The TEM image of the TiO_2-CNT-α-Al_2O_3 composite is show in Figure 3-16B. It can be seen that the surface of the as-grown CNT and α-Al_2O_3 is well covered by TiO_2 nanoparticles with a relatively high homogeneous size. The TEM micrograph in Figure 3-16C clearly evidences the high coverage of the CNTs network by the TiO_2 nanoparticles which could be attributed to the high effective surface area of the CNTs. The medium-resolution TEM of TiO_2 nanoparticles on the CNT surface also clearly shows that the TiO_2 nanoparticles anchored on the CNT wall possess relative homogenous dispersion. The corresponding lattice fringes are clearly observed in the Figure 3-16D, and the interplanar spacing is around 0.35 nm for the TiO_2-promoted hierarchically-structured composite, corresponding to the (101) crystal face in the anatase phase.

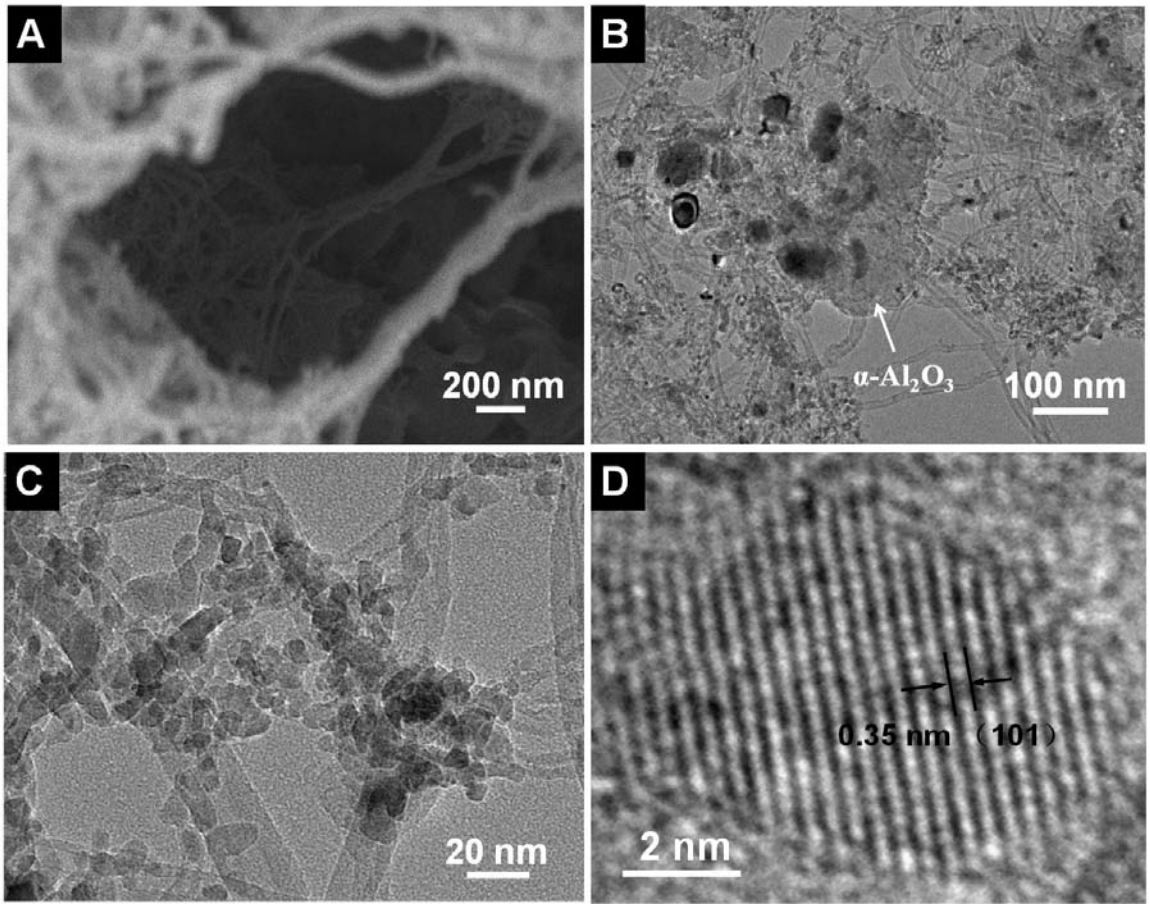

Figure 3-16. SEM micrograph (**A**) and TEM images (**B-D**) of the hierarchical structure TiO_2-CNT-α-Al_2O_3.

3.7.3 Characteristics of the catalysts

The reducibility of the cobalt-based catalysts has been investigated by temperature programmed reduction (H_2-TPR), and the corresponding results are display in Figure 3-17. It is necessary to note that the analysis was carried out at a relatively low temperature ramping rate (10 ^oC/min instead of 15 ^oC/min in Part A) and hydrogenation concentration (5 v/v% in argon instead of 10 v/v% in argon) which allows us to compare well the reducibility of our catalysts with the literature references,[33, 39-40] which are different from the previous study.[29] After the addition of TiO_2, the reducibility of cobalt-based catalyst barely changes. The small reduction peak localized at around 200 °C in all samples (Figure 3-17) can be attributed to the reduction of the residual cobalt nitrate in the catalysts when the calcination is temperature lower than 450 ^oC.[41-42] The reduction peak located at around 310-330 °C is ascribed to the reduction of the Co_3O_4 to CoO, which is overlapped with the other reduction peak. This peak shifts to lower temperature over the CoA and CoTiA catalysts (without

hierarchical structure) compared the hierarchically-structured catalyst (CoCNTA and CoTiCNTA) which can be explained by the higher interaction between the small TiO_2 particles and the cobalt oxide phase. The following reduction peaks of CoA and CoTiA catalyst locate around 367 ^{o}C and 370 ^{o}C, respectively, which are mainly originated from the reduction of CoO to Co^0. The hierarchically-structured catalyst displays broader and overlapped reduction peaks. The peak located at around 400 ^{o}C could also be attributed to the reduction of CoO. The reduction peak around 500 °C could be assigned to the gasification of carbon nanotubes that is partly catalyzed by the presence of the cobalt particles. Similar results have already been reported by Khodakov and co-workers[43] over the cobalt deposited on multi-walled carbon nanotubes catalyst. However, the TiO_2 addition causes a shift of the peak at around 500 ^{o}C to lower temperature. This phenomenon is resulted from the coverage of TiO_2 around the CNT wall, leading to strong contact between cobalt oxide and titanium that efficiently restrains the gasification of carbon nanotubes.

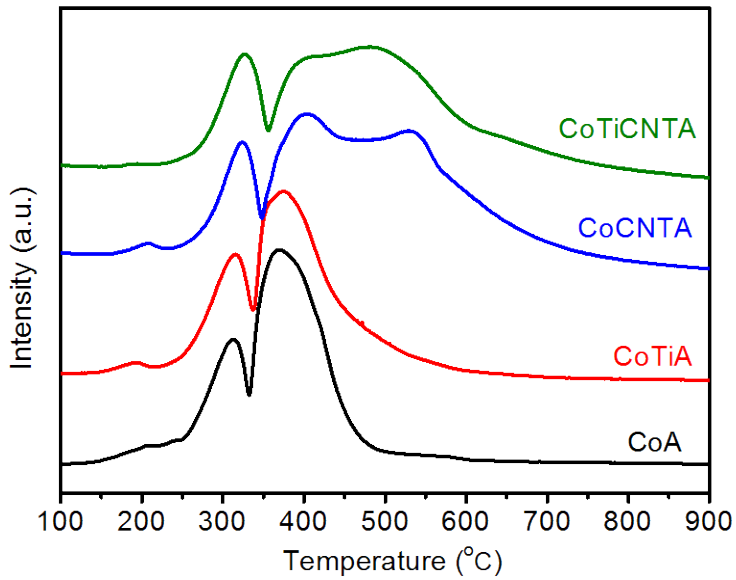

Figure 3-17. TPR profiles of the catalysts of cobalt support on hierarchically-structured composites and macropores materials.

The main textural properties of the ex-situ reduced catalysts are listed in Table 3-5, which displays different tendency for both the surface area and pore volume compared to the bare supports. As shown in Table 3-5, the specific surface area of the alumina-based catalysts (CoA and CoTiA) remaining almost unchanged after cobalt deposition, due to the presence of large pores inside the support that are hardly affected by the cobalt particles. The

BET surface area of the CoCNTA catalyst slightly decreases from 76 $m^2 \cdot g^{-1}$ to 62 $m^2 \cdot g^{-1}$ (Table 3-5) after deposition of cobalt active phase. The slight decrease of the surface area after TiO_2 addition could be attributed to the high effective surface area of the CNT network and the complete absence of any ink-bottled pores within the composite material. Indeed, it has been reported that for supports with micropores or small mesopores a large surface area lost has been observed after depositing an active phase due to the problem of pore plugging by the cobalt active phase.[44] The TiO_2-added catalyst with hierarchical structure shows slight higher specific surface and the same total pore volume versus TiO_2-free hierarchical structure catalyst.

Table 3-5 Structure and textural prosperities of cobalt supported on hierarchically-structured composites.

Catalyst	Co^0 loading (wt %) [a]	Surface area (m^2/g)	Total pore volume (cm^3/g)	BJH pore diameter (nm)	Co^0 particle size (nm) [b]
CoA	10.4 ± 0.5	7	0.02	13	35 ± 3
CoTiA	9.6 ± 0.6	9	0.03	15	30 ± 3
CoCNTA	10.7 ± 0.5	62	0.25	17	20 ± 3
CoTiCNTA	10.3 ± 0.5	71	0.25	13	23 ± 3

[a] Cobalt mass content is confirmed by inductively coupled plasma (ICP) technique
[b] $d(Co^0) = 0.75 \times d(Co_3O_4)$, the cluster size of cobalt oxides was calculated from XRD peaks at $2\theta = 36.9^o$ by using the Scherrer formula for Co_3O_4 on the calcined catalysts.[45-46]

Furthermore, the elemental composition of the CoTiCNTA catalyst is investigated by EDX mapping images, as present in Figure 3-18. Apparently, SEM image and EDX mapping reveal the similar distribution of elementals distribution (Al, Ti, Co, O and C), conforming the uniform deposition of promoter and active phase species onto the hierarchical structure. It can be seen in Figure 3-18C and D that titanium and cobalt are uniformly dispersed throughout the whole structure. The cobalt mapping image shows a stronger signal than that of Ti in the titanium mapping image, which could be attributed to the high amount of cobalt nanoparticles on the catalyst surface or interact with TiO_2. This suggestion is confirmed by the TEM-EELS of the CoTiCNTA catalyst (see below).

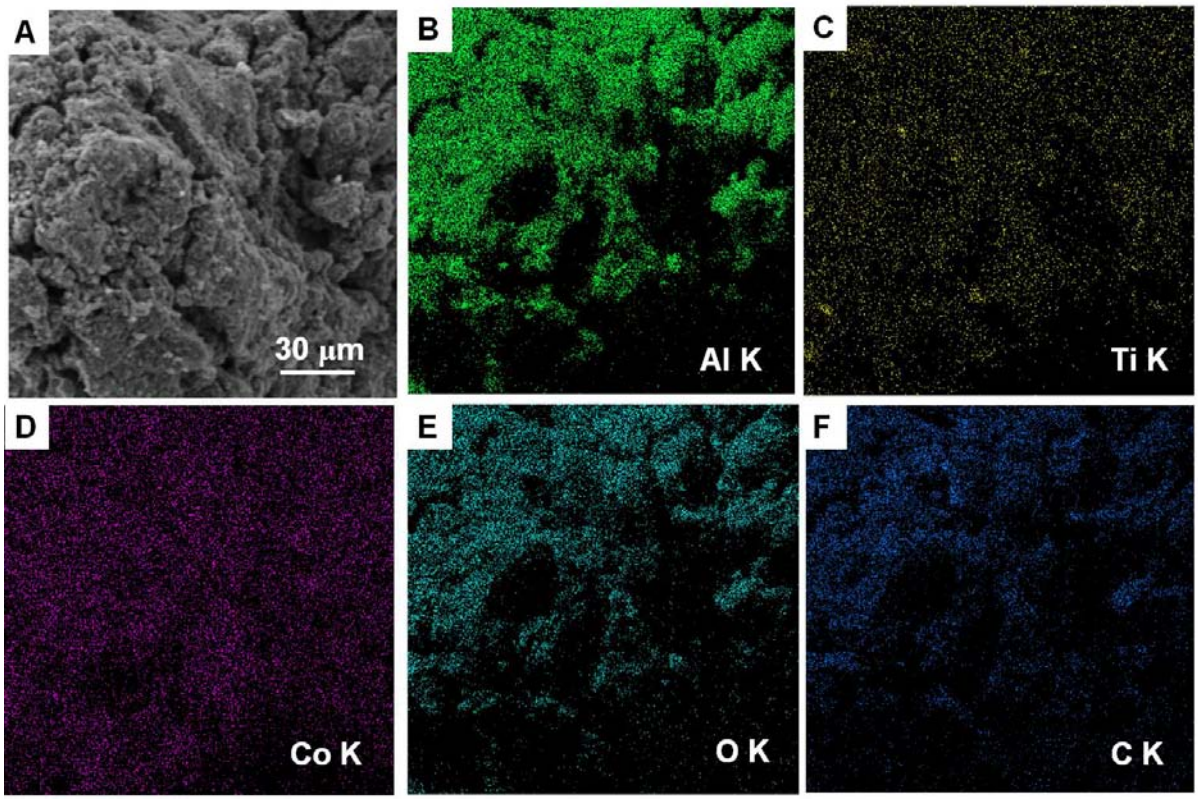

Figure 3-18. EDX characterization of the hierarchically-structured CoTiCNTA catalyst. (A) SEM image of the hierarchically-structured catalyst. EDX elemental mapping of (B) Aluminum, (C) titanium, (D) cobalt, (E) oxygen and (F) carbon in the region of (A). The EDX elemental maps demonstrate that the cobalt particles and titania species are well dispersed within the matrix of the hierarchically-structured composite.

3.7.4 Fischer-Tropsch synthesis

The catalytic performance under steady-state conditions over macroporous and hierarchically structured supports are presented in Table 3-6. The CO_2 selectivity for all the catalysts is less than 0.1% on basis of CO conversion indicating that the water-gas shift reaction does not occur over these cobalt-based catalysts. The selectivity to C_{5+} hydrocarbons of all catalysts fall in the range of 92 - 95 %. As shown in Table 3-6, Ti-promoted cobalt catalysts are much more active in FT synthesis than those un-doped ones. Besides, the TiO_2 based hierarchically-structured catalyst performs the highest activity among all the tested catalysts (Table 3-6). Carbon monoxide conversion increases from about 17.7 % over conventional Co/α-Al_2O_3 (CoA) to 33.4 % on the Co/TiO_2-α-Al_2O_3 (CoTiA) macropores catalyst. The TiO_2 promoted hierarchically-structured catalyst (CoTiCNTA) exhibited a carbon monoxide conversion of 44.3 %, which is higher than that

obtained over conventional hierarchically catalyst (28.2 %, CoCNTA). The results of catalytic evaluation are consistent with the characterization data, indicative of the much better cobalt dispersion when TiO_2 was introduced to the hierarchical composite support.

Table 3-6. Comparison of the FTS catalytic performance of the hierarchically structured Titania/Carbon Nanotubes/α-Al_2O_3 composites supported cobalt catalysts.[a]

Catalyst	CO conversion (%)	Product selectivity (%)				CoTY [c]	α [d]
		CO_2	CH_4	C_2-C_4	C_{5+}		
CoA	17.7	0	3.3	1.9	94.8	2.6	0.92
CoTiA[b]	33.4	0	3.7	2.2	94.1	5.0	0.92
CoCNTA	28.2	0.1	4.2	3.6	92.1	4.2	0.91
CoTiCNTA	44.3	0	3.3	2.0	94.7	6.6	0.92

[a] All data was obtained after 20 h of time on stream where stable catalytic performance at testing conditions was achieved. Reaction conditions: reaction temperature = 215 °C, GHSV (STP) = 3600 $ml \cdot g_{cat}^{-1} \cdot h^{-1}$, H_2/CO = 2, pure syngas, total pressure = 40 bar. The catalysts tested have already been evaluated in the FTS reaction at 215 °C about three days.
[b] 2.5g of catalysts were diluted with 2.5g of SiC (150-400 μm).
[c] Cobalt Time Yield (10^{-5} $mol_{co} \cdot g_{Co}^{-1} s^{-1}$, molar CO conversion rate per gram of Co per hour).
[d] Chain growth probability factor (α).

Catalytic performance for the reaction temperature at 215 °C shows that the TiO_2 addition significantly enhances the FTS activity of the catalyst under the same reaction conditions. The different reaction temperature impacting the catalytic behaviors for the FTS reaction will be investigated in details in the following work. The CO conversion and C_{5+} selectivity obtained on the CoTiA and CoTiCNTA catalysts as a function of reaction temperature under a relatively high GHSV, 4800 $ml \cdot g_{cat}^{-1} \cdot h^{-1}$ (STP), are displayed in Figure 3-19 and Table 3-7. The FTS rate steadily increases over both catalysts with increasing reaction temperature, whereas S_{C5+} selectivity remains relatively high at more than 90 % on both catalysts. The FTS rate on the CoTiCNTA catalyst remains higher than the one obtained on the CoTiA catalyst and steadily increases as the reaction temperature rises. The high FTS catalytic performance of the TiO_2-promote hierarchically-structured catalyst could be attributed to the better dispersion of cobalt particles in the presence of TiO_2 nanoparticles dispersed on the CNTs surface according to the XRD analysis and also to the high accessibility of the composite surface area according to the N_2 adsorption-desorption.

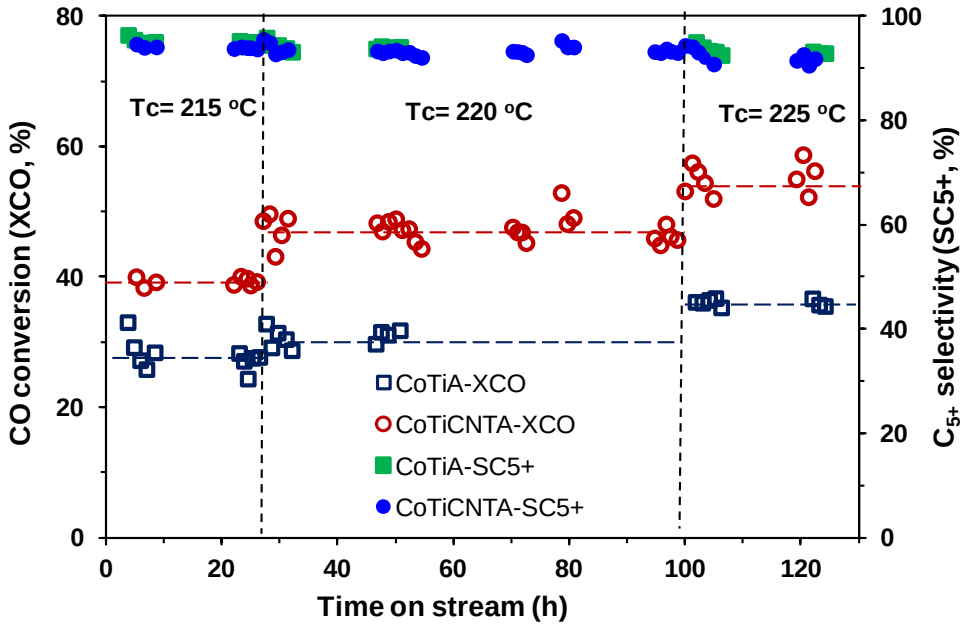

Figure 3-19. CO conversion and C_{5+} selectivity as a function of the reaction temperature on the hierarchically structured cobalt supported on the titania/carbon nanotubes/α-Al_2O_3 and the Co/TiO_2/Al_2O_3 catalysts . Reaction conditions: H_2/CO molar ratio = 2, pure syngas, total presure = 40 bar, GHSV (STP) = 4800 ml·g_{cat}^{-1}·h^{-1}.

Table 3-7. FTS performance of the hierarchically structured titania/carbon nanotubes/ α-Al_2O_3 composite supported cobalt catalyst (CoTiCNTA).[a]

T(°C)	GHSV(STP) (ml·g_{cat}^{-1}·h^{-1})	CO Conversion (%)	Product selectivity (%)				CoTY [b]	ASM[c]
			CO_2	CH_4	C_2–C_4	C_{5+}		
215	3600	44.3	0	3.3	2.0	94.7	6.6	0.31
215	4800	36.2	0	3.0	1.9	95.1	7.2	0.34
220	4800	46.9	0.1	4.4	2.6	92.9	9.3	0.44
225	4800	55.5	0	5.4	3.0	91.6	11.0	0.51
225	7200	40.7	0	4.8	2.5	92.7	12.1	0.57
230	7200	47.1	0.1	6.4	3.3	90.2	14.0	0.64

[a] All data were obtained after 20 h time on stream with stable catalytic performance at testing conditions. Reaction conditions: H_2/CO = 2, pure syngas, total pressure = 40 bar, 2.5g catalyst

[b] Cobalt-Time-Yield (10^{-5} mol_{co}·$g_{Co}^{-1}$$s^{-1}$, molar CO conversion rate per g of cobalt per hour).

[c] FTS rate to C_{5+} hydrocarbons (g_{C5+}·g_{cat}^{-1}·h^{-1}, mass of C_{5+} formed per g catalyst per hour).

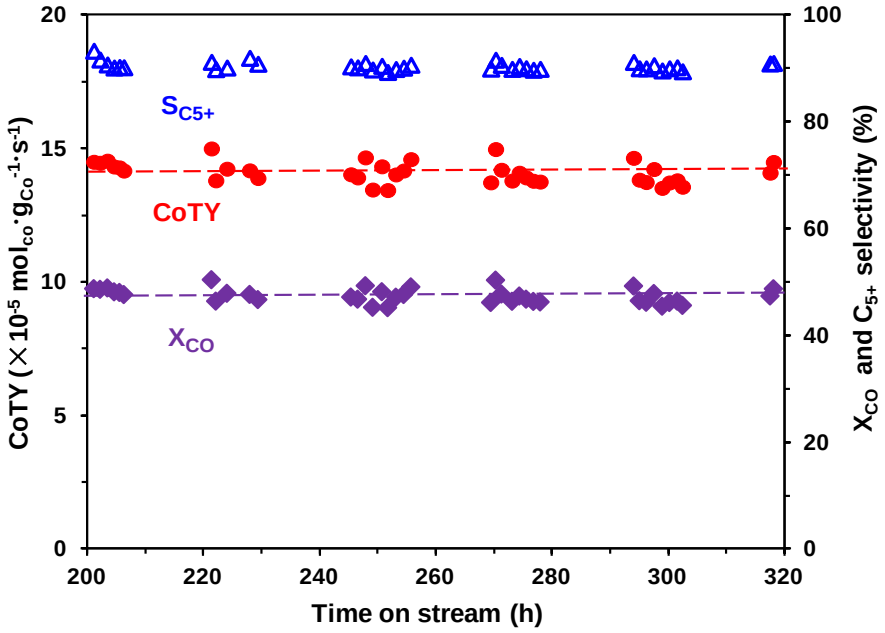

Figure 3-20. Catalytic performance of CoTiCNTA catalyst under severe reaction condition as a function of time on stream. Reaction conditions: H_2/CO molar ratio = 2, pure syngas, total pressure = 40 bar, T = 230 ^{o}C, GHSV (STP) = 7200 ml·g_{cat}^{-1}·h^{-1}.

Figure 3-20 presents the FTS reaction performance over 120 h on the hierarchically-structured CoTiCNTA catalyst. The test was carried out under severe reaction conditions, i.e. high space velocity and high reaction temperature. The CO conversion remains stable at around 47 % for the whole duration of the test which confirms the excellent stability of the catalyst over prolonged reaction time. The high stability observed could be attributed to the existence of a high interaction between the cobalt particles and the TiO_2 nanoparticles decorating the support which prevents excessive sintering of the active phase. The high stability of the FTS activity also indicates that deactivation linked to cobalt surface oxidation is unlikely to occur over the current materials under the reaction conditions used in the present work.[10] The C_{5+} selectivity is also extremely high at around 90 % indicates that the nature of the active phase was not modified during the course of the reaction. It is mentionable that the catalyst had already run for more than 200 h under different reaction conditions before the present test.

3.7.5 Cobalt microstructure analysis by ^{59}Co NMR technique

To get more evidences about the relationship between the FTS activity and the microstructure of the cobalt active sites, the zero field spin-echo ^{59}Co NMR analysis is carried out on the different tested catalysts.[30, 47-49] It is worth noting that particle sizes measured from XRD and low resolution TEM are not reflecting the real crystal sizes of the active phase. The small cobalt crystal could aggregate to a large particle with big voids, which cannot be detected by the techniques mentioned above. Moreover, for the crystalline atomic arrangement in microstructures, a considerable number of defects and stacking faults which present inside the metal structure are also not accurately detected by XRD technique. Indeed, the real cobalt crystal particles and structure could be measured by high resolution TEM analysis, however, due to the limitation of visual field, only a small part of the active phase is analyzed by using HRTEM. In addition, the statistical analysis by HRTEM is a time consuming experiment and is not representative of the whole microstructure of the active phase in the catalyst. The real advantage of NMR technique is that it is a bulk technique allowing to have a general view of the cobalt phase inside the catalyst.

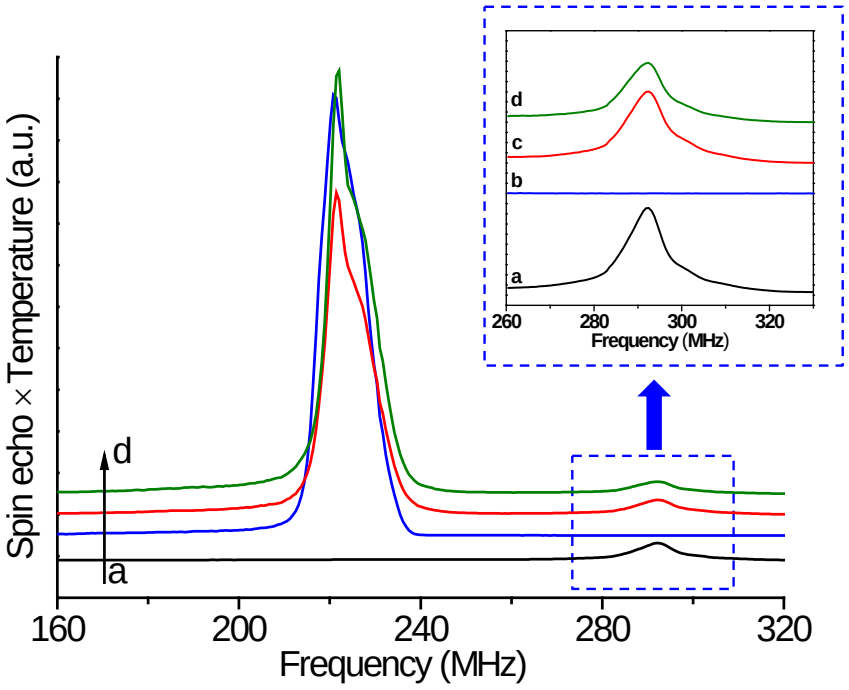

Figure 3-21. ^{59}Co NMR spectra of hierarchically-structured support and catalysts recorded at liquid helium temperature (4.2 K). (a) CNT-α-Al_2O_3, (b) CoA, (c) CoCNTA and (d) CoTiCNTA.

To eliminate the influence of the CNTs grown catalysts (Co-Fe) from the FTS active sites cobalt, the CNT-α-Al_2O_3 support was also analyzed by ^{59}Co NMR and the results are compared with those of the cobalt-based catalysts. The ^{59}Co zero field NMR spectra of the CNT-α-Al_2O_3 support and catalysts recorded at 4.2 K are presented in Figure 3-21. The NMR peaks located at higher frequency (>270 MHz) on CNT-α-Al_2O_3 support (CNTA) and the different catalysts, either TiO_2 promoted or not (CoCNTA and CoTiCNTA), is attributed to the embedded cobalt particles by graphene layers (Figure 3-15) which barely influence the microstructure of the FTS active site.[29] For comparison, at the same experimental conditions, the NMR spectrum of the α-Al_2O_3 support cobalt catalyst (CoA) is also presented in Figure 3-21b. No NMR spin echo peak higher than 270 MHz is observed which confirms that the NMR peak at high frequency was directly associated with the encapsulated cobalt growth catalyst (Co-Fe) alloy or Co^{2+} ions as mentioned in ref [50].

To get further microscopic structural information about the influence of the doping with TiO_2 on the FTS catalysts, NMR spectra were measured at 2, 4.2, and 77 K on the different catalysts, and the corresponding results are display in Figure 3-22. The NMR signal decreases with the increase of the measurement temperature. As explained in the experimental part this decrease in intensity is attributed to the presence of superparamagnetic Co particles that vanish from the NMR spectra when the measurement temperature is increased. Therefore the higher NMR measurement temperature, the larger the observed particles are, i.e. only large cobalt particles were measured while those with smaller size have disappeared. In Figure 3-22A, C and E, NMR intensity at 217 MHz is observed on the CoA catalyst, showing a large number of Co atoms forming large face centered cubic (fcc) particles with size larger than 30 nm (size for which the regular resonance frequency of bulk fcc Co is obtained). There is no pronounced NMR peak at 217 MHz for the cobalt on hierarchically structured composite catalysts, either CoCNTA or CoTiCNTA catalysts. Therefore these catalysts do not present any Co particles larger than 30 nm. This could be attributed to the fact that the CNT-based composite, pure and doped with titania, offered higher specific area and medium metal-support interaction leading to a higher cobalt dispersion with smaller cobalt particle size. Figure 3-22 D and F shows the NMR spectra obtained by differences of the NMR spectra established for consecutive measurement temperatures (see experimental part). It shows the microstructure of each Co particle size range. As it can be seen the spectra have the same shape for both the hierarchically structured catalysts (Figure 3-22 D and F). These results indicate that TiO_2 has no influence

on the cobalt particles structure, but participate in the enhancement of the cobalt nanoparticles dispersion (see below) and even introduce defect sites in the metal particle.[30, 51]

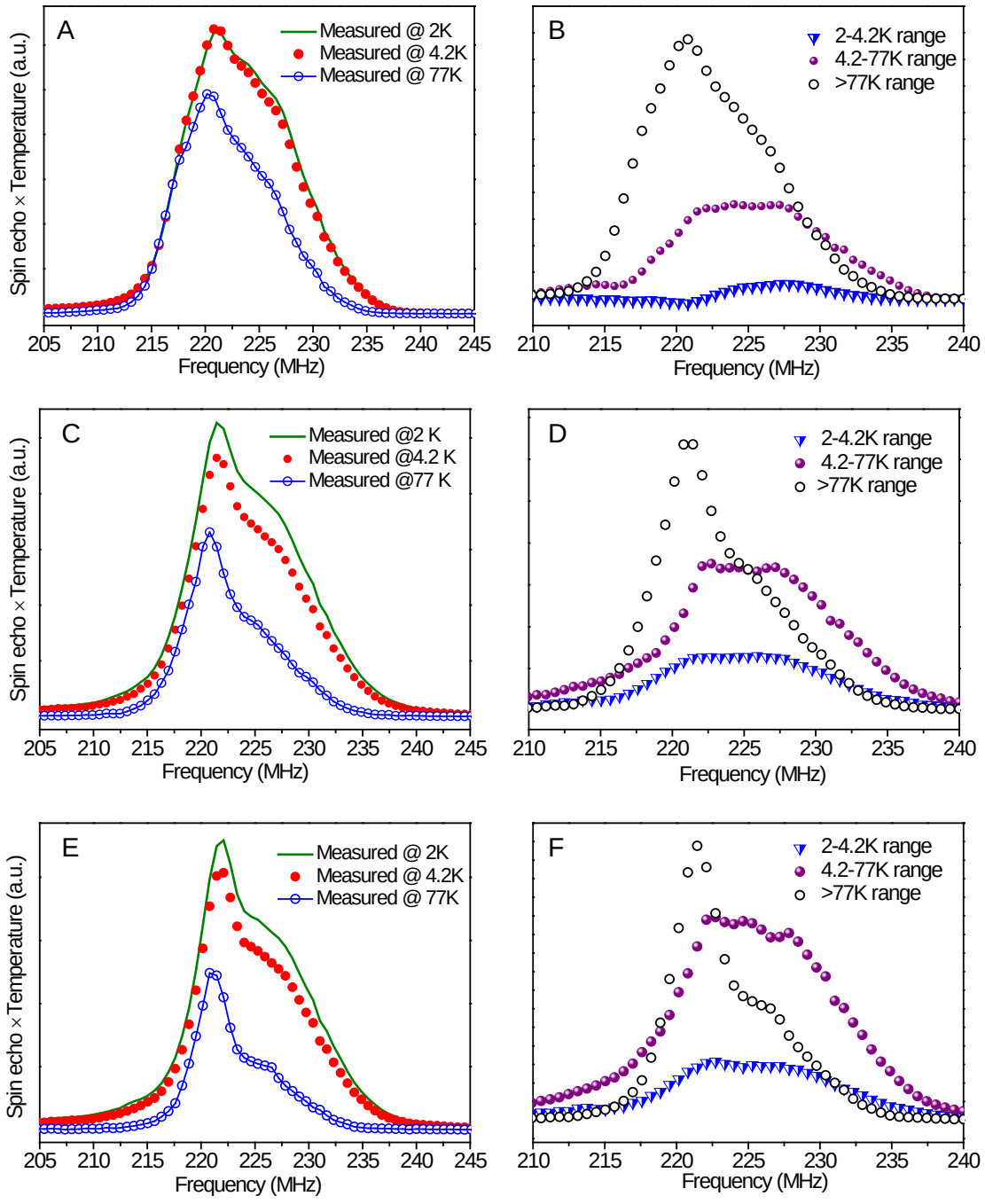

Figure 3-22. ^{59}Co zero field NMR spectra recorded at 2, 4.2 and 77 K, respectively, and analyzed in term of different blocking temperature range. (A, B) CoA, (C, D) CoCNTA and (E, F) CoTiCNTA, catalysts after FTS test decorated with wax solid.

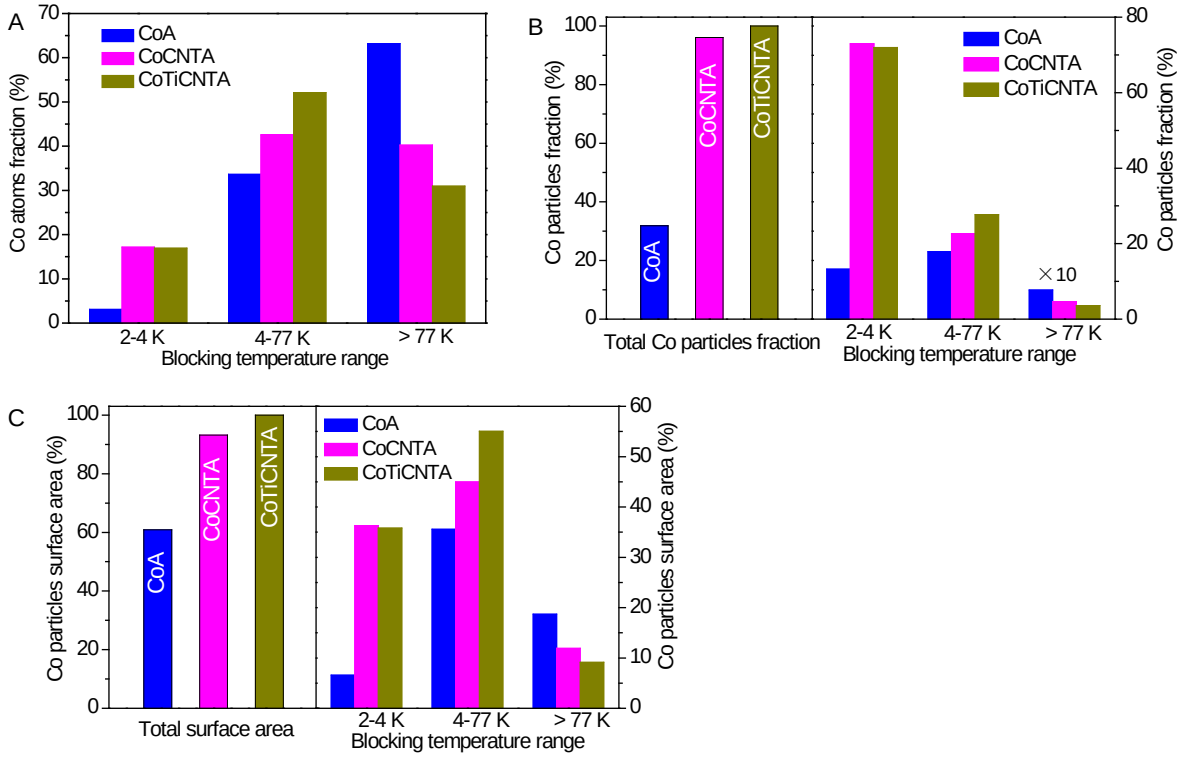

Figure 3-23 ^{59}Co zero field NMR results. (A) The fraction of cobalt atoms engaged in the different blocking temperature. (B) Total cobalt particles calculated from the same amount of Co atoms, and the relative cobalt particles as a function of the blocking temperature. (C) Total cobalt particles surface area calculated from the same amount of Co atoms, and the relative particles surface area as a function of the blocking temperature particle surface area. Particle number and surface area is normalized to the value of the catalyst giving the largest number of particles and largest particle surface area.

The fraction of cobalt atoms deduced for different blocking temperature range (equivalent to size ranges), as well as the relative surface area of cobalt nanoparticles (Co NP), based on the same amount of cobalt atoms, is presented in Figure 3-23 (Calculation details can be found in Experimental part (Chapter II)). The particle sizes range according to the blocking temperture could be as follows: 3 - 4 nm for the blocking temperature form 2 - 4.2K; 4 - 10 nm for blocking temperature from 4.2 - 77K and more than 10 nm for the blocking temperature above 77 K. According to the results, the fraction of cobalt atoms engaged in the small particles (3-10 nm, blocking temperature range from 2-4.2 K and 4.2-77K) is higher on the hierarchically structured catalysts than on the pure α-Al_2O_3 supported catalyst: 40 % of cobalt atoms on the CoA catalyst and more than 60% of cobalt atoms on the hierarchical catalysts. However, the activity is instead related to the amount of the cobalt particles surface area rather than to the distribution of cobalt atoms. The results in

Figure 3-23B and C show that the CNTs introduced increases significantly the amount of small cobalt particles and particles surface area via high efficient surface area of support, which in turn leads to a higher F-T activity.[29] The large particles (measured blocking temperature higher than 77 K which particle diameter range from 10 nm to 30 nm or more) only offer less than 20 % of activity sites in total cobalt particles (Figure 3-23). In the literature,[20] the authors have come to the conclusion that the activity and selectivity in the Fischer-Tropsch reaction are strongly dependent on cobalt particle size for catalysts using carbon nanofibers as support. They have suggested that for low pressure conditions (1 bar) average sizes smaller that 6 nm are less efficient, while at high pressure conditions (35 bar) the upper average size limit is 8 nm. Prieto et al[52] demonstrated by in situ spectroscopic that the catalytic activity decreases when cobalt metallic particle size is smaller than 10 nm on the surface functionalized zeolite supports. According our NMR results, we speculate that the small particles (3-10 nm) have multiple active sites depending on the preparation and materials used as support. The Goodman and coworkers[53] are also mentioning that Co particles in the range 3.5-10.5 nm show the higher catalytic activity and low methane selectivity. They propose that the divergence in particle sizes range compared to the previous research work (Prieto et al[52]) is due to the difference in catalysts preparation and complexity of FT synthesis itself.

From the NMR spectra we can see that Figure 3-22 D and F show exactly the same shapes in all blocking temperature range, therefore the FTS activity is solely influenced by the size distribution of the Co particles on these two hierarchical catalysts (CoCNTA and CoTiCNTA). More interestingly, after TiO_2 introduction, the total cobalt particle specific surface area in CoTiCNTA increases by 10% compared to TiO_2-free catalyst (CoCNTA). This highlights the efficient of TiO_2 phase on the dispersion of the cobalt phase (Figure 3-23B and C). The largest increase in total particles and atoms surface area is due to the particles ranging from 4-10 nm. It means that small particles (4-10 nm) play the key role in FTS activity.

The cobalt microstructures of the different tested catalysts, a quantitative analysis of cobalt atoms distributed in the different phases according to the deconvolution of ^{59}Co NMR spectra at different blocking temperature range are shown in Figure 3-24 and Table 3-8. The presented NMR signals from 215 to 235 MHz correspond to the presence of various cobalt microstructures which measured at relatively lower temperature ($\leq$ 77K). As described in details in the experimental part the NMR signal at 217 MHz corresponds the large face

centered cubic structured (fcc) of cobalt (> 30 nm) and the one at 225 MHz corresponds to the hexagonal closed packed (hcp) cobalt.[49, 54-55] The lines between 217 and 225 MHz are attributed to the stacking faults. As also mentioned previously the frequency of the same phases for small particle (< 30 nm) can be increased by up to 6 MHz depending on the particle shape. However without much doubts the resolved line at 221 MHz can be attributed to fcc Co into small magnetically single domain particles.

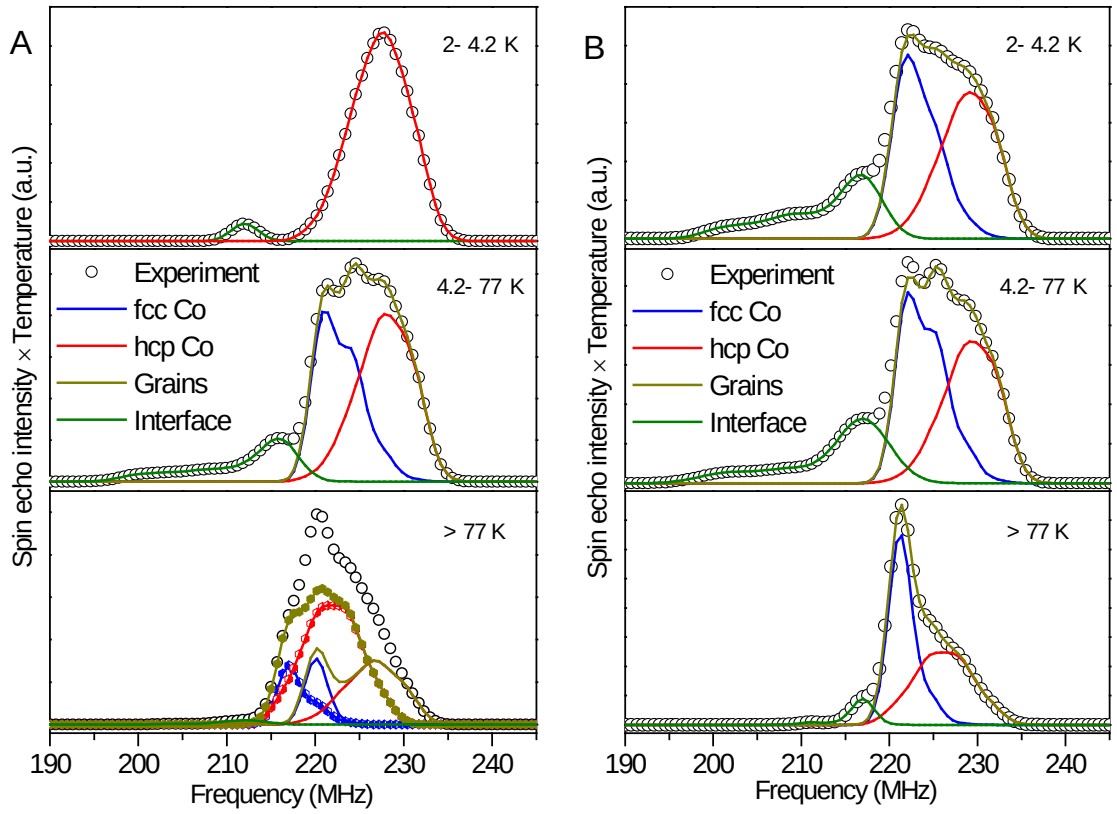

Figure 3-24. ^{59}Co NMR spectra decomposition peaks of CoA (A) and CoTiCNTA (B) catalysts on the different blocking ranges. The lines show the decomposition into fcc cobalt, hcp cobalt and interface of grains.

In Table 3-8, no data is given for CoCNTA because the results of the fits is similar to CoToCNTA as mentioned previously. It can be noticed that the amount of hcp like atoms (pure hcp phase and hcp stacking faults in the fcc phase) on both investigated samples is significantly high (> 45 %) for each blocking temperature. Moreover, the stacking faults dominates the hcp phase with an amount of faults are in the range of 30 to 50% (i.e. if C/h = 50%, there is no pure hcp phase observed in the crystal structure; it is like a random stacking of compact atomic planes). Indeed, FTS reaction consists of a large number of elementary

processes, i.e. adsorption, dissociation, hydrogenation, and insertion, in which a variety of sites involved are needed in the whole approach. Khodakov and coworkers[56-57] found that the FTS catalytic performance could be enhanced in the presence of the hcp phase fraction. The hcp phase in the three catalysts is relatively high (> 45%). However the hcp phase in CoCNTA and CoTiCNTA catalysts (the more active ones) seems lower than the one in CoA catalyst what seems contradictory to the literature. But a closer look, in Table 3-8 also indicates that the fcc phase is significantly more faulted in the CoTiCNTA samples. The presence of these numerous hcp faults into the fcc phase might lead to an increase of the activities of CoTiCNTA and CoCNTA samples compared to the CoA sample. However, it is difficult to conclude because the total particle surface area ratio between CoTiCNTA and CoA is very different: 100 compared to 56 (fraction, %), respectively. The effect of particle size is probably more remarkable than the effect of the microstructure in this work.

Table 3-8. Distribution of cobalt atoms in the different crystal phases according to the deconvolution of the 59Co NMR envelope.

Sample	Blocking temperature range (K)	Cobalt atoms (at. %)				fcc frequency (MHz)
		fcc	H/c[a]	C/h[b]	hcp	
CoA	2-4.2	0.1	-	36.5	99.9	221.0
	4.2-77	44.3	19.5	30.2	55.7	220.9
	>77	29.5	0.7	39.4	70.5	220.1
		19.4	9.7	50.0	80.6	217.0[c]
CoTiCNTA	2-4.2	48.3	15.8	29.0	51.7	221.8
	4.2-77	51.7	20.1	28.2	48.3	222.0
	>77	52.4	4.7	50.0	47.6	221.2

[a] H/c: hcp stacking faults in the fcc phase.
[b] C/h: fcc stacking faults in the hcp phase.
[c] The big fcc particle diameter is larger than 30 nm which is determined at the frequency at 217 MHz.

3.7.6 TiO_2-promoted hierarchically-structured catalyst under severe FTS reaction conditions

The catalytic performance of the CoTiCNTA catalyst was further evaluated under more severe FTS reaction conditions, i.e. relative high reaction temperature (T= 245 ^{o}C), high pressure (40 bar) and high flow rate (GHSV (STP) =9600 $ml \cdot g_{cat}^{-1} \cdot h^{-1}$). As shown in Figure

3-25 and Table 3-9, the TiO_2-promoted hierarchically-structured catalyst gives approximately 84.5% selectivity to C_{5+} at 47.4 % CO conversion. The FTS rate expressed in terms of the weight of long chain hydrocarbon formed per gram of catalyst per hour ($g_{C5+} \cdot g_{cat}^{-1} \cdot h^{-1}$) is around 0.80 $g_{C5+} \cdot g_{cat}^{-1} \cdot h^{-1}$, which is the best result among all the noble-free cobalt-based catalysts previously reported to our knowledge, including the cobalt on CNF catalysts.[20] It is also worthy to note that the C_{5+} selectivity remains relatively high under these severe reaction conditions, especially with the high reaction temperature, and thus, highlight the fact that CNTs introduced in the skeleton of support in the FTS reaction allows one to maintain the high selectivity towards long chain hydrocarbons.

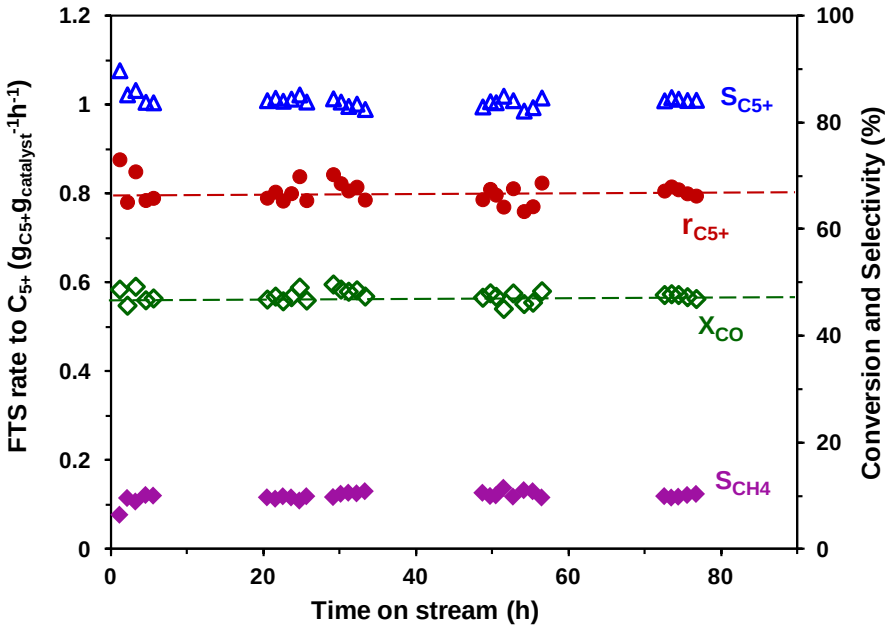

Figure 3-25. Catalytic activity as a function of time of hierarchically structured cobalt based catalyst (CoTiCNTA) at severe FTS reaction. Reaction conditions: T= 245 ^{o}C, GHSV (STP) =9600 $ml \cdot g_{cat}^{-1} \cdot h^{-1}$, total pressure = 40 bar, 2.5g catalyst diluted with 7.5g SiC, $H_2/CO = 2$.

The products distribution is expressed as chain-growth probability factors (α) calculated from the linear portion of the hydrocarbons by using Anderson-Schulz-Flory (ASF) model.[46, 58] The product distribution is obtained from mass balance after FT reaction and by analyzing the solid wax phase products. The chain growth factor is calculated according to the following equation:

$$W_n/n = (1-\alpha)^2 \alpha^{(n-1)}$$

where W_n is the weight fraction of hydrocarbon molecules containing n carbon atoms. α is the chain growth probability. When α is equal to 0 all the CO molecules are converted to CH_4, and when α is equal to 1 all the CO molecules are converted to liquid hydrocarbons.

Table 3-9 FTS catalytic performance on the hierarchically-structured cobalt (CoTiCNTA) based catalyst at severe FTS reactions.[a]

CO Conv.(%)	Product selectivity (%)				CoTY [b]	r_{C5+} [c]	α[d]
	CO_2	CH_4	C_2–C_4	C_{5+}			
47.4	0.3	9.7	5.5	84.5	18.8	0.80	0.89

[a] All data were obtained after 20h time on stream with stable catalytic performance at testing conditions. Reaction condition: T = 245 °C, GHSV (STP) = 9600 ml·g_{cat}^{-1}·h^{-1}, total pressure = 40 bar, 2.5g catalyst diluted with 7.5g SiC.
[b] Cobalt-time-yield (10^{-5} mol_{co}·$g_{Co}^{-1}$$s^{-1}$, molar CO conversion rate per gram Co per hour).
[c] FTS rate to C_{5+} hydrocarbons (g_{C5+}·g_{cat}^{-1}·h^{-1}, mass of C_{5+} formed per g catalyst per hour).
[d] Chain growth probability factor (α).

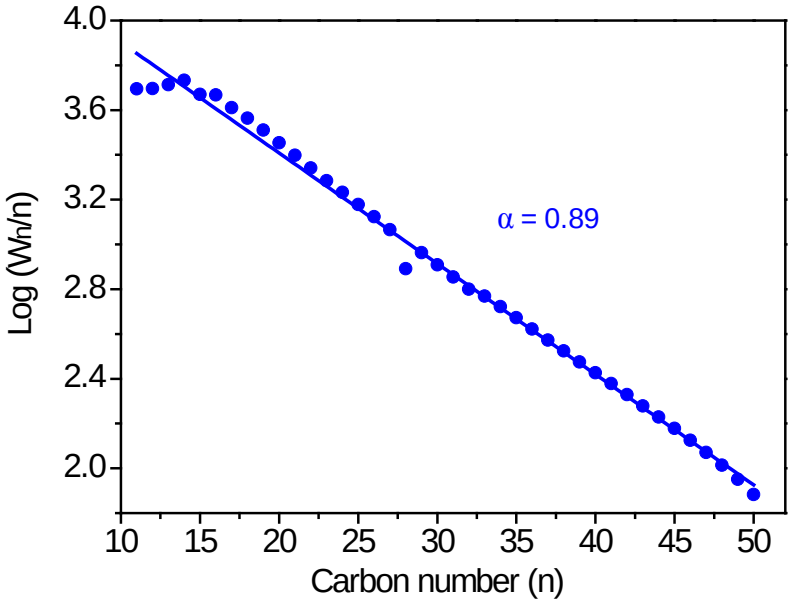

Figure 3-26. Anderson-Schulz-Flory plots for TiO_2-promoted hierarchically structured cobalt based catalyst under severe FTS reaction conditions.

The ASF plots shows that the CoTiCNTA catalyst provides a relatively high α value of about 0.89 (Figure 3-26), even under severe conditions. The relative high α value reveals the good agreement with the relatively low methane selectivity (< 10%) obtained on the

CoTiCNTA catalyst. This high α value on TiO_2-promoted hierarchically structured catalyst could be attributed to the opened structure of tested catalyst which favours the diffusion of the reactant towards the active site, and may also thanks to the thermal conductivity of the CNTs on the support which prevents local hot spot formation. [30, 59-60]

3.8 Conclusion

In summary, we demonstrated a hierarchically structured TiO_2-CNT-α-Al_2O_3 composite consisting of single crystal TiO_2 nanoparticles homogeneously coated on macroscopic shaped α-Al_2O_3 decorated with a layer of carbon nanotubes. The obtained composite possessed high specific surface area and fully accessible effective surface area, which significantly improve the cobalt nanoparticles dispersion which exhibits high and stable FTS performance. The FTS rate towards long chain hydrocarbon (C_{5+}) on the Co/TiO_2-CNT-α-Al_2O_3 (CoTiCNTA) can reach 0.64 $g_{C5+}\cdot g_{cat}^{-1}\cdot h^{-1}$ along with a selectivity toward C_{5+} as high as 90%. Moreover, under severe FTS reaction conditions (high reaction temperature, high pressure and flow rate) the CoCNTA catalyst achieving a FTS rate to C_{5+} of about 0.80 $g_{C5+}\cdot g_{cat}^{-1}\cdot h^{-1}$ along with a long chain hydrocarbon selectivity of 85 %, which can be pointed out as the most outstanding noble promoter-free catalyst for the FTS reaction.

The high catalytic performance in the FTS reaction was attributed to the presence of TiO_2-promoted surface which displayed a high interaction with the deposited cobalt phase leading to the formation of small cobalt particles in the range of 5 to 15 nm. The high activity was also linked with the high effective surface area of the CNTs network on the catalyst surface which provides high accessibility of the reactant towards the active sites. On the other hand, the nanoscopic size of the carbon nanotubes also provided short diffusion pathway for the product escaping.

3.9 References

[1] K. Aleklett, M. Hook, K. Jakobsson, M. Lardelli, S. Snowden, B. Soderbergh, *Energ Policy* **2010**, *38*, 1398-1414.

[2] G. Centi, S. Perathoner, *Chemsuschem* **2011**, *4*, 913-925.

[3] G. W. Huber, S. Iborra, A. Corma, *Chemical Reviews* **2006**, *106*, 4044-4098.

[4] J. R. Rostrup-Nielsen, *Science* **2005**, *308*, 1421-1422.

[5] F. Fischer, H. Tropsch, *Brennstoff Chem* **1923**, *4*, 276-285.

[6] F. Fischer, H. Tropsch, *Brennstoff Chem* **1926**, *7*, 97-104.

[7] A. Y. Khodakov, W. Chu, P. Fongarland, *Chemical Reviews* **2007**, *107*, 1692-1744.

[8] E. de Smit, B. M. Weckhuysen, *Chem Soc Rev* **2008**, *37*, 2758-2781.

[9] A. M. Saib, D. J. Moodley, I. M. Ciobica, M. M. Hauman, B. H. Sigwebela, C. J. Weststrate, J. W. Niemantsverdriet, J. van de Loosdrecht, *Catal Today* **2010**, *154*, 271-282.

[10] N. E. Tsakoumis, M. Ronning, O. Borg, E. Rytter, A. Holmen, *Catal Today* **2010**, *154*, 162-182.

[11] H. M. T. Galvis, J. H. Bitter, C. B. Khare, M. Ruitenbeek, A. I. Dugulan, K. P. de Jong, *Science* **2012**, *335*, 835-838.

[12] J. C. Kang, K. Cheng, L. Zhang, Q. H. Zhang, J. S. Ding, W. Q. Hua, Y. C. Lou, Q. G. Zhai, Y. Wang, *Angew Chem Int Edit* **2011**, *50*, 5200-5203.

[13] Q. H. Zhang, J. C. Kang, Y. Wang, *ChemCatChem* **2010**, *2*, 1030-1058.

[14] R. Luque, A. R. de la Osa, J. M. Campelo, A. A. Romero, J. L. Valverde, P. Sanchez, *Energ Environ Sci* **2012**, *5*, 5186-5202.

[15] H. F. Xiong, Y. H. Zhang, S. G. Wang, J. L. Li, *Catal Commun* **2005**, *6*, 512-516.

[16] A. Y. Khodakov, *Catal Today* **2009**, *144*, 251-257.

[17] E. Iglesia, *Appl Catal a-Gen* **1997**, *161*, 59-78.

[18] R. Oukaci, A. H. Singleton, J. G. Goodwin, *Appl Catal a-Gen* **1999**, *186*, 129-144.

[19] S. Storsaeter, B. Totdal, J. C. Walmsley, B. S. Tanem, A. Holmen, *J Catal* **2005**, *236*, 139-152.

[20] G. L. Bezemer, J. H. Bitter, H. P. C. E. Kuipers, H. Oosterbeek, J. E. Holewijn, X. D. Xu, F. Kapteijn, A. J. van Dillen, K. P. de Jong, *J Am Chem Soc* **2006**, *128*, 3956-3964.

[21] W. Chu, L. N. Wang, P. A. Chernavskii, A. Y. Khodakov, *Angew Chem Int Edit* **2008**, *47*, 5052-5055.

[22] X. W. Zhu, X. J. Lu, X. Y. Liu, D. Hildebrandt, D. Glasser, *Ind Eng Chem Res* **2010**, *49*, 10682-10688.

[23] R. Myrstad, S. Eri, P. Pfeifer, E. Rytter, A. Holmen, *Catal Today* **2009**, *147*, *Supplement*, S301-S304.

[24] M. Lacroix, L. Dreibine, B. de Tymowski, F. Vigneron, D. Edouard, D. Begin, P. Nguyen, C. Pham, S. Savin-Poncet, F. Luck, M. J. Ledoux, C. Pharn-Huu, *Appl Catal a-Gen* **2011**, *397*, 62-72.

[25] Y.-h. Chin, J. Hu, C. Cao, Y. Gao, Y. Wang, *Catal Today* **2005**, *110*, 47-52.

[26] J. J. Delgado, R. Vieira, G. Rebmann, D. S. Su, N. Keller, M. J. Ledoux, R. Schlögl, *Carbon* **2006**, *44*, 809-812.

[27] K. Chizari, A. Deneuve, O. Ersen, I. Florea, Y. Liu, D. Edouard, I. Janowska, D. Begin, C. Pham-Huu, *Chemsuschem* **2012**, *5*, 102-108.

[28] S. Zarubova, S. Rane, J. Yang, Y. Yu, Y. Zhu, D. Chen, A. Holmen, *Chemsuschem* **2011**, *4*, 935-942.

[29] Y. Liu, T. Dintzer, O. Ersen, C. Pham-Huu, *Journal of Energy Chemistry* **2013**, *22*, 279-289.

[30] Y. Liu, B. de Tymowski, F. Vigneron, I. Florea, O. Ersen, C. Meny, P. Nguyen, C. Pham, F. Luck, C. Pham-Huu, *ACS Catalysis* **2013**, *3*, 393-404.

[31] S. J. Park, S. M. Kim, M. H. Woo, J. W. Bae, K. W. Jun, K. S. Ha, *Appl Catal a-Gen* **2012**, *419*, 148-155.

[32] S. Hinchiranan, Y. Zhang, S. Nagamori, T. Vitidsant, N. Tsubaki, *Fuel Process Technol* **2008**, *89*, 455-459.

[33] M. Lualdi, G. Di Carlo, S. Logdberg, S. Jaras, M. Boutonnet, V. La Parola, L. F. Liotta, G. M. Ingo, A. M. Venezia, *Appl Catal a-Gen* **2012**, *443*, 76-86.

[34] A. M. Venezia, V. La Parola, L. F. Liotta, G. Pantaleo, M. Lualdi, M. Boutonnet, S. Järås, *Catal Today* **2012**, *197*, 18-23.

[35] Y. F. Liu, L. D. Nguyen, T. Truong-Huu, Y. Liu, T. Romero, I. Janowska, D. Begin, C. Pham-Huu, *Mater Lett* **2012**, *79*, 128-131.

[36] M. Trepanier, A. K. Dalai, N. Abatzoglou, *Appl Catal a-Gen* **2010**, *374*, 79-86.

[37] B. Erdem, R. A. Hunsicker, G. W. Simmons, E. D. Sudol, V. L. Dimonie, M. S. El-Aasser, *Langmuir* **2001**, *17*, 2664-2669.

[38] G. Gulino, R. Vieira, J. Amadou, P. Nguyen, M. J. Ledoux, S. Galvagno, G. Centi, C. Pham-Huu, *Appl Catal a-Gen* **2005**, *279*, 89-97.

[39] B. C. Enger, A. L. Fossan, O. Borg, E. Rytter, A. Holmen, *J Catal* **2011**, *284*, 9-22.

[40] J.-Y. Park, Y.-J. Lee, P. R. Karandikar, K.-W. Jun, K.-S. Ha, H.-G. Park, *Applied Catalysis A: General* **2012**, *411–412*, 15-23.

[41] A. Lapidus, A. Krylova, V. Kazanskii, V. Borovkov, A. Zaitsev, J. Rathousky, A. Zukal, M. Jancalkova, *Appl Catal* **1991**, *73*, 65-82.

[42] O. Borg, S. Erib, E. A. Blekkan, S. Storsaeter, H. Wigum, E. Rytter, A. Holmen, *J Catal* **2007**, *248*, 89-100.

[43] H. Zhang, C. Lancelot, W. Chu, J. P. Hong, A. Y. Khodakov, P. A. Chernavskii, J. Zheng, D. G. Tong, *J Mater Chem* **2009**, *19*, 9241-9249.

[44] P. Nguyen, C. Pham, B. de Tymowski, C. Pham-Huu, F. Luck, in *France Patent 11-01704, Vol. 11-01704*, France Patent ed., France, **2011**.

[45] D. Schanke, S. Vada, E. A. Blekkan, A. M. Hilmen, A. Hoff, A. Holmen, *J Catal* **1995**, *156*, 85-95.

[46] S. Logdberg, M. Lualdi, S. Jaras, J. C. Walmsley, E. A. Blekkan, E. Rytter, A. Holmen, *J Catal* **2010**, *274*, 84-98.

[47] C. Meny, P. Panissod, (Ed.: G. A. Webb), Springer, Heidelberg, Germany **2006**.

[48] P. Panissod, C. Meny, *Appl Magn Reson* **2000**, *19*, 447-460.

[49] B. de Tymowski, Y. F. Liu, C. Meny, C. Lefevre, D. Begin, P. Nguyen, C. Pham, D. Edouard, F. Luck, C. Pham-Huu, *Appl Catal a-Gen* **2012**, *419*, 31-40.

[50] E. Dujardin, C. Meny, P. Panissod, J. P. Kintzinger, N. Yao, T. W. Ebbesen, *Solid State Commun* **2000**, *114*, 543-546.

[51] I. Florea, Y. Liu, O. Ersen, C. Meny, C. Pham-Huu, *ChemCatChem* **2013**, 10.1002/cctc.201300103.

[52] G. Prieto, A. Martinez, P. Concepcion, R. Moreno-Tost, *J Catal* **2009**, *266*, 129-144.

[53] Z. J. Wang, S. Skiles, F. Yang, Z. Yan, D. W. Goodman, *Catal Today* **2012**, *181*, 75-81.

[54] R. Speight, A. Wong, P. Ellis, P. T. Bishop, T. I. Hyde, T. J. Bastow, M. E. Smith, *Phys Rev B* **2009**, *79*.

[55] J. L. Bubendorff, C. Meny, E. Beaurepaire, P. Panissod, J. P. Bucher, *Eur Phys J B* **2000**, *17*, 635-643.

[56] H. Karaca, J. P. Hong, P. Fongarland, P. Roussel, A. Griboval-Constant, M. Lacroix, K. Hortmann, O. V. Safonova, A. Y. Khodakov, *Chemical Communications* **2010**, *46*, 788-790.

[57] H. Karaca, O. V. Safonova, S. Chambrey, P. Fongarland, P. Roussel, A. Griboval-Constant, M. Lacroix, A. Y. Khodakov, *J Catal* **2011**, *277*, 14-26.

[58] A. Tavakoli, M. Sohrabi, A. Kargari, *Chem Eng J* **2008**, *136*, 358-363.

[59] A. Martinez, G. Prieto, J. Rollan, *J Catal* **2009**, *263*, 292-305.

[60] S. Rane, O. Borg, J. Yang, E. Rytter, A. Holmen, *Appl Catal a-Gen* **2010**, *388*, 160-167.

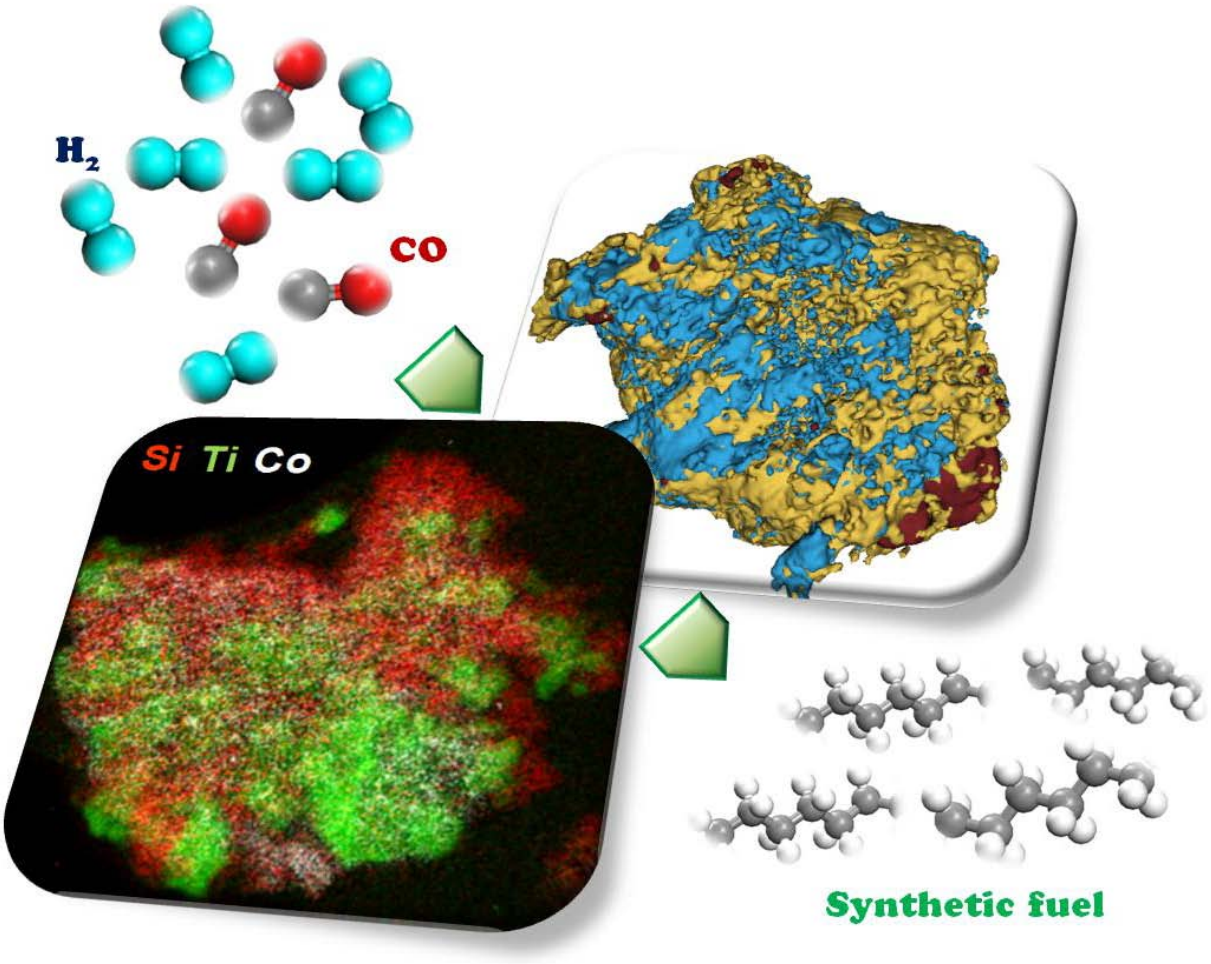

Chapter IV

Titania-doped silicon carbide containing cobalt catalyst

Chapter IV Titania-doped silicon carbide containing cobalt catalyst

Brief introduction of Chapter IV

Despite the high FTS performance observed the main drawback linked with the use of CNT in the FTS reaction is the high sensitivity of the CNT towards oxidation which render difficult the regeneration of the catalyst. The main objective of this chapter is to investigate the development of a new hybrid support consisted by a titanium doped silicon carbide (SiC), with high oxidative resistance, high specific surface area and improved metal-support interactions. The titanium oxide exhibits a higher metal-support interaction with the deposited cobalt active phase precursor which leads to a higher dispersion of the cobalt particles compared to those deposited on the undoped SiC surface. This chapter is consisted of two sections:

[Part A] Titania-decorated SiC containing cobalt catalyst for the FT Synthesis

In this section, the metal-support interactions of titanium dioxide decorated silicon carbide (β-SiC) supported cobalt catalyst for Fischer-Tropsch synthesis (FTS) were explored by a combination of energy-filtered transmission electron microscopy (EFTEM), ^{59}Co zero field nuclear magnetic resonance (^{59}CoNMR) and other conventional characterization techniques. From the 2D elemental maps deduced by EFTEM tomography and ^{59}Co NMR analyses, it can be concluded that the nanoscale introduction of the TiO_2 into the β-SiC matrix significantly enhances the formation of small and medium-size cobalt particles. The results revealed that the proper metal-support interaction between cobalt nanoparticles and TiO_2 led to the formation of smaller cobalt particles (4-15 nm), which possess a large

fraction of surface atoms and, thus significantly contribute to the great enhancement of conversion and reaction rate. The cobalt time yield of the catalyst after modification increased to 7.5×10^{-5} $mol_{co}g_{Co}^{-1}s^{-1}$ at 230 °C, whilst the C_{5+} selectivity maintained a high level (> 90%). Besides, the adequate meso- and macro-pores of the SiC-based support facilitated an intimate contact between reactants and active sites and also accelerated the evacuation of the intermediate products. It was also worth noting that superior and stable FTS specific rate of 0.56 $g_{HC}\cdot g_{catalyst}^{-1}\cdot h^{-1}$ together with high C_{5+} selectivity of 91% were obtained at common industrial content of 30 wt.% cobalt.

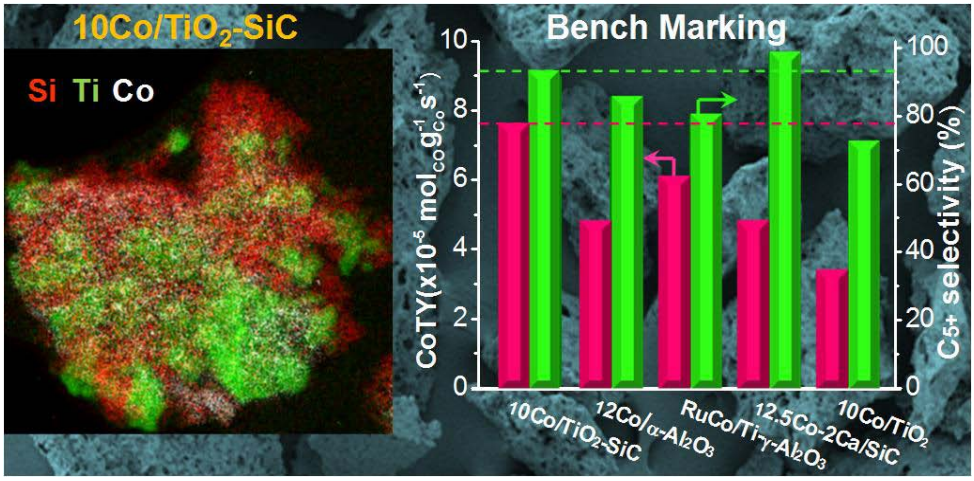

[Part B] Microstructural analysis and energy filtered TEM imaging to investigate the structure-activity relationship in Fischer-Tropsch catalysts

In the second section of Chapter V, we present here the application of the chemical imaging based on energy-filtered transmission electron microscopy (EFTEM) in 2D and 3D modes to determine the distribution of phases in Co/TiO_2-SiC catalysts used in the Fischer-Tropsch synthesis. In combination with other more traditional techniques such as high resolution TEM imaging, it allowed us to precisely characterize the microstructure and the relative distribution of the three compounds, Co, Si and Ti, before and after the catalytic reaction. We show that the TiO_2 doping is relative homogenous within the bi-modal porous

structure of beta-SiC. The characteristics of cobalt nanoparticles depend on the phase they are in contact, small nanoparticles on TiO_2 and bigger nanoparticles close to SiC. An enhancement of the catalytic performances and a higher stability were observed for the Co/TiO_2-SiC catalyst compared to Co/SiC, due to a better dispersion of cobalt on TiO_2 doped SiC support and to the relatively high Co-TiO_2 interaction. From a general point of view, this work illustrates once again that the advanced TEM-based techniques are unavoidable for the characterization and the optimization of the heterogeneous catalysts.

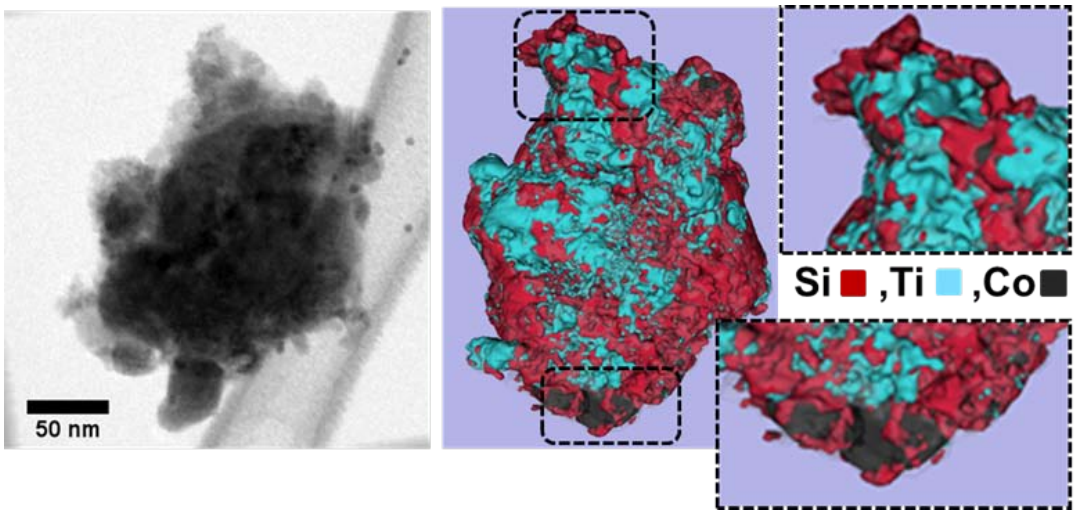

[Part A] Titania-decorated SiC containing cobalt catalyst for the F-T Synthesis

4.1 Introduction

Fischer-Tropsch synthesis (FTS) is a key technology in the more global Gas-To-Liquids (GTL) process which allows the transformation of synthesis gas ($2H_2$ + CO), issued from natural gas reforming into liquid hydrocarbons, followed by hydrocracking of the heavy fraction into useful compounds such as naphtha, diesel, lubricants and others.[1-6] The most employed active phase for the low-temperature FTS process is supported cobalt, either pure or doped with trace amounts of noble metal in order to enhance the reduction of the active phase and to improve the dispersion of metal particles.[7-11] Cobalt presents several advantages such as: high stability, high activity for liquid hydrocarbons formation and low selectivity towards oxygenated products, resistance towards oxidation, low water-gas shift (WGS) tendency and acceptable price for industrial development. However, the high activity of the cobalt phase also leads to an extremely high sensitivity of the catalyst selectivity to the reaction temperature. Cobalt active phase is typically employed in a supported form for the FTS process. The support should display a relatively high specific surface area to achieve a high dispersion of the metal particles, good mechanical and hydrothermal resistance and a medium level of metal-support interaction to allow complete reduction of the active phase and to prevent sintering of the cobalt. The most employed supports for the FTS are alumina; silica; titania; and carbon-based materials such as activated carbon, carbon nanotubes and nanofibers.[12-19] Among these supports, alumina, either pure or promoted, is the most employed as commercial catalysts support. However, on traditional supports such as alumina and silica, it is difficult to reduce small particles of metal oxide precursor because of the presence of high metal-support interactions which prevent the complete reduction of the active phase oxide precursor at moderate temperatures.[20-22] In addition, the low thermal

conductivity of alumina could lead to the formation of local hot spots during FTS which compromise the selectivity of the reaction and the plant safety, especially at high CO conversion. Wang et al.[23] reported that the heat release by the FTS cannot be properly evacuated to the entire body of the alumina support and thus, leads to the formation of hot spots on the catalyst surface which favors formation of light products. It is therefore of interest to develop new supports with improved thermal conductivity to reduce as much as possible the temperature gradient within the catalyst bed. Supports with high chemical inertness also show advantages for the recovery of the active phase at the end-life of the catalyst, taking into account the toxicity of cobalt and its relatively high amount in the FTS plant. Such new supports should also be inexpensive and readily available in various shapes to reduce the costs linked with the reactor modifications.

Recently, silicon carbide (β-SiC) with medium specific surface area (20-40 $m^2 \cdot g^{-1}$) has been reported as an efficient support for FTS allowing working at high CO conversion along with a high C_5^+ selectivity, as well as for the FTO (Syngas to Olefins) reaction with high selectivity towards light olefins.[24-29] Silicon carbide possesses all the physical properties required for being used as catalyst support[30-32], namely: high mechanical strength, high thermal conductivity (which allows a rapid homogenization of the temperature within the catalyst bed), high oxidative resistance, and chemical inertness (which facilitate the recovery of the active phase and the support for subsequence re-use[24]). It is also worth noting that the pore network of SiC is mainly constituted by meso- and macropores which significantly enhance mass transfer during FTS and prevents the formation of concentration gradients between hydrogen and carbon monoxide which lead to the formation of light products. A catalyst containing 30 wt.% Co-1.0 wt.% Ru support on high surface area and hierarchical macromesoporous structure γ-Al_2O_3 nanofibers has been reported by Martínez et al.[33] to evidence the diffusion and dispersion effects during FTS comparable to commercial alumina (Sasol). The benefits of using the macro-mesoporous nanofibrous support (high Co^0 dispersion and fast CO transport rate through the liquid phase filling the pores) are evidenced at high metal loadings (30 wt.% Co), at which the nanofibrous catalyst displays the highest

specific activity and productivity to diesel products. Indeed, during FTS the catalyst pores are mostly filled with liquid waxes and thus, both gaseous reactants and FTS products have to diffuse through a liquid layer. Such a gas-liquid diffusion layer causes more severe concentration gradients for CO than for H_2 because of the higher diffusivity of the latter. The difference in terms of the diffusivity of the reactants leads to the formation of high local concentration of H_2 versus CO, and as a consequence, a higher selectivity toward light products formation. It was suggested that a higher diffusion rate of hydrogen inside the pores filled up with liquid products compared to that of carbon monoxide entailed an increase in the local H_2/CO ratio in the catalyst pores and, thus, a shift toward the formation of lighter hydrocarbons, especially methane.[34-35]

The β-SiC support also presents a low metal-support interaction which allows an easy reduction of the deposited metal particles at moderate reduction temperature.[24-25] However, the low metal-support interaction also prevents the high and homogeneous dispersion of the metal nanoparticles on the SiC-based support, leading to a relatively large metal particle size (30-40 nm), which is higher than that desired for the optimum operation of the FTS process (6-20 nm).[16, 36] It is thus of interest to develop a new SiC-based support for such a highly demanding catalytic process, with a higher surface area and a stronger metal-support interaction to improve active phase dispersion and also to prevent excessive metal particle size growth by hydrothermal sintering during the course of the reaction.

In the general framework related to the study of multiphase nanomaterials synthesized in a powder form, a key challenge is the determination of the relative spatial distribution of the components, especially at the surface of the grains. For instance, for the catalytic supports made of several components, one of the crucial parameters is their relative amount at the surface, to be correlated to the distribution of the active phase nanoparticles. In that regard, the most appropriate technique that can provide elemental maps on field of view of few hundred nanometers is the energy-filtered transmission electron microscopy (EFTEM) tomography.[37-38]

The aim of the present study is to report on the development of a new hybrid support, titanium dioxide decorated silicon carbide with improved metal-support interactions, and its use in the Fischer-Tropsch synthesis. Titanium dioxide exhibits a high metal-support interaction with the cobalt active phase precursor, which leads to a higher dispersion of the cobalt particles compared to those deposited on the SiC surface. These small cobalt particles (6-15 nm) significantly improve the performance of the FTS catalyst without sacrificing the high selectivity towards liquid hydrocarbons already observed on such oxide supports. The correlation between catalyst structure and catalytic performance was supported by advanced characterization techniques such as ^{59}Co zero field nuclear magnetic resonance (^{59}Co NMR) and EFTEM tomography along with more conventional characterization techniques (high resolution TEM, Temperature-Programmed Reduction (TPR), XRD, etc.). The potential industrial development of this catalyst will be also evaluated with a long-term FTS test. Finally, the catalytic performance of the Co/TiO_2-SiC catalyst will be benchmarked with those of different FTS catalysts reported in the literature.

4.2. Results and discussion

4.2.1 Physicochemical properties of the supports and catalysts

Silicon carbide (β-SiC) was synthesized via a gas-solid reaction between SiO vapour and dispersed solid carbon. The detailed synthesis of the SiC-based materials was summarized in a recent review.[39] The titania decorated β-SiC, which was kindly provided by SICAT SARL, was synthesized by mixing microsized silicon powder and TiO_2 nanoparticles with a carbon-containing resin. The paste was further processed into various shapes, such as extrudates, grains, beads, etc. Examples of SiC with different size and shape are presented in Figure 4-1. The XRD patterns of the SiC, TiC-SiC and TiO_2-SiC supports are presented in Figure 4-2. The calcination step at 500 °C allows the complete transformation of the TiC into TiO_2, as confirmed by the XRD pattern, since no diffraction lines corresponding to TiC were observed.

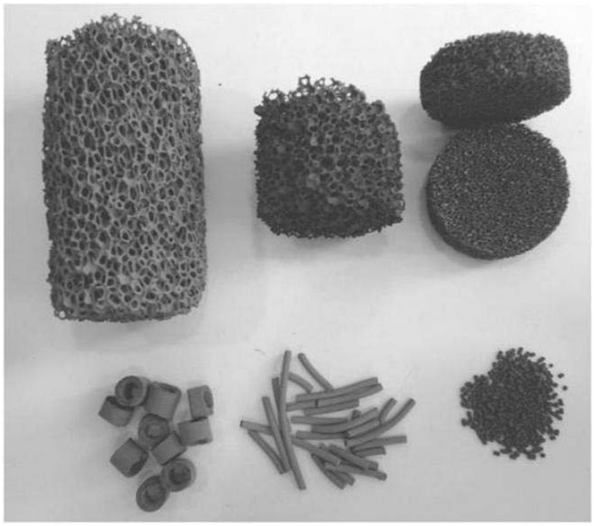

Figure 4-1. Silicon carbide (β-SiC) with different sizes and shapes synthesized via a gas-solid reaction (ICPEES copyright).

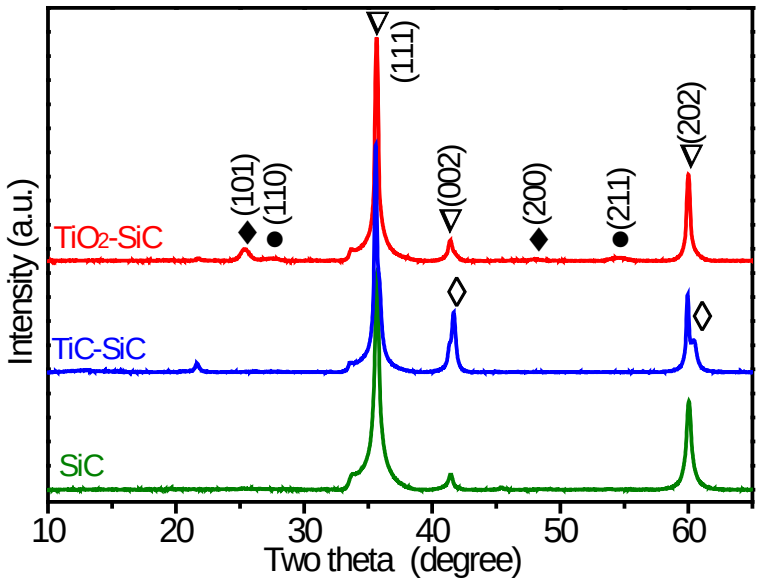

Figure 4-2. XRD patterns of SiC, TiC-SiC and TiO_2-SiC supports; The TiO_2-SiC support was obtained by calcinations of the TiC-SiC at 500 ^oC for 2 h in air. Diamond (♦): Anatase TiO_2; circles (●): Rutile TiO_2; Triangle (▽): β-SiC; diamond (◊): TiC

SEM micrographs representing the morphology of titanium carbide- and titanium dioxide- decorated SiC are presented in Figure 4-3. The low magnification SEM micrographs confirm the presence of macroporosity within the SiC- decorated materials, before and after calcination. Medium and high-resolution SEM micrographs evidence fragmentation of TiC particles into smaller TiO_2 particles during the calcination step.

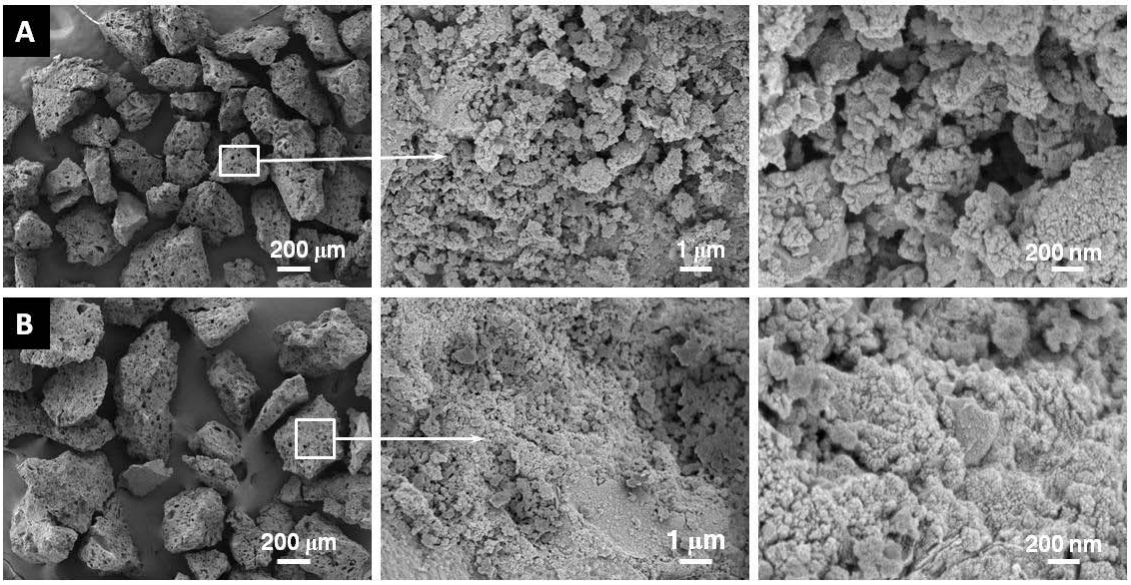

Figure 4-3. Representative SEM micrographs of **(A)** TiC-SiC and **(B)** TiO_2-SiC carriers. The TiC-to-TiO_2 transformation was carried out by calcination at 500 °C for 2 h in air.

The BET surface area, pore volume and average pore diameter of carriers and catalysts as prepared are shown in Table 4-1. The introduction of TiC into the SiC matrix leads to a strong improvement of the composite specific surface area compared to the undecorated one: 77 $m^2 \cdot g^{-1}$ instead of 40 $m^2 \cdot g^{-1}$. Such a specific surface area increase could be attributed to the formation of TiC particles evenly dispersed throughout the SiC matrix which prevents the formation of large SiC particles with low specific surface area. According to the results the TiC-to-TiO_2 transformation leads to a significant increase of the specific surface area of the decorated support, i.e. from 77 $m^2 \cdot g^{-1}$ to 101 $m^2 \cdot g^{-1}$. The TiO_2-SiC also contains a relatively large amount of micropores which are expected to be generated during the calcination step to transform TiC into TiO_2. The deposition of cobalt affects the two supports differently: the surface area of the undecorated SiC slightly decreases from 40 to 33 $m^2 \cdot g^{-1}$ after deposition of 10 wt% of cobalt active phase, whereas that of the decorated SiC significantly drops from 101 to 25 $m^2 \cdot g^{-1}$ which is mostly due to the plugging of the micropores and the formation of a new mesoporous network (Figure 4-4).

Table 4-1 BET surface area and pore volume of the undecorated and decorated SiC carriers and the same after cobalt deposition. The corresponding cobalt particle size, before and after reduction, determined by the Scherrer formula is also presented.

Sample	S_{BET} (m^2/g)	V_{total} (cm^3/g)	D_{BJH} (nm)	Co^0 particle size[a] (nm)	Co^0 particle size[b] (nm)	
					Co^0 fcc[c]	Co^0 hcp[d]
SiC	40	0.120	12.8	-	-	-
TiO_2-SiC	101	0.123	4.4	-	-	-
10Co/SiC	33	0.139	17.1	42 ± 5	51 ± 5	29± 5
10Co/TiO_2-SiC	25	0.082	13.0	22 ± 5	44 ± 5	14± 5

[a] $d(Co^0) = 0.75 \times d(Co_3O_4)$. [b] $d(Co^0) = k \cdot \lambda / (\tau \cdot \cos\theta)$, The sample was reduced by H_2 at 300 °C for 6h. [c] Face centered cubic (fcc) diffraction plane (111) of Co^0 particles. [d] Hexagonal close-packed (hcp) diffraction plane (101) of Co^0 particles.

XRD was also used to characterize the crystalline structure of the catalysts. The XRD patterns of the catalysts after reduction under H_2 at 300 °C for 6 h are presented in Figure 4-5. The 10Co/SiC catalyst displays only diffraction lines corresponding to the SiC support and metallic cobalt phase without diffraction lines corresponding to the cobalt oxide phases, confirming the complete reduction of the cobalt phase. A similar reduction pattern is also observed on the decorated catalyst. The TPR results indicate that the presence of doping (TiO_2 with a loading of 17 wt%) does not alter the reduction behavior of the cobalt oxide precursor (Figure 4-5). The complete reduction of the cobalt phase was directly attributed to the low interaction between the cobalt oxide phase and the support, SiC and TiO_2, which avoids the formation of a hardly reducible cobalt phase as usually observed with the alumina or silica supports.[22, 40] The average cobalt particle size determined by the Scherrer formula is reported in Table 4-1. Two methods are used to calculate the cobalt particle size. The average nanoparticle crystal size of the cobalt is about 40-50 nm for the 10Co/SiC, and about 15-25 nm for the 10Co/TiO_2-SiC, the later being predicted to be the most active particle size for the FTS process.[16] The results indicate that introduction of the TiO_2 phase into the SiC matrix significantly decreases the particle size of cobalt, probably by generating a higher

chemical interaction with the metal salt precursor without modifying the reduction behavior of the sample.

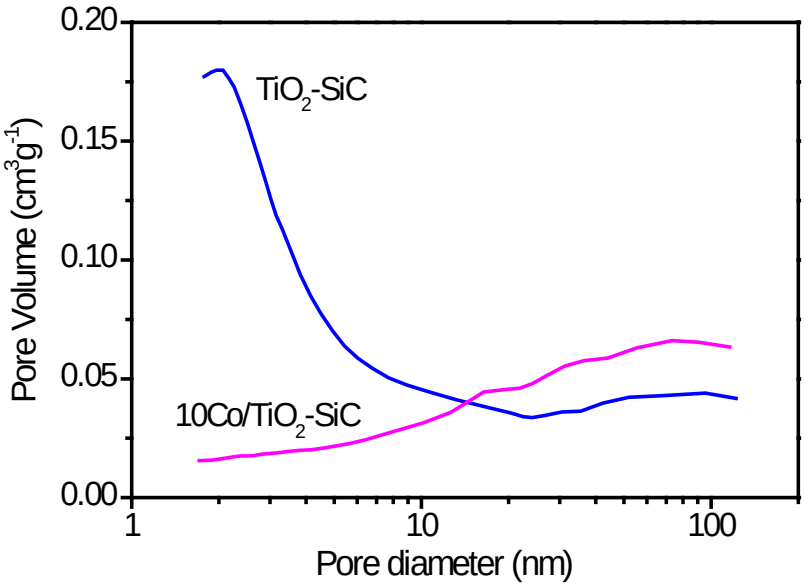

Figure 4-4. BJH pore size distribution of TiO_2-SiC support and 10Co/TiO_2-SiC catalyst.

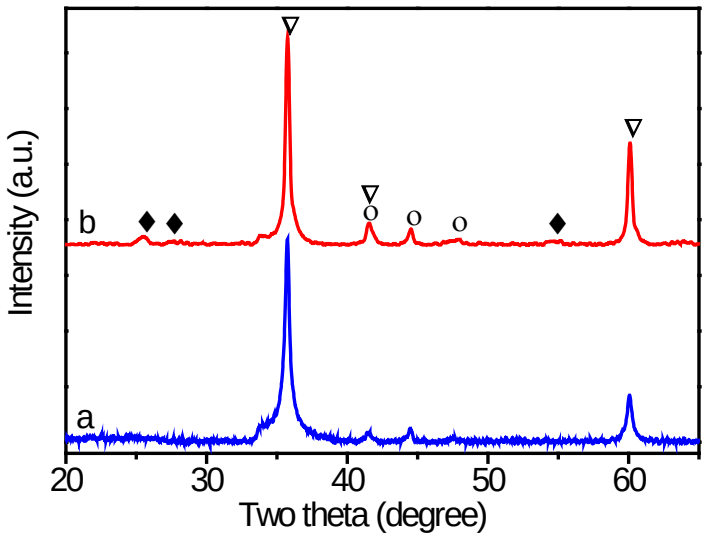

Figure 4-5. Ex-situ X-ray diffraction patterns of the catalysts: (a) 10Co/SiC; (b) 10Co/TiO_2-SiC. The catalysts were calcined at 350 ^oC for 2 h followed by reduction under H2 at 300 °C for 6 h. Legends: Diamond (♦): TiO_2; circles (○): Co; triangle (▽): SiC.

4.2.2 Reduction behavior of catalysts

The TPR spectra of the 10Co/SiC and 10Co/TiO_2-SiC catalysts are presented in Figure 4-6. The first reduction peak for both catalysts, located at around 230 °C, can be attributed to the decomposition of residual cobalt nitrate in the presence of hydrogen.[14, 41] In the paper published by Borg et al.[14], calcination temperatures above 450 °C are needed to completely decompose the supported cobalt nitrate. At lower calcination temperatures some nitrate still remains in the calcined sample which further decomposed in the presence of hydrogen at a relatively low temperature. The reduction of cobalt oxide species started at 230 °C and the first oxide reduction peak is typically assigned to the reduction of Co_3O_4 to CoO, although a fraction of the peak likely comprises the reduction of the larger, bulk-like CoO species to Co. The second reduction step is composed of overlapping peaks that are due to the reduction of CoO to Co. These peaks also include the reduction of cobalt species that interact with the support.[25, 27-28, 42] The tailing was observed after 500 °C in the TPR profile of 10Co/TiO_2-SiC which is likely attributed to small cobalt in strong interaction with TiO_2 and the reduction of cobalt silicate- and titanate-like species.[43] The reduction of cobalt silicate-like species was observed after 550 °C on 10Co/SiC catalyst.[27-28]

The sequential TPR analysis of 10Co/TiO_2-SiC catalyst is also performed, i.e. isothermal reduction at 300 °C for 2, 3, 4 and 6 h followed by a second in situ TPR (Figure 4-7), to ensure the complete reduction of the catalyst under the applied reduction conditions. According to the results one can state that after the reduction at 300 °C for 6 h all the cobalt oxide was reduced and no additional reduction peaks were observed in the TPR spectrum of the reduced catalyst. The reduction peaks located at around 700 ^oC in sequential TPR profiles (Figure 4-7) can be ascribed to the reduction of either cobalt titanate/silicate from the reaction between cobalt and the titania-silica layer or the fraction of cobalt in the inner cavities of the TiO_2-SiC support.[28, 43] This peak is absent in the TiO_2-SiC support which could again confirm the hypothesis above (Figure 4-7). Note that TPR experiments were conducted in 10 % H_2/Ar mixtures, whereas the catalysts were reduced in pure hydrogen for catalytic measurements which implies a much higher reduction rate. Chernavskii[44] reported

that the hydrogen partial pressure can significantly affect the extent of the cobalt reduction. A lower reduction temperature of cobalt is usually obtained in pure hydrogen. The TPR experiment was carried out under diluted hydrogen which could considerably lower the extent of the cobalt reduction compared with the reduction conducted under pure hydrogen flow. During the transfer one should expect that some superficial oxidation could occur, leading to the formation of a core-shell CoO-Co phase (see TEM analysis below). Such a surface oxide layer will be rapidly reduced by the CO and H_2 mixture during the FTS process.[26, 42, 44]

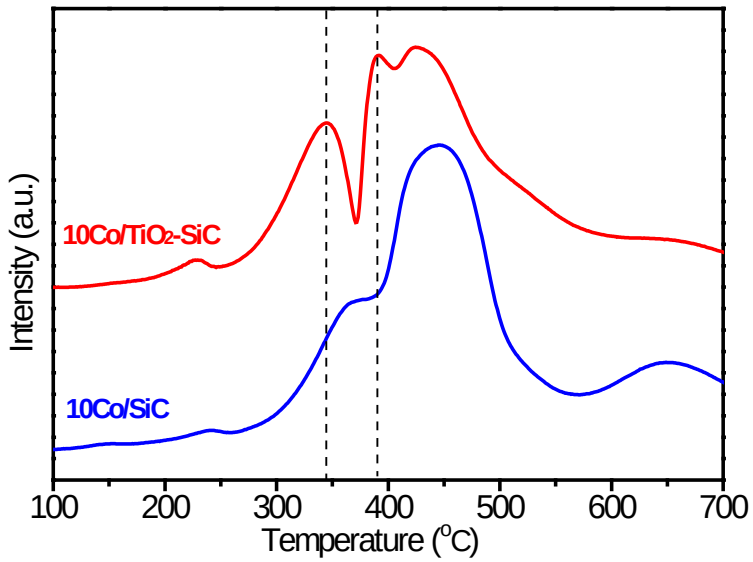

Figure 4-6. TPR profiles of the 10Co/SiC and 10Co/TiO_2-SiC catalysts after calcinations at 350 °C in air for 2 h.

4.2.3 Morphological and microstructural characterization

The corresponding SEM micrographs of the two catalysts after reduction are presented in Figure 4-8 and reveal the presence of a smaller average cobalt particle size in the decorated catalyst. The cobalt particle size is more homogeneous on the TiO_2 decorated SiC catalyst in comparison with the SiC catalyst. The cobalt particle size on the pure and TiO_2-decorated SiC catalysts was evaluated by TEM; the results are presented in Figure 4-9.

The TEM micrographs of the 10Co/SiC catalyst indicate the presence of a relatively homogeneous cobalt particle size with an average size of around 40 nm (Figure 4-9A and B) dispersed throughout the support surface. The 10Co/TiO_2-SiC catalyst shows (Figure 4-9C and D) two difference sizes particle on catalysts surface.

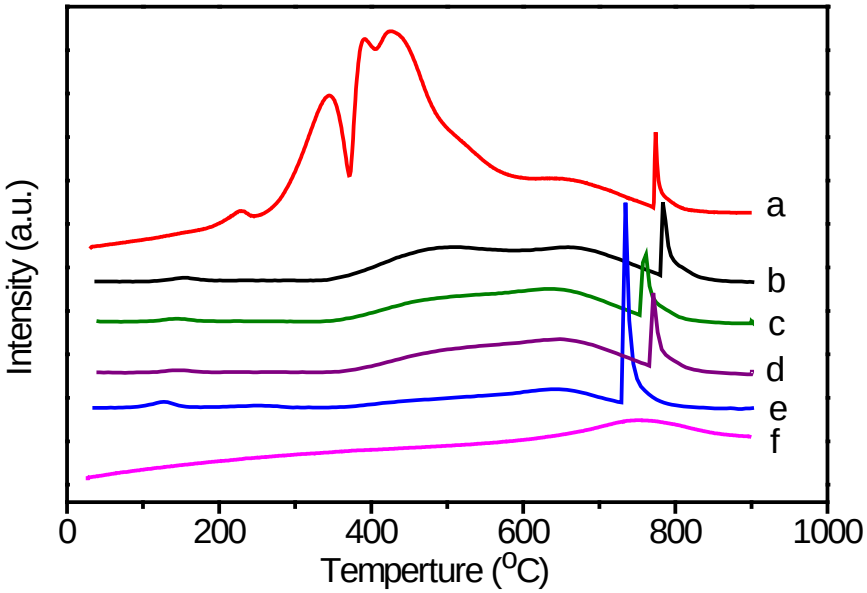

Figure 4-7. (a) The TPR of 10Co/TiO_2-SiC was directly test under diluted H_2 with heating rate of 15 $^oC\ min^{-1}$; sequential TPR of 10Co/TiO_2-SiC sample was reduced by diluted H_2 (10 vol. % in argon) at 300 ^oC for (b) 2h; (c) 3h; (d) 4h; (e) 6h in TPR equipment, and then reduced under the diluted H_2 with heating rate of 15 $^oC\ min^{-1}$. (f) TPR profile of TiO_2-SiC support.

To get more insight about the influence of the doping on the cobalt dispersion high-resolution TEM analysis and 2D EFTEM were carried out and the results are presented in Figures 4-10 and 4-11. The HR-TEM analysis was carried out on several areas within a large grain of catalyst (Figure 4-10A). TEM micrographs of the cobalt particles localized on or next to the TiO_2 phase clearly evidence the formation of cobalt metal nanoparticles with size smaller than 10 nm and well separated from each other due to the relatively high metal-support interaction with the TiO_2 phase underneath (Figure 4-10B). Similar results have also been reported by Park et al.[45] on the cobalt supported alumina support decorated

with titanium dioxide. The suppression of the cobalt aggregation during the thermal treatment step has been attributed by the authors to the presence of a local mixed phase containing both titanium and alumina which presents a medium metal-support interaction. It is expected that a similar phase could also be formed in the present work which provides a highly stable anchorage surface for the cobalt particles. High-resolution TEM micrographs (Figure 4-10C and D) clearly evidence that the cobalt particles were highly faceted and disordered which could provide anchorage sites for the adsorption and catalytic transformation of the carbon monoxide.

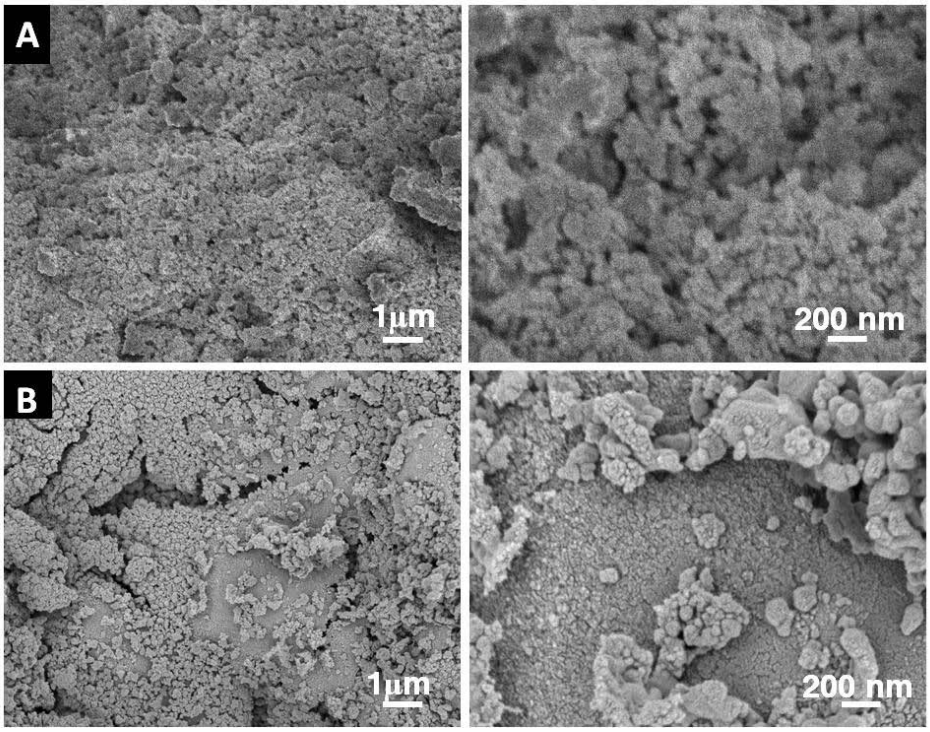

Figure 4-8. SEM micrographs of the catalysts after reduction under H_2 at 300 °C for 6 h. (A) 10Co/SiC, (B) 10Co/TiO_2-SiC.

From a classical 2D analysis by EFTEM imaging based on electron energy loss spectroscopy (EELS) (Figure 4-11), one can observe that the cobalt particle size becomes smaller in contact with the TiO_2 phase. As can be seen in Figure 4-11, the size of the cobalt particles was significantly changed depending on which surface they were in contact with,

i.e. 5 to 15 nm for the Co particles in contact with TiO_2 surface and 30 to 50 nm for Co particles directly supported on the SiC surface. Such results again confirm the high dispersion of the cobalt particles on the TiO_2 phase which will play a crucial role in the improvement of the FTS performance.

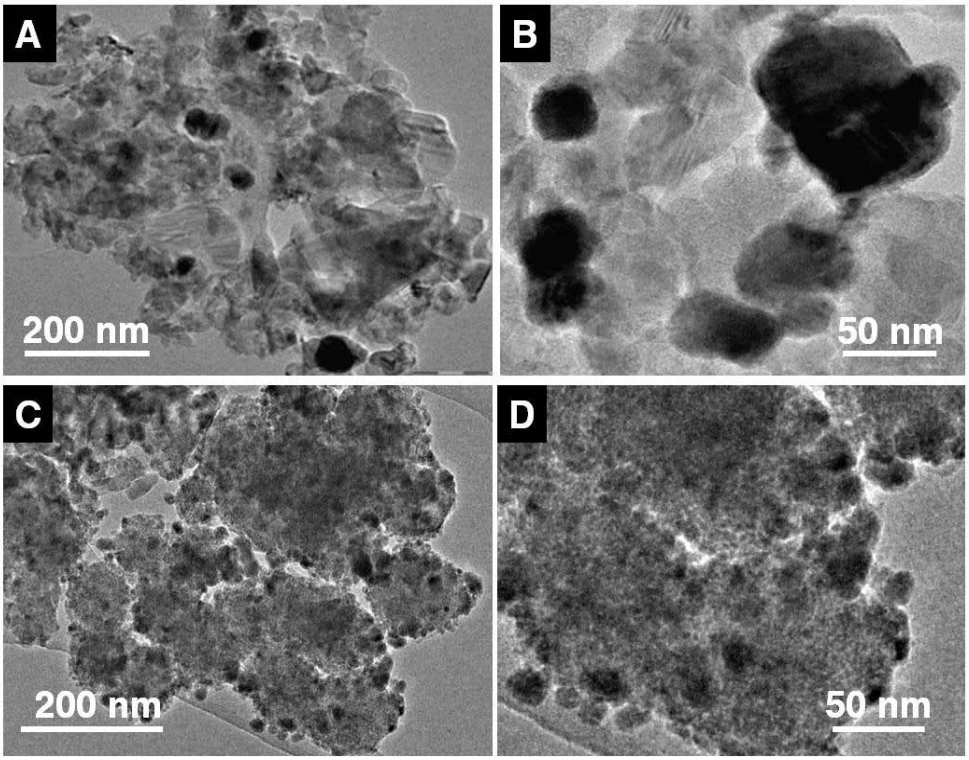

Figure 4-9. TEM images of (**A**, **B**) 10Co/SiC and (**C**, **D**) 10Co/TiO_2-SiC after reduction under H_2 at 300 °C for 6 h.

The formation of small cobalt particles when TiO_2 was introduced to the SiC support was also confirmed by ^{59}Co solid state NMR[25, 46-47]. The real advantage of this technique is that it is a bulk technique that allows one to have a general view of the cobalt phase inside the catalyst, which is not the case for the TEM and/or EFTEM techniques where only a small part of the active phase was analyzed. First of all, it has to be noted that the shape of the NMR spectra of the two samples under investigation is very similar (Figure 4-12A). In contrast to the results reported in ref.[25], it shows that the difference in activity of the

samples is not linked to the Co structure or chemical environment but, rather to the difference between the amount of surface area of the cobalt nanoparticles (Co NP). From the NMR data we have determined the fraction of cobalt atoms with different blocking temperature ranges (different size ranges) presented in Figure 4-13A.

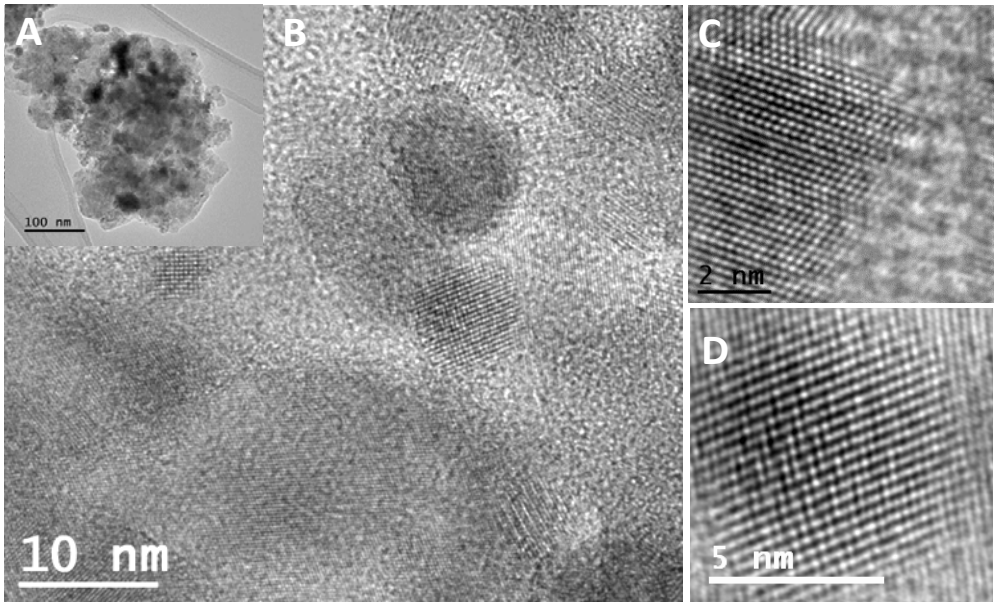

Figure 4-10. TEM analysis of the reduced 10Co/TiO_2-SiC catalyst. (**A**) Low-magnification TEM analysis. (**B**) Medium-resolution TEM micrograph showing the presence of several small cobalt particles next to the TiO_2 phase. (**C, D**) High-resolution TEM micrographs of the faceted cobalt particles.

According to the results, one can state that the fraction of cobalt atoms engaged in the small cobalt particles ∅ (< 4 nm) is higher in the 10Co/TiO_2-SiC than in the 10Co/SiC catalyst. There is almost no change of the number of Co atoms in the average size range, only is there a decrease in the number of Co atoms in the biggest particles size range. However, the activity is more related to the surface area of the Co NP active sites which contact with syngas (CO and H_2) than to the distribution of Co atoms itself. It is easy to understand that the largest the surface area of active sites offered by the catalyst (with the same cobalt microstructure), the largest is the amount of reactant molecules that can be activated. From the distribution of Co atoms, assuming an average particle size in each blocking temperature range, we worked out the Co NP surface area in the sample (Figure

4-13). The result in Figure 4-13B shows that the doping of the SiC support by TiO_2 increases the amounts of the cobalt particles in the small size range, via a strong metal-support interaction between the deposited cobalt precursor and the TiO_2 surface in the catalyst. This in turn leads to a higher FT performance (see below). This analysis also shows that there is a large number of Co atoms (about 60%) that are clustered into a very few number (less that 20%) of large (> 10 nm) Co particles. Research focusing on decreasing the number of large cobalt clusters to obtain highly active cobalt surface also requires further investigation.

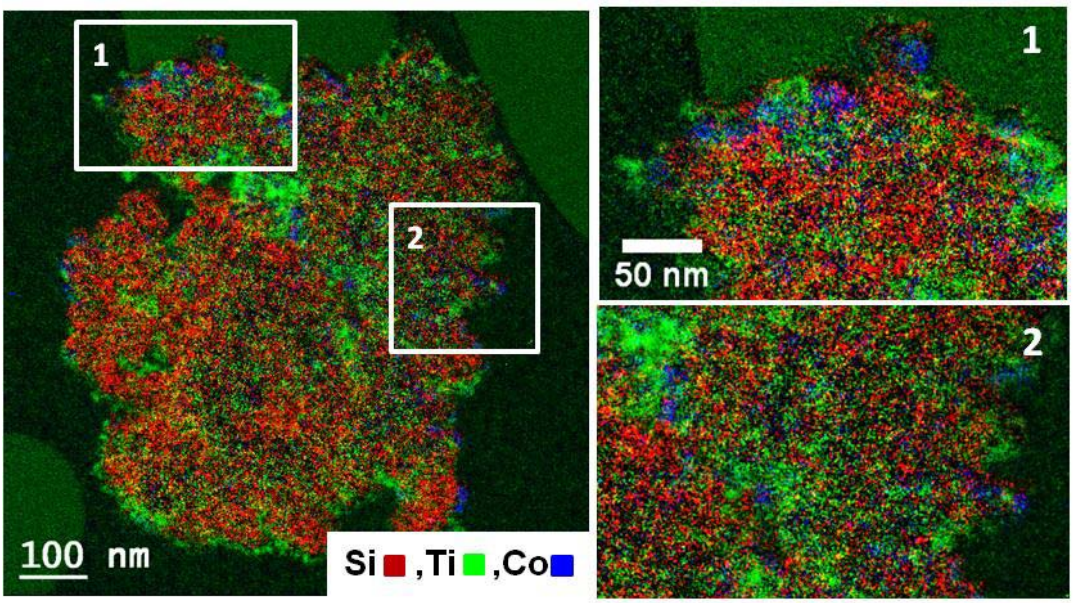

Figure 4-11. Representative 2D elemental relative maps deduced by EFTEM analysis for the 10Co/TiO_2-SiC sample; Ti (green), Si (red), Co (blue). The catalyst was calcined at 350 ^{o}C for 2 h followed by a reduction under H_2 at 300 ^{o}C for 6 h.

In addition, de Jong and co-workers[16, 48] found that small cobalt particles (< 6 nm) led to low FTS activity and high methane selectivity. Bezemer et al.[16] studied the influence of the cobalt particles size on the FTS reaction using carbon nanofibers as support. The highest CoTY (19.2 $\times 10^{-5}$ $mol_{co}g_{Co}^{-1}s^{-1}$) was observed with cobalt particle size centered at about 8 nm under severe reaction conditions, i.e. 35 bar and 250 $^{\circ}$C. In this work, most of the cobalt atoms (> 94%, Figure 4-13A) resulted in particles large than 6 nm and which provide active sites with high FTS activity. Similar results have also been reported previously on SiC foam

coated with a thin layer of alumina.[24] Indeed, the introduction of a thin alumina layer led to higher cobalt dispersion and an improvement in the FTS performance of the catalyst.[24] Reuel and Bartholomew[49] have reported that the FTS activity strongly depends on the nature of the support according to the following activity sequence: Co/TiO_2 > Co/Al_2O_3 > Co/SiO_2 > 100% Co > Co/MgO. However, it is worthy to note that the metal-support interaction between the cobalt oxide and the TiO_2 phase was not too strong, due to the relatively low reduction temperature used in the present work, which allows the facile reduction of the cobalt phase according to the XRD and TPR experiments presented above. It is well known that metal particles deposited on TiO_2 surface exhibit higher dispersion due to the strong metal-support interaction (SMSI) when reduction was conducted at temperature higher than 300 ^oC.[50] The local mixed phase formed between the TiO_2 and the surface SiO_2 on the SiC support could also be in part responsible for the high dispersion of the cobalt particles as well.

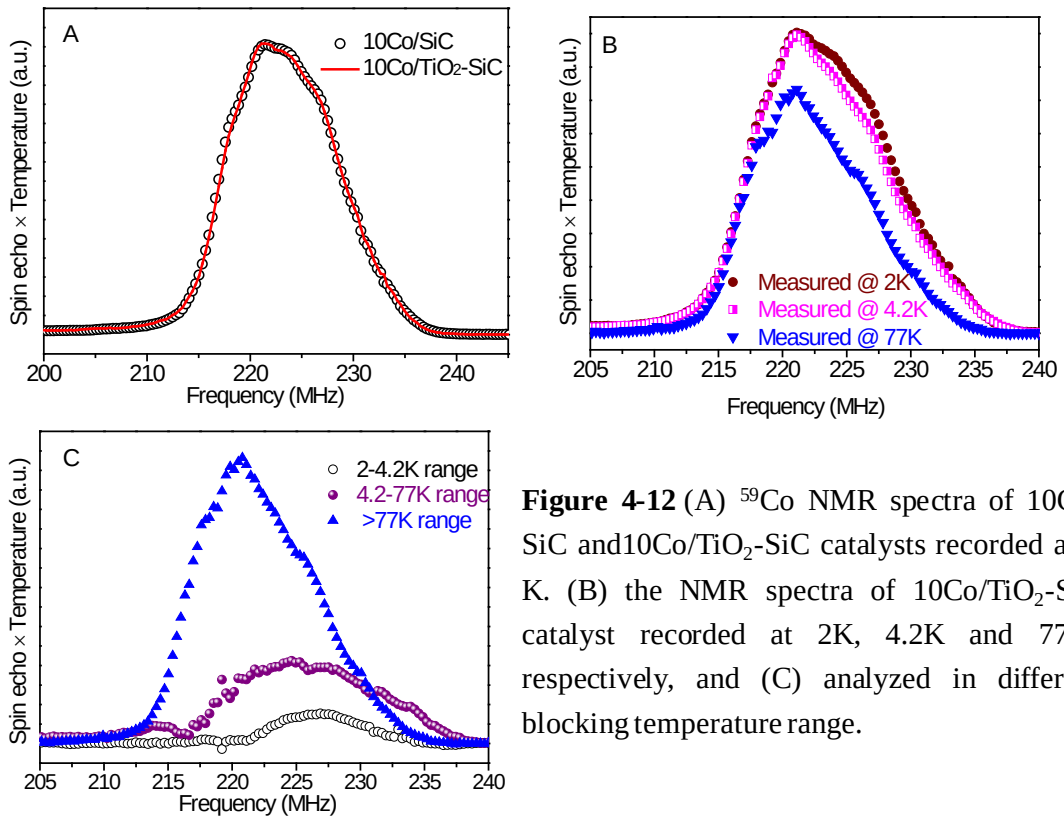

Figure 4-12 (A) ^{59}Co NMR spectra of 10Co/SiC and10Co/TiO_2-SiC catalysts recorded at 2 K. (B) the NMR spectra of 10Co/TiO_2-SiC catalyst recorded at 2K, 4.2K and 77K, respectively, and (C) analyzed in different blocking temperature range.

4.2.4 Fischer-Tropsch synthesis (FTS) catalytic performance

The FTS conversion rate (expressed in terms of cobalt time yield, $mol_{co}g_{Co}^{-1}s^{-1}$) and C_{5+} selectivity obtained on the 10Co/SiC and 10Co/TiO_2-SiC catalysts as a function of the reaction temperature and under a relatively high GHSV, 2850 h^{-1} (STP), are presented in Figure 4-14, the results are summarized in Table 4-2. The FTS rate steadily increases on both catalysts with increasing reaction temperatures, whereas S_{C5+} selectivity remains relatively high at around 91 % on both catalysts. It is worth noting that the FTS rate on the 10Co/TiO_2-SiC remains higher than the one obtained on the 10Co/SiC catalyst and steadily increases with increasing reaction temperatures. The high FTS catalytic performance of the decorated-SiC catalyst could be attributed to the better dispersion of the cobalt particles in the presence of the TiO_2 phase according to the XRD and EFTEM analysis. The FTS activity is linked to the active phase dispersion, and thus, the smaller the active phase particle size is (down to a certain level), the higher the FTS activity is. On the undecorated SiC-based catalyst the relatively low cobalt dispersion, i.e. 40-50 nm, was linked to the lower FTS activity observed. In the decorated catalyst the small cobalt particle size associated with the TiO_2 phase, i.e. 5-15 nm, seems to be responsible for the FTS activity enhancement. The relative percent of the small cobalt particles between the decorated and undecorated catalysts, calculated by the ^{59}Co NMR method, was about 30 % and correlates well with the 30 % FTS conversion rate improvement between the two catalysts (Table 4-2). Karaca et al.[51] reported that CoPt/Al_2O_3-N1 catalyst has much higher cobalt-time yields, i.e. 8.4 $\times 10^{-5}$ $mol_{co}g_{Co}^{-1}s^{-1}$ could be attributed to higher reducibility of smaller cobalt particles and higher concentration of cobalt active sites. The FTS activity also remains stable for the whole test, i.e. > 200 h, indicating that deactivation, i.e. carbonaceous deposition, sintering and/or superficial oxidation, is extremely low on such catalysts after stabilization. Similar results have already been reported by several research groups in the literature.[35, 40]

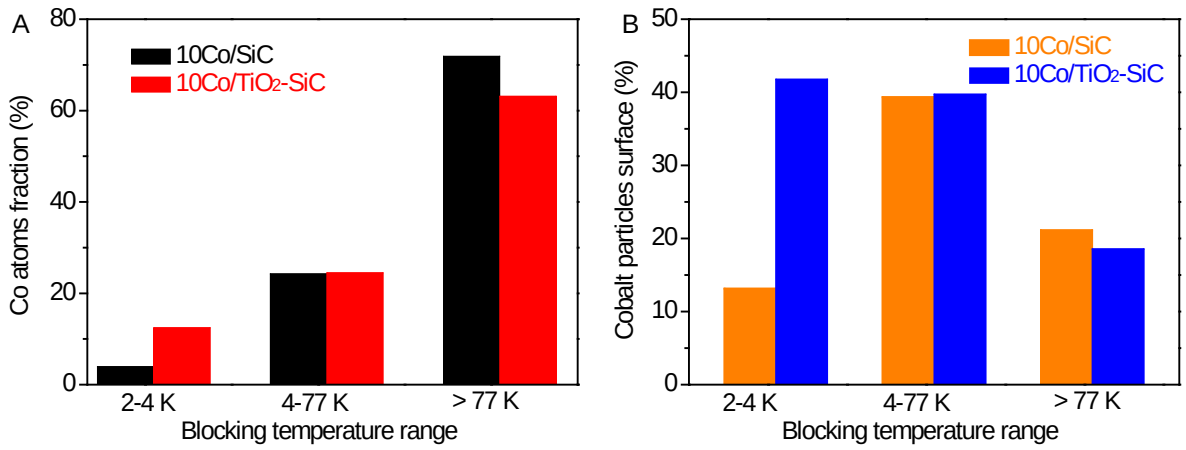

Figure 4-13. ^{59}Co zero field NMR results. (A) The fraction of cobalt atoms engaged in the different cobalt particle sizes as a function of the blocking temperature. (B) The relative number of cobalt nanoparticles surface as a function of the blocking temperature.

Table 4-2. The Fischer-Tropsch results obtained on the undecorated and decorated SiC containing cobalt catalysts.[a]

Catalyst	T(°C)	CO Conversion (%)	Product selectivity (%)				CoTY [b]
			CO_2	CH_4	C_2–C_4	C_{5+}	
10Co/SiC	215	26.9	0	2.9	1.6	95.5	4.0
	220	28.8	0	3.7	2.0	94.3	4.3
	225	32.3	0	4.5	2.4	93.1	4.8
	230	35.4	0.1	5.4	2.9	91.6	5.3
10Co/TiO_2-SiC	215	33.9	0	3.2	1.5	95.3	5.0
	220	37.0	0	3.9	1.7	94.4	5.5
	225	43.4	0	4.5	1.9	93.6	6.5
	230	50.5	0.2	5.9	2.2	91.7	7.5

[a] Reaction conditions: GHSV (STP) = 2850 h^{-1}, H_2/CO = 2, pure syngas, total pressure = 40 bar. [b]Cobalt-Time-Yield (CoTY, 10^{-5} $mol_{co}\cdot g_{Co}^{-1}s^{-1}$, molar CO conversion rate per g atom Co per hour)

The final carbon balance calculated from different experiments is 90 ± 4 wt% (Table 4-2). The discrepancy between the experimental and theoretical carbon balance could be due to several facts: (i) the uncertainty on the CO flow rate before and after reaction, which leads

to a carbon error of 5 ± 2 wt% in the carbon balance, (ii) the waxes which were lost during the recovery of waxes from the different traps accounting for about 5 ± 2 wt%. The most remarkable fact is that the S_{C5+} selectivity remains high whatever the reaction temperature up to 230 °C. The high S_{C5+} selectivity obtained in the present work could be attributed to several possibilities: (i) first, the homogeneous catalyst bed temperature thanks to the good thermal conductivity of the support and the liquid hydrocarbon film formed on the catalyst surface[52], (ii) second, the increased partial pressure of steam within the catalyst bed due to the relatively low space velocity.[53-54] The promoting effect of steam on the S_{C5+} has been proposed to be due to its inhibition of hydrogenation reactions leading to a lower methane selectivity.[55] (iii) The meso- and macro-porosity of the support which favor the evacuation of the products and a better accessibility to the reactants. A recent work published by Holmen and co-workers[14] on the low surface area α-Al_2O_3 catalyst has also pointed out the strong influence of the support porosity on the C_{5+} selectivity. Similar high C_{5+} selectivity was also reported recently by de la Osa et al.[26-27] on the large pore SiC-based catalysts either undecorated or decorated with calcium. The strong influence of the support porosity on the S_{C5+} selectivity could be explained by the enhanced evacuation of liquid hydrocarbons from the pores of the catalyst which significantly reduce the concentration gradients for CO versus H_2, as a result of the higher diffusivity of the later, next to the active sites localized within the pore. Indeed, high local concentration of H_2 versus CO next to the active site leads to higher selectivity toward formation of light products by rapid hydrogenation of the intermediate olefins.

The high reaction temperature contributes to higher cobalt time yields of both catalysts in this work; however, most catalysts with relatively high activity in the literature significantly result to more rapid deactivation.[56-57] It is interesting to see that the 10Co/SiC and 10Co/TiO_2-SiC catalysts also exhibit an extremely high stability as a function of the FTS test duration according to the results presented in Figure 4-15. Almost no deactivation is observed on the catalyst up to 100 h on stream which indicates that deactivation linked with

cobalt surface oxidation or sintering is unlikely to occur under the reaction conditions used in the present work.[57-58]

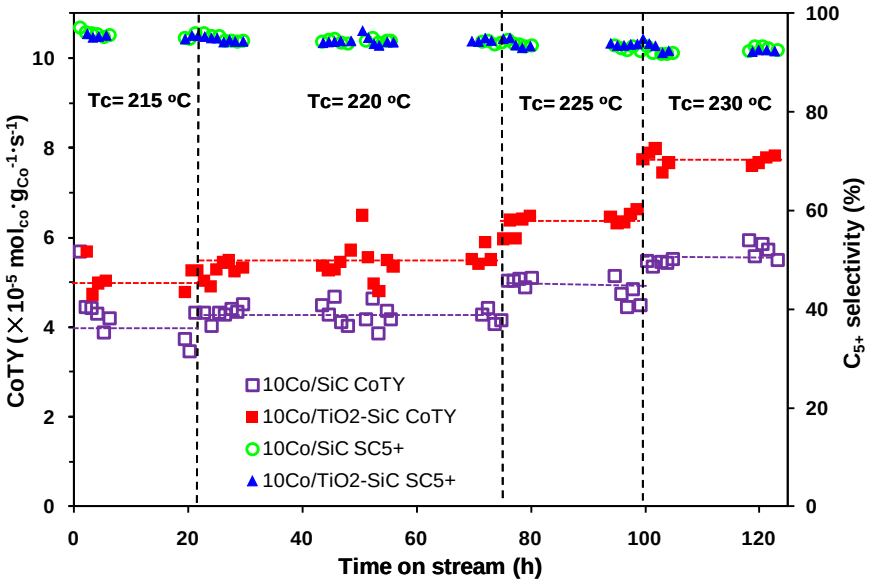

Figure 4-14. FTS rate and C_{5+} selectivity of the 10Co/SiC and 10Co/TiO_2-SiC catalyst as a function of the reaction temperature. Reaction conditions: H_2/CO = 2, pure syngas, total pressure = 40 bar, GHSV (STP) = 2850 h^{-1}.

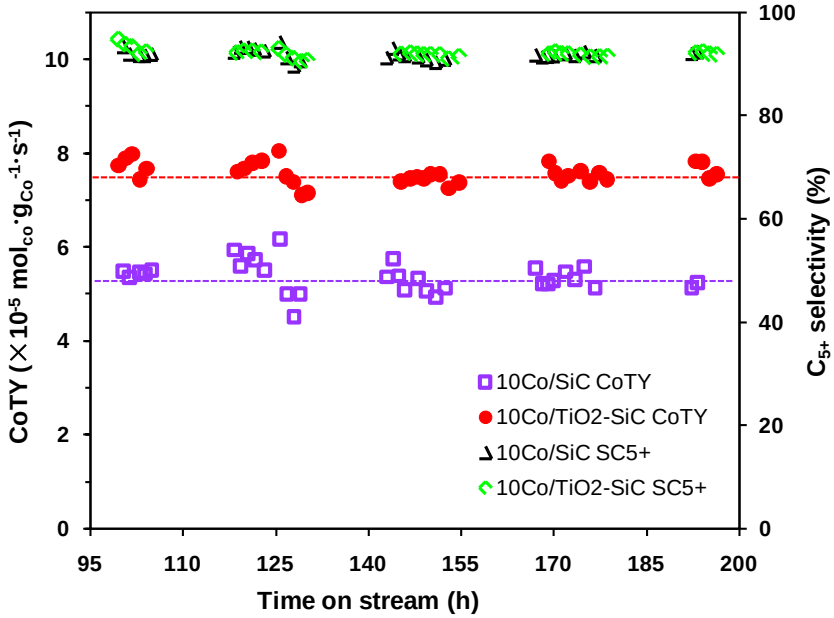

Figure 4-15. FTS performance and stability of the 10Co/SiC and 10Co/TiO_2-SiC catalyst as a function of time on stream at 230 °C. Reaction conditions: H2/CO molar ratio = 2, pure syngas, total pressure = 40 bar, GHSV (STP) = 2850 h^{-1}.

Furthermore, the product distribution of 10Co/SiC and 10Co/TiO_2-SiC catalysts is calculated; the results are presented in Figure 4-16. The chain growth factor (α) is obtained from the curve of ln(W_n/n) against n, where n is the chain length, W_n is the weight fraction of hydrocarbon with carbon numbers n. According to the results one can state that the chain growth factor (α) is relatively high on both catalysts, (0.92 for 10Co/SiC and 0.92 for TiO_2 doping catalyst), which is in good agreement with the relatively high C_{5+} selectivity obtained on both catalysts. The relatively high α-value observed on the SiC-based catalysts could be linked in part to with the intrinsic thermal conductivity of the support which prevents local hot spot formation, or to the inaccuracy linked to the analysis of waxes.

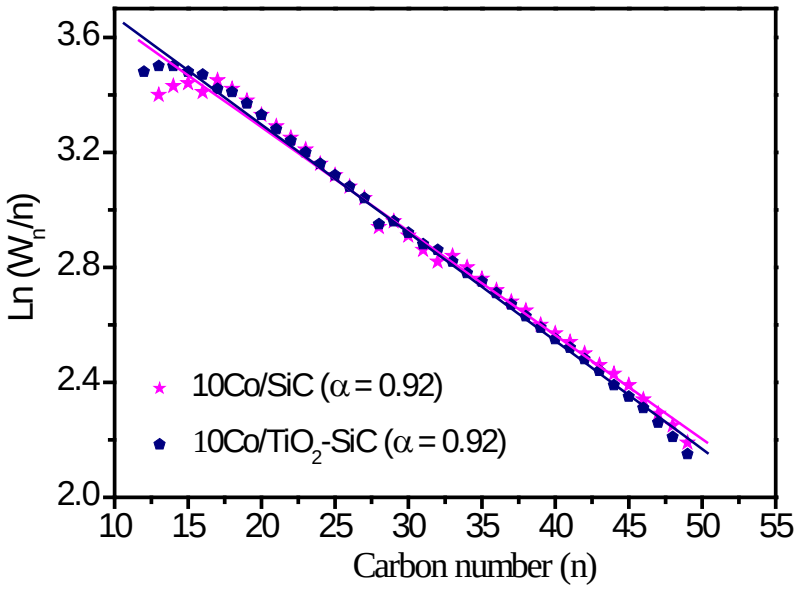

Figure 4-16. Calculated chain growth factor (α) from the linear portion of the liquid hydrocarbons recovered after FTS tests on the 10Co/SiC and 10Co/TiO_2-SiC catalysts.

In Figure 4-17, the FTS performances of the Ti-decorated SiC-based catalyst are compared with those reported on a similar catalyst supported on different supports.[28, 45, 59-61] These results clearly demonstrate that the cobalt time yield of the 10Co/TiO_2-SiC catalyst measured at 230 ^oC and GHSV of 2850 h^{-1} is 7.5×10^{-5} $mol_{co}g_{Co}^{-1}s^{-1}$ with a C_{5+} selectivity of

91.7%, which are typical for high catalytic activity without losing selectivity of long chain hydrocarbons.[25, 28] de la Osa et al.[28] investigated the influence of the calcium as promoter on the cobalt supported SiC catalyst and have observed a relatively high C_{5+} selectivity with high CO conversion on the 12Co-2Ca/SiC catalyst at 250 °C. The high S_{C5+} could be explained by the relatively high space velocity used by de la Osa et al.[28] during the FTS reaction.

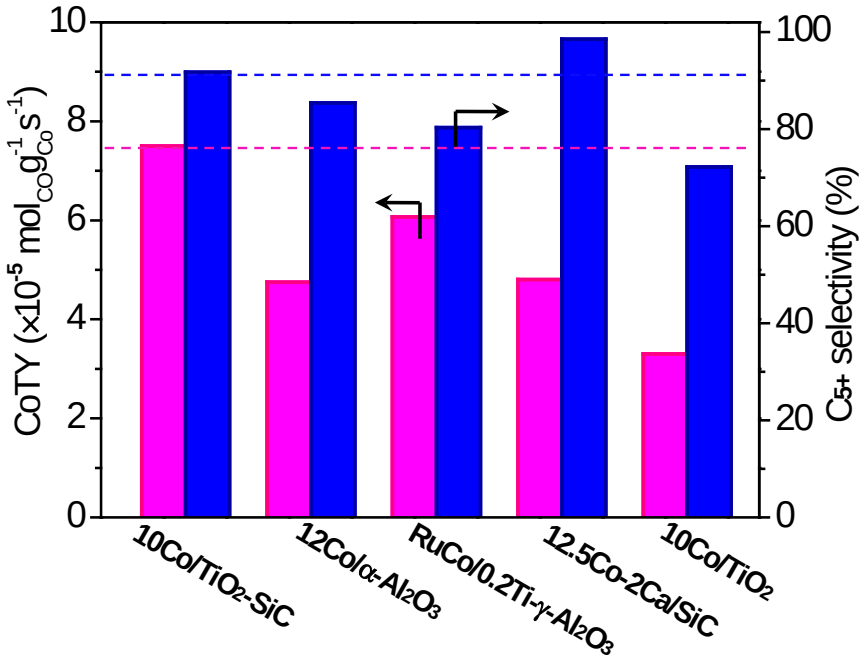

Figure 4-17. Comparison of FTS catalytic performance over different catalysts reported in literature.

The small porous network support γ-Al_2O_3 replaced by the one with larger pore size for the α-Al_2O_3-based catalyst to increase C_{5+} selectivity was investigated by Holmen and co-workers.[59, 62] The large pore α-Al_2O_3 support significantly reduces the problem of diffusion of reactants allowing the maintaining of a balance between CO and H_2, which leads to a high selectivity towards liquid hydrocarbons. Jalama et al.[60] used pure TiO_2 as support and even reduced the 10Co/TiO_2 catalyst with synthesis gas instead of pure H_2 during the FTS reaction. When the catalyst was activated under synthesis gas at 350 °C, the highest FTS activity of 3.3×10^{-5} $mol_{co}g_{Co}^{-1}s^{-1}$ was obtained compared to 1.5×10^{-5} $mol_{co}g_{Co}^{-1}s^{-1}$ for

the catalyst activated under pure hydrogen. The methane selectivity and C_{5+} selectivity were 17 % and 72 %, respectively. Breejen et al.[61] introduced MnO on $Co/Pt/SiO_2$ catalyst, followed by a calcinations step in a flow of 1vol% NO/He. For the $Co/Mn/Pt/SiO_2$ catalyst with an optimum Mn/Co atomic ratio of 0.08, an increase in C_{5+} selectivity from 32 wt% (unpromoted) to 54 wt% (promoted with Mn) was found, without a significant loss in cobalt time yield, that is 4.6×10^{-5} $mol_{co}g_{Co}^{-1}s^{-1}$ compared with 4.9×10^{-5} $mol_{co}g_{Co}^{-1}s^{-1}$.

4.2.5 Influence of the cobalt weight loading

In the industrial process, the metal loading is generally high at around 30 wt% to ensure a highest CO conversion per pass and to avoid costly recycling of the unreacted products. To study in depth the FTS performance of TiO_2-SiC support, the 30 wt% cobalt loading is introduced to obtain higher hydrocarbon productions per weight of catalyst.[63-64] Increasing the active phase loading per unit weight of catalyst inevitably decreases the CoTY value, and thus, comparison of the FTS performance between both cobalt-based catalysts with different cobalt loadings is carried out using a specific activity, FTS reaction rate representing the weight of long chain hydrocarbons (C_{5+}) formed per gram of catalyst per hour [$g_{C5+} \cdot g_{catalyst}^{-1} \cdot h^{-1}$], instead of the cobalt time yield value, as before. Figure 4-18 illustrates the influence of temperature (215 °C and 220 °C) on the catalytic performance of 10 wt% and 30 wt% cobalt on TiO_2-SiC catalysts. On the highly cobalt-loaded catalyst (Table 4-3), the FTS activity approaches a specific rate of 0.47 $g_{C5+} \cdot g_{catalyst}^{-1} \cdot h^{-1}$ with C_{5+} selectivity of 92.5%.

The stability of the Co/TiO_2-SiC catalyst under FTS conditions is also evaluated with time on stream under more severe FTS reaction conditions on cobalt-based catalysts (space velocity of 3800 h^{-1} and reaction temperature of 230 °C), and compared with the one obtained on an undecorated SiC containing a cobalt phase promoted with 0.1 wt% of ruthenium (Figure 4-19 and Table 4-4).[25] According to the results the TiO_2 decorated SiC-based catalyst exhibits a higher FTS performance than the undecorated one promoted with noble metal. The FTS activity also remains stable for about 30 h on stream and

confirms the relatively high stability of the catalyst promoted with TiO_2. The specific rate steadily increased to 0.56 $g_{C5+} \cdot g_{catalyst}^{-1} \cdot h^{-1}$ with a relatively higher C_{5+} selectivity, i.e. 90.6%. On the basis of our knowledge, the current result is the best among all the noble metal, promoter-free, cobalt-based catalysts in the literature, with both the highest specific rate and long-chain hydrocarbon selectivity. It is also worth noting that the specific rate obtained on the unpromoted 30Co/TiO_2-SiC catalyst is also relatively high and more stable compared to those promoted by noble metal obtained on the Co-Re/Al_2O_3, Co-Re/SiO_2 and Co-Re/TiO_2 catalysts as reported by Tsakoumis et al.[57] The most active catalyst reported in the work of Tsakoumis et al.[57] is the Co-Re/Al_2O_3 with an initial reaction rate of about 0.56 $g_{CH2} \cdot g_{catalyst} \cdot h^{-1}$ followed by a rapid deactivation down to 0.45 $g_{CH2} \cdot g_{catalyst}^{-1} \cdot h^{-1}$ after about 22 h on stream. It is also worth mentioning that the 30Co/TiO_2-SiC catalyst has been run for more than 200 h under different reaction conditions.

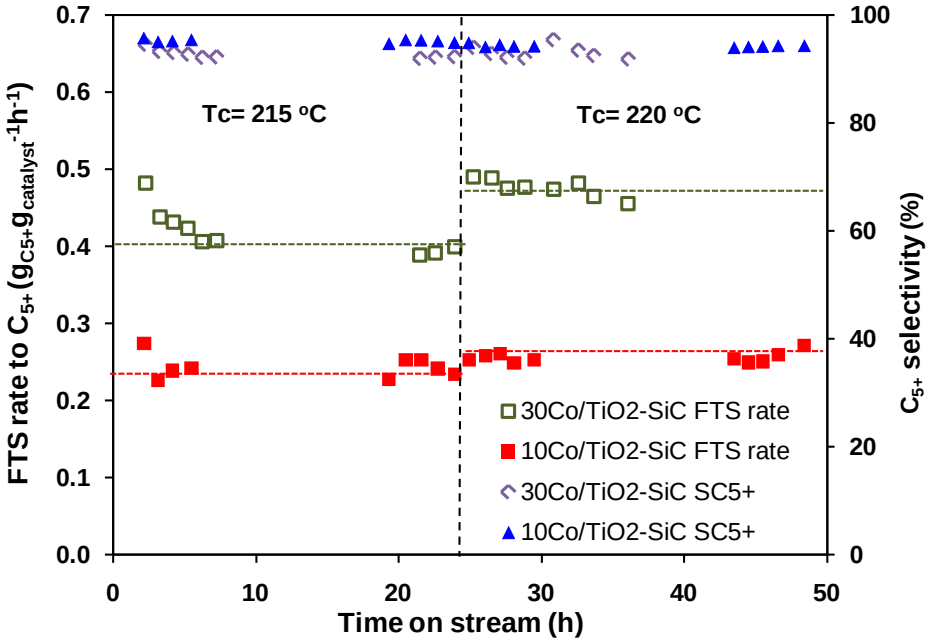

Figure 4-18. FTS reaction rate and C_{5+} selectivity as functions of time on stream on 10Co/TiO_2-SiC and 30Co/TiO_2-SiC catalysts. Reaction conditions: H_2/CO molar ratio = 2, pure syngas, total pressure = 40 bar, GHSV (STP) = 2850 h^{-1}

Table 4-3. Fischer-Tropsch results obtained on 10 wt% and 30 wt% cobalt on Titanium oxide decorated SiC-based.[a]

Catalyst	T(°C)	CO Conversion (%)	Product selectivity (%)				FTS rate[b]
			CO_2	CH_4	C_2–C_4	C_{5+}	
10Co/TiO_2-SiC	215	33.9	0	3.2	1.5	95.3	0.24
	220	37.0	0	3.9	1.7	94.4	0.26
30Co/TiO_2-SiC	215	57.7	3.1	4.7	0	92.2	0.40
	220	68.3	2.7	4.7	0	92.5	0.47

[a] Reaction conditions: GHSV = 2850 h^{-1}, H_2/CO = 2, pure syngas, total pressure = 40 bar.
[b] FTS rate, $g_{C5+} \cdot g_{catalyst}^{-1} \cdot h^{-1}$ (Mass C_{5+} produced per g catalyst per hour)

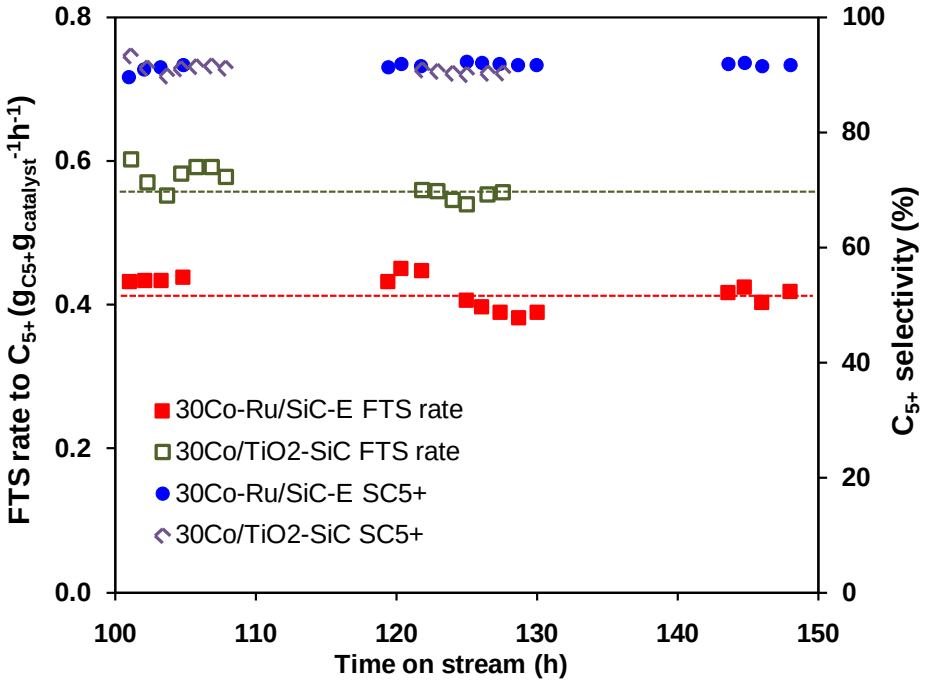

Figure 4-19. FTS reaction rate and C_{5+} selectivity as functions of time on stream on 30Co/TiO_2-SiC and Co-Ru/SiC-E[25] catalysts. Reaction conditions: H_2/CO = 2, pure syngas, total pressure = 40 bar, GHSV (STP) = 3800 h^{-1}, reaction temperature = 230 °C.

Table 4-4. Fischer-Tropsch synthesis performance under more severe reaction conditions. Reaction conditions: reaction temperature = 230 °C, GHSV = 3800 h^{-1}, H_2/CO = 2, pure syngas, total pressure = 40 bar.

Catalyst	CO Conversion (%)	Product selectivity (%)				FTS rate[#]
		CO_2	CH_4	C_2–C_4	C_{5+}	
30Co/TiO_2-SiC	61.8	3.1	6.2	0.1	90.6	0.56
30Co-Ru/SiC-E[25]	47.0	3.0	5.5	0.0	91.5	0.43

[#] FTS rate, $g_{C5+} \cdot g_{catalyst}^{-1} \cdot h^{-1}$ (Mass C_{5+} produced per g catalyst per hour)

4.3. Conclusions

Silicon carbide decorated with TiO_2 can be efficiently employed as a support for the cobalt phase in the low-temperature fixed-bed Fischer-Tropsch synthesis (FTS) reaction. The adequate pore size distribution of the support (meso- and macro-pores contribution) also facilitates the evacuation of the intermediate products, keeping the active sites more available for reactants. The intermediate product evacuation thus reduces the gradient concentration of the H_2 and CO next to the active site and prevents the formation of a light product while keeping the liquid hydrocarbon selectivity in a high range even at high conversion rate. The meso- and macroporosity of the support also prevent deactivation of the catalyst by pore plugging due to the formation of carbonaceous residues.

This study underlines once again the benefit of electron tomography applied in analytical mode for providing one-to-one correspondence between the morphology and chemical composition on a three-dimensional surface at the nanoscale. In particular and for the first time, it allows showing that the medium metal-support interaction between the cobalt nanoparticles and TiO_2 leads to the formation of small cobalt particles with enhanced FTS activity compared to the same catalyst supported on the undecorated SiC support. The presence of a higher amount of small and medium cobalt particles on the TiO_2-decorated SiC catalyst compared with that was observed on the undecorated one was also confirmed by

^{59}Co NMR. Indeed, such small metal particles (4-15 nm) with a large fraction of surface atoms significantly contribute to the enhancement of the conversion rate of reactants into products. After titanium doping, the cobalt time yield increased from 5.3×10^{-5} $mol_{co}g_{Co}^{-1}s^{-1}$ to 7.5×10^{-5} $mol_{co}g_{Co}^{-1}s^{-1}$ at 230 ^{o}C, while the C_{5+} selectivity is maintained in the same level, i.e. 91.7% and 91.6%, respectively. It is interesting to note that TiO_2-SiC-supported catalysts exhibit a relatively high specific rate along with a high liquid hydrocarbon selectivity compared with those previously reported in the literature under differential conditions. It can also be noted that the NMR analyses revealed that a large fraction of Co atoms (about 70 %) are included into a small number of very large particles that most probably are not very efficient for the FTS process. This allow us to think that it is still possible to strongly improve the efficiency of this kind of catalyst.

Finally, the high metal loading of 30 wt% cobalt is similar to those of commercial FTS catalysts and avoids costly recycling of the unreacted products. The superior FT specific rate of 0.56 $g_{HC}\cdot g_{catalyst}^{-1}\cdot h^{-1}$ with C_{5+} selectivity still at 91% was observed along the whole test. Work is ongoing to evaluate the influence of the support morphology on the Fischer-Tropsch performance on such kind of catalyst.

4.4 References

[1] A. Y. Khodakov, W. Chu, P. Fongarland, *Chemical Reviews* **2007**, *107*, 1692-1744.

[2] M. E. Dry, *Catal Today* **2002**, *71*, 227-241.

[3] A. Y. Khodakov, *Catal Today* **2009**, *144*, 251-257.

[4] D. Leckel, *Energ Fuel* **2009**, *23*, 2342-2358.

[5] Q. H. Zhang, J. C. Kang, Y. Wang, *ChemCatChem* **2010**, *2*, 1030-1058.

[6] G. M. Whitesides, G. W. Crabtree, *Science* **2007**, *315*, 796-798.

[7] T. M. Eggenhuisen, J. P. den Breejen, D. Verdoes, P. E. de Jongh, K. P. de Jong, *J Am Chem Soc* **2010**, *132*, 18318-18325.

[8] C. Perego, R. Bortolo, R. Zennaro, *Catal Today* **2009**, *142*, 9-16.

[9] J. I. Yang, J. H. Yang, H. J. Kim, H. Jung, D. H. Chun, H. T. Lee, *Fuel* **2010**, *89*, 237-243.

[10] N. Tsubaki, S. L. Sun, K. Fujimoto, *J Catal* **2001**, *199*, 236-246.

[11] W. Chu, L. N. Wang, P. A. Chernavskii, A. Y. Khodakov, *Angew Chem Int Edit* **2008**, *47*, 5052-5055.

[12] R. Oukaci, A. H. Singleton, J. G. Goodwin, *Appl Catal a-Gen* **1999**, *186*, 129-144.

[13] S. Storsaeter, O. Borg, E. A. Blekkan, B. Totdal, A. Holmen, *Catal Today* **2005**, *100*, 343-347.

[14] O. Borg, P. D. C. Dietzel, A. I. Spjelkavik, E. Z. Tveten, J. C. Walmsley, S. Diplas, S. Eri, A. Holmen, E. Ryttera, *J Catal* **2008**, *259*, 161-164.

[15] G. L. Bezemer, P. B. Radstake, V. Koot, A. J. van Dillen, J. W. Geus, K. P. de Jong, *J Catal* **2006**, *237*, 291-302.

[16] G. L. Bezemer, J. H. Bitter, H. P. C. E. Kuipers, H. Oosterbeek, J. E. Holewijn, X. D. Xu, F. Kapteijn, A. J. van Dillen, K. P. de Jong, *J Am Chem Soc* **2006**, *128*, 3956-3964.

[17] W. Chen, Z. L. Fan, X. L. Pan, X. H. Bao, *J Am Chem Soc* **2008**, *130*, 9414-9419.

[18] G. L. Bezemer, T. J. Remans, A. P. van Bavel, A. I. Dugulan, *J Am Chem Soc* **2010**, *132*, 8540-+.

[19] S. Zarubova, S. Rane, J. Yang, Y. D. Yu, Y. Zhu, D. Chen, A. Holmen, *Chemsuschem* **2011**, *4*, 935-942.

[20] G. Jacobs, Y. Y. Ji, B. H. Davis, D. Cronauer, A. J. Kropf, C. L. Marshall, *Appl Catal a-Gen* **2007**, *333*, 177-191.

[21] A. Voss, D. Borgmann, G. Wedler, *J Catal* **2002**, *212*, 10-21.

[22] G. Jacobs, T. K. Das, Y. Q. Zhang, J. L. Li, G. Racoillet, B. H. Davis, *Appl Catal a-Gen* **2002**, *233*, 263-281.

[23] Y. V. Wang, D.P.; Tonkovich A.L.Y.; Gao,Y.; Eddie G. Baker E.G., (Ed.: B. M. Institute), US, **2006**.

[24] M. Lacroix, L. Dreibine, B. de Tymowski, F. Vigneron, D. Edouard, D. Begin, P. Nguyen, C. Pham, S. Savin-Poncet, F. Luck, M. J. Ledoux, C. Pharn-Huu, *Appl Catal a-Gen* **2011**, *397*, 62-72.

[25] B. de Tymowski, Y. F. Liu, C. Meny, C. Lefevre, D. Begin, P. Nguyen, C. Pham, D. Edouard, F. Luck, C. Pham-Huu, *Appl Catal a-Gen* **2012**, *419*, 31-40.

[26] A. R. de la Osa, A. De Lucas, A. Romero, J. L. Valverde, P. Sanchez, *Catal Today* **2011**, *176*, 298-302.

[27] A. R. de la Osa, A. De Lucas, J. Diaz-Maroto, A. Romero, J. L. Valverde, P. Sanchez, *Catal Today* **2012**, *187*, 173-182.

[28] A. R. de la Osa, A. de Lucas, L. Sanchez-Silva, J. Diaz-Maroto, J. L. Valverde, *Fuel* **2012**, *95*, 587-598.

[29] H. M. T. Galvis, J. H. Bitter, C. B. Khare, M. Ruitenbeek, A. I. Dugulan, K. P. de Jong, *Science* **2012**, *335*, 835-838.

[30] M. J. Ledoux, C. Pham-Huu, *Cattech* **2001**, *5*, 226-246.

[31] A. Deneuve, I. Florea, O. Ersen, P. Nguyen, C. Pham, D. Begin, D. Edouard, M. J. Ledoux, C. Pham-Huu, *Appl Catal a-Gen* **2010**, *385*, 52-61.

[32] R. Philippe, M. Lacroix, L. Dreibine, C. Pham-Huu, D. Edouard, S. Savin, F. Luck, D. Schweich, *Catal Today* **2009**, *147*, S305-S312.

[33] A. Martinez, G. Prieto, J. Rollan, *J Catal* **2009**, *263*, 292-305.

[34] C. Lesaint, W. R. Glomm, O. Borg, S. Eri, E. Rytter, G. Oye, *Appl Catal a-Gen* **2008**, *351*, 131-135.

[35] T. Witoon, M. Chareonpanich, J. Limtrakul, *Fuel Process Technol* **2011**, *92*, 1498-1505.

[36] H. F. Xiong, M. A. M. Motchelaho, M. Moyo, L. L. Jewell, N. J. Coville, *J Catal* **2011**, *278*, 26-40.

[37] P. A. Midgley, M. Weyland, *Ultramicroscopy* **2003**, *96*, 413-431.

[38] G. Mobus, R. C. Doole, B. J. Inkson, *Ultramicroscopy* **2003**, *96*, 433-451.

[39] P. Nguyen, C. Pham, *Appl Catal a-Gen* **2011**, *391*, 443-454.

[40] S. Storsaeter, B. Totdal, J. C. Walmsley, B. S. Tanem, A. Holmen, *J Catal* **2005**, *236*, 139-152.

[41] O. Borg, E. A. Blekkan, S. Eri, D. Akporiaye, B. Vigerust, E. Rytter, A. Holmen, *Top Catal* **2007**, *45*, 39-43.

[42] A. Tavasoli, R. M. M. Abbaslou, A. K. Dalai, *Appl Catal a-Gen* **2008**, *346*, 58-64.

[43] R. Riva, H. Miessner, R. Vitali, G. Del Piero, *Appl Catal a-Gen* **2000**, *196*, 111-123.

[44] P. A. Chernavskii, A. Y. Khodakov, G. V. Pankina, J. S. Girardon, E. Quinet, *Appl Catal a-Gen* **2006**, *306*, 108-119.

[45] S. J. Park, S. M. Kim, M. H. Woo, J. W. Bae, K. W. Jun, K. S. Ha, *Appl Catal a-Gen* **2012**, *419*, 148-155.

[46] C. Meny, P. Panissod, (Ed.: G. A. Webb), Springer, Heidelberg, Germany **2006**.

[47] P. Panissod, C. Meny, *Appl Magn Reson* **2000**, *19*, 447-460.

[48] J. P. den Breejen, P. B. Radstake, G. L. Bezemer, J. H. Bitter, V. Froseth, A. Holmen, K. P. de Jong, *J Am Chem Soc* **2009**, *131*, 7197-7203.

[49] R. C. Reuel, C. H. Bartholomew, *J Catal* **1984**, *85*, 78-88.

[50] Y. Z. Li, Y. N. Fan, H. P. Yang, B. L. Xu, L. Y. Feng, M. F. Yang, Y. Chen, *Chem Phys Lett* **2003**, *372*, 160-165.

[51] H. Karaca, O. V. Safonova, S. Chambrey, P. Fongarland, P. Roussel, A. Griboval-Constant, M. Lacroix, A. Y. Khodakov, *J Catal* **2011**, *277*, 14-26.

[52] X. W. Zhu, X. J. Lu, X. Y. Liu, D. Hildebrandt, D. Glasser, *Ind Eng Chem Res* **2010**, *49*, 10682-10688.

[53] E. Rytter, S. Eri, T. H. Skagseth, D. Schanke, E. Bergene, R. Myrstad, A. Lindvag, *Ind Eng Chem Res* **2007**, *46*, 9032-9036.

[54] S. Krishnamoorthy, M. Tu, M. P. Ojeda, D. Pinna, E. Iglesia, *J Catal* **2002**, *211*, 422-433.

[55] E. Iglesia, *Appl Catal a-Gen* **1997**, *161*, 59-78.

[56] O. Borg, N. Hammer, S. Eri, O. A. Lindvag, R. Myrstad, E. A. Blekkan, M. Ronning, E. Rytter, A. Holmen, *Catal Today* **2009**, *142*, 70-77.

[57] N. E. Tsakoumis, M. Ronning, O. Borg, E. Rytter, A. Holmen, *Catal Today* **2010**, *154*, 162-182.

[58] G. B. Yu, B. Sun, Y. Pei, S. H. Xie, S. R. Yan, M. H. Qiao, K. N. Fan, X. X. Zhang, B. N. Zong, *J Am Chem Soc* **2010**, *132*, 935-+.

[59] S. Rane, O. Borg, J. Yang, E. Rytter, A. Holmen, *Appl Catal a-Gen* **2010**, *388*, 160-167.

[60] K. Jalama, J. Kabuba, H. F. Xiong, L. L. Jewell, *Catal Commun* **2012**, *17*, 154-159.

[61] J. P. den Breejen, A. M. Frey, J. Yang, A. Holmen, M. M. van Schooneveld, F. M. F. de Groot, O. Stephan, J. H. Bitter, K. P. de Jong, *Top Catal* **2011**, *54*, 768-777.

[62] C. Aaserud, A. M. Hilmen, E. Bergene, S. Eric, D. Schanke, A. Holmen, *Catal Lett* **2004**, *94*, 171-176.

[63] F. Diehl, A. Y. Khodakov, *Oil Gas Sci Technol* **2009**, *64*, 11-24.

[64] B. H. Davis, *Ind Eng Chem Res* **2007**, *46*, 8938-8945.

[Part-B] Microstructural analysis and energy filtered TEM imaging to investigate the structure-activity relationship in Fischer-Tropsch catalysts

4.5 Introduction

The decrease of the proven oil reserves and the huge increase in the worldwide energy demand, especially in emerging countries such as China and India, have driven the industrial interest to other sources of energy supply such as coal, natural and biomass.[1-3] These primary materials are subsequently transformed by reacting either with steam or oxygen to synthesis gas mixture following its conversion into valuable ultra clean synthetic fuels. The Fischer-Tropsch synthesis (FTS) is a key technology in the more global Gas-To-Liquids (GTL) process which allows the transformation of synthesis gas ($2H_2$ + CO), originated from natural gas reforming into liquid hydrocarbons, followed by hydrocracking of the heavy fraction into useful compounds such as naphtha, diesel, lubricants and others.[2-4] The FTS fuels are free of sulfur, nitrogen and aromatic compounds which render them extremely useful in the field of transportation taken into account the increasingly stringent environmental legislation on transportation fuels. In addition, the FTS has received a renewed interest during the last decade according to the number of FTS plants operated since the last years.[5] The industrial interest in the FTS development is mostly induced by the recent oil price volatility and is also driven by a low price of gas consecutively to the large scale exploitation of shale gas. A large research effort has been devoted to the improvement of the FTS catalyst both in terms of activity and selectivity to reduce the cost of the process. High activity allows to reduce the amount of catalyst needed for the same production and to decrease the amount of waste generated during the catalyst forming. High selectivity allows the maximizing of the desired products and to reduce the by-products such as light hydrocarbons or CO_2. Among the

parameters which could strongly influence the FTS performance the development of new support represents a core issue.

The most employed active phase for the low-temperature FTS process is cobalt, either pure or doped with trace amounts of noble metal, to enhance the reduction of the active phase and to improve the metal particles dispersion.[6-9] Cobalt presents several advantages such as: high stability, high activity for liquid hydrocarbons formation and low selectivity towards oxygenated products, resistance towards oxidation, low water-gas shift (WGS) tendency and acceptable price for industrial development. Industrial cobalt catalysts consist of cobalt nanoparticles well dispersed on a high surface area support to increase as much as possible the active site density along with a relatively high cobalt loading.[3] The support should display a relatively high specific surface area to promote a high dispersion of the metal particles, good mechanical and hydrothermal resistance and a medium level of metal-support interaction to allow a complete reduction of the active phase and to prevent sintering of the latter. The most employed supports for the FTS are alumina, silica, titania and carbon-based materials such as activated carbon, carbon nanotubes and nanofibers.[6, 10-16] Amongst the different industrial catalyst supports, silicon carbide (β-SiC), pure or doped, with medium to high specific surface area (20 to > 100 $m^2. g^{-1}$) synthesized by a gas-solid process[17-18] has received an over increasing scientific and industrial interest for replacing traditional supports such as alumina and silica in several catalytic processes such as selective izomerization of long chain alkanes, selective oxidation of sulfur compounds and short chain alkanes, natural gas reforming and hydrogenation of C=C bond.[19-27] Silicon carbide-based catalysts have also been successfully used as support for cobalt in the low-temperature fixed bed FTS process. The SiC-based catalysts exhibit a relatively high activity along with an extremely high selectivity towards long chain hydrocarbons.[28-33] The high C_{5+} selectivity obtained on the SiC-based catalysts was attributed to the better thermal conductivity of the SiC support compared to the traditional ones, alumina, silica, which allows the significant reduction of the hot spot formation within the catalyst bed, especially in a highly exothermic reaction. The high C_{5+} selectivity was also linked with the porosity of the support. Indeed, SiC

also exhibits a meso- and macroporous network[34] which allows a high accessibility of the reactant towards the active site and also to favor the escaping of the products from the catalyst bed. The relatively high chemical inertness of the SiC also allows facilitate the active phase and support recovery by a simple acid washing which is not the case with traditional oxide supports.[28]

Transmission electron microscopy (TEM) applied in its different modes is a characterization tool often used in catalysis, especially in the case of heterogeneous nanomaterials. A large variety of information can be obtained (structural, morphological, chemical, magnetic and so on) by analyzing the same object, providing thus a complete analysis of the studied specimens within a multi-selective approach. For instance, the crystallographic structure and the chemical composition of a catalytic grain can be simultaneously determined by combining the high-resolution and energy filtered TEM (EFTEM) modes. The first set-up of the tomographic approach in electron microscopy (3D-TEM or electron tomography) was devoted to the analysis of the porous network in mesoporous catalysts.[35] During the last decade, the benefits of this 3D selective technique for solving the shape, internal structure and morphology of complex nano-objects and aggregated was largely demonstrated. By combining the tomographic approach with EFTEM imaging, 3D chemical maps at the nanometer scale can be obtained, opening the way of a new TEM-based characterization tool at the nanometers scale, i.e. analytical tomography. Its usefulness for the characterization of chemically inhomogeneous nanomaterials was particularly demonstrated in the case of a beta-SiC grain, where a difference in the oxidation degree between the two type of pores was thus evidenced.[36]

The first goal of the present article is to illustrate the ability of the advanced characterization techniques based on TEM to precisely solve the microstructural and chemical characteristics of the heterogenous nanomaterials used currently in catalysis. Performing detailed analysis of these materials at different steps of their synthesis allowed us to develop a new type of FTS support based on the silicon carbide doped with titanium dioxide, which was the second goal of this work. The main characterization technique used for this purpose was

transmission electron microscopy in traditional and high resolution mode coupled with EFTEM imaging based on electron energy loss spectroscopy (TEM-EELS). They allowed us to investigate the influence of the doping on the microstructure of the active phase and also on the stability of this latter during the course of the reaction. Xin et al.[37] demonstrated the correlation between cobalt valence state and nanoporous structure by in-situ environmental TEM and EELS, which proved efficiently the optimum reduction temperature at around 400 ^{o}C in commercial process using SiO_2 as support. Herein, the results obtained by HR-TEM, 2D EFTEM and analytical tomography will be directly correlated with the catalytic ones to make a clear structure-activity relationship in the Co/TiO_2-SiC catalyst used in the F-T process. Such structure-activity correlation will allows one to optimize the support regarding the development of a new F-T catalyst with better performance and life-time.

4.6 Results and discussion

4.6.1 Support characteristics

The XRD pattern of the TiO_2-SiC (Ti loading of ca. 17 wt.% according to elemental analysis) support is presented in Figure 1A and confirms the complete oxidation of the TiC into TiO_2. XRD analysis indicates that TiO_2 is presented in two crystalline phases: anatase and rutile. The average crystallite size of the TiO_2 deduced from the X-ray line broadening using the Scherrer formula was about 21 ± 3 nm for the anatase phase and 16 ± 3 nm for the rutile phase. The TiC to TiO_2 transformation was also accompanied by a significant increase of the overall specific surface area of the support from 77 to 110 m^2 g^{-1}. The increase of the specific surface area after the calcinations process was attributed to the formation of a microporous network consecutively to the TiC-to-TiO_2 transformation according to the pore size distribution determined from the desorption branch of the N_2 isotherm (not shown). The final support consists in small TiO_2 particles dispersed within the matrix of silicon carbide made of relatively large crystals, which is in good agreement with the TEM and EFTEM results (see below). The oxidation process does not modify considerably the morphology of the material according to the SEM analysis (not shown). The representative SEM images of

the calcined support indicate that the large macropores of the TiC-SiC were completely retained after the calcinations process (Figure 4-20B).

It is worthy to note that the SiC synthesized by the gas-solid reaction typically contains large pore network as evidenced by the TEM tomography presented in Figure 4-21. Such pores will speed-up the mass transfer of the liquid hydrocarbons from the inner to the outer surface of the catalyst during the F-T reaction and prevent gradient concentration of the reactant within the pore which ultimately leads to a higher selectivity towards light products.

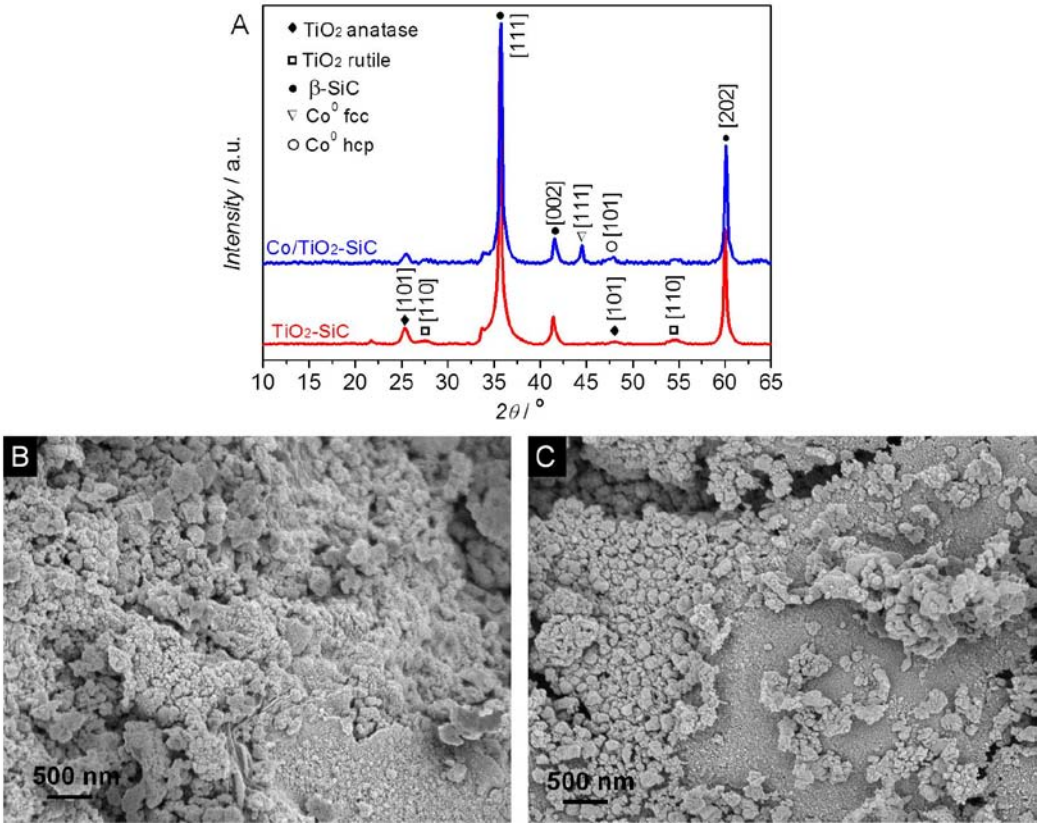

Figure 4-20. (A) XRD patterns of the TiO_2-SiC and Co/TiO_2-SiC catalysts after reduction in H_2 at 300 ^oC for 6 h, (B), (C) SEM micrographs of the TiO_2-SiC support and reduced Co/TiO_2-SiC catalyst, respectively.

Figures 4-22 displays the results obtained from the chemical EFTEM analysis of two typical grains of the as-prepared TiO_2 doped SiC support. Though the superposition effect is

present in such 2D projections, reliable qualitative information can be yet deduced by comparing the two elemental Si and Ti maps or the 2D relative map obtained by superposing Si (in red) and Ti (in green). We can observe that the TiO_2 phase is relatively well dispersed throughout the support that confirms the high efficiency of the synthesis method to generate doped material. The average particle size of the TiO_2 determined from such Ti elemental maps is about 20 ± 5 nm. In some parts of the grains the dispersion of the doping seems to be less homogeneous. This inhomogeneity could be attributed to the problem of mechanical mixing of the two phases within the precursor matrix. Note that work is ongoing to optimize the mixing of the precursors before carburization to improve the dispersion of the doping inside the final composite material.

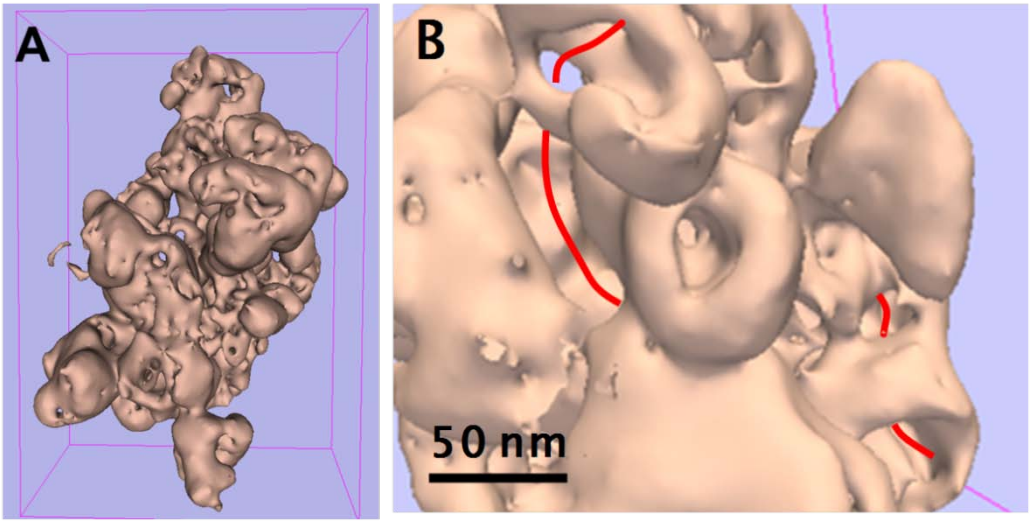

Figure 4-21. 3D model of a typical beta-SiC grain obtained by classical TEM tomography, illustrating the global morphology and the coexistence of two type of pores (left) and the presence of interconnected large pores (right), indicated by a red line.

4.6.2 Catalyst characteristics

The cobalt content determined by the elemental analysis was 10.5 ± 0.5 wt% and 10.7 ± 0.5 wt% for Co/SiC and Co/TiO_2-SiC (Table 4-5), respectively, which is relatively close to

the theoretical loading value fixed at 10 wt%. The XRD pattern of the Co/TiO_2-SiC is presented in Figure 4-20A and confirms the complete reduction of cobalt in the catalyst. However, during the catalysts transfer it is expected that some superficial oxidation could occurr leading to the formation of a thin layer of cobalt oxide on the topmost surface which was not detected by XRD. This superficial oxide layer is expected to be reduced during the reaction under the synthesis gas mixture. It was attributed to the relatively low metal-support interactions between the active phase and the SiC and TiO_2 surfaces.[29] The cobalt is presented in two crystalline structure, i.e. hexagonal close packed (hcp) and face centered cubic (fcc), while the average crystallite size deduced from the X-ray line broadening is 14 ± 5 nm (hcp) and 44 ± 5 nm (fcc).[38]

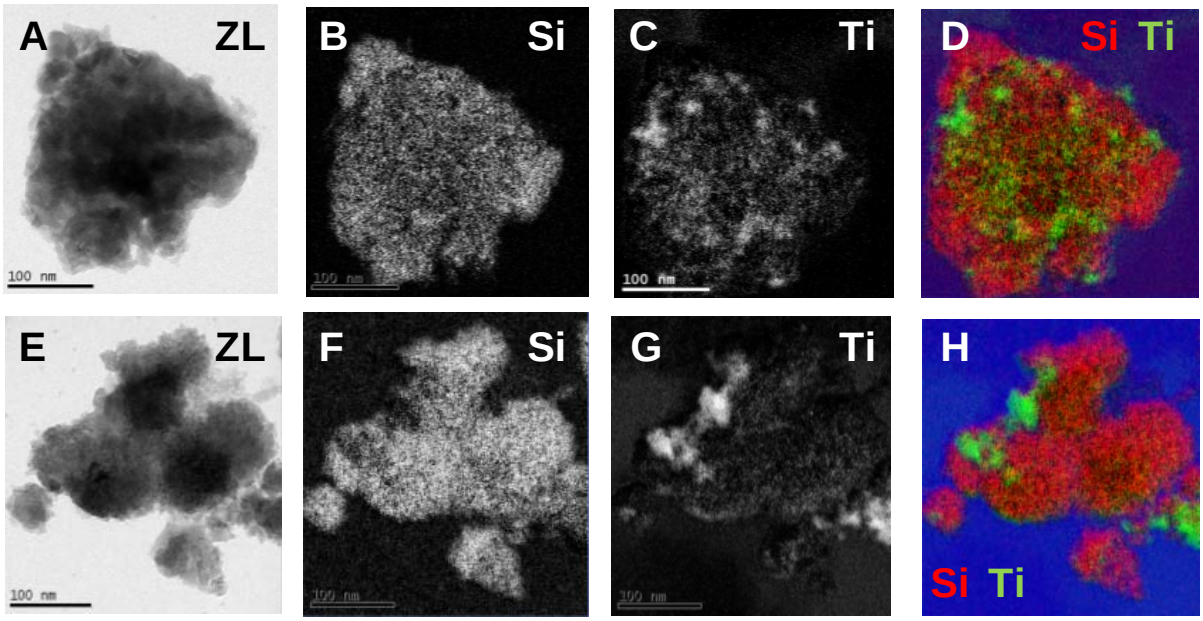

Figure 4-22. Chemical 2D analysis of two typical grains of TiO_2-SiC support obtained by EFTEM imaging at the L_{23} edges of Si and Ti. (A), (E) Zero loss (ZL) images, (B), (F) Si 2D elemental maps obtained by using the three windows method from the energy-filtered images recorded at the Si-L_{23} ionization edge. (C), (G) Ti 2D elemental maps calculated at the Ti-L_{23} ionization edge. (D), (H) 2D Relative map with Si in red and Ti in green showing the relative distribution of SiC and TiO_2 compounds.

The SEM micrograph of the Co/TiO_2-SiC catalyst after reduction is presented in Figure 4-20C and shows the presence of a homogeneous layer of cobalt nanoparticles covering the surface of the catalyst. To check out the homogeneous coverage of the support surface by the cobalt phase, EDX analysis was also performed on the sample and the corresponding results are presented in Figure 4-23. According to the results, the titania and the cobalt phases are well distributed over the catalyst surface and confirm the high dispersion of this latter.

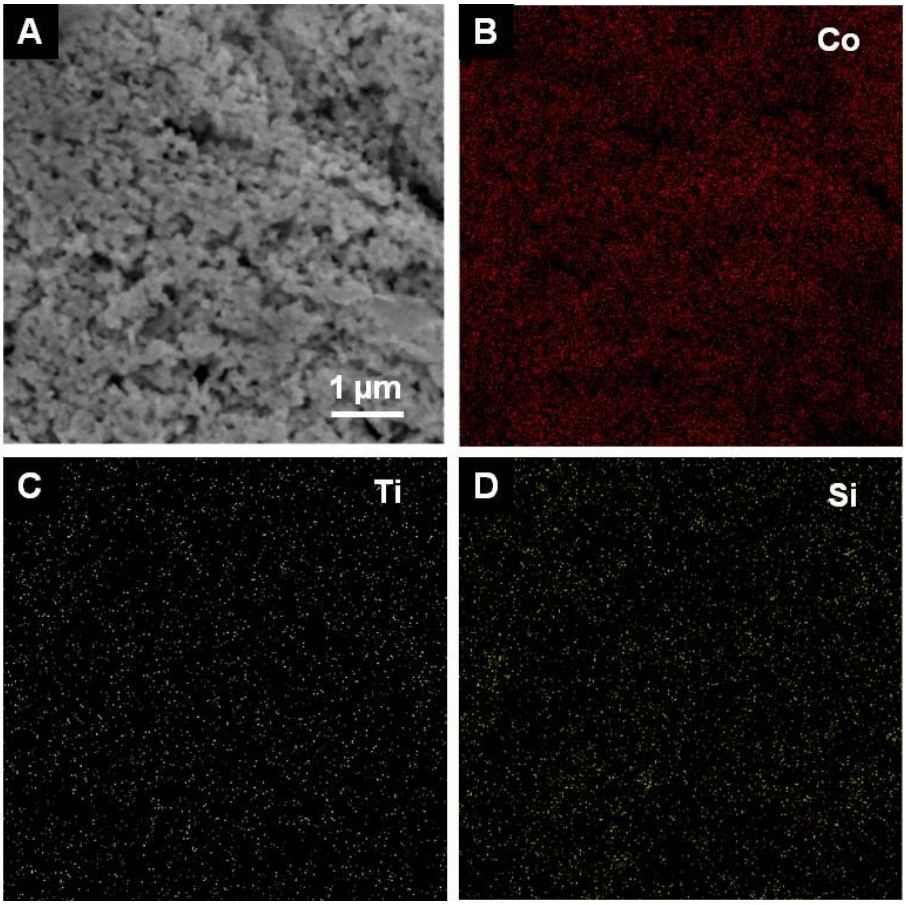

Figure 4-23. SEM micrograph and the corresponding EDX mapping of the reduced Co/TiO_2-SiC catalyst showing the homogeneous distribution of the TiO_2 and Co phases on the catalyst surface.

It is also worthy to note that the TiO_2 phase was not modified during the reduction process according to the TPR results presented in Figure 4-24. The TPR spectrum recorded on the TiO_2/SiC alone indicates that no reduction of TiO_2 phase has occurred up to about 650 °C

and thus, during the reduction at 300 °C, even for 6 h, one should not expect a substantial reduction of the TiO_2 phase. The first oxide reduction peak is typically assigned to the reduction of Co_3O_4 to CoO, although a fraction of the peak likely comprises the reduction of the larger, bulk-like CoO species to Co. The second reduction step is composed of several overlapping peaks which are due to the reduction of CoO to Co. These peaks also include the reduction of cobalt species that interact with the support.[29, 31, 39] The shoulder observed after 500 °C in the TPR profile of 10Co/TiO_2-SiC is likely attributed to small cobalt in strong interaction with TiO_2 and the reduction of cobalt silicate- and titanate-like species.[38, 40] The reduction of cobalt silicate-like species was observed after 550 °C on 10Co/SiC catalyst. The reduction peaks located at around 700 ^oC can be assigned to the reduction of the cobalt titanate/silicate from the reaction between cobalt and titania-silica layer or the fraction of cobalt in the inner cavities of the TiO_2-SiC support. This peak is absent in the TiO_2-SiC support confirming thus the hypothesis mentioned above.[31, 40]

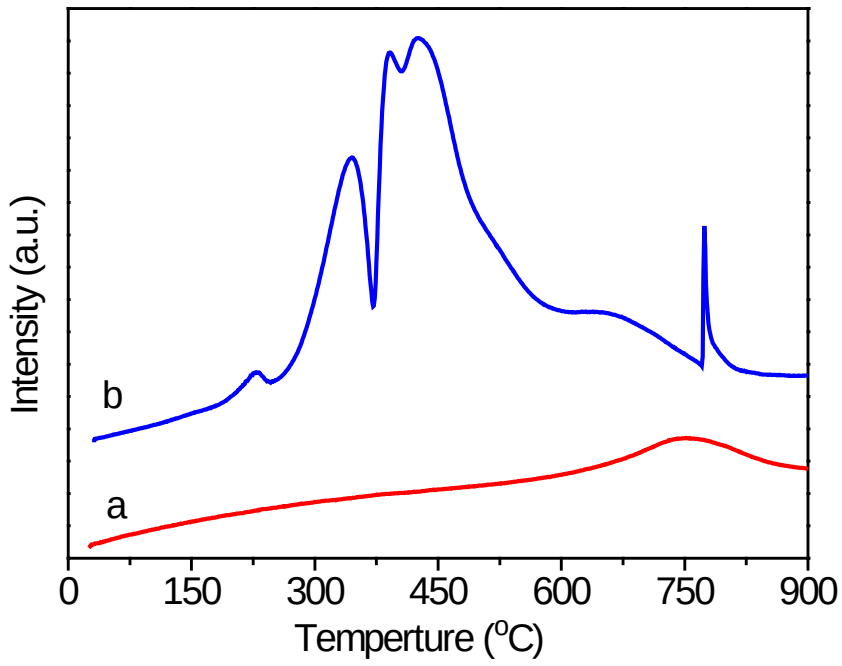

Figure 4-24. The TPR profiles of (a) TiO_2-SiC support and (b) 10Co/TiO_2-SiC catalysts.

The microstructure of the Co/TiO_2-SiC catalyst was further analyzed by classical TEM and HR-TEM imaging modes. The corresponding micrographs and HR images are presented in Figure 4-25. HR-TEM images taken in the areas where cobalt particles seem to be present close to the TiO_2 phase clearly evidence the formation of metal nanoparticles with size smaller than 10 nm and a highly faceted and faulted structure (Figures 4-25C). The cobalt particles seem to be well separated from each other (Figure 4-25A and B) due probably to the relatively high metal-support interaction with the TiO_2 phase.

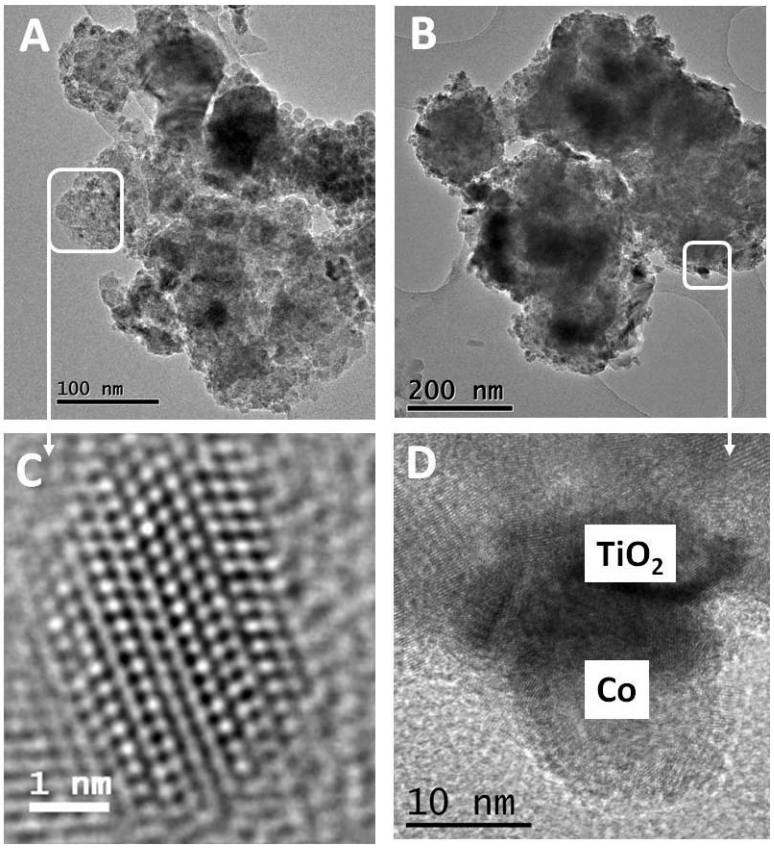

Figure 4-25. Representative TEM images (A, B) of two typical grains of Co/TiO_2-SiC catalyst and HR-TEM image (C, D) taken on areas where cobalt nanoparticles are present.

The average cobalt particle size was also statistically determined from TEM images and the particle size distribution is presented in Figure 4-26. The corresponding particle size distribution for Co/SiC is also presented in the same figure for comparison. According to the

results one can state that the introduction of TiO_2 in the SiC matrix leads to a significant modification of the cobalt particle size dispersion: a large portion of the cobalt particles was shifted to the region between 5 to 20 nm whereas on the SiC catalyst a large portion of the cobalt particles was ranged between 25 to 45 nm. The results clearly evidence the positive influence of the TiO_2 on the cobalt dispersion which is in good agreement with the EFTEM results reported below.

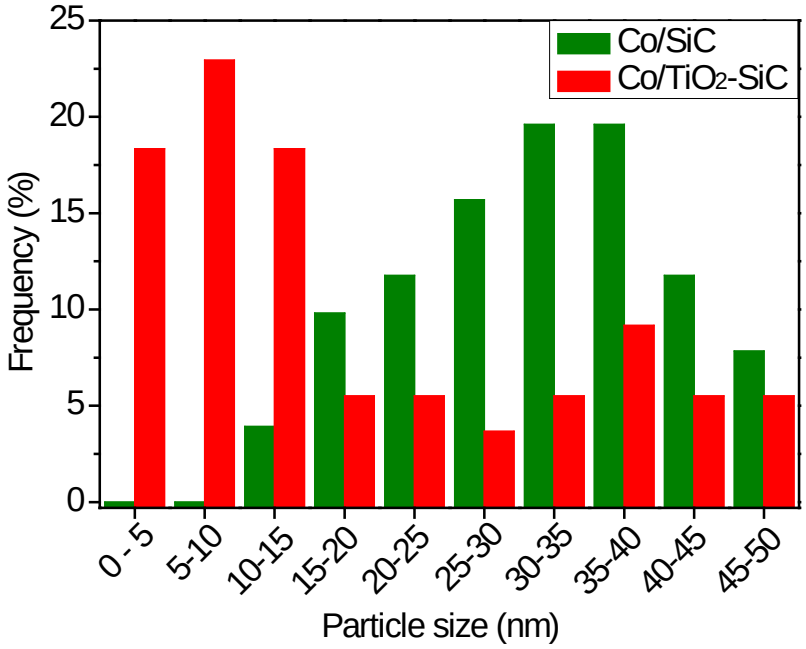

Figure 4-26. Particle size distribution of the cobalt phase in the SiC and TiO_2-SiC catalysts determined from a statistical TEM analysis.

To get more insight about the direct influence of the phase nature of the support on the cobalt dispersion, an EFTEM tomographic study was performed. Indeed, precise information on the localization and characteristics of the cobalt nanoparticles are difficult to obtain by analyzing the 2D Si and Ti elemental maps, due to the superposition effect which happens in such complex porous 3D structures. A 3D elemental analysis of the 10% Co/TiO_2-SiC catalyst based on the implementation of EFTEM chemical imaging in the tomographic mode was thus used, to individually solve the relative distribution of SiC, TiO_2 and Co compounds

(see details in experimental method's section). The results are schematized in Figure 4-27. According to the 3D chemically-selective volume of the catalyst particle where the spatial localizations of the three constituting elements are solved with a resolution of few nanometers one can observe the strong influence of the TiO_2 on the dispersion of the cobalt particles compared to those directly deposited on the naked SiC surface. The average cobalt particle size in close contact with the TiO_2 phase is centered at around 5-15 nm while that of the particles deposited on SiC surface is about 40 nm. In fact, a more detailed analysis of the 3D analytical model of the catalyst grain reveals that the small cobalt particles observed in TEM (smaller than 5 nm) are inserted in the macro- or mesopores of the TiO_2-SiC support; in this case the 2D TEM images reveal only small parts of the cobalt nanoparticles, illustrating thus once again the interest of 3D analyses for obtaining more precise microstructural information. The obtained results could be attributed to a higher metal-support interaction between the cobalt and the TiO_2 phase which prevent excessive cobalt particle agglomeration and/or sintering during the impregnation and thermal treatment steps.

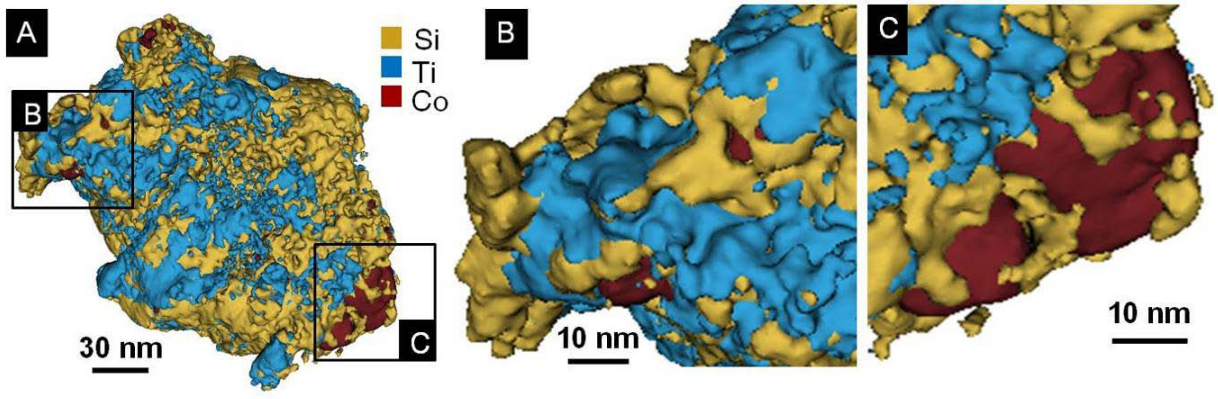

Figure 4-27. Typical 3D view of the analytical 3D model obtained for the selected grain of 10% Co/TiO_2-SiC sample by using an EFTEM tomographic analysis applied to Si, Ti and Co elements. It provided direct information on the localization of cobalt particles on the different compounds of the support. Ti is represented in blue, Si in yellow and Co in red. The catalyst was calcined at 350 ^{o}C for 2 h followed by a reduction under H_2 at 300 ^{o}C for 6 h.

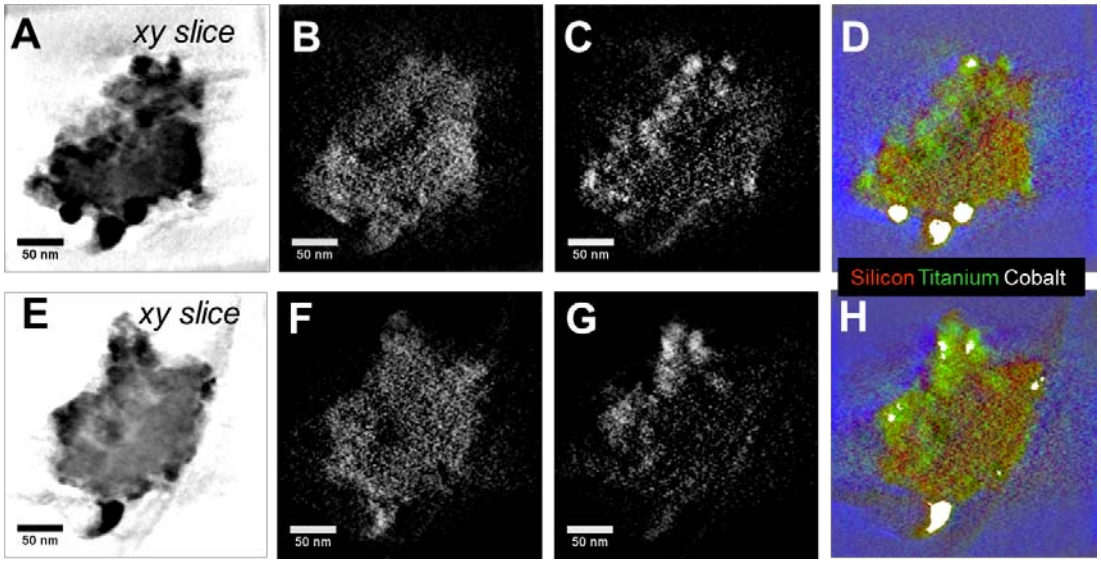

Figure 4-28. Typical slices extracted from the density-sensitive (A, E), Si elemental (B, F) and Ti elemental (C, G) reconstructions for a Co/TiO_2-SiC catalyst grain. The corresponding slices from the 3D chemical relative volume obtained by superposing Si (in red), Ti (in green) and Co (in white) are also presented. They illustrate the decoration of the SiC support by a TiO_2 phase and also the mesoporous structure of the catalyst.

The slice by slice analysis of the density-sensitive reconstruction (calculated from the ZL recording) highlights the presence of an interconnected mesoporous network inside the SiC grain (Figures 4-28A and E). A more detailed analysis allows us to observe that the high porous structure of the support is mostly constituted by mesopores. Their presence greatly facilitates the reactant supply and the product escaping to and from the active sites located far from the support surface. By analyzing the individual Si and Ti reconstructions and the chemical relative volume, one can finally observed that the TiO_2 phase is relatively well dispersed through the SiC matrix and that both phases provide anchorage sites for the cobalt particles. The presence of small cobalt particles with diameter lying between 5 to 10 nm can be observed in Figure 4-28D and H as bright spots on a green area of TiO_2 while the praticle localized next to SiC surface exhibit a bigger size.

4.6.3 FTS performance

The FTS catalytic performance obtained on the SiC and TiO_2-SiC based catalysts are presented in Table 4-5. The FTS activity, expressed in terms of cobalt-time-yield (CoTY), obtained on the Co/TiO_2-SiC is relatively high at 7.5×10^{-5} $mol_{CO}\cdot g_{Co}^{-1}\cdot s^{-1}$ compared to that obtained on the undoped SiC catalyst, 5.3×10^{-5} $mol_{CO}\cdot g_{Co}^{-1}\cdot s^{-1}$. The C_{5+} selectivity is around 92 % on both catalysts at 230°C. Such high selectivity towards long chain hydrocarbons has already been observed on the SiC-based catalysts [29, 31] and was attributed to the meso- and macroporous network and the good thermal conductivity of the support. The FT activity of the Co/TiO_2-SiC catalyst also exhibits an extremely high stability as a function of the reaction conditions, i.e. temperature and space velocity, indicating that the active phase was well and highly anchored onto the support surface which prevent any deactivation by sintering as will be confirmed by the HR-TEM and 2D EFTEM analysis below.

Table 4-5. The catalytic performance for Fischer-Tropsch synthesis on TiO_2 doped SiC supported cobalt catalysts.[a] Reaction conditions: 230 °C, P_{total} = 40 bar, GHSV (STP) = 2850 h^{-1}, H_2/CO = 2, pure syngas.

Catalyst	Co[b]/wt.%	X_{CO}/%	S_{CO2}/%	S_{CH4}/%	S_{C2-C4}/%	S_{C5+}/%	CoTY[c]	α[d]
Co/SiC	10.5 ± 0.5	35.4	0.1	5.4	2.9	91.6	5.3	0.92
Co/TiO_2-SiC	10.7 ± 0.5	50.5	0.2	5.9	2.2	91.7	7.5	0.92

[a] All data were obtained after 20 h time on stream with stable catalytic performance at testing conditions. [b] Cobalt mass content is confirmed by ICP technique. [c] Cobalt Time Yield (10^{-5} $mol_{CO}\cdot g_{Co}^{-1}\cdot s^{-1}$, molar CO conversion rate per gram of Co per hour). [d] Chain growth factor: the chain growth factor (α) calculated from the linear portion of the hydrocarbons, according to the following equation $Wn/n = (1-\alpha)^2\alpha^{(n-1)}$ where Wn is the weight fraction of hydrocarbon molecules containing n carbon atoms, α is the chain growth probability. When α is equal to 0 all the CO molecules are converted to CH_4 and when α is equal to 1 all the CO molecules are converted to liquid hydrocarbons

It is worthy to note that the carbon mass balance calculated, from several FTS experiments, was around 90 ± 3 wt.% taken into account the amount of incomplete wax recovery in the traps (the loss was mostly due to the need to heat up the trap to melt the solid waxes which were trapped between the condenser lines of the high-temperature trap), and the error margin in the CO flow rate (± 5 wt.%) at the entrance of the reactor and at the exit of the gas-chromatograph. The error margin is added to the total C_{5+} selectivity.

During the FT reaction several parameters contribute to the deactivation of the catalyst such as active phase oxidation by steam, sintering, fouling and carbonaceous encapsulation. The deactivation could also be induced by the active phase reconstruction and/or segregation as well. Each parameter contributes to the whole deactivation with different timescale and thus the long-term evaluation, at least several hundred hours on stream, of the catalyst is a prerequisite before any conclusion can be pronounced on the catalyst performance. The stability of the catalyst was further evaluated by submitting the catalyst to a long-term test at high reaction temperature and space velocity (Figure 4-29). According to the results, the FTS activity and the CO conversion remain stable for the whole test lasted for about 100 h confirming thus the extremely high stability of the catalyst under severe reaction conditions. It is also worthy to note that the catalyst was run for more than 200 h under different reaction conditions before the long-term test which highlight the resistance of the tested catalyst towards deactivation by surface oxidation by steam or by active phase sintering.

The FTS activity, CO conversion and C_{5+} selectivity obtained on the Co/TiO_2-SiC catalyst was also compared to the values obtained in different cobalt-based catalysts reported in the literature (Figure 4-30). According to the results one can observe that the SiC-based catalysts allow performing F-T reaction with an extremely high selectivity towards liquid hydrocarbon independently of the total conversion, which is not the case when using other supports. The results clearly indicate that the Co/TiO_2-SiC is not only active but also extremely selective for long chain hydrocarbons formation compared to the other catalysts supported on different supports.[32, 41-44]

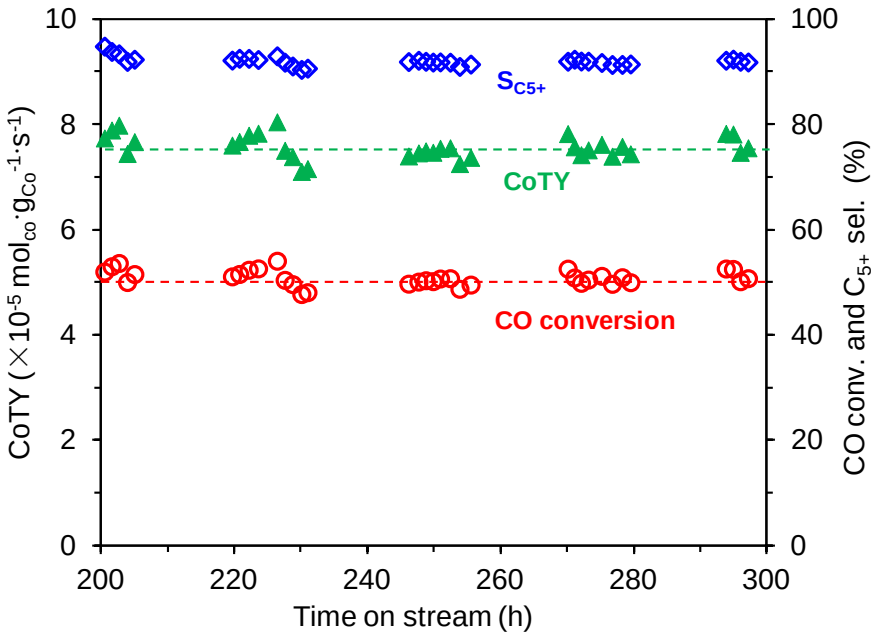

Figure 4-29 Cobalt time yield, CO conversion and C_{5+} selectivity of the Co/TiO_2-SiC catalyst as a function of time on stream. Reaction conditions: 230 °C, P_{total} = 40 bar, GHSV (STP) = 2850 h^{-1}, H_2/CO = 2, pure syngas.

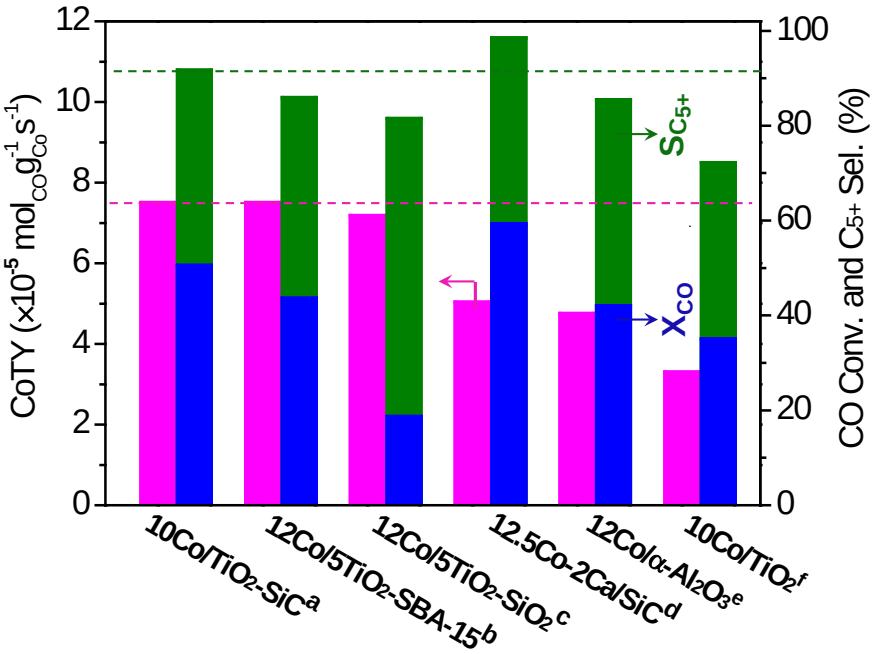

Figure 4-30. A comparison of the catalytic activity and C_{5+} selectivity of the Co/TiO_2-SiC catalysts with some different Co-based catalysts reported in literatures. [a]Data from this work; [b]Data from ref.[41]; [c]Data from ref.[42] ; [d]Data from ref.[32]; [e]Data from ref.[43]; [f]Data from ref.[44].

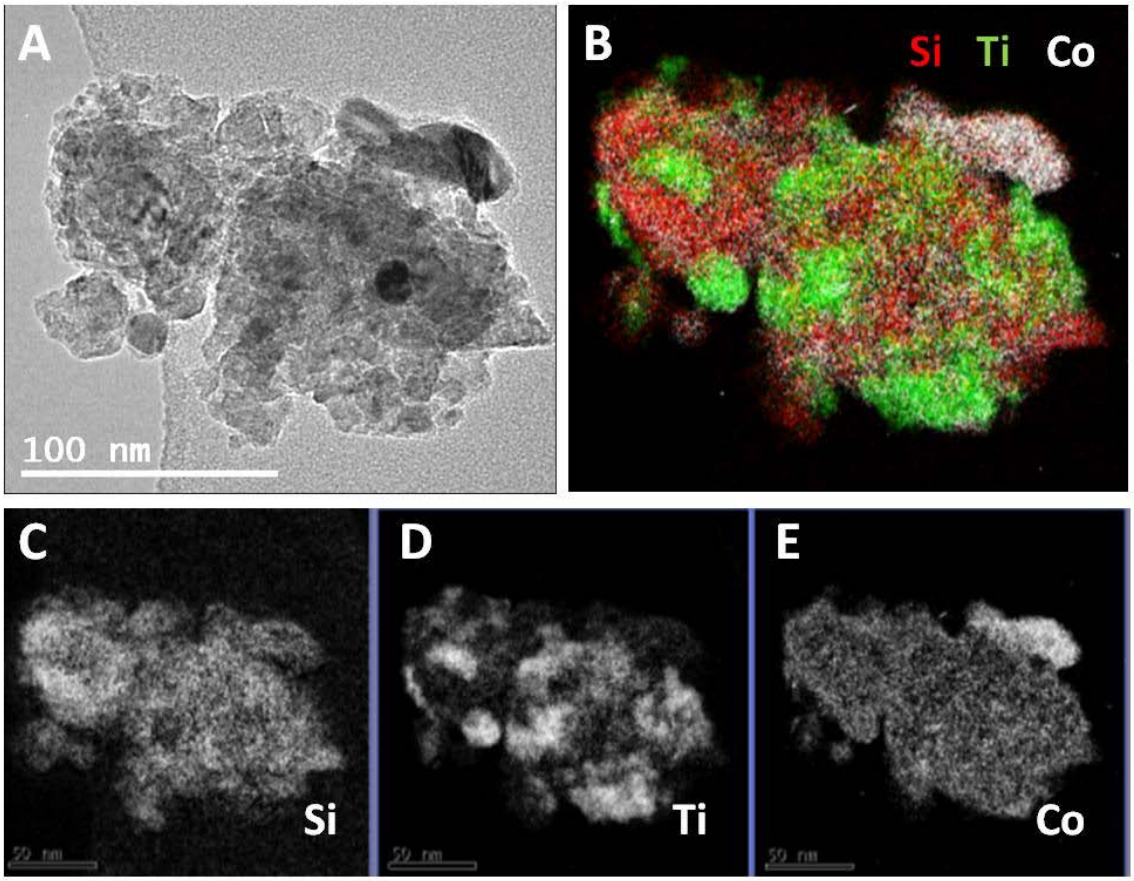

Figure 4-31. 2D chemical analysis of the spent Co/TiO_2-SiC catalyst after > 300 h of FTS experiment showing the relatively high stability of the small cobalt particles in close contact with the TiO_2 phase. (A) TEM image taken on the grain selected for the analysis. (B) The chemical relative map obtained by superposing the elemental maps with different colors (Si in red, Ti in green and Co in white).(C-E) 2D elemental maps for Si, Ti and Co obtained by applying the three window method to the energy filtered images recorded at the L_{23} edges of the three elements (two pre-edge and one post-edge image for each element).

The microstructure of the spent catalyst was again analyzed by TEM and EFTEM imaging to check out any modification of the active phase characteristics during the course of the reaction. The cobalt microstructure and valence state formed during the reaction were retained thank to the presence of a thin layer of solid waxes on its surface which prevent surface oxidation during the transfer. The results are presented in Figure 4-31. Low magnification TEM micrograph (Figure 4-31A) indicates that the global morphology of the spent catalyst remains unchanged after reaction. The 2D elemental maps obtained on one of

the selected grain are presented in Figures 4-31B to D. Their analysis clearly confirms the high dispersion of the cobalt particles even after the reaction. The average size of cobalt nanoparticles localized on TiO_2 remains smaller than ten nanometers, while for the cobalt particles localized on SiC a size similar to that before reaction was observed.

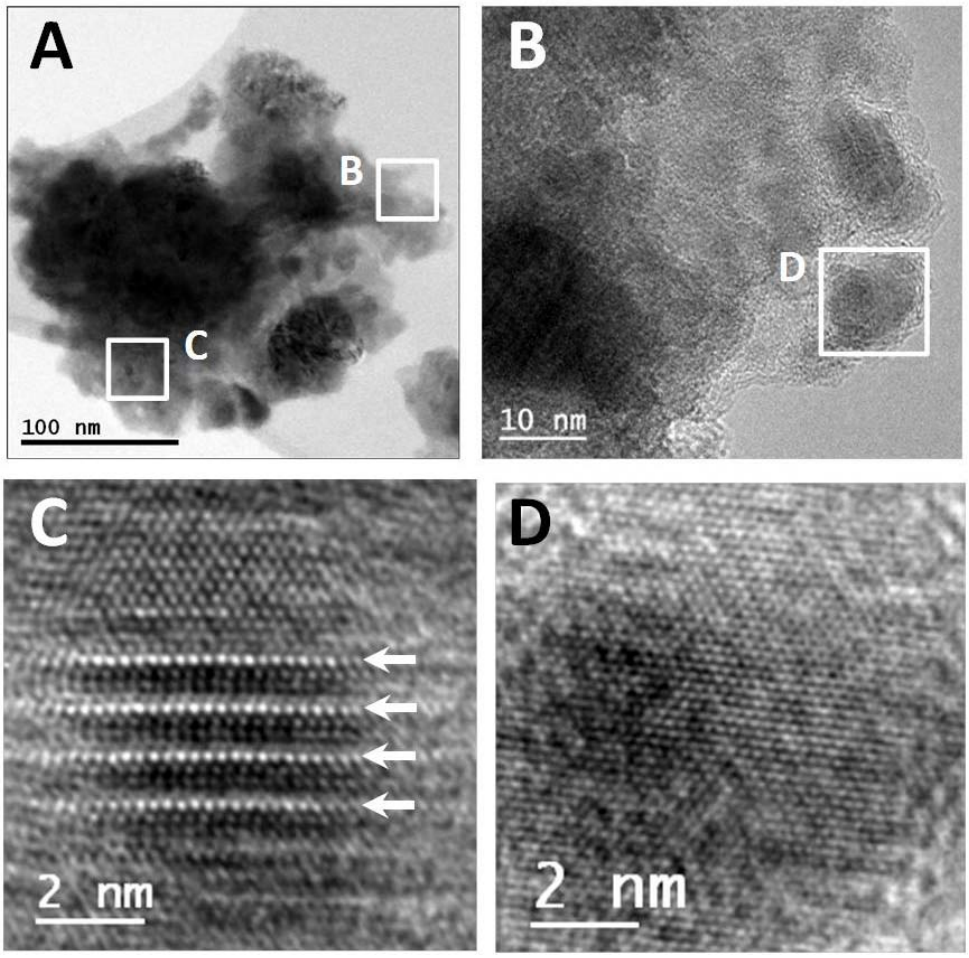

Figure 4-32. TEM and HR-TEM analysis of the spent Co/TiO_2-SiC catalyst after > 300 h of FTS experiment. (A, B) TEM micrographs of the cobalt particles in close contact with the TiO_2 phase. (C, D) HR-TEM images taken on the cobalt particles denoted by white squares in (A) and (B). A large number of stacking faults within the particle can be observed (indicated by arrows).

The presence of small cobalt particles close to the TiO_2 phase was also evidenced by TEM and HR-TEM analyses (Figure 4-32). It is worthy to note that the density of the stacking faults in the cobalt particles is relatively high (indicated by arrows), which could provide a

large number of anchorage sites for the reactants and confirms the high FTS activity obtained on this catalyst. Note that the cobalt particles located on the SiC surface are rather large in size and are not presented here.

4.6.4 Correlation structure-activity for the FTS process

The results obtained above have shown that the introduction of TiO_2 into the SiC matrix significantly improves the dispersion of the deposited cobalt nanoparticles by providing a higher metal-support interaction compared to that of the SiC surface alone. The analysis by EFTEM tomography has revealed a strong dependence of the cobalt particle size on the nature of the support underneath, 5-15 nm, when Co particles were in close contact with a TiO_2 phase and 25-45 nm when cobalt was in contact with a SiC phase (Figure 4-27 and 4-28). Such high cobalt dispersion is directly responsible for the enhancement of the FTS performance compared to that obtained on the un-doped support. Xiong et al.[45] have reported that cobalt particles between 15 and 20 nm are the most active for the FT reaction where smaller ones (< 6 nm) exhibit poor FT activity as well as lower selectivity due to the possible surface oxidation under FT conditions and electronic surface modification.[6] The FTS results obtained during the long-term test seem to indicate that deactivation by surface oxidation of small cobalt particles does not occur under the applied reaction conditions. HR-TEM analysis carried out on the catalyst after long-term test suggests no surface oxidation of the cobalt particles and confirms the high resistance of these cobalt particles towards surface oxidation by steam generated during the course of the reaction. Such high resistance could be attributed to the high escaping of the products from the internal network of the catalyst, due to the presence of meso- and macropores of the support (see also the slices extracted from the 3D reconstructions), and also to a relatively high space velocity employed. This velocity significantly reduces the surface oxidation of the active phase by reducing the residence time of steam next to the active site. In addition, the high activity of the Co/TiO_2-SiC could also be attributed to the presence of defect sites on the cobalt surface, as observed by HR-TEM, which are more active for dissociation of CO.

It is well known that metal particles deposited on TiO_2 surface exhibit higher dispersion due to the strong metal-support interaction when the reduction is realized at temperature higher than 300 °C.[46] Reuel and Bartholomew[47] have reported that the FTS activity strongly depends on the nature of the support according to the following activity sequence: Co/TiO_2 > Co/Al_2O_3 > Co/SiO_2 > 100% Co > Co/MgO. The better metal-support interaction between the TiO_2 and the deposited cobalt nanoparticles also prevents the deactivation of the catalyst, by active phase sintering, as observed during the FTS test and also during the start-stop process. The low sintering process during the course of the reaction, according to the HR-TEM and EFTEM analysis on the spent catalyst, could also be attributed to the intrinsic thermal conductivity of the SiC support which prevents local hot spot formation within the catalyst body.

The high C_{5+} selectivity obtained on both the SiC-based catalysts, doped and un-doped, is directly linked to the intrinsic thermal conductivity of the SiC material and also to the meso- and macropores presents in the support and evidenced by TEM tomography. The intrinsic thermal conductivity of the support allows the rapid heat dissipation to the entire body of the catalyst and thus, contributes to the reduction of surface hot spots which are detrimental for the selectivity. The open porous network of the SiC support is of primordial interest for the FT reaction as it allows a rapid freeing of the pathway of the gaseous reactant towards the active site localized far from the catalyst surface. Indeed, in the FT reaction the catalyst pores were rapidly filled with liquid hydrocarbons which render the diffusion of the reactant towards the active site more and more difficult. The low diffusion rate will induce a local enrichment of H_2 next to the active site which favors the methane formation. In the case of support with large pore size, i.e. SiC, the liquid hydrocarbons formed were rapidly evacuated from the catalyst body which allows a balance diffusion of both the reactants to the active site and significantly reduce the selectivity towards methane formation.[48] The high C5+ selectivity could also be attributed to the relatively low conversion in the FTS experiments. Indeed, it has been reported by Dalai et al.[49] and by Lögdberg et al.[50] that at low CO conversion the steam formed could even increase the C_{5+} selectivity by competitive

adsorption with the hydrogenation reaction termination leading to a lower methane selectivity and α-olefins re-adsorption for further chain growth.

4.7 Conclusion

The detailed analysis of the Co/TiO_2-SiC catalyst by 2D and 3D chemical imaging based on energy filtered TEM, combined with the more traditional high-resolution TEM mode, allows one to precisely solve the microstructure, the porous characteristics and the distribution of the constituting phases. The catalytic tests show that silicon carbide doped with titanium dioxide can be efficiently employed as cobalt support in the FTS process under severe reaction conditions. The characteristics deduced by HR-TEM and EFTEM tomography were correlated to the enhancement of the FT performance of the Co/TiO_2-SiC catalyst which seems to be due to a better dispersion of the cobalt particles in close contact with the TiO_2 phase. The 3D reconstructions of the selected grains allow one also to access to the internal porosity of the support which is expected to play an important role in the product evacuation and reactant supply. In addition, the TEM imaging and EFTEM chemical mapping allows one to confirm the complete retention of the small cobalt particle size in contact with the TiO_2 phase after long-term reaction. It is expected that the high FTS performance and stability of the catalyst were directly linked with the high stability of the small cobalt particles in close contact with the TiO_2 phase and also to the intrinsic thermal conductivity of the support to prevent the local hot spot formation which could favor the lost of the active sites by sintering. The high selectivity towards liquid hydrocarbons is attributed to the intrinsic thermal conductivity and a meso-/macroporosity of the support. Additional work is on going to evaluate the F-T performance of such hybrid catalyst with different titanium dioxide loading and under more severe reaction conditions, i.e. high temperature and low space velocity, to optimize such catalyst for future industrial development of the Fischer-Tropsch synthesis.

From a general point of view, this study illustrates the uniqueness and the high potential of the characterization tools based on electron microscopy that applied in a combined manner, allow a complete description of heterogeneous nanomaterials of interest in catalysis from the

point of view of their morphology, crystallographic structure and chemical composition., to be subsequently correlated with the catalytic properties.

4.8 References

[1] J. R. Rostrup-Nielsen, *Science* **2005**, *308*, 1421-1422.

[2] A. Y. Khodakov, W. Chu, P. Fongarland, *Chemical Reviews* **2007**, *107*, 1692-1744.

[3] C. Perego, R. Bortolo, R. Zennaro, *Catal Today* **2009**, *142*, 9-16.

[4] M. E. Dry, *Catal Today* **2002**, *71*, 227-241.

[5] R. Luque, A. R. de la Osa, J. M. Campelo, A. A. Romero, J. L. Valverde, P. Sanchez, *Energ Environ Sci* **2012**, *5*, 5186-5202.

[6] G. L. Bezemer, J. H. Bitter, H. P. C. E. Kuipers, H. Oosterbeek, J. E. Holewijn, X. D. Xu, F. Kapteijn, A. J. van Dillen, K. P. de Jong, *J Am Chem Soc* **2006**, *128*, 3956-3964.

[7] W. Chu, L. N. Wang, P. A. Chernavskii, A. Y. Khodakov, *Angew Chem Int Edit* **2008**, *47*, 5052-5055.

[8] J. I. Yang, J. H. Yang, H. J. Kim, H. Jung, D. H. Chun, H. T. Lee, *Fuel* **2010**, *89*, 237-243.

[9] N. Tsubaki, S. L. Sun, K. Fujimoto, *J Catal* **2001**, *199*, 236-246.

[10] R. Oukaci, A. H. Singleton, J. G. Goodwin, *Appl Catal a-Gen* **1999**, *186*, 129-144.

[11] S. Storsaeter, O. Borg, E. A. Blekkan, B. Totdal, A. Holmen, *Catal Today* **2005**, *100*, 343-347.

[12] O. Borg, P. D. C. Dietzel, A. I. Spjelkavik, E. Z. Tveten, J. C. Walmsley, S. Diplas, S. Eri, A. Holmen, E. Ryttera, *J Catal* **2008**, *259*, 161-164.

[13] G. L. Bezemer, P. B. Radstake, V. Koot, A. J. van Dillen, J. W. Geus, K. P. de Jong, *J Catal* **2006**, *237*, 291-302.

[14] W. Chen, Z. L. Fan, X. L. Pan, X. H. Bao, *J Am Chem Soc* **2008**, *130*, 9414-9419.

[15] S. Zarubova, S. Rane, J. Yang, Y. D. Yu, Y. Zhu, D. Chen, A. Holmen, *Chemsuschem* **2011**, *4*, 935-942.

[16] G. L. Bezemer, T. J. Remans, A. P. van Bavel, A. I. Dugulan, *J Am Chem Soc* **2010**, *132*, 8540-8541.

[17] P. Nguyen, C. Pham, *Appl Catal a-Gen* **2011**, *391*, 443-454.

[18] M. J. Ledoux, C. Pham-Huu, *Cattech* **2001**, *5*, 226-246.

[19] C. Pham-Huu, P. Delgallo, E. Peschiera, M. J. Ledoux, *Appl Catal a-Gen* **1995**, *132*, 77-96.

[20] K. Chizari, A. Deneuve, O. Ersen, I. Florea, Y. Liu, D. Edouard, I. Janowska, D. Begin, C. Pham-Huu, *Chemsuschem* **2012**, *5*, 102-108.

[21] N. Keller, C. Pham-Huu, C. Estornes, M. J. Ledoux, *Appl Catal a-Gen* **2002**, *234*, 191-205.

[22] P. Nguyen, D. Edouard, J. M. Nhut, M. J. Ledoux, C. Pham, C. Pham-Huu, *Appl Catal B-Environ* **2007**, *76*, 300-310.

[23] S. Ivanova, E. Vanhaecke, B. Louis, S. Libs, M. J. Ledoux, S. Rigolet, C. Marichal, C. Pham, F. Luck, C. Pham-Huu, *Chemsuschem* **2008**, *1*, 851-857.

[24] D. L. Nguyen, P. Leroi, M. J. Ledoux, C. Pham-Huu, *Catal Today* **2009**, *141*, 393-396.

[25] Y. Liu, S. Podila, D. L. Nguyen, D. Edouard, P. Nguyen, C. Pham, M. J. Ledoux, C. Pham-Huu, *Appl Catal a-Gen* **2011**, *409*, 113-121.

[26] S. Ivanova, C. Lebrun, E. Vanhaecke, C. Pham-Huu, B. Louis, *J Catal* **2009**, *265*, 1-7.

[27] A. Deneuve, I. Florea, O. Ersen, P. Nguyen, C. Pham, D. Begin, D. Edouard, M. J. Ledoux, C. Pham-Huu, *Appl Catal a-Gen* **2010**, *385*, 52-61.

[28] M. Lacroix, L. Dreibine, B. de Tymowski, F. Vigneron, D. Edouard, D. Begin, P. Nguyen, C. Pham, S. Savin-Poncet, F. Luck, M. J. Ledoux, C. Pharn-Huu, *Appl Catal a-Gen* **2011**, *397*, 62-72.

[29] B. de Tymowski, Y. F. Liu, C. Meny, C. Lefevre, D. Begin, P. Nguyen, C. Pham, D. Edouard, F. Luck, C. Pham-Huu, *Appl Catal a-Gen* **2012**, *419*, 31-40.

[30] A. R. de la Osa, A. De Lucas, A. Romero, J. L. Valverde, P. Sanchez, *Catal Today* **2011**, *176*, 298-302.

[31] A. R. de la Osa, A. De Lucas, J. Diaz-Maroto, A. Romero, J. L. Valverde, P. Sanchez, *Catal Today* **2012**, *187*, 173-182.

[32] A. R. de la Osa, A. de Lucas, L. Sanchez-Silva, J. Diaz-Maroto, J. L. Valverde, *Fuel* **2012**, *95*, 587-598.

[33] P. Nguyen, C. Pham, B. de Tymowski, C. Pham-Huu, F. Luck, in *France Patent 11-01704, Vol. 11-01704*, France Patent ed., France, **2011**.

[34] I. Florea, M. Houlle, O. Ersen, L. Roiban, A. Deneuve, I. Janowska, P. Nguyen, C. Pham, C. Pham-Huu, *J Phys Chem C* **2009**, *113*, 17711-17719.

[35] A. J. Koster, U. Ziese, A. J. Verkleij, A. H. Janssen, K. P. de Jong, *J Phys Chem B* **2000**, *104*, 9368-9370.

[36] I. Florea, O. Ersen, C. Hirlimann, L. Roiban, A. Deneuve, M. Houlle, I. Janowska, P. Nguyen, C. Pham, C. Pham-Huu, *Nanoscale* **2010**, *2*, 2668-2678.

[37] H. L. Xin, E. A. Pach, R. E. Diaz, E. A. Stach, M. Salmeron, H. M. Zheng, *Acs Nano* **2012**, *6*, 4241-4247.

[38] Y. Liu, B. de Tymowski, F. Vigneron, I. Florea, O. Ersen, C. Meny, P. Nguyen, C. Pham, F. Luck, C. Pham-Huu, *ACS Catalysis* **2013**, *3*, 393-404.

[39] A. Tavasoli, R. M. M. Abbaslou, A. K. Dalai, *Appl Catal a-Gen* **2008**, *346*, 58-64.

[40] R. Riva, H. Miessner, R. Vitali, G. Del Piero, *Appl Catal a-Gen* **2000**, *196*, 111-123.

[41] M. Lualdi, G. Di Carlo, S. Logdberg, S. Jaras, M. Boutonnet, V. La Parola, L. F. Liotta, G. M. Ingo, A. M. Venezia, *Appl Catal a-Gen* **2012**, *443*, 76-86.

[42] A. M. Venezia, V. La Parola, L. F. Liotta, G. Pantaleo, M. Lualdi, M. Boutonnet, S. Järås, *Catal Today* **2012**, *197*, 18-23.

[43] S. Rane, O. Borg, J. Yang, E. Rytter, A. Holmen, *Appl Catal a-Gen* **2010**, *388*, 160-167.

[44] K. Jalama, J. Kabuba, H. F. Xiong, L. L. Jewell, *Catal Commun* **2012**, *17*, 154-159.

[45] H. F. Xiong, M. A. M. Motchelaho, M. Moyo, L. L. Jewell, N. J. Coville, *J Catal* **2011**, *278*, 26-40.

[46] Y. Z. Li, Y. N. Fan, H. P. Yang, B. L. Xu, L. Y. Feng, M. F. Yang, Y. Chen, *Chem Phys Lett* **2003**, *372*, 160-165.

[47] R. C. Reuel, C. H. Bartholomew, *J Catal* **1984**, *85*, 78-88.

[48] Y. Liu, T. Dintzer, O. Ersen, C. Pham-Huu, *Journal of Energy Chemistry* **2013**, *22*, 279-289.

[49] A. K. Dalai, B. H. Davis, *Appl Catal a-Gen* **2008**, *348*, 1-15.

[50] S. Logdberg, M. Lualdi, S. Jaras, J. C. Walmsley, E. A. Blekkan, E. Rytter, A. Holmen, *J Catal* **2010**, *274*, 84-98.

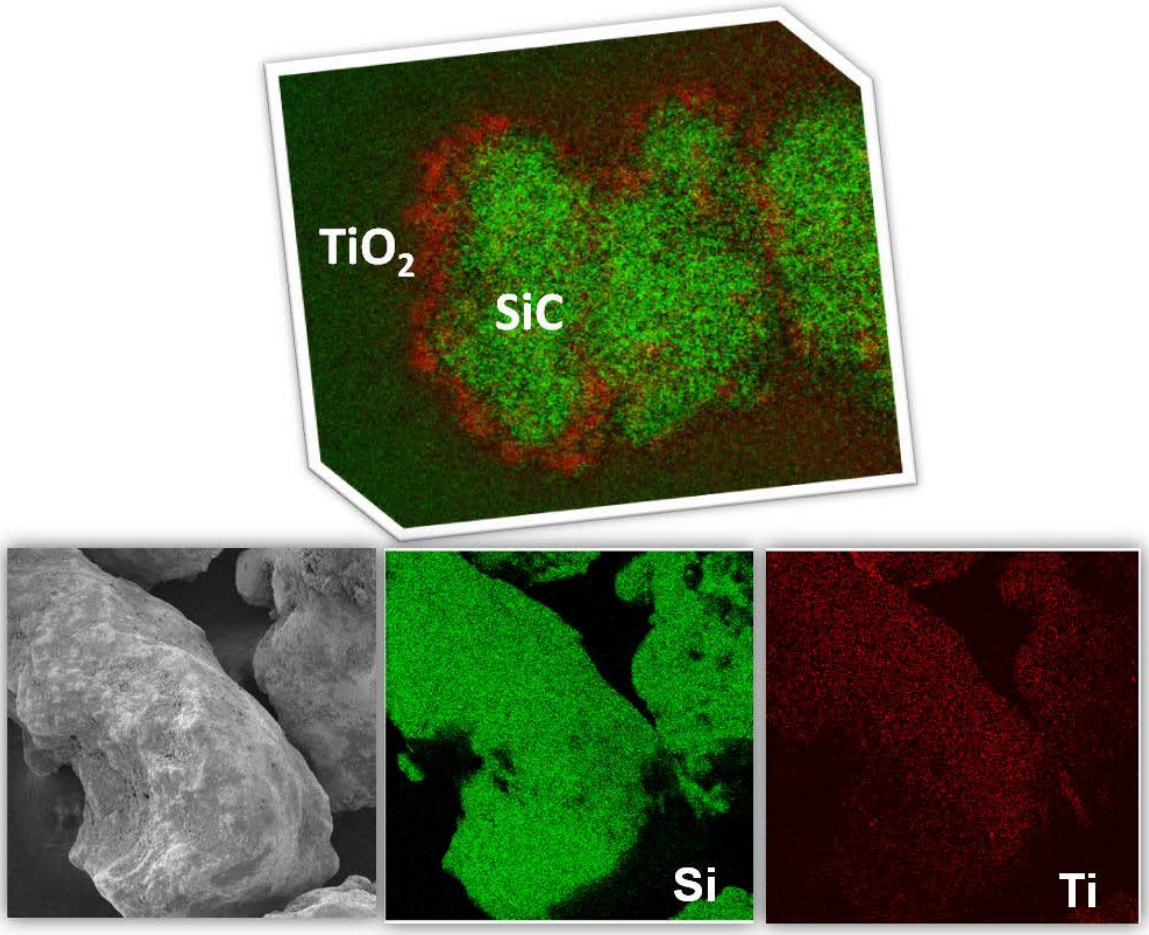

Chapter V

Titania coated silicon carbide support cobalt nanoparticles

Chapter V Macroporous Thermal Conductive Titania Coated Silicon Carbide Supported Cobalt Catalysts for Fischer-Tropsch Synthesis

5.1 Introduction

Fischer-Tropsch synthesis (FTS), which converts synthesis gas (syngas) derived from coal, natural gas or biomass, into synthetic liquid fuels and chemicals, continues to attract more interest as a result of diminishing petroleum reserves.[1-3] The FTS process is one of the most complex one, regarding the various reactions that take place during the gas-to-liquid transformation. The most employed active phase, i.e. cobalt, for the low-temperature FTS, was typically deposited on a support which significantly enhances the metallic sites for the reaction. The most employed supports used include Al_2O_3, SiO_2, TiO_2, and MgO which are insulator character.[4-7]

The FTS reaction is strongly exothermic, i.e. ΔH = -165 to 204 $kJmol^{-1}_{CO}$. In the case of insulator supports, the heat generated on the catalyst surface cannot be effectively removed by the gas phase which leads to the formation of local hot spots on the catalyst surface which significantly affects the overall selectivity of the reaction. In addition, the strong metal-support interactions between the deposited cobalt phase and the supports like alumina or silica also leads to the formation of hardly reducible cobalt phase which is not efficient for the FTS reaction. To lower the detrimented effect of this interaction, some costly metals such as Ru, Pt, and Re can be added to the Co to assist with the reduction of the cobalt oxides, and an alternative is to use carbon as the support instead of a metal oxide.[8-13] The metal-support interactions between the deposited cobalt phase and the alumina and silica supports also render difficult the recovery of the metal and support after the end-life of the catalyst. It is consequently of interest to develop new support materials that can efficiently replace those cited above, mainly in terms of physical properties, which could provide an improvement of

the catalytic performance along with active phase recovery as well. The new support should also be cheap and be readily available in the same shape as those usually employed in order to reduce the cost incentive linked with extra additional modifications of the plant itself.

Silicon carbide (β-SiC) has been recently reported to be an efficient support for fixed-bed FTS reaction due to its intrinsic medium thermal conductivity which facilitate heat dissipation throughout the catalyst body and thus, avoid the formation of local hot spots which could modify the overall selectivity of the reaction.[14-18] The large porosity of the support also allows a rapid escaping of the intermediate liquid hydrocarbons and water and thus, significantly contributes to the improvement of the liquid hydrocarbon selectivity as well. The chemical inertness of the support also allows the easy recovery of both the active phase and the support by a simple acid or basic treatment, which is unlike the traditional catalysts based on alumina or silica where recovery needs a complex chemical treatment to be efficiently achieved.

However, the metal-support interaction between the cobalt phase and the SiC surface is relatively weak and thus, leads to the formation of large cobalt particles which are less efficient for the FTS reaction. In our previous attempts the SiC surface was modified by introducing doping which exhibits a higher metal-support interaction in order to achieve the better dispersion of the deposited cobalt phase. The SiC doped with TiO_2 (17 wt. %) enhanced the cobalt dispersion efficiently to obtained relative high FTS activity for cobalt-time yield (CoTY) of 7.5×10^{-5} $mol_{co} \cdot g_{Co}^{-1} s^{-1}$ at 230 ^{o}C.[19] However, part of the Co is also deposited on the SiC phase which leads to the formation of larger cobalt particles with lower F-T activity. It is expected that a new doping could be useful to homogeneously decorate the SiC surface with a thin layer of TiO_2. To date, there has been no report on the utilization the TiO_2 coated on high porosity, thermal conductivity support such as SiC for the F-T synthesis. Herein, we reports on the development of a highly active Fischer-Tropsch catalyst based on titania coated high porosity β-SiC containing well dispersed cobalt particles. The high dispersion of the cobalt particles on the thin TiO_2 layer leads to a significant improvement of the catalyst activity for the F-T reaction compared to the

undoped SiC and TiO_2 doped SiC catalysts. The influence of the TiO_2 loading on the F-T reaction performance will be also conducted in view of an optimization process. The cobalt dispersion on both type of supports, i.e. TiO_2 and naked SiC, was also investigated by different advanced characterization techniques such as transmission electron microscopy coupled with the Energy Electron Loss Spectroscopy (TEM-EELS) and the ^{59}Co zero field Nuclear Magnetic Resonance (NMR).

5.2. Results and discussion

5.2.1 Synthesis and Physicochemical Properties of *x*TiO_2 -SiC Supports

Titanium oxide coated high porosity SiC can be synthesized in facile way through the wet impregnation method using an ethanol solution containing $Ti(iOC_3H_7)_4$. SEM micrographs of the different content of TiO_2, i.e. 5, 10 and 15 wt%, coated high porosity SiC are displayed in Figure 5-1.

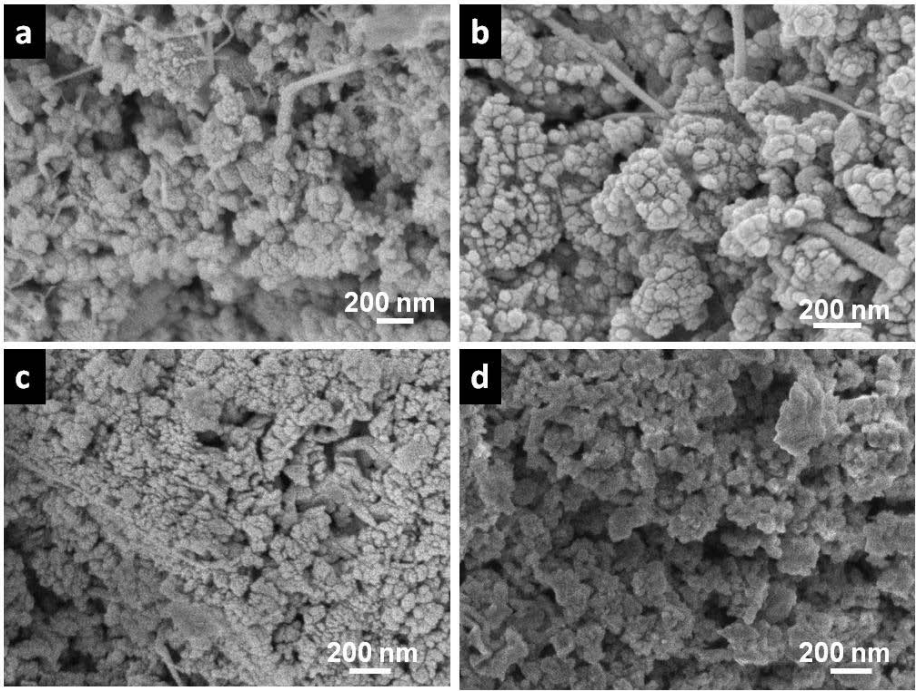

Figure 5-1. SEM micrographs of various content of TiO_2 coated high porosity SiC. **(A)** SiC; **(B)** 5TiO_2-SiC; **(C)** 10TiO_2-SiC; **(D)** 15TiO_2-SiC.

After TiO_2 coating, the SiC surface seems to be more rough which could be attributed to the presence of the layer of TiO_2 covering the SiC surface. The elemental composition of the TiO_2 coated SiC sample is investigated by EDX and the corresponding mapping images ($10TiO_2$-SiC), are presented in Figure 5-2. Apparently, SEM image and EDX mapping reveal the similar trends of morphologies and elemental distribution (see Si map and Ti map), and confirm the homogeneous coating of the support (Figure 5-2C). The EDX analysis (Figure 5-2D) from the marked square area in Figure 5-2A shows the weight concentration of titanium of 11.5 wt%.

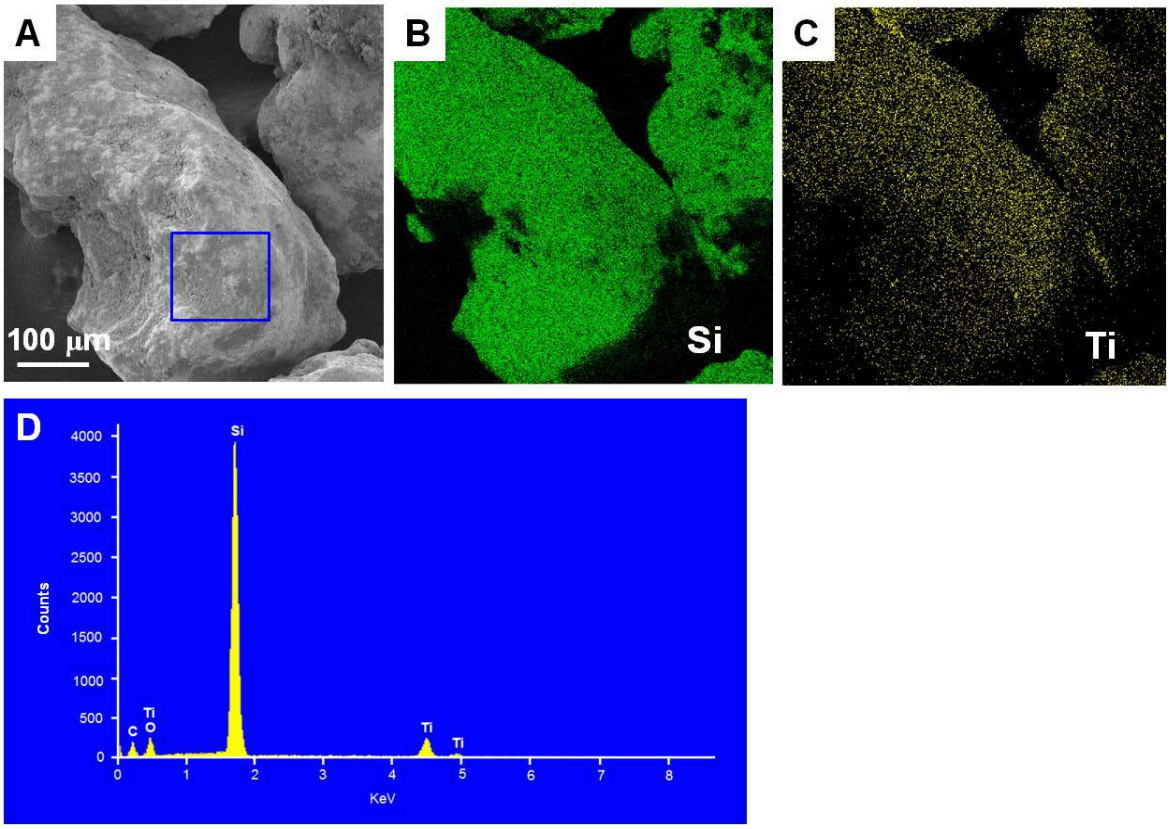

Figure 5-2. SEM-EDX micrographs of granular $10TiO_2$-SiC support. (A) SEM image of the SiC particle coated with TiO_2; (B, C) Silicon and titanium EDX maps of the same particle surface shown in (A); (D) EDX in the square area from the image in (A).

The crystal structure and composition of the different supports are characterized by wide-angle XRD. As can be seen in Figure 5-3, XRD patterns of the xTiO$_2$-SiC show four

resolved diffraction peaks, located at 25°, 48°, 55° and 56°, which can be assigned to the (101), (200), (105) and (211) reflections of the anatase TiO_2 phase.[20-21] The results indicate that the obtained TiO_2 layer is well crystallized in single anatase phase. The diffraction line enhancement indicates the anatase TiO_2 phase is well-crystallized with the mass loading increases. The crystal size determined by the Scherrer formula is about 25, 39 and 40 nm for TiO_2 mass loading range from 5 wt% to 15 wt%, respectively. The diffraction peaks of SiC (Figure 5-3) found in the XRD patterns confirm the presence of face-centered-cubic (β-SiC) with the stacking faults of hexagonal (α-SiC). The diffraction peak of α-SiC at $2\theta = 33.7^o$ is appeared as the stacking faults along the growth direction (111) of β-SiC, and according to the HR-TEM study of the SiC published previously.[22-23]

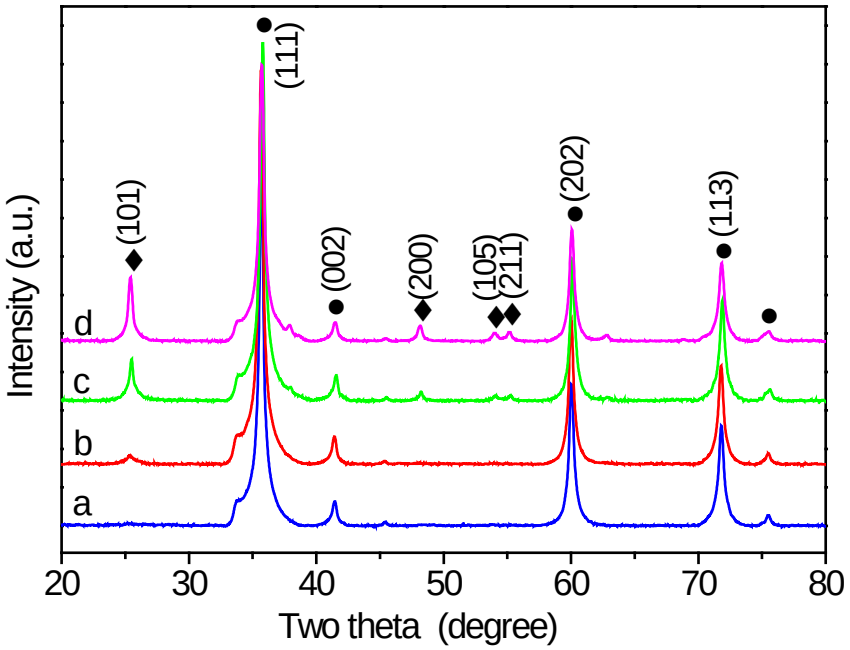

Figure 5-3. X-ray diffraction patterns of various TiO_2 loading on high porosity SiC: (a) SiC; (b) 5TiO_2-SiC; (c) 10TiO_2-SiC, (d) 15TiO_2-SiC. Diamond (♦): anatase TiO_2; circles (●): SiC.

The typical TEM images and energy-filtered TEM of TiO_2 coated SiC with 10 wt % TiO_2 are shown in Figure 5-4. The EFTEM in Figure 1B clearly shows the presence of a thin

and homogeneous TiO_2 layer covering the surface of the SiC support. The N_2 adsorption-desorption data of *x*TiO_2-SiC are summarized in Table 5-1. The BET specific surface area of TiO_2 coated SiC are in the range of 39-41m^2/g, which are nearly the same as the pure SiC (40 m^2/g). Such result indicates that the depositing of a thin layer of TiO_2 on the SiC surface has a small effect on the overall surface area of the final composite which is due to the high porosity of the host support. The pore size distribution curves in the range of 2 -150 nm derived from adsorption branches of the N_2 isotherms using BJH method is presented in Figure 5-5. According to the N_2 adsorption-desorption experiment all TiO_2 coated SiC and SiC support display irregular and broad pore size distribution. While the TiO_2 loading on SiC increased, the mesopores in the range of 10-20 nm increase. The materials in this work are not typical mesopores or nanopores size distribution as the reported SiO_2 and Al_2O_3 supports.[24-25]

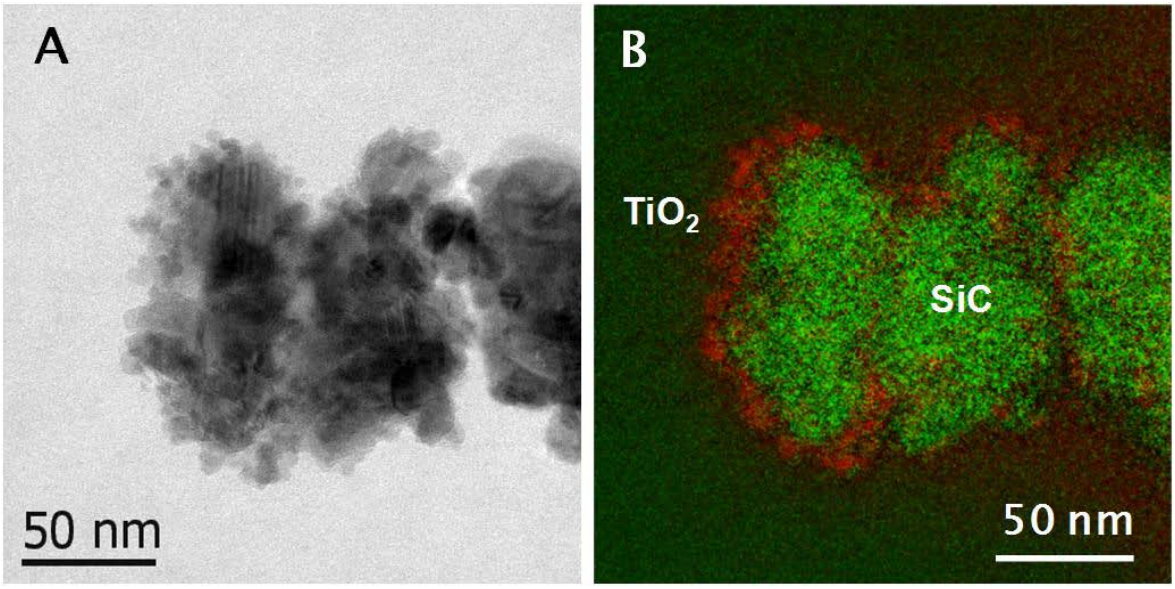

Figure 5-4. (A) Typical TEM image of TiO_2-SiC (10 wt.%) and (B) EFTEM image corresponding to the classical 2D TEM map clearly showing the well distribution of TiO_2 on the around the surface of SiC. TiO_2 (red), SiC (green).

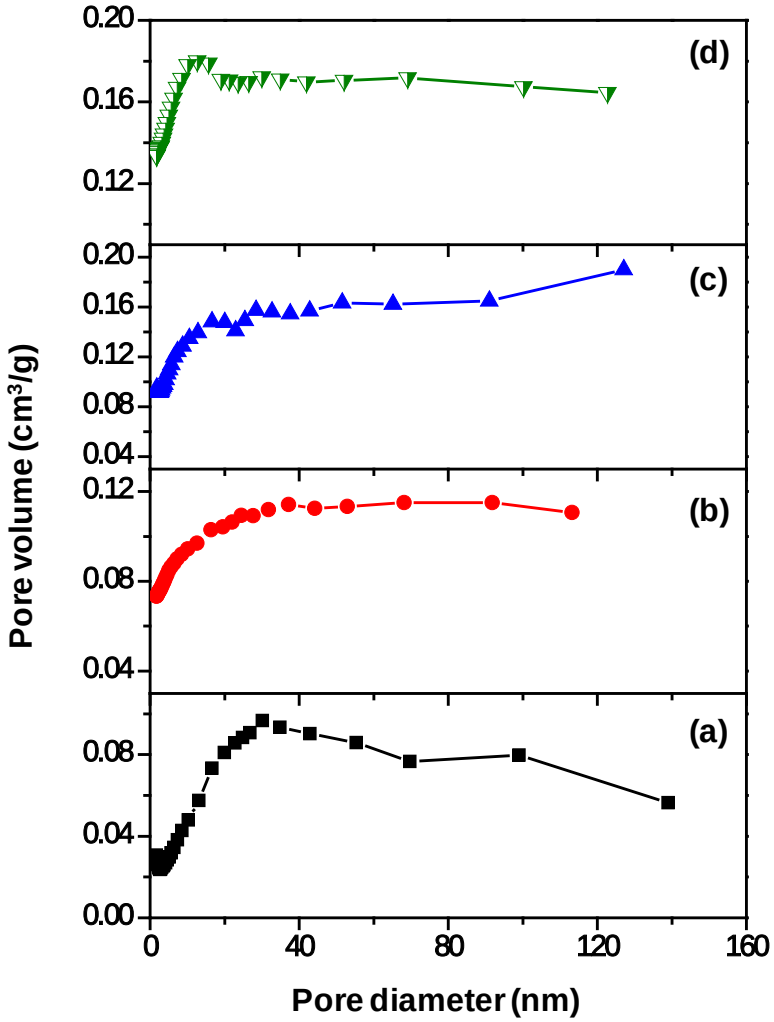

Figure 5-5. Pore size distributions derived from N_2 adsorption- desroption by using the BJH methods for various TiO_2 loading on high porosity SiC (a) SiC (SB0670J); (b) 5TiO_2-SiC; (c) 10TiO_2-SiC, (d) 15TiO_2-SiC

5.2.3 Surface and structure analysis of prepared catalysts

The XRD patterns of the cobalt supported on the SiC-based catalysts are presented in Figure 5-6. Before XRD experiments, the catalysts were reduced under hydrogen at 300 °C for 6 h. The 10Co/SiC catalyst only displays diffraction lines corresponding to the SiC support and metallic cobalt phase without diffraction lines corresponding to the cobalt oxide phases, confirming the complete reduction of the cobalt phase. A similar reduction pattern is also observed on the TiO_2 coated catalysts. However, on the catalyst with 15 wt. % of TiO_2 a diffraction line appears at around 42.5° which could be assigned to a CoO phase. Such

results seem to indicate that at high TiO_2 loading some hardly reducible phase of cobalt was formed after reduction of the catalyst.

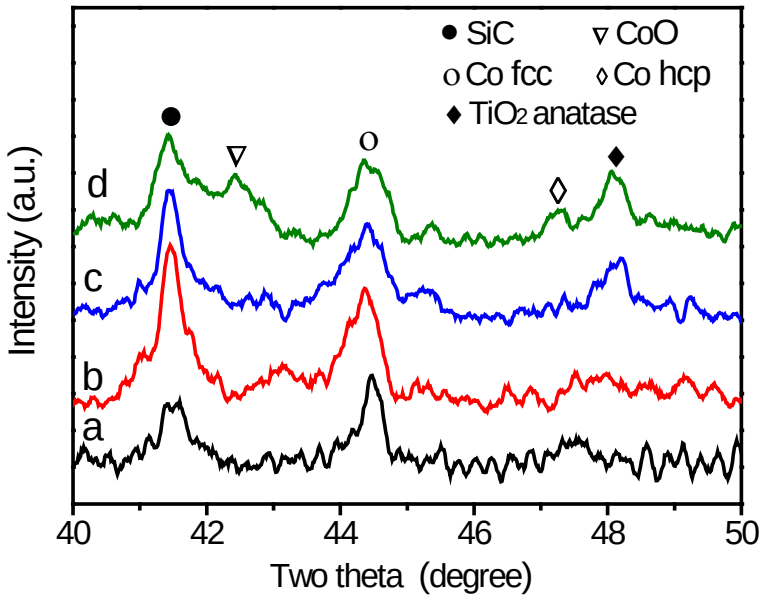

Figure 5-6 . Ex situ X-ray diffraction patterns of prepared catalysts: (a) 10Co/SiC ; (b)10Co/5TiO_2-SiC; (c)10Co/10TiO_2-SiC (d) 10Co/15TiO_2-SiC

The TPR results indicate that in the case of composite support the reduction of the cobalt phase was not affected by the dopant even at high loading, i.e. TiO_2 with a loading of 17 wt. %. The complete reduction of the cobalt phase was directly attributed to the low interaction between the cobalt oxide phase and the support, SiC and TiO_2, which avoids the formation of a hardly reducible cobalt phase as usually observed with the alumina or silica supports.[26-27] In the present case where the dopant was coated on the topmost surface of the SiC host matrix one should expected that the layer of TiO_2 is become thicker which could induce a stronger interaction between the cobalt precursor and the TiO_2 phase and thus, lead to the incomplete reduction of the deposited cobalt phase.

The average cobalt particle size determined by the Scherrer formula is reported in Table 5-1**.** Two methods are used to calculate the cobalt particle size in the different catalysts. The

average nanoparticle crystal size of the cobalt is about 40-50 nm for the 10Co/SiC, and about 15-25 nm for the 10Co/TiO_2-SiC, the later being predicted to be the most active particle size for the FTS process.[10] The results also indicate that the introduction of the TiO_2 phase onto the SiC matrix significantly decreases the particle size of cobalt, probably by generating a higher chemical interaction with the metal salt precursor without modifying the reduction behavior of the sample.

Table 5-1. BET surface area and pore volume of the different SiC carriers and the 10 wt. % Co catalysts after reduction under H_2 at 300 ^oC for 6h and the corresponding cobalt particle size calculated by Scherrer formula.

Sample	Surface area (m^2/g)	Total pore volume (cm^3/g)	BJH pore diameter (nm)	Co^0 particle size[a] (nm)	Co^0 particle size[b](nm)
SiC	40.4	0.120	12.8	-	-
5TiO_2-SiC	38.5	0.099	10.4	-	-
10TiO_2-SiC	41.4	0.134	13.6	-	-
15TiO_2-SiC	40.5	0.102	10.1	-	-
Co/SiC	32.7	0.139	17.1	42±5	51±5
Co/5TiO_2-SiC	36.7	0.115	13.1	31±5	30±5
Co/10TiO_2-SiC	40.4	0.113	11.2	24±5	24±5
Co/15TiO_2-SiC	40.7	0.100	10.2	34±5	-

[a] $d(Co^0) = 0.75 \times d(Co_3O_4)$

[b] $d(Co^0) = k.\lambda / (\tau \cdot \cos\theta)$,The sample was reduced by H_2 at 300 ℃ for 6h

5.2.4 Reduction behavior of the cobalt-based catalysts

TPR spectra of the TiO_2 coated and uncoated Co/SiC catalysts are displayed in Figure 5-7. Generally, as can be seen in Figure 5-7, the TPR peaks localized between the ranges of

300 ^{o}C -550 ^{o}C were attributed to the two-step reduction of Co_3O_4 into metallic cobalt. The low cobalt reduction temperature peak is typically assigned to the reduction of Co_3O_4 to CoO while the higher reduction temperature peak corresponded the reduction of CoO to Co^0.[28-30] The profile of the reduction peaks was found to depend on the concentration of TiO_2. For uncoated catalyst, the reduction of cobalt fraction in strong interaction with supports is observed after 550 ^{o}C.[15, 17-18] The peaks at ca. 650 ^{o}C and 730 ^{o}C in the TPR profile of Co/SiC are attributied to the reduction of cobalt species that interact with the support.[15, 17] Upon addition of titanium oxide on SiC supported cobalt catalysts, the reduction peaks disappear and instead of the broad tailing after the cobalt oxide reduction peaks. The tailing was observed after 550 ^{o}C in the profiles of 10Co/*x*TiO_2-SiC (*x* =5, 10, 15) is likely attributed to small cobalt interaction with TiO_2 and the reduction of cobalt silicate-like species.[15]

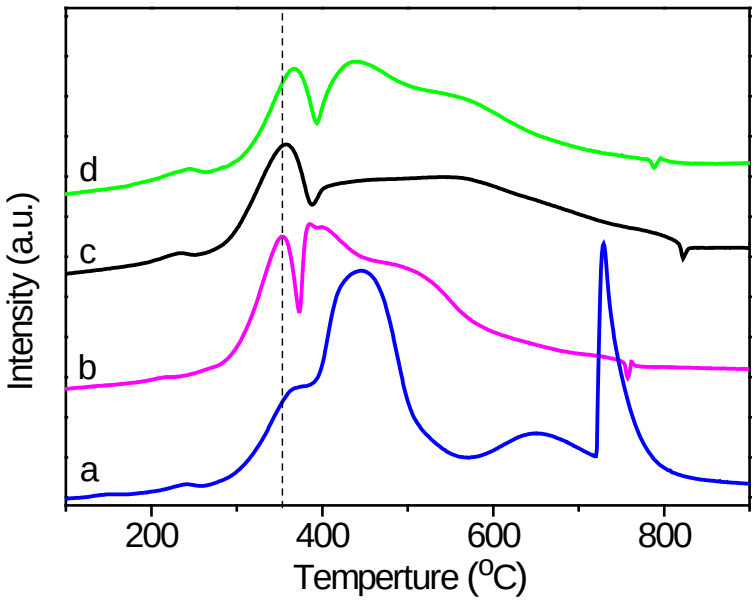

Figure 5-7. TPR profiles of higher porosity SiC supported catalysts (SB00670J), (a)10Co/SiC; (b)10Co/5TiO_2-SiC; (c)10Co/10TiO_2-SiC; (d)10Co/15TiO_2-SiC

The corresponding SEM micrographs of the oxide 10Co/10TiO_2-SiC catalyst and reduced one are presented in Figure 5-8 and clearly evidence the presence of a smaller cobalt particle size. The cobalt particle size is more homogeneous on TiO_2 coated SiC in comparison with the SiC.

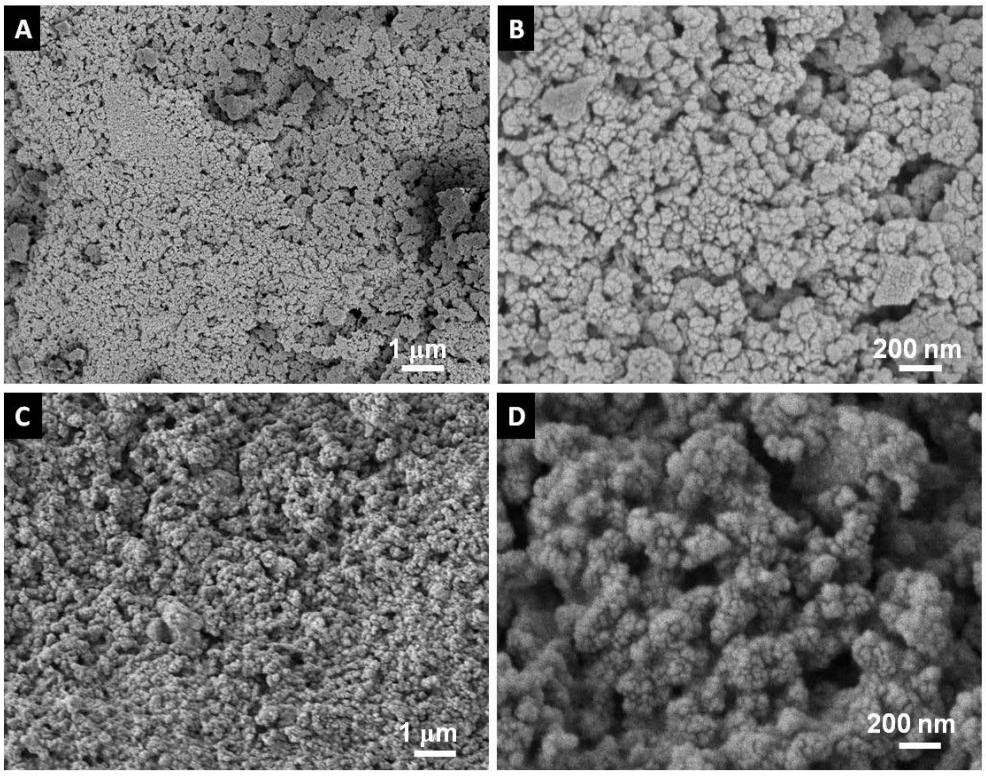

Figure 5-8. (A, B) SEM micrograph of the 10Co/10TiO_2-SiC after calcination by air at 350 ^oC for 2h, (C, D**)** SEM micrographs of the 10Co/10TiO_2-SiC after reduction under H_2 at 300 °C for 6 h.

The TEM and TEM-EELS images in Figure 5-9 show the cobalt particle dispersion on the surface of the 10Co/10TiO_2-SiC catalyst recovered after approximately 400 hours of testing in FTS. It was found that the particle size of cobalt is in contact with the TiO_2 layer is relatively small and homogeneous. This result is in relatively good agreement with those obtained from the broadening of the diffraction peaks of cobalt previously reported. Good preservation of the size of the cobalt particles observed on the catalyst after reaction indicates that the sintering is not occuring in this supported catalyst.

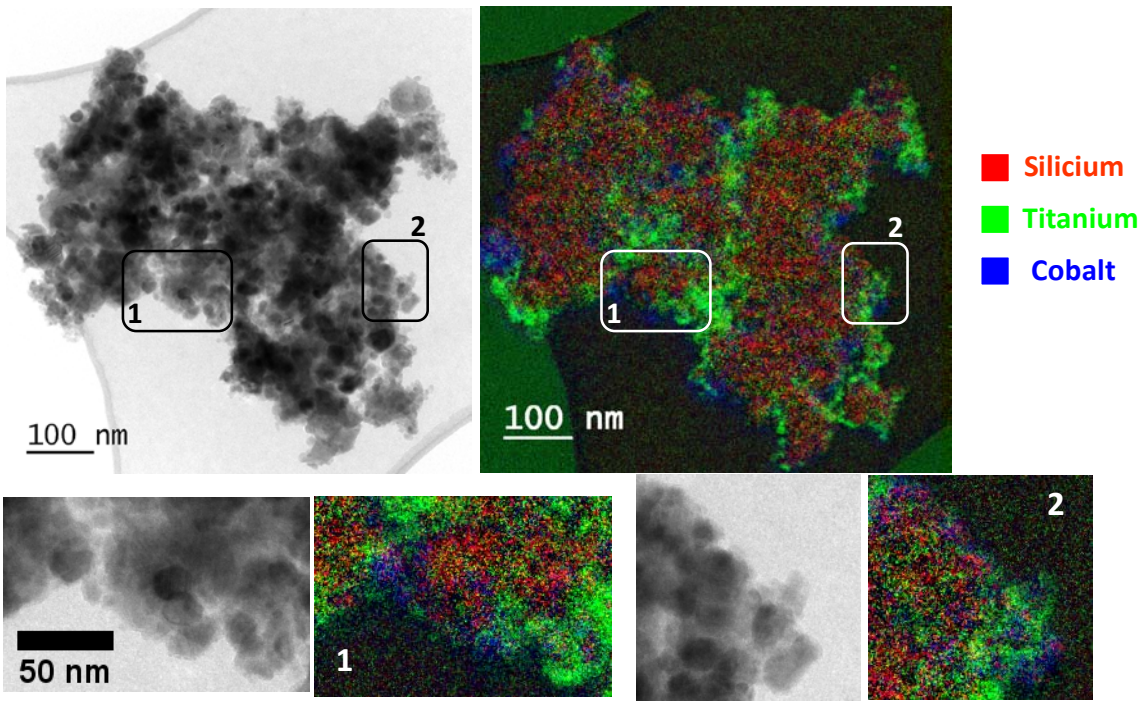

Figure 5-9. (A) Classical TEM and (B) 2D elemental relative maps deduced by EFTEM analysis for the TiO_2 coated SiC support; Ti (green), Si (red), Co (white).

5.2.5 Fischer-Tropsch reaction

The CO conversion, cobalt time yield (CoTY, $\times 10^{-5}$ $mol_{co}g_{Co}^{-1}s^{-1}$) and C_{5+} selectivity obtained on cobalt supported on TiO_2 coated SiC with different titania content, i.e. 5%, 10% and 15%, are shown in Figure 5-10A and Table 5-2. The same cobalt catalyst supported on SiC without TiO_2, noted Co/SiC, is also plotted in the same figure to compare the catalytic performance obtained under the same reaction conditions. The introduction of TiO_2 in the support leads to a considerable improvement of the catalyst activity for the reaction of FTS. The cobalt time yield increases from 4.0 to 4.9 $mol_{co}g_{Co}^{-1}s^{-1}$ over the Co/5TiO_2-SiC catalyst promoted with 5 wt% TiO_2 comparing to TiO_2-free catalyst. The CoTY of 8.2 $mol_{co}g_{Co}^{-1}s^{-1}$ was obtained on the Co/10TiO_2-SiC at 215 ^{o}C. When the TiO_2 loading was increased up to 15%, the cobalt time yield decreases to 5.2 $mol_{co}g_{Co}^{-1}s^{-1}$. This decay of the FTS activity as increasing the TiO_2 loading could be attributed to an increase of the metal-support interaction between the TiO_2 with the cobalt precursor which contribute to lower cobalt

dispersion. The increase of the FTS catalytic activity is accompanied by a slight decrease of selectivity for liquid hydrocarbons. The C_{5+} selectivity decreases from 95% for an unpromoted catalyst to about 92% for the promoted catalyst loaded with 10% of TiO_2. Figure 10 presents the chain growth factor (α) determined on various tested catalysts. According to the results one can stated that the chain growth factor (α), which is calculated by using the Anderson-Schulz-Flory (ASF) model,[3] is relatively high on these TiO_2 promoted SiC support catalysts (from 0.91 to 0.92), which is in good agreement with the relatively high C_{5+} selectivity and low methane selectivity obtained on prepared catalysts.(Figure 5-11) As we know, if α is equal to 0 all the CO molecules are converted to CH_4 and when α is equal to 1 all the CO molecules are converted to liquid hydrocarbons.The high α-value observed in the present work could be attributed to the high porosity of SiC supports which favor the diffusion of the reactant towards the active site.[31-32]

Figure 5-10B presents the FT performance over 80 h on the 10Co/10TiO_2-SiC catalyst at 215 ^oC and under the same reaction conditions as mentioned above. The CoTY and C_{5+} selectivity keep the same value at 8.2 $\times 10^{-5}$ $mol_{co}g_{Co}^{-1}s^{-1}$ and 92%, respectively. These results clearly reveal an excellent stability of the tested catalyst, which indicates that deactivation linked with cobalt surface oxidation or sintering is unlikely to occur under the reaction conditions used in the present work. It is also worthy to note that the catalyst tested has already been evaluated in the FTS reaction at 215 ^oC and under a GHSV of 1900 h^{-1} for 100 hours on stream (not reported).

The influence of the FT reaction temperature on the 10Co/10TiO_2-SiC at relative high space velocity, i.e. 80 $ml \cdot g_{cat}^{-1} \cdot min^{-1}$, is also evaluated and the results are shown in Figure 5-12 and Table 5-3. The FTS activity significantly increases as increasing the reaction temperature while the selectivity of liquid hydrocarbons remains high and stable for the whole range of tests. The CO conversion increases rapidly to around 60% when the reaction temperature was increased to 225 ° C. The CoTY is reached 12.1 $mol_{co}g_{Co}^{-1}s^{-1}$ with the selectivity for long chain hydrocarbons of around 91% were obtained at 225 °C. Increasing the reaction temperature also causes a slight increase in light fractions, C_1 and C_2-C_4 in the

reaction products (Table 5-3), however, the overall selectivity to liquid hydrocarbons remains extremely high at around 90%. It is also worthy to note that the catalyst has a relatively high stability and no deactivation was observed at each test conditions.

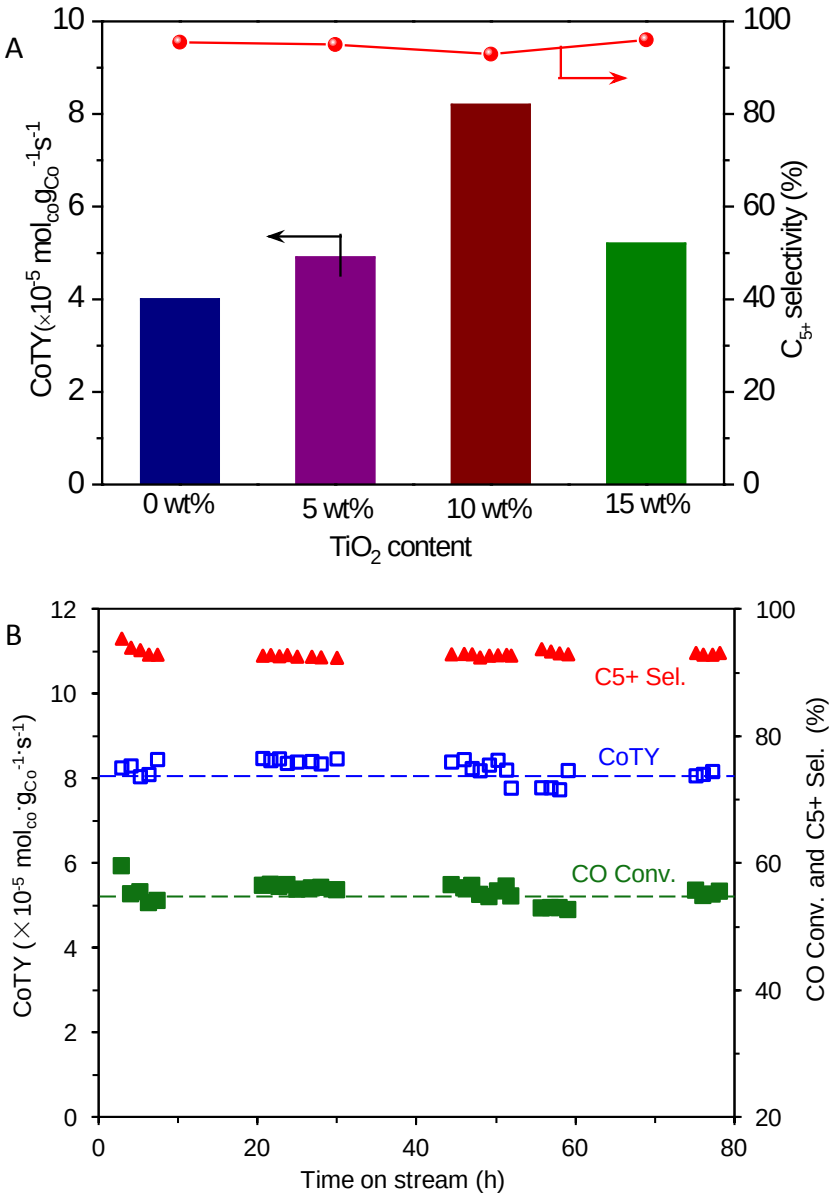

Figure 5-10. (A) FTS activity and C_{5+} selectivity as functions of time on stream on various TiO_2 loading on catalysts. (B) FTS activity and C_{5+} selectivity as functions of time on stream on 10Co/10TiO_2-SiC catalysts. Reaction conditions: H_2/CO molar ratio = 2, reaction temperature = 215 °C, total pressure = 40 bar, GHSV (STP) = 60 ml·g_{cat}^{-1}·min^{-1}.

Table 5-2. Product distribution on the cobalt catalysts supported on SiC and SiC promoted with TiO_2[a]

Catalyst	CO conversion (%)	Selectivity (%)				CoTY[b]	r_{C5+}[c]
		CO_2	CH_4	C_2-C_4	C_{5+}		
10Co/SiC	26.9	0	2.9	1.6	95.5	4.0	0.19
10Co/5TiO_2-SiC	33.8	0	3.4	1.6	95.0	4.9	0.23
10Co/10TiO_2-SiC	55.3	0	4.4	2.7	92.9	8.2	0.39
10Co/15TiO_2-SiC	34.8	0	2.8	1.2	96.0	5.2	0.25

[a] All data were collected after 20 h time-on stream with stable catalytic performance. Reaction conditions: Co loading = 10wt. %, H_2: CO = 2, temperature = 215 ^oC, total pressure =40 atm, GHSV = 60 $ml \cdot g_{cat}^{-1} \cdot min^{-1}$.

[b] Cobalt-Time-Yield ($\times 10^{-5}$ $mol_{co} \cdot g_{Co}^{-1} s^{-1}$), molar CO conversion rate per g atom Co per hour.

[c] FTS rate (r_{C5+}, $g_{C5+} \cdot g_{cat}^{-1} \cdot h^{-1}$): the mass product of long-chain-hydrocarbons (>C_{5+}) per gram catalyst per hours

The FTS performance normalized as cobalt time yield for the sample Co/10TiO_2-SiC is comparable to those of the Co-based catalysts reported previously (Table 5-4). To our knowledge, the F-T activity obtained on the Co/TiO_2-SiC catalyst is the highest one among all the cobalt-based, undoped or doped with trace amount of noble metal, catalysts previously reported in the literature, including CNF and CNT supported catalysts.[10, 17, 19, 33] It is worthy to note that the cobalt supported on the CNF (IEN8), tested at the industrially relevant conditions, represents the best FTS results with a CoTY at 19.2×10^{-5} $mol_{co} \cdot g_{Co}^{-1} s^{-1}$, however, due to the high reaction temperature the C_{5+} selectivity was relatively low at 74%.[10] It is also worthy to note that the IEN8 catalyst was consisted by a cobalt nanoparticles supported on carbon nanofibers with exclusive prismatic planes exposure and nanoscopic dimension which are significantly different compared to traditional supports in the grain size shape reported in the literature for the F-T reaction. These specific characteristics leads to the conclusion that the high CoTY obtained on this catalyst is unlikely to be bench-marked with the traditional grains or extrudates-based F-T catalysts. In

addition, such catalyst is not expected to be able to be used in the fixed bed F-T reaction due to the relatively high pressure drop linked with its nanoscopic dimension.

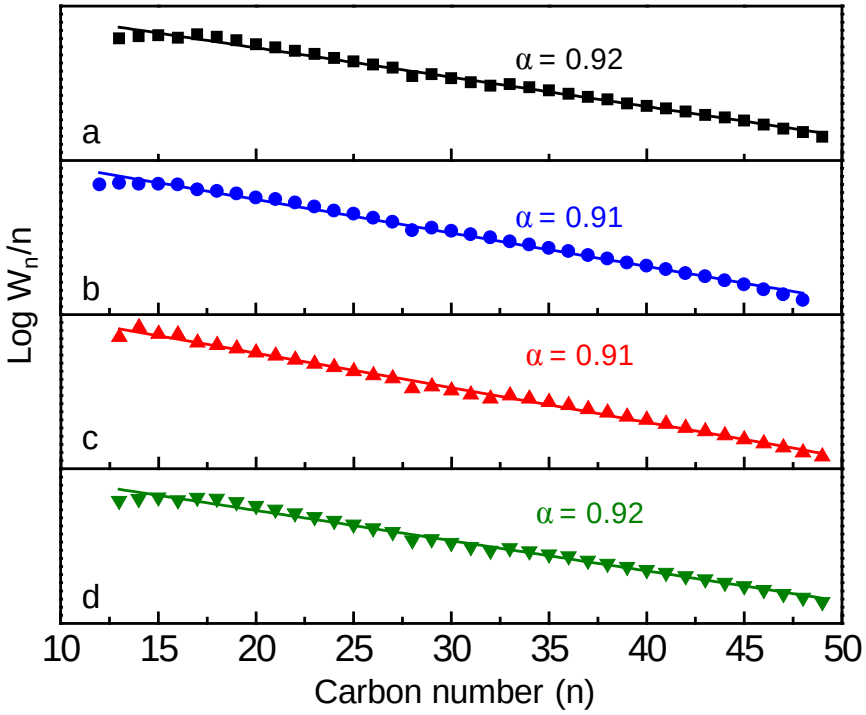

Figure 5-11. Anderson-Schulz-Flory plots for different TiO_2 content promoted cobalt based catalyst. (a) 10Co/SiC; (b) 10Co/5TiO_2-SiC; (c) 10Co/10TiO_2-SiC; (d) 10Co/15TiO_2-SiC

Table 5-3 Product distribution on 10Co/10TiO_2-SiC catalyst in FT synthesis [a] .

T(°C)	CO Conv. (%)	Sel.(%)				CoTY[b]	r_{C5+} [c]
		CO_2	CH_4	C_2-C_4	C_{5+}		
215	40.9	0	4.5	2.5	93.0	8.1	0.38
220	48.7	0	5.3	2.8	91.9	9.7	0.45
225	61.0	0.1	5.8	2.9	91.2	12.1	0.56

[a] All data were collected after 20 h time-on stream with stable catalytic performance (Figure 1d).

[b] Cobalt-Time-Yield (CoTY, $\times 10^{-5}$ $mol_{co} \cdot g_{Co}^{-1} s^{-1}$), molar CO conversion rate per g atom Co per hour.

[c] FTS rate (r_{C5+}, $g_{C5+} \cdot g_{cat}^{-1} \cdot h^{-1}$): the mass product of long-chain-hydrocarbons (>C_{5+}) per gram catalyst per hours.

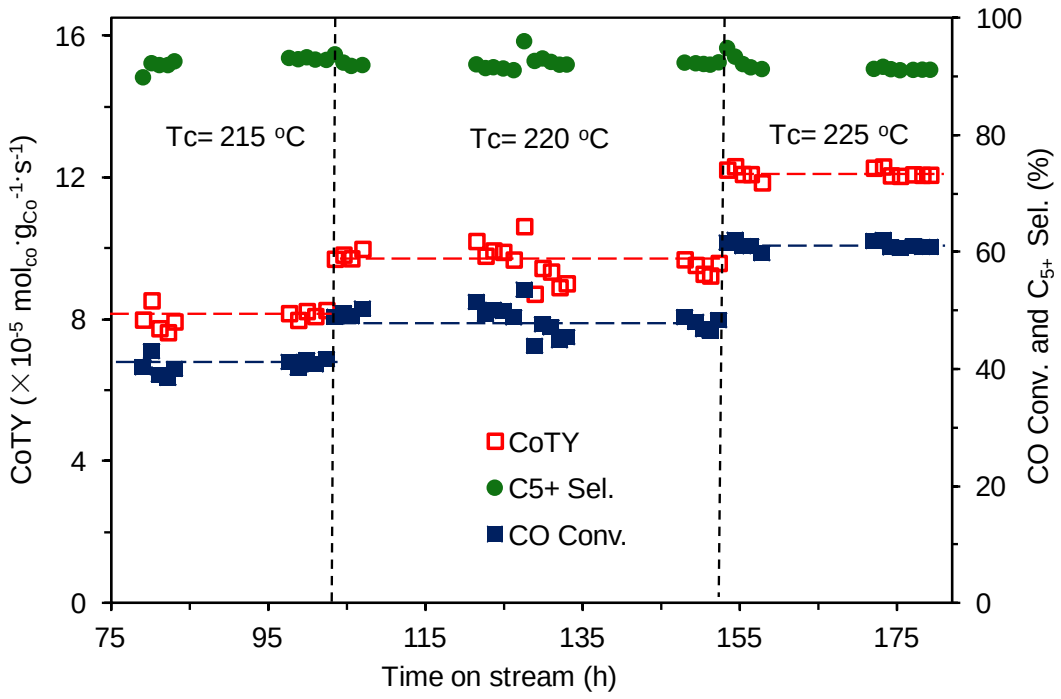

Figure 5-12. FTS catalytic performance and C_{5+} selectivity as functions of reaction temperature on 10Co/10TiO_2-SiC catalyst at higher flow rate (Reaction time on stream continue from Figure 10B. Recaton conditions: H_2/CO molar ratio = 2, pure synthesis gas, total presure = 40 atm, GHSV (STP) = 80 ml·g_{cat}^{-1}·min^{-1}.

In order to have a better understanding of the cobalt particle sizes and microstructures, we studied the cobalt phase inside the catalysts with zero field spin-echo ^{59}Co NMR technique.[18, 34-36] In Figure 5-13, NMR spectra of Co/SiC, Co/TiO_2(D)-SiC and Co/10TiO_2-SiC are measured at 2, 4.2, and 77 K together with spectra of the particles with selected blocking temperature ranges (see NMR experimental part). Similarly to what has been observed in previous chapters, the NMR signal decreases with the increase of the measurement temperature. In the Figure 5-13A, C and E, NMR intensity at 217 MHz is observed in the Co/SiC and Co/TiO_2(D)-SiC catalyst, showing a large number of Co atoms forming big face centered (fcc) particles larger than 30 nm. There is no pronounced NMR peak at 217 MHz from the cobalt on TiO_2 coated SiC catalysts. This could be attributed to the homogenous thin layer of TiO_2 offering relatively high metal-support interaction that increases cobalt dispersion. The cobalt microstructures are similar for each blocking

temperature range on Co/SiC and Co/TiO_2(D)-SiC catalysts according to the NMR spectra shape in Figure 5-13 B and D. It is interesting to note that the NMR shape of Co/10TiO_2-SiC is different from both the TiO_2-free or doped catalyst, indicating that when the TiO_2 homogeneous layer is introduced on thermal conductive SiC surface it will influence both the cobalt particles structure and dispersion of cobalt nanoparticles. Since the NMR shapes of Co/SiC and Co/TiO_2(D)-SiC catalysts are similar it is indicating that the difference in activity of these two catalysts is therefore only due to the difference among the particle size distributions (see below).[36]

Table 5-4. Comparison of FTS catalytic performance of the SiC-based catalysts and the other cobalt containing catalysts reported in the literature.

Catalyst	Reaction conditions	X(CO)/%	S(CH_4)	SC_{5+}	CoTY	Ref.
10Co/10TiO_2-SiC	225 ^oC, 40 bar	61.0	5.8	91.2	12.1	This work
IEN8	250 ^oC, 35 bar	84	-	74.0	19.2	[10]
CoMCNTs	220^oC, 20bar	34.4	5.8	84.4	7.1	[37]
12Co-2Ca/SiC	250 ^oC 20 bar	59.3	-	98.5	4.8	[17]
10Co/TiO_2-SiC (doped)	230 ^oC, 40 bar	50.5	5.9	91.7	7.5	[19]
12Co/$TiSiO_2$	210^oC, 20 bar	c.a. 30	9.8	81.5	7.2	[38]
12CoTi5SBA	210^oC, 20 bar	c.a. 40	7.5	85.9	7.5	[33]
10Co/TiO_2	220 ^oC, 20 bar	30-35	16.7	72.2	3.3	[39]
ReCo/TiO_2	230 ^oC, 23.5 bar	73.4	10.5	80.8	5.5	[28]
CoPt/Al_2O_3-N	220 ^oC, 20 bar	39	8.0	-	8.4	[40]
1Ru30Co/Al_2O_3_nf	220^oC, 2.0 MPa	c.a.40	13.8	< 73	4.9	[31]
RuCo/0.2Ti-Al_2O_3	240 ^oC, 20 bar	57.4	9.5	80.3	2.9	[41]

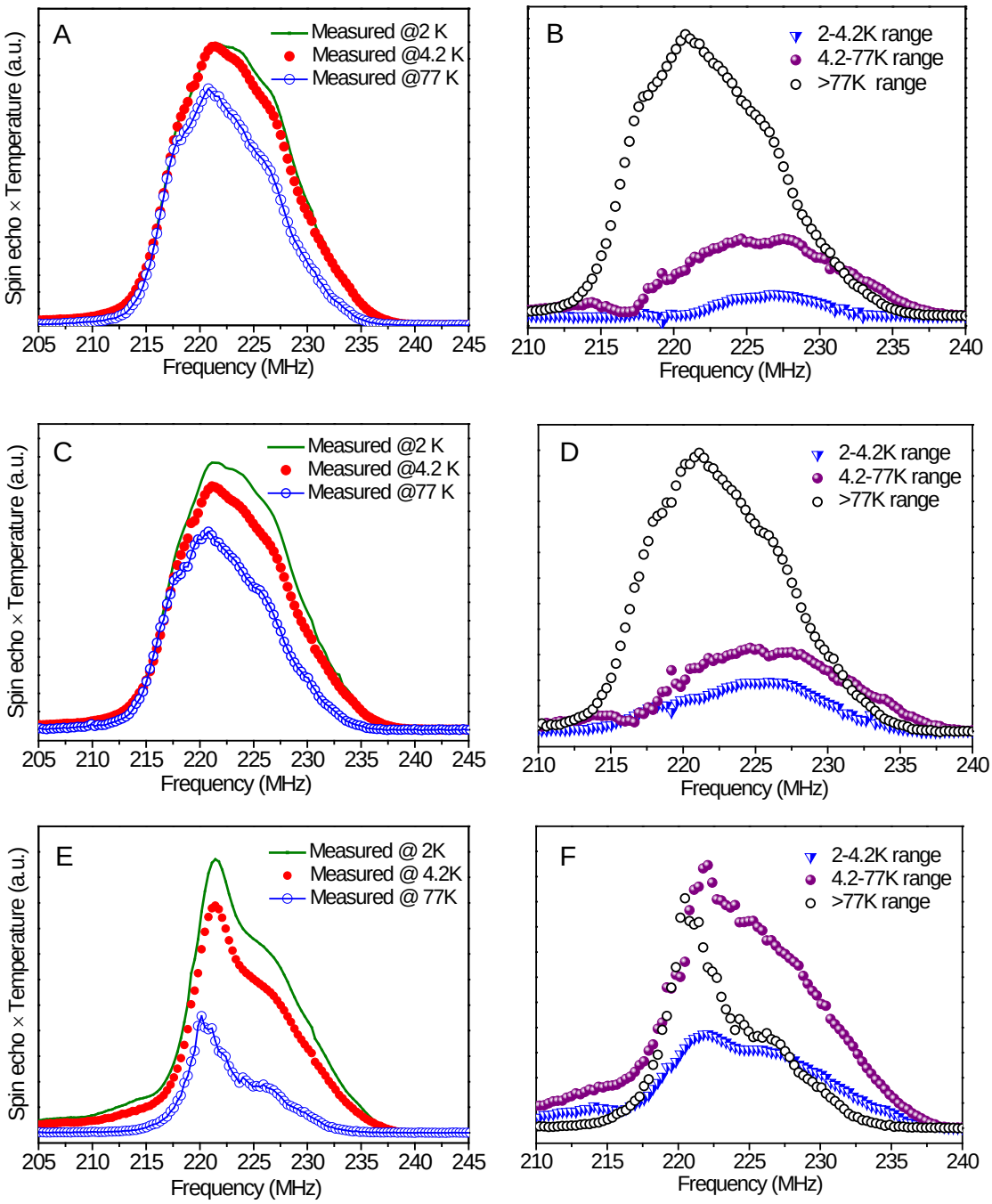

Figure 5-13. ^{59}Co zero field NMR spectra and different blocking temperature range of the (A, B) Co/SiC and (C, D) Co/TiO_2 (D)-SiC, (E,F) Co/10TiO_2-SiC catalysts after FTS test with wax solid retained recorded the blocking temperature at 2, 4.2 and 77K.

The fraction of cobalt atoms which derived from the NMR spectra in the different blocking temperature range, as well as the relative percentage of cobalt nanoparticles (Co NP) sizes and surface area based on the same amount of cobalt atoms, is presented in Figure 5-14.

According to the results, on the Co/10TiO_2-SiC catalyst, more than >70 % of cobalt atoms are engaged in the small particles (< 10 nm, blocking temperature range from 2-4.2 K and 4.2-77K). This is significantly higher than for Co/SiC and Co/TiO_2 (D)-SiC (< 40%). It is also interesting to note that the total amount of cobalt particle increases when the TiO_2 coverage is increased. If we have a closer look in Figure 5-14B we can observe that the TiO_2-coated catalyst shows a significant increase of the amount of small cobalt particles via high efficient metal-support interaction, which in turn leads to a higher FT activity.[42] Moreover, the activity is instead related to the amount of cobalt surface area rather than to the distribution of cobalt atoms. It is known that surface cobalt active sites (atoms surface area) are most probably activating the reaction by direct contact with the reactant molecules. As can be seen in Figure 5-14 A and B, the Co/TiO_2 (D)-SiC catalyst for example contains 60% of cobalt atoms forming large particles (measured blocking temperature higher than 77 K whith particle diameter ranging from 10 nm to 30 nm or even more) but those represents only < 2% in term of particles fraction, or only offer less than 20 % of the total atoms surface (active sites). It means that small particle (< 10 nm) play the key effects in FTS activity. In the Co/10TiO_2-SiC catalyst, about 80% of atoms formed > 90 % of the fraction of the particles in the range of 3-4 nm and 4-10 nm, which contribute for more than 90% to the particles surface area (3-4 nm and 4-10 nm offered 43% and 50 % of atoms surface area fraction). De Jong and co-workers[10] have come to the conclusion that the activity and selectivity in the Fischer-Tropsch reaction are strongly dependent on cobalt particle size for catalysts using carbon nanofibers as support. They have suggested that for low pressure conditions (1 bar) average sizes smaller that 6 nm are less efficient, while at high pressure conditions (35 bar) the upper average size limit is 8 nm. Prieto et al[43] demonstrated by in situ spectroscopic that the catalytic active decreased when cobalt metallic particle size is smaller than 10 nm on the surface functionalized zeolite supports. According our NMR results, we speculate that the small particles (3-10 nm) have multiple active sites depending on the preparation and materials used as support. The Goodma and coworkers[44] are also mentioning that Co particles in the range 3.5-10.5 nm show the higher catalytic activity and

low methane selectivity. They propose that the divergence in particle sizes range compared to the previous research work (Prieto et al[43]) is due to the difference in catalysts preparation and complexity of FT synthesis itself.

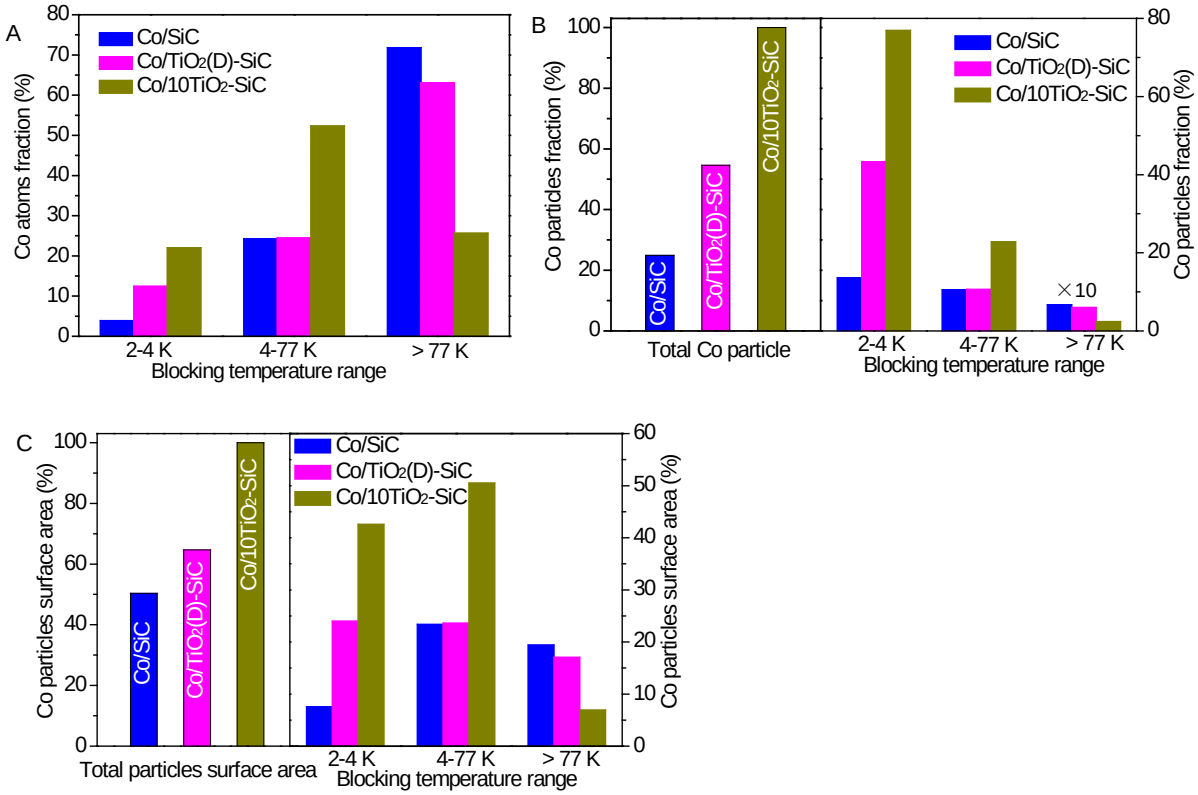

Figure 5-14 ^{59}Co zero field NMR results. (A) The fraction of cobalt atoms engaged in the different blocking temperature. (B) Total cobalt particles calculated from the same amount of Co atoms, and the relative cobalt particles as a function of the blocking temperature (C) Total cobalt particles surface area calculated from the same amount of Co atoms, and the relative particles surface area as a function of the blocking temperature particle surface area.

For a better vision of the cobalt microstructures of tested catalysts, a quantitative analysis of cobalt atoms distributed in different phases according to the deconvolution (see experimental chapter) of the ^{59}Co NMR spectra for different blocking temperature range are shown in Table 5-5 and Figure 5-15. From the Table 5-5, it can be noticed that the total amount of hcp like atoms (pure hcp phase and hcp stacking faults in the fcc phase) in the investigated samples are significantly high (> 45%) in each blocking temperature range. FTS

catalytic performance could be enhanced in the presence of the higher hcp phase fraction as suggested by Khodakov and coworkers[40, 45]. Bezemer et al.[10] proposed that very small particle size leads to low FTS activity and that in addition inside such small particles the active sites might not be stable from the crystallography viewpoint. The relative high activity on SiC supported cobalt catalysts could be attribute to high hcp phase in the Co particles structure. The hcp phase in Co/10TiO_2-SiC catalysts seems lower than the one in other two catalysts (Table 5-5). However, form the Table 5-5 it can also be found that there is less hcp stacking faults in the Co/10TiO_2-SiC sample. This makes difficult to give any conclusive remark about the influence of the structure on the FTS activity in these samples. Indeed the structural effect is completely screened by the size effect.

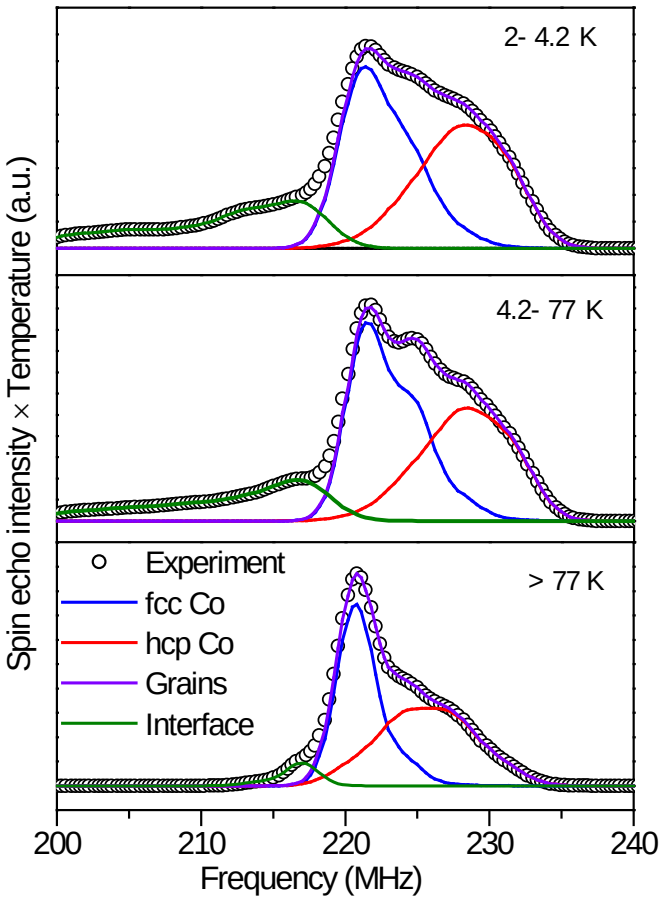

Figure 5-15. ^{59}Co NMR spectra decomposition peaks of Co/10TiO_2-SiC catalyst on the different blocking ranges. The lines show the decomposition into fcc cobalt, hcp cobalt and interface of grains.

Table 5-5. Distribution of cobalt atoms in the different crystal phases according to the deconvolution of the 59Co NMR envelope.

Sample	Blocking temperature range (K)	Cobalt atoms (at. %)				fcc frequency (MHz)
		fcc	H/c[a]	C/h[b]	hcp	
CoSiC	2-4.2	3.3	49.8	50.0	96.7	221.8
	4.2-77	47.3	24.4	25.0	52.7	221.1
	>77	47.2	44.5	23.3	52.8	219.6
		4.2	23.3	50.0	54.8	217[c]
$CoTiO_2$(D)SiC	2-4.2	56.3	40.5	28.5	43.7	220.2
	4.2-77	49.2	22.9	24.1	50.8	220.9
	>77	41.5	50.0	24.1	59.5	219.8
		40.0	25.6	50.0	60.0	217[c]
Co10TiO_2SiC	2-4.2	51.7	15.2	29.7	48.3	221.1
	4.2-77	55.0	16.2	30.7	45.0	221.4
	>77	49.5	4.6	49.8	50.5	220.7

[a] H/c: hcp stacking faults in the fcc phase.
[b] C/h: fcc stacking faults in the hcp phase.
[c] The big fcc particle diameter is larger than 30 nm which is determined at the frequency at around 217 MHz.

5.2.6 FTS performance with high cobalt loading

Industrial F-T plants are generally operated with a high conversion and selectivity per pass in order to avoid the costly downstream separation process. The industrial F-T catalysts are thus heavily charged with the active phase, 30 to 50 wt. %, on one hand along with reasonable metal active phase dispersion on the other hand in order to achieve the high conversion of the reactant per pass. [46-47] In order to compare the FT performance in a more reliable reaction conditions high cobalt loading, i.e. 30 wt %, catalyst (30Co/10TiO_2-SiC) is also evaluated and the results are presented in Figure 13. Increasing the active phase loading per unit weight of catalyst will inevitably decrease the CoTY value, as more cobalt particles are localized in the metal bulk and thus, are not accessible to the reactants, and thus, the comparison of the FTS performance between both cobalt-based

catalysts with different cobalt loadings will be carried out using a specific activity, i.e. FTS reaction rate representing the weight of long chain hydrocarbons (C_{5+}) formed per gram of catalyst per hour [$g_{C5+} \cdot g_{catalyst}^{-1} \cdot h^{-1}$], instead of the cobalt time yield value as before. The F-T performance obtained on the 30Co/10TiO_2-SiC catalyst as a function of time on stream under realistic FTS reaction conditions, i.e. space velocity of 320 $ml \cdot g_{cat}^{-1} \cdot min^{-1}$ and reaction temperature of 240 ^{o}C, is presented in Figure 5-16. It is also worth mentioning that the catalyst has already been evaluated in the FTS reaction under different conditions more than 240 h on stream (not reported) before performing this test. According to the results the thermal conductor TiO_2-SiC-based catalyst exhibits a higher FTS performance, and the FTS activity remains also stable for about 100 h on stream and confirms the relatively high stability of the catalyst promoted with TiO_2. The specific rate steadily increased to 1.22 $g_{C5+} \cdot g_{catalyst}^{-1} \cdot h^{-1}$ with a relatively higher C_{5+} selectivity, i.e. 85.8 %.

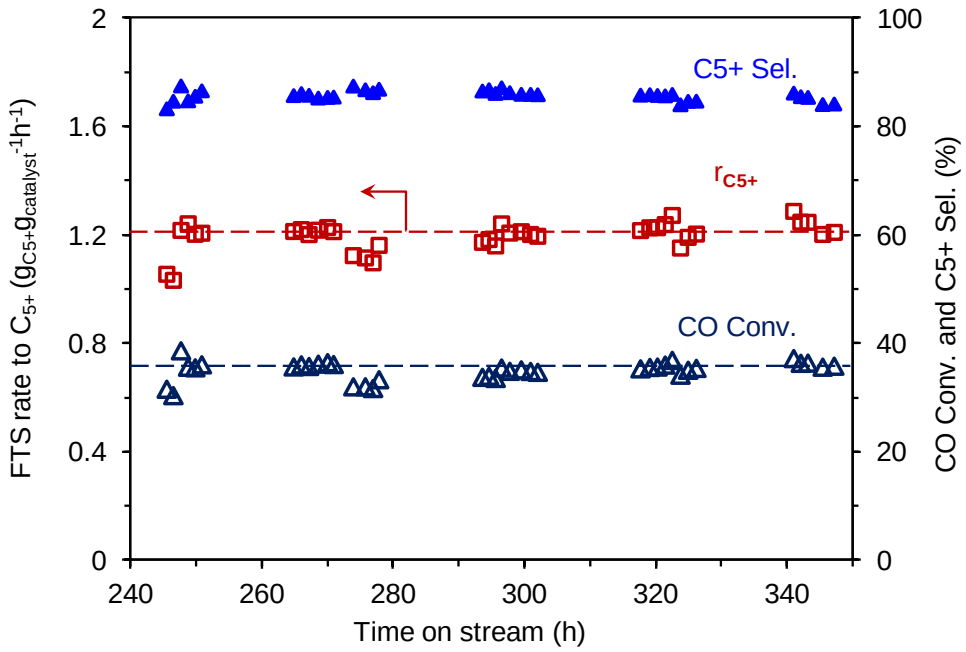

Figure 5-16. FTS activity and C_{5+} selectivity as functions of time on stream on 30Co/10TiO_2-SiC catalysts. Reaction conditions: H_2/CO molar ratio = 2, reaction temperature = 240 °C, total pressure = 40 bar, GHSV (STP) = 320 $ml \cdot g_{cat}^{-1} \cdot min^{-1}$, total pressure = 40 bar, 1.25 g catalyst diluted with 3.75g SiC.

The product distribution was also analyzed and the results are summarized in Table 5-6. The catalyst showed a relatively low selectivity towards methane (< 10 %) as well as oxygenate compounds (< 2 %, not shown), which evidences the high efficiency of the catalyst to convert the syngas (CO and H_2) to the valuable hydrocarbons. Chain-growth probability factor (α) determined on the 30Co/10TiO_2-SiC catalyst is 0.88 which can be found in Figure 5-17. The relative high α value obtained in the present work is directly linked with the relatively low methane selectivity (< 10%) obtained on the catalyst. It is also worthy to note that the specific rate obtained on the un-promoted 30Co/10TiO_2-SiC catalyst is also relatively high and more stable compared to those promoted by noble metal obtained on the Co-Re/Al_2O_3, Co-Re/SiO_2 and Co-Re/TiO_2 catalysts as reported by Tsakoumis et al.[48] The most active catalyst reported in the work of Tsakoumis et al.[48] is the Co-Re/Al_2O_3 (cobalt concentration) with an initial reaction rate of about 0.56 $g_{CH2}\cdot g_{catalyst}\cdot h^{-1}$ followed by a rapid deactivation down to 0.45 $g_{CH2}\cdot g_{catalyst}^{-1}\cdot h^{-1}$ after about 22 h on stream.

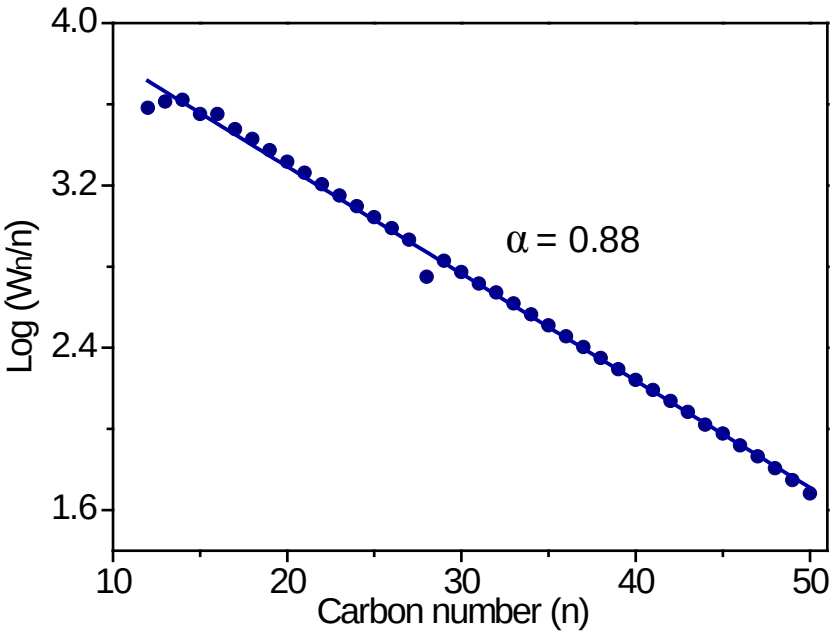

Figure 5-17. Anderson-Schulz-Flory plots for 30Co/10TiO_2-SiC catalyst on realistic FTS reaction conditions.

Table 5-6 Catalytic performance on the TiO_2-SiC supported 30 wt % cobalt based catalyst at realistic FTS reaction.[a]

CO Conv. (%)	Product selectivity (%)				r_{C5+} [b]	α [c]
	CO_2	CH_4	C_2–C_4	C_{5+}		
35.5	0.1	9.8	4.3	85.8	1.22	0.88

[a] All data were obtained after 20h time on stream with stable catalytic performance at testing conditions. Reaction condition: T = 240 °C, 320 $ml \cdot g_{cat}^{-1} \cdot min^{-1}$, total pressure = 40 bar, 1.25 g catalyst diluted with 3.75g SiC.

[b] FTS rate to C_{5+} hydrocarbons ($g_{C5+} \cdot g_{cat}^{-1} \cdot h^{-1}$, mass of C_{5+} formed per gram catalyst per hour).

[c] Chain growth probability factor.

5.3 Conclusion

This work has shown that the Fischer-Tropsch reaction can be performed with high activity and selectivity on a cobalt-based catalyst supported on a thermal conductor support of silicon carbide coated with a thin layer of TiO_2. The coated layer of TiO_2 significantly improves the metal-support interaction between the cobalt oxide and the support leading to a better dispersion of the cobalt active phase. Detailed study has shown that the TiO_2 loading exhibits a significant influence on the cobalt oxide size and its reducibility which in turn, strongly modify the F-T performance of the catalyst. The optimum TiO_2 coating was around 10 wt% which leads to an active, selective and highly stable F-T catalyst. The catalysts, either with low (10 wt%) or high (30 wt%) cobalt loading, exhibit a high and stable F-T activity and long chain hydrocarbons selectivity along with a long-term stability. ^{59}Co NMR analysis indicates that the cobalt particles were relatively well dispersed on the support with an average particle size ranged between 4 to 15 nm. Such a high dispersion was advanced to explain the high F-T performance of the catalyst while the thermal conductivity of the support was expected to be at the origin of a high C_{5+} selectivity even at a relatively high reaction temperature. On the high cobalt loading, i.e. 30 wt %, the F-T specific rate of 1.2 $g_{C5+} \cdot g_{cat}^{-1} \cdot h^{-1}$ and a C_{5+} selectivity of 86 % were obtained at 240 °C which are among the highest F-T performance reported up to now in the literature. The meso- and macroporosity

of the support is also responsible for the long-term stability of the catalyst by reducing the problem of pore plugging due to the accumulation of residual carbonaceous species. This study provides a new design strategy for preparing stable thermal conductive Fischer-Tropsch catalysts with both excellent activity and long-chain hydrocarbon selectivity.

References

[1] J. R. Rostrup-Nielsen, *Science* **2005**, *308*, 1421-1422.

[2] G. M. Whitesides, G. W. Crabtree, *Science* **2007**, *315*, 796-798.

[3] H. M. T. Galvis, J. H. Bitter, C. B. Khare, M. Ruitenbeek, A. I. Dugulan, K. P. de Jong, *Science* **2012**, *335*, 835-838.

[4] A. Y. Khodakov, W. Chu, P. Fongarland, *Chemical Reviews* **2007**, *107*, 1692-1744.

[5] E. Iglesia, *Appl Catal a-Gen* **1997**, *161*, 59-78.

[6] E. de Smit, B. M. Weckhuysen, *Chem Soc Rev* **2008**, *37*, 2758-2781.

[7] Q. H. Zhang, J. C. Kang, Y. Wang, *ChemCatChem* **2010**, *2*, 1030-1058.

[8] J. C. Kang, K. Cheng, L. Zhang, Q. H. Zhang, J. S. Ding, W. Q. Hua, Y. C. Lou, Q. G. Zhai, Y. Wang, *Angew Chem Int Edit* **2011**, *50*, 5200-5203.

[9] W. Chu, L. N. Wang, P. A. Chernavskii, A. Y. Khodakov, *Angew Chem Int Edit* **2008**, *47*, 5052-5055.

[10] G. L. Bezemer, J. H. Bitter, H. P. C. E. Kuipers, H. Oosterbeek, J. E. Holewijn, X. D. Xu, F. Kapteijn, A. J. van Dillen, K. P. de Jong, *J Am Chem Soc* **2006**, *128*, 3956-3964.

[11] J. P. den Breejen, P. B. Radstake, G. L. Bezemer, J. H. Bitter, V. Froseth, A. Holmen, K. P. de Jong, *J Am Chem Soc* **2009**, *131*, 7197-7203.

[12] J. C. Kang, S. L. Zhang, Q. H. Zhang, Y. Wang, *Angew Chem Int Edit* **2009**, *48*, 2565-2568.

[13] S. Storsaeter, O. Borg, E. A. Blekkan, B. Totdal, A. Holmen, *Catal Today* **2005**, *100*, 343-347.

[14] M. Lacroix, L. Dreibine, B. de Tymowski, F. Vigneron, D. Edouard, D. Begin, P. Nguyen, C. Pham, S. Savin-Poncet, F. Luck, M. J. Ledoux, C. Pharn-Huu, *Appl Catal a-Gen* **2011**, *397*, 62-72.

[15] A. R. de la Osa, A. De Lucas, J. Diaz-Maroto, A. Romero, J. L. Valverde, P. Sanchez, *Catal Today* **2012**, *187*, 173-182.

[16] A. R. de la Osa, A. De Lucas, A. Romero, J. L. Valverde, P. Sanchez, *Catal Today* **2011**, *176*, 298-302.

[17] A. R. de la Osa, A. de Lucas, L. Sanchez-Silva, J. Diaz-Maroto, J. L. Valverde, *Fuel* **2012**, *95*, 587-598.

[18] B. de Tymowski, Y. F. Liu, C. Meny, C. Lefevre, D. Begin, P. Nguyen, C. Pham, D. Edouard, F. Luck, C. Pham-Huu, *Appl Catal a-Gen* **2012**, *419*, 31-40.

[19] Y. Liu, B. de Tymowski, F. Vigneron, I. Florea, O. Ersen, C. Meny, P. Nguyen, C. Pham, F. Luck, C. Pham-Huu, *ACS Catalysis* **2013**, 393-404.

[20] B. Jongsomjit, T. Wongsalee, P. Praserthdam, *Mater Chem Phys* **2006**, *97*, 343-350.

[21] J. Y. Shen, H. Wang, Y. Zhou, N. Q. Ye, G. B. Li, L. J. Wang, *Rsc Adv* **2012**, *2*, 9173-9178.

[22] N. Keller, C. Pham-Huu, M. J. Ledoux, C. Estournes, G. Ehret, *Appl Catal a-Gen* **1999**, *187*, 255-268.

[23] P. Nguyen, C. Pham, *Appl Catal a-Gen* **2011**, *391*, 443-454.

[24] J. P. Hong, W. Chu, P. A. Chernavskii, A. Y. Khodakov, *Appl Catal a-Gen* **2010**, *382*, 28-35.

[25] O. Borg, S. Erib, E. A. Blekkan, S. Storsaeter, H. Wigum, E. Rytter, A. Holmen, *J Catal* **2007**, *248*, 89-100.

[26] G. Jacobs, T. K. Das, Y. Q. Zhang, J. L. Li, G. Racoillet, B. H. Davis, *Appl Catal a-Gen* **2002**, *233*, 263-281.

[27] S. Storsaeter, B. Totdal, J. C. Walmsley, B. S. Tanem, A. Holmen, *J Catal* **2005**, *236*, 139-152.

[28] J. L. Li, G. Jacobs, Y. Q. Zhang, T. Das, B. H. Davis, *Appl Catal a-Gen* **2002**, *223*, 195-203.

[29] W. Chu, P. A. Chernavskii, L. Gengembre, G. A. Pankina, P. Fongarland, A. Y. Khodakov, *J Catal* **2007**, *252*, 215-230.

[30] J. P. Hong, W. Chu, P. A. Chernavskii, A. Y. Khodakov, *J Catal* **2010**, *273*, 9-17.

[31] A. Martinez, G. Prieto, J. Rollan, *J Catal* **2009**, *263*, 292-305.

[32] S. Rane, O. Borg, J. Yang, E. Rytter, A. Holmen, *Appl Catal a-Gen* **2010**, *388*, 160-167.

[33] M. Lualdi, G. Di Carlo, S. Logdberg, S. Jaras, M. Boutonnet, V. La Parola, L. F. Liotta, G. M. Ingo, A. M. Venezia, *Appl Catal a-Gen* **2012**, *443*, 76-86.

[34] C. Meny, P. Panissod, (Ed.: G. A. Webb), Springer, Heidelberg, Germany **2006**.

[35] P. Panissod, C. Meny, *Appl Magn Reson* **2000**, *19*, 447-460.

[36] Y. Liu, B. de Tymowski, F. Vigneron, I. Florea, O. Ersen, C. Meny, P. Nguyen, C. Pham, F. Luck, C. Pham-Huu, *ACS Catalysis* **2013**, *3*, 393-404.

[37] H. Zhang, C. Lancelot, W. Chu, J. P. Hong, A. Y. Khodakov, P. A. Chernavskii, J. Zheng, D. G. Tong, *J Mater Chem* **2009**, *19*, 9241-9249.

[38] A. M. Venezia, V. La Parola, L. F. Liotta, G. Pantaleo, M. Lualdi, M. Boutonnet, S. Jaras, *Catal Today* **2012**, *197*, 18-23.

[39] K. Jalama, J. Kabuba, H. F. Xiong, L. L. Jewell, *Catal Commun* **2012**, *17*, 154-159.

[40] H. Karaca, O. V. Safonova, S. Chambrey, P. Fongarland, P. Roussel, A. Griboval-Constant, M. Lacroix, A. Y. Khodakov, *J Catal* **2011**, *277*, 14-26.

[41] S. J. Park, S. M. Kim, M. H. Woo, J. W. Bae, K. W. Jun, K. S. Ha, *Appl Catal a-Gen* **2012**, *419*, 148-155.

[42] Y. Liu, T. Dintzer, O. Ersen, C. Pham-Huu, *Journal of Energy Chemistry* **2013**, *22*, 279-289.

[43] G. Prieto, A. Martinez, P. Concepcion, R. Moreno-Tost, *J Catal* **2009**, *266*, 129-144.

[44] Z. J. Wang, S. Skiles, F. Yang, Z. Yan, D. W. Goodman, *Catal Today* **2012**, *181*, 75-81.

[45] H. Karaca, J. P. Hong, P. Fongarland, P. Roussel, A. Griboval-Constant, M. Lacroix, K. Hortmann, O. V. Safonova, A. Y. Khodakov, *Chemical Communications* **2010**, *46*, 788-790.

[46] F. Diehl, A. Y. Khodakov, *Oil Gas Sci Technol* **2009**, *64*, 11-24.

[47] B. H. Davis, *Ind Eng Chem Res* **2007**, *46*, 8938-8945.

[48] N. E. Tsakoumis, M. Ronning, O. Borg, E. Rytter, A. Holmen, *Catal Today* **2010**, *154*, 162-182.

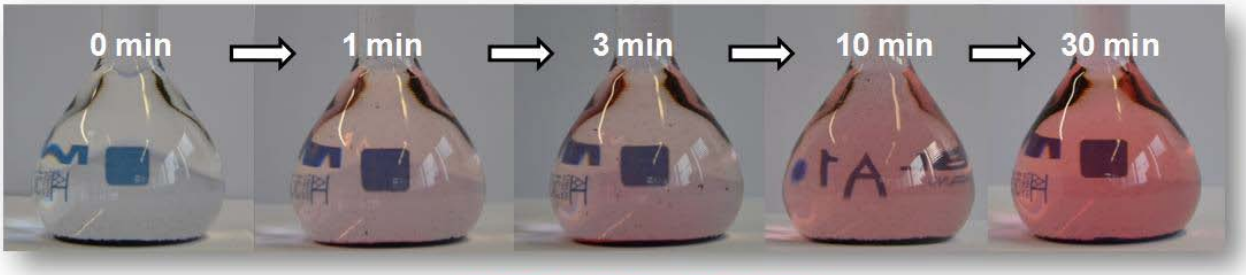

PERSPECTIVES

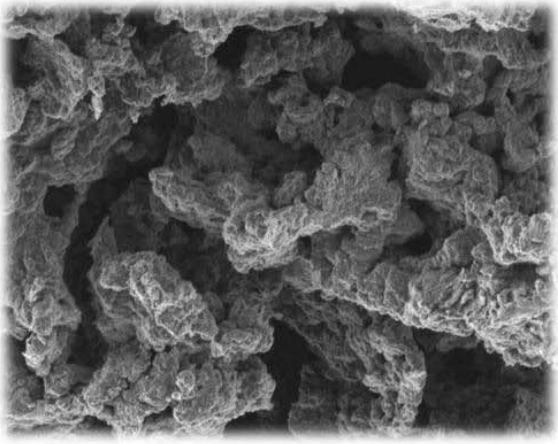

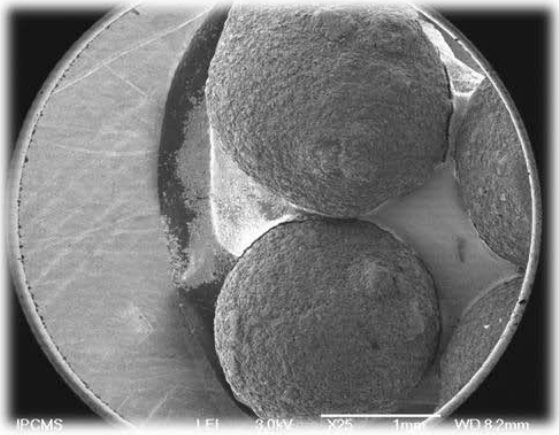

Chapter VI

Conclusion and perspectives

Chapter VI Conclusion and perspectives

6.1 General conclusion

According to the previous work in the literatures and patents, the supported cobalt catalysts with high thermal conductivity (which allows rapid homogenization of temperature within the catalyst bed) and open structure (which possesses macro- and mesoporosity or hierarchical structure) are essential to accelerate Fischer-Tropsch synthesis (FTS) process for industry development. The main work of this report is focused on the optimization of the supports for the FTS process. The combination of conventional characterization techniques including high resolution TEM, XRD, TPR, etc, and advanced characterization techniques such as energy-filtered transmission electron microscopy (EFTEM) and ^{59}Co zero field nuclear magnetic resonance (^{59}CoNMR) allows one to investigate the different physical properties of the supported cobalt catalyst, i.e. dispersibility, reducibility and morphology, and to correlate them with the FTS performance and stability.

The general introduction of the process, technologies, FTS catalysts, along with the advantages and drawbacks of various carriers for the Fischer-Tropsch synthesis were summarized in Chapter I. Chapter II illustrated the synthesis and characterization of supports and catalysts, and the details of the catalytic reaction process. The main results obtained in the present work are summarized in Chapters III to V.

6.1.1 Hierarchical-structured conductive CNT- based supports

√ *Carbon nanotubes decorated α-Al_2O_3 (CNT-α-Al_2O_3) containing cobalt nanoparticles*

A new hierarchical support, based on the homogenous decoration of a low specific surface area α-Al_2O_3 by a layer of carbon nanotubes, was successfully synthesized. The composite exhibited a relatively high and fully accessible surface (specific surface area of i.e. 76 $m^2.g^{-1}$), comparing to the origin support, i.e. 5 $m^2.g^{-1}$. The cobalt based catalyst

supported on this hierarchically- structured material was turned out to be a high efficient catalyst for the FTS reaction. The extremely high selectivity towards liquid hydrocarbons along with great catalytic activity is observed on the hierarchical catalyst comparing to the pristine α-Al_2O_3 or traditional CNT supported cobalt catalysts. The high selectivity towards long chain hydrocarbons was attributed to the intrinsic thermal conductivity of CNT layer which can help in the heat dissipation throughout the catalyst body and thus, avoid the formation of local hot spots which appeared at high CO conversion in the FTS reaction. The CNT decorated α-Al_2O_3 catalyst also exhibited satisfied high stability during more than 200 h of reaction under relative severe conditions compared to the reported catalysts in the literature. Finally, the macroscopic shape of such composite renders easily its usage as catalyst support in a fixed-bed configuration without facing problems of transport and pressure drop which are encountered with the bulk carbon nanotubes.

√ ***Hierarchically structured TiO_2/CNT-a-Al_2O_3 supported nano-cobalt catalyst***

By coating a thin layer of TiO_2 on the surface of the CNT-a-Al_2O_3 support, the cobalt dispersion and the FTS performance were significantly improved, exhibiting the highest activity among all the TiO_2-based catalysts reported nowadays. The TiO_2 promoted hierarchically structured catalyst (CoTiCNTA) exhibited a carbon monoxide conversion of 44.3%, which was higher than that obtained with conventional hierarchically catalyst (28.2%, CoCNTA) and conventional TiO_2 promoted catalysts (33.4%, CoTiA). Moreover, the TiO_2-promoted hierarchically-structured catalyst gave approximately 84.5% selectivity of C_{5+} at 47.4% CO conversion under severe FTS reaction conditions, i.e. relative high reaction temperature (T = 245 ^oC), total pressure (40 bar) and flow rate (GHSV (STP) =9600 $mL \cdot g_{cat}^{-1} \cdot h^{-1}$). The FTS rate expressed in terms of weight of long chain hydrocarbon formed per gram of catalyst per hour ($g_{C5+} \cdot g_{cat}^{-1} \cdot h^{-1}$) was around 0.80 $g_{C5+} \cdot g_{cat}^{-1} \cdot h^{-1}$, which was the best result among all the noble-free cobalt-based catalysts previously reported to our knowledge, including the cobalt supported on carbon nanofibers (CNF) catalysts.

6.1.2. Titania-doped silicon carbide supported cobalt catalyst

Despite the high FTS performance observed, the main drawback of using CNT in the FTS reaction was the high sensitivity of the CNT towards oxidation which render difficult the regeneration of the catalyst. The main objective of this chapter is to investigate the development of a new hybrid support consisted by a titanium doped silicon carbide (SiC), with high oxidative resistance, high specific surface area and improved metal-support interactions.

√ ***Novel cobalt catalyst supported by titania-doped silicon carbide***

The results have shown that the medium metal-support interaction between the cobalt nanoparticles and TiO_2 led to the formation of small cobalt particles with enhanced FTS activity comparing to the same catalyst supported on the undecorated SiC support. The presence of higher amount of small and medium cobalt particles on the TiO_2-decorated SiC was also confirmed by ^{59}Co NMR comparing to the undecorated SiC. Indeed, such small metal particles (4-15 nm) with a large fraction of surface atoms significantly contributed to the enhancement of the conversion rate of reactants into products. After titania doping, the cobalt time yield increased from 5.3×10^{-5} $mol_{co}g_{Co}^{-1}s^{-1}$ to 7.5×10^{-5} $mol_{co}g_{Co}^{-1}s^{-1}$ at 230 ^{o}C, while the C_{5+} selectivity was maintained in the same level, i.e. 91.7% and 91.6%, respectively. The NMR analyses also revealed that a large fraction of Co atoms (about 70 %), in the un-doped catalyst, were engaged into a small number of very large particles that were not very efficient for the FTS process. In the TiO_2 doped catalyst the metal-support interaction leads to the formation of small cobalt particles exhibiting high activity in the FTS reaction.

√ ***Structure-activity relationship investigated by microstructural analysis and EFTEM***

This study underlined once again the benefit of the electron tomography applied in the analytical mode for providing one-to-one correspondence between the morphology and chemical composition on a three-dimensional surface at nanoscale resolution. The detailed analysis of the Co/TiO_2-SiC catalyst by 2D and 3D chemical imaging based on energy filtered TEM, combined with the more traditional high-resolution TEM mode, allows one to

precisely solve the microstructure, the porous characteristics and the distribution of the constituting phases. The catalytic tests show that silicon carbide doped with titanium dioxide can be efficiently employed as cobalt support in the FTS process under severe reaction conditions. The characteristics deduced by HR-TEM and EFTEM tomography were correlated to the enhancement of the FT performance of the Co/TiO_2-SiC catalyst which seems to be due to a better dispersion of the cobalt particles in close contact with the TiO_2 phase. The 3D reconstructions of the selected grains also allow one to access to the internal porosity of the support which is expected to play an important role in the product evacuation and reactant supply. In addition, the TEM imaging and EFTEM chemical mapping allow one to confirm the complete retention of the small cobalt particle size in contact with the TiO_2 phase after long-term FTS reaction. It is expected that the high FTS performance and stability of the catalyst were directly linked with the high stability of the small cobalt particles in close contact with the TiO_2 phase and also to the intrinsic thermal conductivity of the support to prevent the local hot spot formation which could favor the lost of the active sites by sintering. The high selectivity towards liquid hydrocarbons is attributed to the intrinsic thermal conductivity and a meso-/macroporosity of the support. Additional work is on going to evaluate the F-T performance of such hybrid catalyst with different titanium dioxide loading and under more severe reaction conditions, i.e. high temperature and low space velocity, in order to optimize such catalyst for future industrial development of the Fischer-Tropsch synthesis.

6.1.3. Titania coated silicon carbide support cobalt nanoparticles

In this chapter, we have investigated the influence of the TiO_2 not as doping but as a thin coating layer on the SiC surface. The deposited TiO_2 layer strongly interacts with cobalt precursor, leading to the formation of small cobalt particles (3-10 nm) with high dispersion and better resistance towards sintering, accounting for the better activity and stability in FTS reaction.. The obtained catalysts exhibit excellent catalytic performance along with high C_{5+} selectivity (> 85%) in the FTS reaction. The long-term FT reaction over 80 h was evaluated on the $Co/10TiO_2$-SiC catalyst at 215 ^oC. The cobalt time yield and C_{5+} selectivity keep the

same value at around 8.2 $\times 10^{-5}$ $mol_{co}g_{Co}^{-1}s^{-1}$ and 92%, respectively. These results clearly revealing an excellent stability of the catalyst, which indicates that deactivation linked with cobalt surface oxidation or sintering is unlikely to occur under the reaction conditions. It was noted that the catalyst tested has already been evaluated in the FTS reaction at 215 ^{o}C and under a GHSV of 2400 $ml \cdot g_{cat}^{-1} \cdot h^{-1}$ about 100 hour on stream before.

6.2 Perspectives

The future investigation will be focused on the catalyst regeneration, and active phase support recovery to optimize these novel SiC-based hybrid catalysts in the reaction process for building the bridge between the laboratory scale development and pre-industrialization process. The work is also ongoing to investigate the effect of noble metal promoter including Ru, Re or Pt, on the catalytic activity and selectivity of the FTS process either on the active site dispersion and reducibility. Attention will also be paid to the development of a new type of support based on the macroscopic carbon materials, i.e. carbon nanotubes, carbon nanofibers, and few-layer graphene (FLG) with controlled macroscopic sizes and shapes. These self-supported nanocarbon materials will be further characterized by various techniques and tested in the FTS reaction. The results which will be obtained on such hierarchical supports will allow one to get more insight about the influence of the support nature on the catalytic performance of the catalyst. The more detail potential investigations on basis of the current research work are list as follows.

6.2.1 Active phase and support recovery

Catalyst deactivation as a function of time on stream is an important research topic for industrial catalyst development. A number of different deactivation mechanisms include poisoning, oxidation of metallic cobalt metal, sintering, metal-support compound formation like cobalt silicates and cobalt aluminates surface, sintering of small cobalt particles sintering, carbon formation and surface reconstruction, etc, on cobalt-based catalysts were summarized in the most recent reviews[1-2] The possibility of recovering of both the active phase and the support is extremely important in the catalysis field as it avoids the solid waste

disposal after the end life of the catalyst and also reduces to a significant manner the cost investment of the process regarding the price of the FTS catalyst. The amounts of catalysts required for the planned GTL plants are fairly high, and may thus influence the availability and pricing of the constituent metals concerned, for example, the FTS plan of the capacity 1,000,000 barrels per day needs 25,000 t of FT catalysts in which contains around 5000 t of cobalt and/or trace amount of noble metals that depending on the intrinsic market value of the metal.[3]

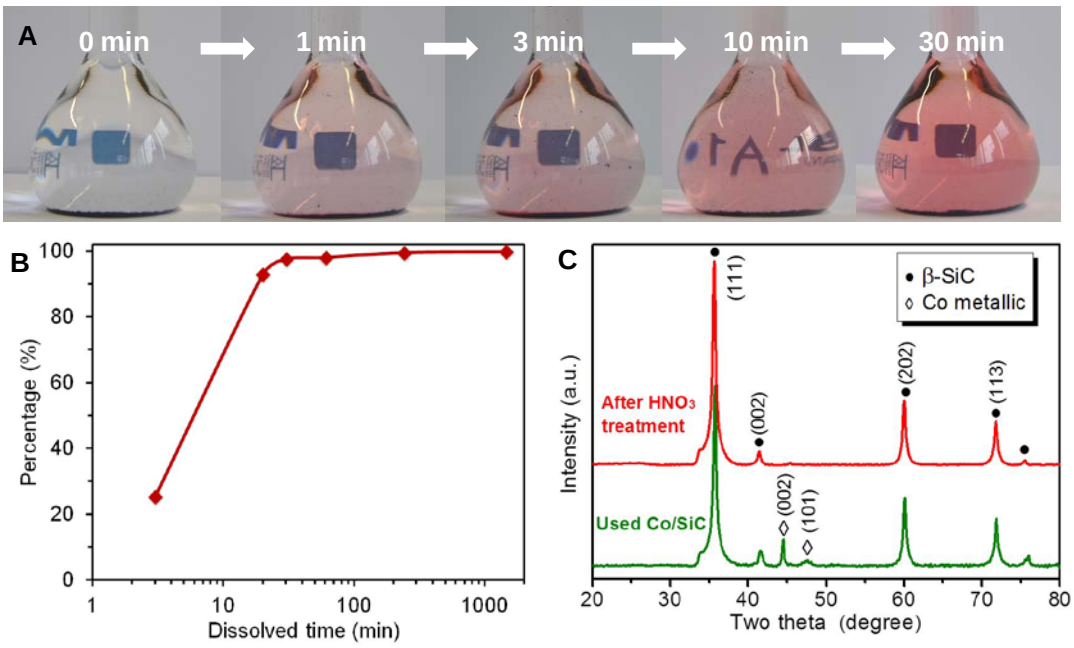

Figure 6-1. (**A**) Optical photos showing the coloration of the HNO_3 medium as a function of time of treatment of the Co/SiC catalyst at room temperature indicating the gradual dissolving of the cobalt phase in the acid medium. (**B**) ICP-MS curve showing the amount of cobalt dissolved into the HNO_3 medium as a function of time with an almost completion after 30 minutes of treatment. (**C**) XRD patterns of the Co/SiC and the same after an acid treatment showing the complete disappearance of the cobalt diffraction lines.

The chemical inertness of the SiC support also render easy the recovery of the active phase and the support for subsequence re-uses as illustrated in Figure 6-1**.** The Co/SiC catalyst, after reaction, was reduced under H_2 flow to convert all the cobalt phases into metallic cobalt. The total cobalt content on the catalyst was analyzed by ICP-MS technique

after dissolving the cobalt phase in a HNO_3 solution. The presented results confirm that the recovered support exhibits a similar physical behavior as the fresh one and indicate that recovery process did not modify the support properties as generally encountered with other supports such as alumina or silica. Detailed investigation will be conducted on such area regarding the optimization of the metal-support interaction after an acidic treatment.

6.2.2 Open-structured self-macronized carbon-based materials

The macroscopic shaping of the CNT with full accessible surface also leads to a drastic decrease of the pressure drop across the packed bed compared to that obtained on the un-shaped material.[4] The difference in the pressure drop behaviour between the CNTs and micronized CNTs beads is displayed in Figure 6-2 and confirms the high advantageous of using micronized material.

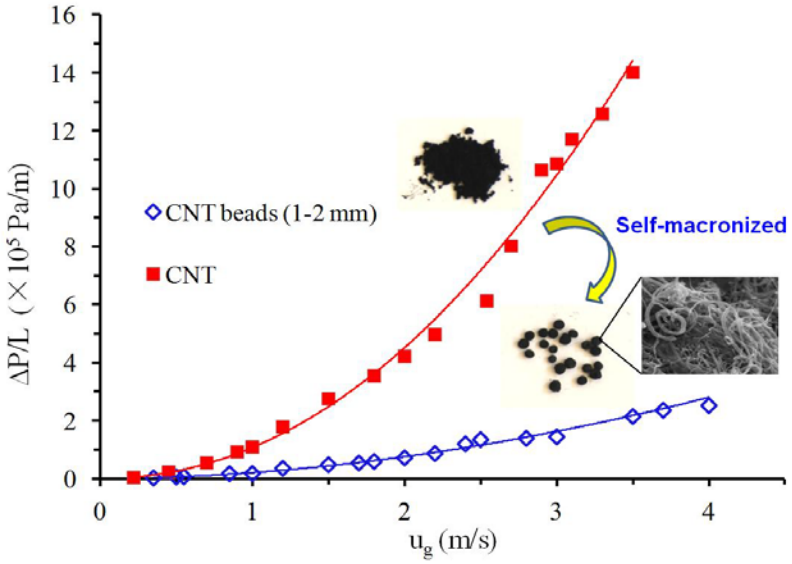

Figure 6-2. Pressure drop measurements on the origin CNT and the self-micronized CNT beads.

The representative SEM micrographs of the self-macronized CNT composite material after thermal treatment step are presented in Figure 6-3. Low-magnification SEM micrograph shows the gross morphology of the beads with regular shape (Figure 6-3A). A closer view indicates that the beads were constituted by a highly entangled CNT forming a

dense network with high mechanical strength allowing it to be efficiently employed as catalyst support either in a gas- or liquid-phase medium (Figure 6-3B). High-magnification observation shows the CNT assembled from each other with a presence of large voids between them (Figure 6-3C). These meso- and macro-voids present within the material will be extremely useful for it further use as catalyst support, especially in the reactions with high mass transfer such as Fischer-Tropsch synthesis.

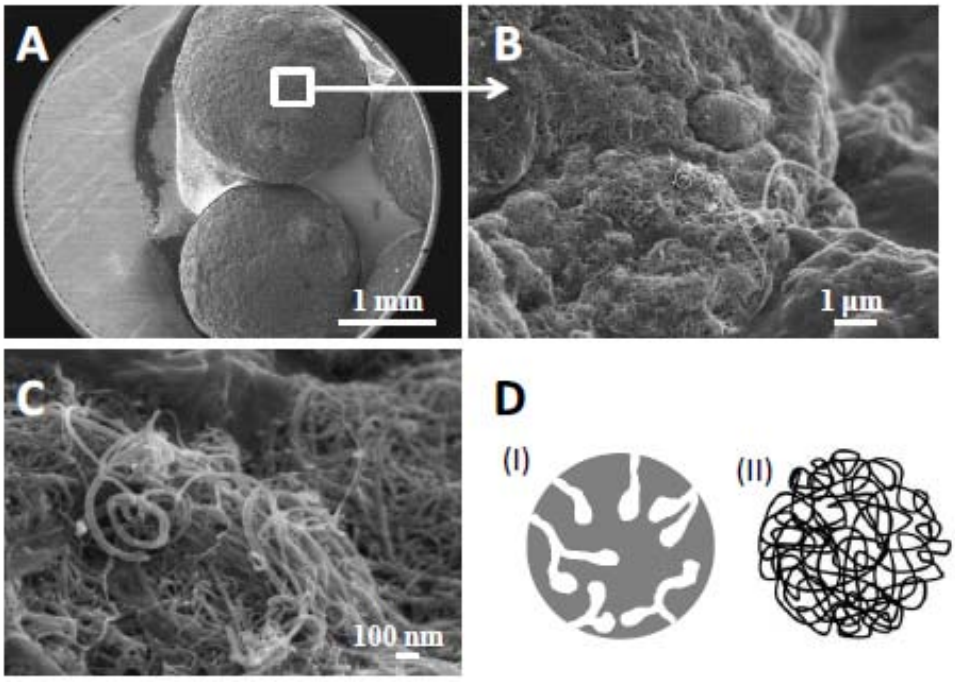

Figure 6-3. SEM micrographs of the CNT composite beads with different magnifications. (**A**) Low magnification SEM micrograph showing the gross morphology of the as-synthesized beads. (**B**, **C**) Medium and high-resolution showing the microstructure of the bead with full accessible porosity. (**D**) Schematic representation of a porous solid packed bed (I) and the self-macronized carbon nanotubes (II) with a fully accessible surface.

The CNT beads can be regarded as a macroscopic object with a fully accessible surface while the porosity is constituted by the voids generated by the entangled carbon nanotubes instead of ink-bottled pores as usually encountered with traditional granular support (Figure 6-3D). In the self-macronized material the diffusion length is much lower due to the

nanoscopic dimension of the carbon nanotubes compared to the traditional porous solid where pores are located far away from the solid surface. These meso- and macroporosity present within the material will be extremely useful for it further use as catalyst support, especially in the reactions with high mass transfer like Fischer-Tropsch synthesis. The post-synthesis treatment also allows a significant improvement of the oxidative resistance of the support for the subsequence use in the FTS reaction.

6.2.3 Porous macroscopic shaping carbon-based materials

A macroscopic shaping of carbon nanostructure materials with tunable porosity, morphologies, and surface chemical functions, such as carbon nanotubes (CNT) or carbon nanofibers (CNF), into integrated structures is of high interest, as it allows a development of novel nano-systems with high performances in filter application and catalysis.

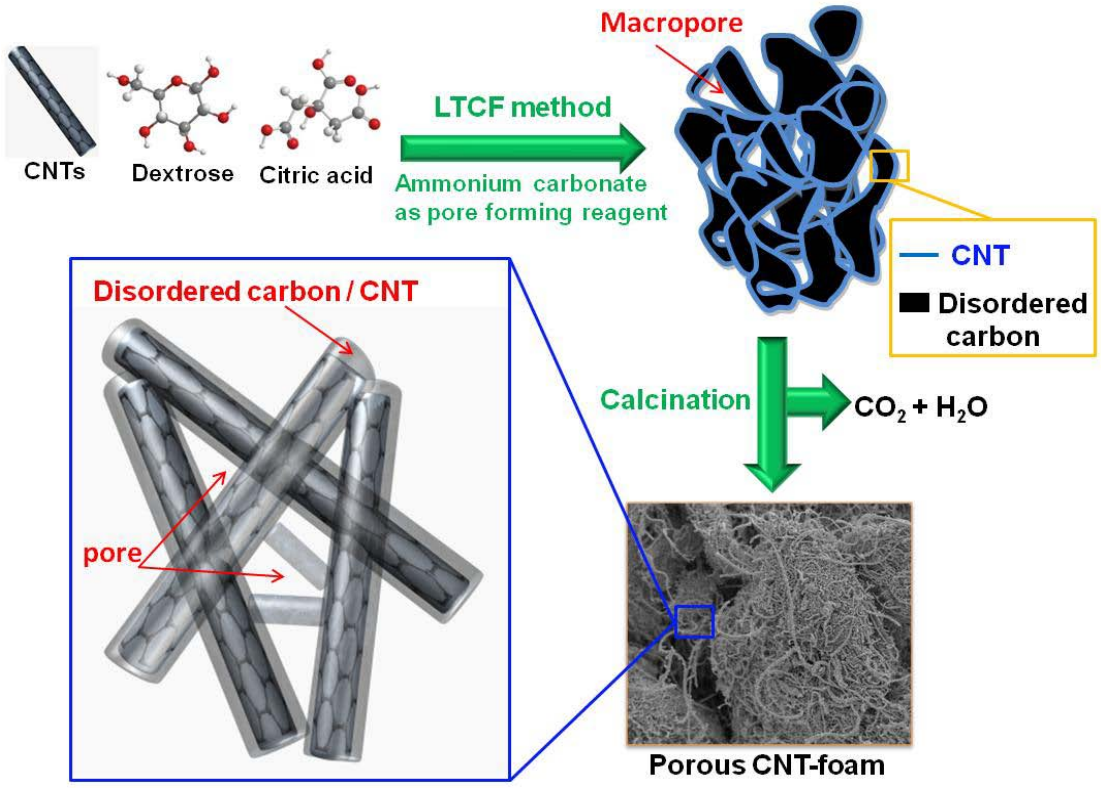

Figure 6-4. Illustration of a low temperature chemical fusion method (LCHF) for the synthesis of porous CNT-foam composites.

As can be seen in Figure 6-4, we developed a low temperature chemical fusion (LTCF) method to synthesize-macronized carbon nanotubes foam (CNT-foam) with controlled size and shape by using CNT as a skeleton, dextrose as a carbon source, and citric acid as carboxyl group donor reacting with hydroxyl group present in dextrose.[5] The obtained composite has a 3D pore structure with high accessible surface area (> 350 m^2/g) and tunable meso- and macro-porosity by adding a variable amount of ammonium carbonate into the starting mixture followed by a direct thermal decomposition.

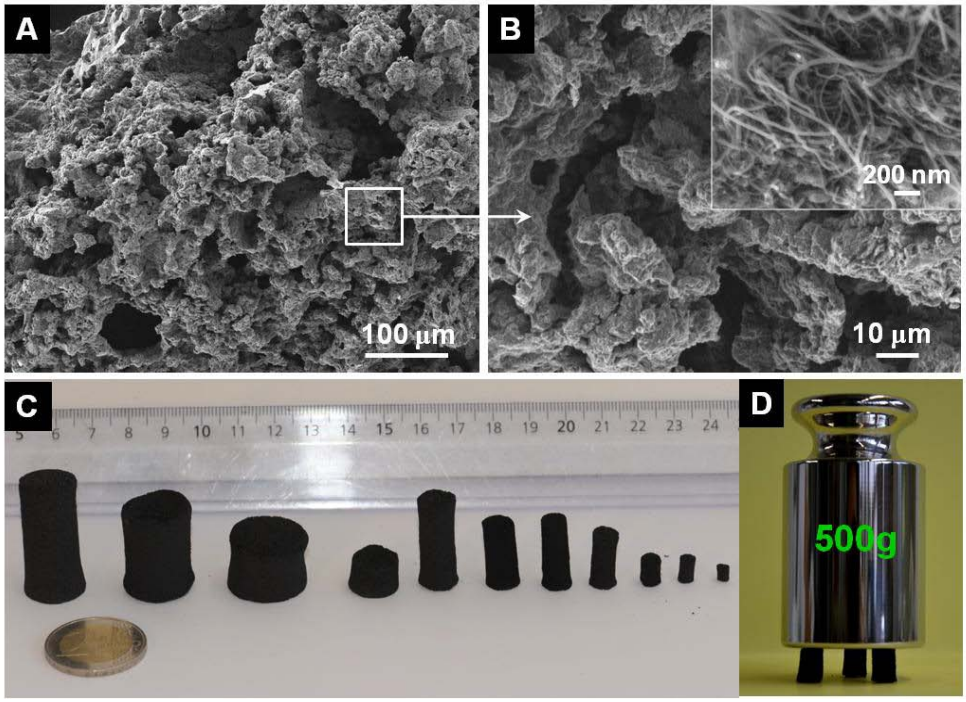

Figure 6-5. (A, B) SEM micrographs of the CNT-foam obtained from calcinations in air flow showing the presence of large voids within the foam and CNT entanglement. (C) Optical photos of representative CNT-foams with different shapes for various applications. (D) Optical photo that shows three CNT-foam cylinders supporting 500g weight without any changes

The representative SEM micrographs of the as-synthesized foam-structured carbon composite are present in the Figure 6-5. The SEM micrograph (Figure 6-5A and B) shows the opened microstructure of the synthesized CNT-foam with full accessible porosity. A developed synthesis method also allows us to synthesize CNT-foam with different size,

ranging from few millimetres to several centimetres, and shape (Figure 6-5C), depending on downstream applications, i.e. waste water treatment or catalytic processes. These high effective surface area and open porosity CNT-foam can be also synthesized with controlled shape, i.e. extrudates, discs, spheres, and size depending to the downstream applications. As shown in Figure 6-5D, CNT-foams can withstand a relative weight load without any changes and the stress tests show that the CNT-foam can withstand a stress pressure of about 1.39 MPa. The as-synthesized CNT-foam exhibits a relatively high mechanical strength which facilitates its handling and transport, while the nanoscopic morphology of the CNT significantly reduces the problem of diffusion and contributes to an improvement of the effective surface area for subsequent applications. It is expected that these hierarchical foams, either made from CNT or CNF, can be efficiently employed as absorbers for removing the trace amounts of metal or impurities present in a waste water, and also as a structured catalyst support for reactions with high mass and heat transfer such as the Fischer-Tropsch synthesis.

References

[1] A. M. Saib, D. J. Moodley, I. M. Ciobica, M. M. Hauman, B. H. Sigwebela, C. J. Weststrate, J. W. Niemantsverdriet, J. van de Loosdrecht, *Catal Today* **2010**, *154*, 271-282.

[2] N. E. Tsakoumis, M. Ronning, O. Borg, E. Rytter, A. Holmen, *Catal Today* **2010**, *154*, 162-182.

[3] A. Brumby, M. Verhelst, D. Cheret, *Catal Today* **2005**, *106*, 166-169.

[4] Y. F. Liu, L. D. Nguyen, T. Truong-Huu, Y. Liu, T. Romero, I. Janowska, D. Begin, C. Pham-Huu, *Mater Lett* **2012**, *79*, 128-131.

[5] Y. Liu, H. Ba, D.-L. Nguyen, O. Ersen, T. Romero, S. Zafeiratos, D. Begin, I. Janowska, C. Pham-Huu, *Journal of Materials Chemistry A* **2013**.

Annex

Annex 1: Publications and Communications

√ ***Publications***

1. Titania-decorated silicon carbide-containing cobalt catalyst for Fischer–Tropsch Synthesis.
   Yuefeng Liu, Benoit de Tymowski, Fabrice Vigneron, Ileana Florea, Ovidiu Ersen, Christian Meny, Patrick Nguyen, Charlotte Pham, Francis Luck, and Cuong Pham-Huu.
   ACS Catalysis 2013, 393-404.

2. Synthesis of porous carbon nanotubes foam composites with high accessible surface area and tunable porosity.
   Yuefeng Liu, Housseinou Ba, Lam D. Nguyen, Ovidiu Ersen, Thierry Romero, Dominique Begin, Izabela Janowska, Cuong Pham-Huu.
   Journal of Materials Chemistry A, 2013, 1, 9508-9516.

3. Microstructural analysis and energy filtered TEM imaging to investigate the structure-activity relationship in Fischer-Tropsch catalysts
   Ileana Florea, **Yuefeng Liu**, Ovidiu Ersen, Christian Meny, Cuong Pham-Huu
   ChemCatChem, 2013, 5, 2610-2620.

4. Carbon nanotubes decorated α-Al_2O_3 containing cobalt nanoparticles for the Fischer-Tropsch reaction.
   Yuefeng Liu, Thierry Dintzer, Ovidiu Ersen, Cuong Pham-Huu.
   Journal of Energy Chemistry, 2013, 22, 279-289.

5. Macroscopic shaping of carbon nanotubes with high specific surface area and full accessibility.
   Yuefeng Liu, Lam D. Nguyen. Tri Truong-Huu, Yu Liu, Thierry Romero, Izabela Janowska, Dominique Begin, Cuong Pham-Huu.

Materials Letter 2012, 79, 128-131.

6. Co-Ru/SiC impregnated with ethanol as an effective catalyst for the Fischer-Tropsch synthesis.
   Benoit de Tymowski, **Yuefeng Liu**, Christian Meny, Christophe Lefèvre, Dominique Begin, Patrick Nguyen, Charlotte Pham, David Edouard, Francis Luck, Cuong Pham-Huu.
   Appllied Catalysis A-Geneneral 2012, 419, 31-40.

7. A facile approach for the preparation of biomorphic CuO-ZrO_2 catalyst for catalytic combustion of methane.
   Jingjie Luo, Huiyuan Xu, **Yuefeng Liu**, Wei Chu, Chengfa Jiang, Xiusong Zhao.
   Appllied Catalysis A-Geneneral, 2012, 423, 121-129.

8. Experimental and modeling study of methane adsorption on activated carbon derived from anthracite.
   Jingjie Luo, **Yuefeng Liu**, Chengfa Jiang, Wei Chu, Wen Jie, Heping Xie.
   J Chem Eng Data, 2011, 56, 4919-4926.

9. Fischer-Tropsch reaction on thermal conductive and re-usable silicon carbide support
   Yuefeng Liu, Ovidiu Ersen, Christian Meny, Francis Luck, Cuong Pham-Huu.
   Submited, 2013.

10. Efficient hierarchical structured composite containing cobalt catalyst for clean synthetic fuel production.
    Yuefeng Liu, Christian Meny, Ovidiu Ersen, Cuong Pham-Huu.
    Under preparation, 2013.

√ ***Patent***

Nouveau support à base de carbure de silicium promu avec du TiO_2 pour la synthèse de Fischer-Tropsch. (FR No: 12 56028)
Yuefeng Liu, Cuong Pham-Huu, Patrick Nguyen, Charlotte Pham.

√ ***Oral presentation***

1. Macroscopic carbon nanotubes foam with high specific surface area and full accessibility
   Y. Liu, L.D. Nguyen, H. Ba, T. Truong-Huu, F. Vigneron, I. Janowska, D. Begin, C. Pham-Huu
   CARBOCAT-V, June 2012, Brixen – Italy

2. Titania-Decorated Silicon Carbide Containing Cobalt Catalyst for the Fischer- Tropsch Synthesis
   Y. Liu, B. de Tymowski, F. Vigneron, I. Florea, O. Ersen, C. Meny, F. Luck, C. Pham-Huu
   11th European Congress on Catalysis – EuropaCat-XI, September 1st-6th, 2013, Lyon, France

3. Titania-doped silicon carbide containing cobalt catalyst for synthetic fuel production
   C. Pham-Huu, **Y. Liu**
   2nd ChemEnergy, January 2013, Berlin – Germany

4. Titania doped silicon carbide (SiC) containing cobalt catalyst for Fischer-Tropsch Synthesis
   Y. Liu, B. Tymowski, F. Vigneron, I. Florea, O. Ersen, P. Nguyen, C. Pham, F. Luck, C. Pham-Huu
   10th Natural Gas Conversion Symposium, March 2013, the Ritz-Carlton Doha

√ ***Poster***

1. Self-supported few-layer graphene beads with high external surface area
   Y. Liu, T. H. Truong1, L. D. Nguyen, I. Janowska, C. Pham-Huu
   ISHHC, September 2011, Berlin- Germany

2. Fischer-Tropsch Synthesis on re-usable silicon carbide containing cobalt catalyst
   B. Tymowski, **Y. Liu**, D. Begin, P. Nguyen, C. Pham, F. Luck, C. Pham-Huu
   ISHHC, September 2011, Berlin- Germany

3. High surface area composite made by α-Al_2O_3 support decorated with a network of carbon nanotubes for catalytic applications

Y. Liu, H. Ba, T. Romero, I. Janowska, D. Begin, C. Pham-Huu
CARBOCAT-V, June 2012, Brixen-Italy

4. High efficient and re-usable Co-Ru/SiC catalyst for the Fischer-Tropsch synthesis
Y. Liu, B. de Tymowski, C. Pham-Huu, P. Nguyen, Ch. Pham, F. Luck
15th International Congress on Catalysis, July 2012, Munich-Germany

5. High surface area composite made by α-Al_2O_3 support decorated with a network of carbon nanotubes for the Fischer-Tropsch Reaction
Y. Liu, T. Dintze, O. Ersen, C. Pham-Huu
2nd ChemEnergy, January 2013, Berlin - Germany

Annex 2: First page of the selected publications

P1: Titania-decorated silicon carbide-containing cobalt catalyst for Fischer–Tropsch Synthesis.

P2 : Microstructural analysis and energy filtered TEM imaging to investigate the structure-activity relationship in Fischer-Tropsch catalysts

P3 : Carbon nanotubes decorated α-Al_2O_3 containing cobalt nanoparticles for the Fischer-Tropsch reaction.

P4 : Macroscopic shaping of carbon nanotubes with high specific surface area and full accessibility.

P5 : Co-Ru/SiC impregnated with ethanol as an effective catalyst for the Fischer-Tropsch synthesis.

P6 : Synthesis of porous carbon nanotubes foam composites with high accessible surface area and tunable porosity.

ACS Catalysis

Research Article

pubs.acs.org/acscatalysis

Titania-Decorated Silicon Carbide-Containing Cobalt Catalyst for Fischer–Tropsch Synthesis

Yuefeng Liu,*[,†] Benoit de Tymowski,[†] Fabrice Vigneron,[†] Ileana Florea,[‡] Ovidiu Ersen,[‡] Christian Meny,[‡] Patrick Nguyen,[§] Charlotte Pham,[§] Francis Luck,[⊥] and Cuong Pham-Huu*[,†]

[†]Laboratoire des Matériaux, Surfaces et Procédés pour la Catalyse (LMSPC), UMR 7515, CNRS-Université de Strasbourg (UdS), 25, rue Becquerel, 67087 Strasbourg Cedex 08, France

[‡]Institut de Physique et Chimie des Matériaux de Strasbourg (IPCMS), UMR 7504, CNRS-Université de Strasbourg (UdS), 23, rue du Loess, 67034 Strasbourg Cedex 02, France

[§]SICAT/ACM Technical Center, Industriestrasse 1, D-77731 Willstätt, Germany

[⊥]Total, Direction Générale-Direction Scientifique, 24 cours Michelet, F-92069 Paris La Défense Cedex, France

Supporting Information

ABSTRACT: The metal–support interactions of titanium dioxide decorated silicon carbide (β-SiC)-supported cobalt catalyst for Fischer–Tropsch synthesis (FTS) were explored by a combination of energy-filtered transmission electron microscopy (EFTEM), ^{59}Co zero-field nuclear magnetic resonance (^{59}Co NMR), and other conventional characterization techniques. From the 2D elemental maps deduced by 2D EFTEM and ^{59}Co NMR analyses, it can be concluded that the nanoscale introduction of the TiO_2 into the β-SiC matrix significantly enhances the formation of small and medium-sized cobalt particles. The results revealed that the proper metal–support interaction between cobalt nanoparticles and TiO_2 led to the formation of smaller cobalt particles (<15 nm), which possess a large fraction of surface atoms and, thus, significantly contribute to the great enhancement of conversion and the reaction rate. The cobalt time yield of the catalyst after modification increased to 7.5×10^{-5} mol_{CO} g_{Co}^{-1} s^{-1} at 230 °C, whereas the C_{5+} selectivity maintained a high level (>90%). In addition, the adequate meso- and macro-pores of the SiC-based support facilitated intimate contact between the reactants and active sites and also accelerated the evacuation of the intermediate products. It was also worth noting that a superior and stable FTS specific rate of 0.56 $g_{C_{5+}}$ $g_{catalyst}^{-1}$ h^{-1} together with high C_{5+} selectivity of 91% were obtained at common industrial content of 30 wt % cobalt.

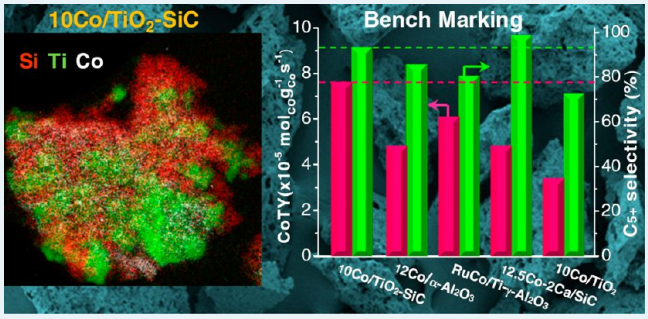

KEYWORDS: *metal–support interaction, Fischer–Tropsch synthesis, silicon carbide, cobalt, titanium oxide, energy-filtered TEM, ^{59}Co NMR, catalysis*

1. INTRODUCTION

Fischer–Tropsch synthesis (FTS) is a key technology in the more global gas-to-liquids (GTL) process, which allows the transformation of synthesis gas ($2H_2$ + CO), issued from natural gas reforming into liquid hydrocarbons, followed by hydrocracking of the heavy fraction into useful compounds, such as naphtha, diesel, lubricants, and others.[1−6] The most employed active phase for the low-temperature FTS process is supported cobalt, either pure or doped with trace amounts of noble metal to enhance the reduction of the active phase and to improve the dispersion of metal particles.[7−11] Cobalt presents several advantages, such as high stability, high activity for liquid hydrocarbons formation and low selectivity toward oxygenated products, resistance to oxidation, low water-gas shift (WGS) tendency, and acceptable price for industrial development. However, the high activity of the cobalt phase also leads to an extremely high sensitivity of the catalyst selectivity to the reaction temperature. Cobalt active phase is typically employed in a supported form for the FTS process. The support should display a relatively high specific surface area to achieve a high dispersion of the metal particles, good mechanical and hydrothermal resistance, and a medium level of metal–support interaction to allow complete reduction of the active phase and to prevent sintering of the cobalt. The most employed supports for the FTS are alumina; silica; titania; and carbon-based materials, such as activated carbon, carbon nanotubes, and nanofibers.[12−19] Among these supports, alumina, either pure or promoted, is the most employed as a support for commercial catalysts. However, on traditional supports such as alumina and silica, it is difficult to reduce small particles of metal oxide

Received: November 11, 2012
Revised: January 17, 2013
Published: January 22, 2013

ChemPubSoc Europe

DOI: 10.1002/cctc.201300103

Microstructural Analysis and Energy-Filtered TEM Imaging to Investigate the Structure–Activity Relationship in Fischer–Tropsch Catalysts

Ileana Florea,[a] Yuefeng Liu,[b] Ovidiu Ersen,*[a] Christian Meny,[a] and Cuong Pham-Huu*[b]

We present herein the application of chemical imaging based on energy-filtered TEM in 2D and 3D modes to determine the distribution of phases in Co/TiO_2–SiC catalysts used in Fischer–Tropsch synthesis. In combination with more traditional techniques such as high-resolution TEM imaging, it allowed us to precisely characterize the microstructure and the relative distribution of the three compounds, Co, Si, and Ti, before and after the catalytic reaction. We show that the TiO_2 doping was almost homogenous within the bimodal porous structure of β-SiC. The characteristics of the cobalt nanoparticles depended on the phase they are in contact with: small nanoparticles are found on TiO_2 and larger nanoparticles close to SiC. Enhancement of the catalytic performance and higher stability were observed for the Co/TiO_2–SiC catalyst relative to Co/SiC, which was attributed to the better dispersion of cobalt on TiO_2-doped SiC support and to the relatively strong Co–TiO_2 interaction. From a general point of view, this work illustrates that the advanced TEM-based techniques are unavoidable for the characterization and the optimization of heterogeneous catalysts.

Introduction

The decrease of the proven oil reserves and the huge increase in the worldwide energy demand, especially in emerging countries such as China and India, have driven the industrial interest to other sources of energy supply such as coal, natural gas and biomass.[1–3] These primary materials are subsequently transformed by reaction with steam or oxygen to a synthesis gas mixture, which is then converted into valuable ultra-clean synthetic fuels. The Fischer–Tropsch synthesis (FTS) is a key technology in the more global gas-to-liquids process, which allows the transformation of synthesis gas ($2H_2 + CO$), originated from natural gas reforming, into liquid hydrocarbons, which are then further processed by hydrocracking of the heavy fraction into useful compounds such as naphtha, diesel, lubricants, and others.[2–4] The FTS fuels are free of sulfur, nitrogen, and aromatic compounds, which render them extremely useful in the field of transportation, taken into account the increasingly stringent environmental legislation on transportation fuels. In addition, FTS has received a renewed interest during the last decade, according to the number of FTS plants operated in recent years.[5] The industrial interest in the FTS development is mostly induced by the recent oil price volatility and is also driven by a low price of gas consecutively to the large-scale exploitation of shale gas. A large research effort has been devoted to the improvement of the FTS catalyst both in terms of activity and selectivity to reduce the cost of the process. High activity allows reducing the amount of catalyst needed and, hence, decreasing the amount of waste generated during catalyst formation. High selectivity allows for maximization of the desired products and reduction of the byproducts such as light hydrocarbons or CO_2. Among the parameters that could strongly influence the FTS performance, the development of new supports represents a core issue.

The most employed active phase for the low-temperature FTS process is cobalt, either pure or doped with trace amounts of noble metal, to enhance the reduction of the active phase and to improve the metal particles dispersion.[6–9] Cobalt presents several advantages, such as high stability, high activity towards liquid hydrocarbons formation and low selectivity towards oxygenated products, resistance towards oxidation, low water gas shift tendency, and acceptable price for industrial development. Industrial cobalt catalysts consist of cobalt nanoparticles that are well dispersed on a high-surface-area support to increase as much as possible the active-site density along with a relatively high cobalt loading.[3] The support should display a relatively high specific surface area to promote a high dispersion of the metal particles, good mechanical and hydrothermal resistance- and a medium level of metal–support interaction to allow complete reduction of the active phase and prevent sintering of the latter. The most employed supports for FTS are alumina, silica, titania, and carbon-based materials such as activated carbon, carbon nanotubes, and nanofibers.[6,10–16] Amongst the different industrial catalyst supports, silicon carbide (β-SiC), pure or doped, with medium to high specific surface area (20 to $>100\ m^2 g^{-1}$), synthesized by a gas–

[a] Dr. I. Florea, Prof. O. Ersen, Dr. C. Meny
Institut de Physique et Chimie des Matériaux de Strasbourg (IPCMS)
UMR 7504 CNRS-Université de Strasbourg
23, rue du Lœss, 67034 Strasbourg cedex 02 (France)
E-mail: ovidiu.ersen@ipcms.u-strasbg.fr

[b] Y. Liu, Dr. C. Pham-Huu
Institut de Chimie et Procédés pour l'Energie, l'Environnement et la Santé (ICPEES)
UMR 7515 CNRS, ECPM, Université de Strasbourg
25, rue Becquerel, 67087 Strasbourg cedex 08 (France)
E-mail: cuong.pham-huu@unistra.fr

Available online at www.sciencedirect.com
ScienceDirect
Journal of Energy Chemistry 22(2013)279–289
JOURNAL OF ENERGY CHEMISTRY
www.elsevier.com/locate/jngc

Carbon nanotubes decorated α-Al_2O_3 containing cobalt nanoparticles for Fischer-Tropsch reaction

Yuefeng Liu[a*], Thierry Dintzer[a], Ovidiu Ersen[b], Cuong Pham-Huu[a*]

a. Laboratoire des Matériaux, Surfaces et Procédés pour la Catalyse (LMSPC), UMR 7515 CNRS-Université de Strasbourg (UdS), 25, rue Becquerel, 67087 Strasbourg Cedex 08, France; b. Institut de Physique et Chimie des Matériaux de Strasbourg (IPCMS), UMR 7504 CNRS-Université de Strasbourg (UdS), 23, rue du Loess, 67037 Strasbourg Cedex 02, France

[Manuscript received October 26, 2012; revised December 14, 2012]

Abstract

A new hierarchical composite consisted of multi-walled carbon nanotubes (CNTs) layer anchored on macroscopic α-Al_2O_3 host matrix was synthesized and used as support for Fischer-Tropsch synthesis (FTS). The composite constituted by a thin shell of a homogeneous, highly entangled and structure-opened carbon nanotubes network and it exhibited a relatively high and fully accessible specific surface area of 76 $m^2 \cdot g^{-1}$, compared with that of 5 $m^2 \cdot g^{-1}$ of the original α-Al_2O_3support. The metal-support interaction between carbon nanotubes surface and cobalt precursor and high effective surface area led to a relatively high dispersion of cobalt nanoparticles. This hierarchically supported cobalt catalyst exhibited a high FTS activity along with an extremely high selectivity towards liquid hydrocarbons compared with the cobalt-based catalyst supported on pristine α-Al_2O_3 or on CNTs carriers. This improvement can attribute to the high accessibility of composite surface area comparing with the macroscopic host structure alone or to the bulk CNTs where the nanoscopic dimension induced a dense packing with low mass transfer which favoured the problem of reactants competitive diffusion towards the cobalt active site. In addition, intrinsic thermal conductivity of decorated CNTs could help the heat dissipating throughout the catalyst body, thus avoiding the formation of local hot spots which appeared in high CO conversion under pure syngas feed in FTS reaction. Cobalt supported on CNTs decorated α-Al_2O_3 catalyst also exhibited satisfied high stability during more than 200 h on stream under relatively severe conditions compared with other catalysts reported in the literature. Finally, the macroscopic shape of such composite easily rendered its usage as catalyst support in a fixed-bed configuration without facing problems of transport and pressure drop as encountered with the bulk CNTs.

Key words

carbon nanotubes; Fischer-Tropsch synthesis; α-Al_2O_3; hierarchical support; cobalt nanoparticles

1. Introduction

Since the middle of the last century, crude oil has been one of the central primary energy carriers compared with other energy sources such as natural gas or coal. The extracted crude oil shows limited availability nowadays with lower quality and thus, new sources of energy supply with better quality need to be developed in order to face the ever-increasing energy demand around the world. Clean fuels which are free of sulfides, nitrides and aromatics can be synthesized from natural gas (gas-to-liquids, GTL), coal (coal-to-liquids, CTL) or biomass (biomass-to-liquids, BTL) via the process of Fischer-Tropsch synthesis (FTS) [1,2]. Among these different raw materials natural gas is very likely to become a principal source of energy that is easy to transport and handle and thus, GTL process will become even more important in the near future. In addition, natural gas also contains higher ratio of hydrogen versus carbon that leads to a H_2/CO ratio of 3 afterreforming process. It is higher than in production processes from other raw materials like crude oil, coal or biomass and H_2/CO ratio will be further adjusted with the aid of water-gas-shift reaction before admitting to FTS unit.

Cobalt components are widely applied as active sites in Fischer-Tropsch synthesis because of their high activity and C_{5+} selectivity, lower water gas shift (WGS) activity and relatively slower deactivation [3−5]. Thus, supported cobalt catalysts are well known to be the best candidates for FTS towards higher hydrocarbons (C_{5+}) [4]. The catalyst productivity can be directly predicted from the number of cobalt atoms exposed on the surface of small cobalt particles. These small cobalt particles are responsible for the significant enhancement of FTS performance compared with that obtained on the undoped catalyst with much bigger active phase particle size.

* Corresponding author. Tel: +33-368852667; Fax: +33-368852674; E-mail: yue-feng.liu@etu.unistra.fr (Y.Liu), cuong.pham-huu@unistra.fr (C.Pham-Huu)

Materials Letters 79 (2012) 128–131

Contents lists available at SciVerse ScienceDirect

Materials Letters

journal homepage: www.elsevier.com/locate/matlet

Macroscopic shaping of carbon nanotubes with high specific surface area and full accessibility

Yuefeng Liu [a], Lam D. Nguyen [b], Tri Truong-Huu [a], Yu Liu [a], Thierry Romero [a], Izabela Janowska [a], Dominique Begin [a], Cuong Pham-Huu [a,*]

[a] Laboratoire des Matériaux, Surfaces et Procédés pour la Catalyse, CNRS-Université de Strasbourg (UdS) UMR 7515, 25, rue Becquerel, 67087 Strasbourg Cedex 08, France
[b] Da-Nang University of Technology, University of Da-Nang, 54, Nguyen Luong Bang, Da-Nang, Viet nam

ARTICLE INFO

Article history:
Received 1 November 2011
Accepted 28 March 2012
Available online 4 April 2012

Keywords:
Carbon nanotubes
Macroscopic shaping
Full accessibility
Pressure drop
Catalyst support

ABSTRACT

Carbon nanotubes (CNTs) with controlled macroscopic shape, i.e. beads, extrudates, disk, etc., were prepared by gelation process. The formed CNT beads (1-2 mm) were constituted by highly entangled CNT forming a dense network exhibiting a rather high specific surface ($>180\ m^2.g^{-1}$) and also full porous network accessibility. The highly opened porosity of this material also drastically reduces the overall pressure drop across the packed bed compared to the bulk CNT material. The macroscopic shaping eases the handling and the transport of these nanoscopic materials and permits the direct use of them as catalyst supports in conventional catalytic processes.

1. Introduction

Carbon nanotubes (CNTs, 1D) have been studied by numerous research groups in many potential applications including electronic, light weight/high strength composites, selective filter, sensor and catalysis [1–5]. In the heterogeneous catalysis application, the nanoscopic dimension of the CNT provides a high effective and fully accessible surface area to the reactant leading to a higher catalytic performance compared to the traditional supports [6]. However, for catalytic applications, the direct use of CNT in a powder form is limited to the liquid-phase reaction while its use in a fixed-bed reactor is hampered due to the problems linked with the high pressure drop across the catalytic bed. In order to solve this problem, some attempts to make CNT with controlled macroscopic shape have been reported either by a direct synthesis of vertically-aligned CNTs (VA-CNTs) [7,8], Bucky Pearls™ pellets from Carbon Nanotechnologies Inc. (CNI), bucky paper [9] or by supporting the CNT on a macroscopic host matrix, i.e. foam, felt, spheres [10–13]. However, in the case of the VA-CNTs, the high density of the CNT induces a low accessibility of the reactants to the active site which is located within the carbon nanotube array. For the supported CNT-based composite, the final specific surface area of the composite is generally lower compared to that of the unsupported CNT due to the presence of a low specific surface area host matrix. In addition, during the catalyst preparation, part of the metal active phase could also be deposited on or within the porosity of the host matrix and thus, would be less accessible towards the reactant. It is then of interest to find a new method to make CNT composites with a macroscopic shape, a high accessible surface area and a high mechanical strength in order to use it as catalyst support in conventional reactors. The highly accessible surface area is of primary importance in the field of heterogeneous catalysis for which the access of the reactants to the active sites and the desorption rate of the products govern in some extent the overall catalytic activity and selectivity as well.

The aim of the present article is to report a new method to elaborate carbon nanotubes with a controlled macroscopic shaping, a high external surface area and good accessibility along with low pressure drop for subsequence use as catalyst support. The synthesis method is based on a coagulation process using alginate as a gelling agent, followed by a thermal step to make entangled carbon nanotubes with homogeneous size and shape. The macroscopic shape of the composite can be finely tuned, i.e. beads, extrudates or plates, depending on the downstream application.

2. Experimental section

2.1. Carbon nanotubes synthesis

Multi-walled carbon nanotubes (CNTs) were synthesized by a chemical vapor deposition (CVD) method using a mixture of C_2H_6/H_2 and the Fe/Al_2O_3 as growth catalyst [14,15]. The reaction temperature

* Corresponding author. Tel.: +33 3 68 85 26 75; fax: +33 3 68 85 27 74.
E-mail address: cuong.pham-huu@unistra.fr (C. Pham-Huu).

0167-577X/$ – see front matter © 2012 Elsevier B.V. All rights reserved.
doi:10.1016/j.matlet.2012.03.107

Applied Catalysis A: General 419–420 (2012) 31–40

Contents lists available at SciVerse ScienceDirect

Applied Catalysis A: General

journal homepage: www.elsevier.com/locate/apcata

Co–Ru/SiC impregnated with ethanol as an effective catalyst for the Fischer–Tropsch synthesis

Benoit de Tymowski[a], Yuefeng Liu[a], Christian Meny[b], Christophe Lefèvre[b], Dominique Begin[a], Patrick Nguyen[c], Charlotte Pham[c], David Edouard[a], Francis Luck[d], Cuong Pham-Huu[a,*]

[a] Laboratoire des Matériaux, Surfaces et Procédés pour la Catalyse, CNRS-Université de Strasbourg (UdS), UMR 7515, 25, rue Becquerel, 67087 Strasbourg Cedex 08, France
[b] Institut de Physique et Chimie des Matériaux de Strasbourg (IPCMS), CNRS-Université de Strasbourg (UdS), UMR 7504, 23, rue du Loess, 67037 Strasbourg Cedex 02, France
[c] SICAT Technical Center, Industriestraße, 1-B310, D-77731 Willstätt, Germany[1]
[d] Total S.A., 2, place Jean Millier, La Défense 6, F-92078 Paris La Défense Cedex, France

ARTICLE INFO

Article history:
Received 3 August 2011
Received in revised form 2 January 2012
Accepted 4 January 2012
Available online 12 January 2012

Keywords:
Silicon carbide
Cobalt
Ruthenium
Fischer–Tropsch synthesis
Ethanol
^{59}Co NMR
Stacking faults

ABSTRACT

Silicon carbide containing cobalt (30 wt.%) doped with 0.1 wt.% of ruthenium catalysts prepared by incipient wetness impregnation of cobalt nitrate with either ethanol or water were tested in the Fischer–Tropsch synthesis (FTS) in a fixed-bed configuration. The catalyst prepared with ethanol exhibits a higher FTS performance compared to the one prepared with water and especially at high reaction temperature, i.e. 230 °C. The FTS performance of the cobalt-based catalyst impregnated with ethanol further increases, under high temperature and high space velocity, to reach a steady state reaction rate of 0.54 g_{CH_2} $g_{catalyst}^{-1}$ h^{-1}, and a relatively high C_{5+} selectivity of about 90%. In addition, the catalyst also exhibits a relatively high stability as a function of time on stream. ^{59}Co zero field NMR analysis has indicates that the proportion of cobalt atoms engaged in the small hcp cobalt particles (<8 nm) was higher for the ethanol impregnated catalyst and also to the more homogeneous dispersion of the ruthenium atoms within the cobalt network forming an alloy.

1. Introduction

Due to the stagnation of proven reserves of crude oil it is expected that the utilization of natural gas will probably become of prime importance in the energy field in the near future. In the Gas-To-Liquid (GTL), Coal-To-Liquid (CTL) and Biomass-To-Liquid (BTL) processes, Fischer–Tropsch synthesis (FTS) is a key technology, which allows the transformation of synthesis gas issued from different sources into very long chain hydrocarbons followed by hydrocracking of the heavy fraction into useful compounds such as naphtha, diesel, lubricants and others. Among these processes which have received increasing scientific and industrial interest in the last decades [1–6] the GTL is the most developed one. Recent advances in catalyst development and reactor technology have significantly contributed to the fast growth of the GTL process during the last decade for supplying ultra-clean fuels (sulfur- and nitrogen-free and no aromatics) for transportation. Cobalt is one of the most active metals for the FTS reaction and is mostly employed as supported catalyst due to its reasonable price, high stability, high activity, high selectivity to higher hydrocarbons and low water–gas shift activity [1]. Typically, the cobalt metal loading ranges from 10 to 30 g per 100 g support. In order to increase the active site density per volume it is generally supported on a high specific surface area carriers such as alumina, silica or titanium dioxide [7–9]. Since FTS is a highly exothermic reaction, the removal of reaction heat at high CO conversion is a major concern. However, the above-mentioned supports are insulating materials which are not able to prevent hot spot formation within the catalyst bed, leading to low liquid hydrocarbon selectivity. Indeed, on insulating supports such as alumina or silica the heat transfer within the catalyst bed could induce temperature gradients in different parts of the bed. In areas where high conversion of CO occur the catalyst temperature could be high whereas in other parts of the bed the temperature could be significantly lower. Depending to the pore size distribution of the support, a temperature gradient could also occur within the catalyst body, i.e. between the catalyst outer surface and the catalyst matrix, which could modify the liquid hydrocarbon selectivity of the reaction. New developments dealing with the use of conductive supports such as metallic foams or monoliths have recently been reported for improving the heat transfer for the FTS reaction [10–14].

* Corresponding author. Tel.: +33 3 68 85 26 67; fax: +33 3 68 85 26 74.
E-mail address: cuong.pham-huu@unistra.fr (C. Pham-Huu).
[1] www.sicatcatalyst.com.

0926-860X/$ – see front matter © 2012 Elsevier B.V. All rights reserved.
doi:10.1016/j.apcata.2012.01.004

Journal of Materials Chemistry A

RSC Publishing

PAPER

View Article Online
View Journal | View Issue

Synthesis of porous carbon nanotubes foam composites with a high accessible surface area and tunable porosity

Cite this: *J. Mater. Chem. A*, 2013, **1**, 9508

Yuefeng Liu,*[a] Housseinou Ba,[a] Dinh-Lam Nguyen,[b] Ovidiu Ersen,[c] Thierry Romero,[a] Spyridon Zafeiratos,[a] Dominique Begin,[a] Izabela Janowska[a] and Cuong Pham-Huu*[a]

Received 15th February 2013
Accepted 11th April 2013

DOI: 10.1039/c3ta10695k

www.rsc.org/MaterialsA

The macroscopic shaping of carbon nanostructure materials with tunable porosity, morphologies, and functions, such as carbon nanotubes (CNT) or carbon nanofibers (CNF), into integrated structures is of great interest, as it allows the development of novel nanosystems with high performances in filter applications and catalysis. In the present work, we report on a low temperature chemical fusion (LTCF) method to synthesize a self-macronized carbon nanotubes foam (CNT-foam) with controlled size and shape by using CNT as a skeleton, dextrose as a carbon source, and citric acid as a carboxyl group donor reacting with the hydroxyl group present in dextrose. The obtained composite has a 3D pore structure with a high accessible surface area (>350 $m^2\ g^{-1}$) and tunable meso- and macro-porosity formed by the addition of a variable amount of ammonium carbonate into the starting mixture followed by a direct thermal decomposition. The as-synthesized CNT-foam also exhibits a relatively high mechanical strength which facilitates its handling and transport, while the nanoscopic morphology of the CNT significantly reduces the problem of diffusion and contributes to an improvement of the effective surface area for subsequent applications. These CNT-foams are successfully employed as selective and recyclable organic absorbers with high efficiency in the field of waste water treatment.

1 Introduction

Carbon nanotubes (CNT) possess a nanoscopic dimension with a high specific surface area (>100 $m^2\ g^{-1}$), high thermal conductivity and high thermal resistance under an inert atmosphere, and high chemical and environmental stability.[1,2] The surface character of these materials can also be fine-tuned, *i.e.* hydrophilic or hydrophobic character, depending on the downstream application.[3,4] Due to the exceptional physical and chemical properties cited above, CNT have been a subject of ever increasing scientific and industrial interest during the last few decades,[5] especially in the field of catalysis,[6–10] electrochemical energy storage[11–13] and waste water treatment.[14–16] For these applications, a nanoscopic size of carbon nanotubes significantly reduces the problem linked with mass transfer limitations while the high specific surface area provides a large number of anchorage sites either to adsorb pollutants (waste water treatment) or to host active nanoparticles (catalysis). As a consequence, the overall adsorption capacity or catalytic activity per unit of volume of such materials is significantly improved. The nanoscopic size, however, is a main drawback, as it renders the handling and transport of the materials and the recovery of used materials difficult, especially in a liquid medium, due to the problem of filter plugging.[17] The development of hybrid materials that can efficiently combine the nanoscopic properties with a macroscopic shape is therefore of great interest.[17–20] According to the literature reports, CNT can be efficiently deposited on several macroscopic supports such as alumina[21] or carbon,[22] allowing their direct use in conventional systems. However, it is worth noting that up to now works dedicated to self-macronization of CNT are relatively scarce.[17,23] It is expected that such self-macronization of CNT can additionally open new application fields for this material.

Here we report on a facile and simple approach to synthesize a macroscopic 3D interconnected carbon nanotubes foam (CNT-foam) with a high accessible surface area and relatively high mechanical strength for subsequent use in the field of waste water treatment. In the case of waste water treatment the foam is pre-treated under appropriate conditions in order to obtain a hydrophobic-type surface which can selectively adsorb organic compounds present in a water medium. The pore size of the foam can also be fine-tuned by changing the content of a pore-forming agent or by adding a removable template, *i.e.* alumina or silica powder. The synthesis method is easy for up-scaling and the final size and shape of the composite can be tailored at will depending on the downstream applications.

[a]*Institut de Chimie et Procédés pour l'Energie, l'Environnement et la Santé (ICPEES), UMR 7515 CNRS-Université de Strasbourg (UdS), 25, rue Becquerel, 67087 Strasbourg Cedex 08, France. E-mail: liuyuefeng307@hotmail.com; cuong.pham-huu@unistra.fr; Fax: +33 3 68 85 26 74; Tel: +33 3 68 85 26 67*

[b]*University of Danang, University of Science and Technology, Chemical Engineering, 54, Nguyen Luong Bang, Danang, Vietnam*

[c]*Institut de Physique et Chimie des Matériaux de Strasbourg (IPCMS), UMR 7504 CNRS-Université de Strasbourg (UdS), 23, rue du Loess, 67034 Strasbourg Cedex 02, France*

Yuefeng LIU

Silicon carbide and nano-carbons containing cobalt catalysts for the Fischer-Tropsch synthesis

Résumé

La Synthèse Fischer-Tropsch (SFT) est une technologie clé pour transformer le gaz de synthèse ($CO + 2H_2$) en hydrocarbures liquides, matières premières pour la chimie de base. Il s'avère que les catalyseurs à base de cobalt sont les plus performants et leur développement dans l'industrie impose au matériau support de posséder une conductivité thermique élevée et une structure ouverte.

Dans ce travail, un nouveau support hiérarchisé constituée de α -Al_2O_3, recouvert homogènement de nanotubes de carbone, a été préparé pour supporter des catalyseurs au cobalt. Ces derniers montrent une très grande sélectivité en hydrocarbures liquides ainsi que de meilleures activités catalytiques. Les performances obtenus ont pu être améliorées en déposant une fine couche de TiO_2 sur la surface des nanotubes de carbone, améliorant considérablement la dispersion du cobalt et l'activité. Le TiO_2, également introduit dans la matrice de β-SiC lors de la synthèse, interagit fortement avec les sites actifs de cobalt, conduisant ainsi à sa grande dispersion et à une meilleure activité et stabilité dans la réaction de SFT. Parallèlement, un catalyseur à base de β-SiC de haute porosité, recouvert d'une couche de dioxyde de titane monocristallin a été développé et testé. Un taux spécifique de 1,2 $g_{C5+}.\ g_{cat}^{-1}.\ h^{-1}$ et une sélectivité en C_{5+} de 86% ont été obtenus. Ces performances sont les plus élevées signalées jusqu'à présent sur des catalyseurs sans cobalt.

Mots clés: Synthèse Fisher-Tropsch, Cobalt, Conductivité Thermique, β-SiC, Nanotube de carbone, Structure hiérarchisée

Résumé en anglais

The Fischer-Tropsch synthesis (FTS) is a key technology to transform the synthesis gas ($2H_2$ + CO) into liquid hydrocarbons as the basic chemical feedstock. It can be found that the cobalt active sites supported on the materials with high thermal conductivity, opened structure is necessary to accelerate FTS synthesis process in the development of industry catalysts.

In this work, a new hierarchical support consisting of α-Al_2O_3, which is homogeneously covered by a layer of carbon nanotubes, is successfully prepared to support cobalt catalyst. The supported cobalt catalysts show extremely high selectivity towards liquid hydrocarbons along with the better catalytic activity. The FTS performance obtained on this support can be further improved by coating a thin layer of TiO_2 on the CNTs surface which significantly improve the cobalt dispersion and in turn, the FTS activity.The TiO_2 is also successfully introduced into the matrix of β-SiC during the synthesis process which strongly interacts with cobalt active sites, leading to high dispersion of cobalt, accounting for the better activity and stability in FTS reaction. In the mean time, a highly activity Fischer-Tropsch catalyst based on single crystalline titanium dioxide coated high porosity β-SiC was also developed. The FT specific rate of 1.2 $g_{C5+}\cdot g_{cat}^{-1}\cdot h^{-1}$ and a C_{5+} selectivity of 86 % are obtained, which are among the highest FT performance reported up to now on cobalt noble-free catalyst .

Keywords: Fishcer-Tropsch Synthesis, Cobalt, Thermal conductivity, β-SiC, Carbon nanotube, hierarchical structure